THE UNIVERSITY OF SYDNEY

Bioengineering Stents for Proactive Biocompatibility

From Biomaterials to Stents

Thamarasee M. Jeewandara

A thesis submitted in fulfilment of the requirements for the degree of Doctor of Philosophy

Sydney Medical School - University of Sydney

Translational Research Group - The Heart Research Institute

September 2015

Declaration

I declare that the work described in this thesis is entirely my own except where specifically stated in the text. This work has not been previously submitted for any degree at any institution.

_____

Thamarasee M. Jeewandara

Acknowledgements

I would like to thank the primary supervisor Dr. Martin Ng for giving me the opportunity to join the Heart Research Institute and the University of Sydney, for the research project in bioengineering. Special thanks to Prof. Marcela Bilek and Prof. Tony Weiss for their input to the project in relation to biochemistry, surface engineering and plasma physics. Special gratitude to Dr. Yixiang Gan of the School of Civil Engineering USyd, for the training facilities in nanoindentation and surface characterization, provided within a very short period of time. Special thanks to co-supervisor Dr. Steven Wise for his support at the early stages of the project, editing/writing assistance with review, and for encouraging me to pursue work on the novel cobalt chromium biomaterial.

I am very grateful to the University of Sydney Medical School, for supporting my candidature with the Elizabeth and Henry Hamilton-Browne scholarship, awarded over the past 3 years. My appreciation and thanks go to Dr. Yongbai Yin for his initial involvement with PAC surface deposition and stent modification. I deeply appreciate the assistance of Physicists Dr. Alexey Kondyurin and Mr. Miguel Santos during subsequent optimization and development of the plasma activated coating process at plasma physics. I thank Miss Barbara James, Prof. Hala Zreiqat and A. Prof. Colin Dunstan in Biomaterials and Tissue Engineering Research unit, for early assistance with resin histopathology techniques. Special mention to Anzac Institute at Concord Hospital for the training provided on resin histology sectioning and staining procedures, prior to obtaining microtome facilities at the HRI. I am very thankful to Dr. Anna Waterhouse, for assisting me with thesis write-up, and allowing me to present and discuss component of data obtained during her candidature, within chapter 2 (credited within chapter).

I couldn't have done extensive level of characterization for material science without the support of SEM, AFM and FIB specialist Steven Moody and TEM specialist Dr. Hongwei Liu at the

Australian Centre for Microscopy and Microanalysis (ACMM) at USyd. Special thanks also to Dr. Patrick Trimby, Miss Naveena Gokoolparsadh, and Adam Sikorski at ACMM, for training me in SEM, biological specimen preparation, and material preparation for microscopy. I thank Pat Pisansarakit at the HRI for providing cell lines for tissue culture. I am immensely grateful to the Library facilities and Staff at Fisher and SciTech, at the University, for assistance during the course of my candidature, and especially during thesis write up. Furthermore I am very grateful to the American Heart Association, for the opportunities provided to present work related to the thesis at various stages overseas. These opportunities specifically assisted our outreach, and helped gain first hand insight to current medical research in cardiovascular disease. I would like to thank Dr. Ng again in encouraging me to actively take part in conferences and presentations nationally and internationally throughout the PhD candidature.

Finally, my very special thanks to all my family, and friends for their love and support. Thank you.

Summary

Briefly, the thesis describes extensive methods to characterize novel modified biomaterial surfaces *in vitro*, and investigate its short term implications at the artery interface *in vivo*. The plasma technology has been previously deposited on a stainless steel biomaterial (316LSS) and investigated initially in the stent form *in vivo*. At the start of this thesis, histopathology characterizations to evaluate artery-stent interface interactions *in vivo*, were conducted with resin-artery-stents. The pilot study was followed by extensive material characterization on novel biomaterial cobalt chromium metal alloy L605, complying to ASTM F90 specifications - used to manufacture new generation cobalt chromium stents, to treat coronary artery disease (CAD).

The plasma technology is unique for its ability to not delaminate from a biomaterial, while providing significant surface hemocompatibility as well as cytocompatibility, and allow covalent attachment of a bioactive protein in its native conformation. In accordance to previous studies, we chose tropoelastin (TE) as an ideal candidate, to bioengineer modified material surfaces via covalent protein binding. The initial investigation aimed to evaluate feasibility of PAC+TE stenting in an established rabbit iliac artery animal model. The primary hypothesis was that PAC+TE stents would assist enhanced endothelialization, reduce thrombosis and markers of inflammation, compared to alloy 316LSS bare metal stents (BMS). Although some results were in partial support of the hypothesis - indicating an improvement to early markers of thrombosis and neointimal hyperplasia, overall at 7 days there was no significant difference to endothelialization between the two stents (BMS vs. PAC+TE) investigated. Since preliminary investigations confirmed feasibility of PAC+TE stents *in vivo* for the first time herein, future studies were implicated with extended endpoints and larger animal cohorts for more robust translational studies.

Extensive investigations thereafter with the novel CoCr biomaterial, provided us opportunity to address two primary questions in relation to plasma technology:

1. How does PAC adhere to a novel biomaterial (L605) surface to prevent delamination under compressive stress
2. How does PAC-L605 maintain superior hemocompatibility and promote homogenous cell culture, compared to alloy L605.

We first investigated the plasma modified biomaterial with plasma kinetics, nanoindentation, followed by surface roughness measurements. The aim was to characterize plasma modification extensively, and calculate coating integrity, compared to bare metal alloy via indentation/external compression. Once coating integrity was confirmed with nanoindentation, we investigated PAC-L605 interface with scanning electron microscopy (SEM), focussed ion beam (FIB), and transmission electron microscopy (TEM), to visualize PAC-CoCr interface. This led to greater understanding of the deposition process, and visualization of the ionic stitching buffer layer at the interface, that prevented delamination. Results were as theorized in plasma physics, and observed for the first time in response to question 1, on modified alloy L605 biomaterial.

Following initial investigations on surface engineering, we analysed surface biofunctionalization with whole blood flow, platelet rich plasma (PRP) assays, surface shelf-life, fibrinogen deposition, endothelial cell culture as well as plasma biomarkers of coagulation and inflammation. We observed markedly reduced surface blood coagulation for PAC-L605 compared to alloy L605, followed by similar trends; of lowered fibrin deposition, improved cell culture and reduced markers of coagulation, platelet and complement activation. Given that both surfaces were equally subject to similar physiological conditions, the markedly

different biological results observed were explained in relation to surface characteristics, specifically hydrophilicity.

The PAC surfaces showed significantly improved hydrophilicity compared to bare metal alloys. To address question 2, results were explained in accordance to in-depth protein-biomaterial investigations previously conducted by Leo Vroman, discussed at length within thesis. The "Vroman effect" or phenomenon is summarized via five statements below, also in agreement with our study:

1. The concentration of proteins available in plasma, decrease with increasing molecular weight (i.e higher molecular weight proteins are less abundant in plasma).
2. Sequence of plasma protein deposition on a surface was: albumin, immunoglobin (IgG), fibrinogen, factor XII and HMWK (high molecular weight kininogen).
3. Any surface-adsorbed protein species can only be removed by a molecule of the same species, i.e., forming a temporary dimer that forces the adsorbed molecule back into its original conformation, and into solution.
4. However, on ***hydrophobic*** surfaces the sequence of proteins displacing each other stops at fibrinogen, preventing step 3, and leading to protein aggregation.
5. Platelets adhere to surfaces where fibrinogen is adsorbed, therefore on ***hydrophilic*** surfaces platelets arrive too late to adhere, due to high turnover rate.

It appears our studies on biofunctionalization were in agreement with the Vroman effect. Significantly higher deposition of fibrinogen was seen on L605 vs. PAC-L605 (hydrophobic vs. hydrophilic), alongside correlating higher blood coagulation and platelet activity on L605 vs. PAC-L605. We therefore assume high turnover rate of albumin on PAC-L605 surfaces (compared to L605), prevent fibrinogen and low abundance HMWK protein aggregation, integral to progression of the coagulation cascade. This phenomenon may account for lowered

blood clot formation, and platelet activation for PAC-L605 in contrast to L605, in response to the 2nd question of our study.

In the immediate future, we can conduct further studies to stain and identify surface proteins albumin and HMWK comparatively on the two biomaterials, to confirm this hypothesis. Since we essentially confirmed superiority of PAC-L605 vs. L605 within this study, an optimized PAC recipe (suggested in context) can be deposited on a commercial stent platform for further *in vitro* investigations, as outlined herein. The alloy L605, ASTM F90 specifications of CoCr biomaterial utilized here meet specifications of the commercially available cobalt chromium coronary stent platform Multi Link 8 (ML8, Abbott Vascular). Further studies should aim to comparatively assess PAC-ML8 stents vs. ML8 stents *in vitro*, prior to any *in vivo* translational studies.

Publications arising from this work

Accepted for publication

- Thamarasee Jeewandara, Anna Waterhouse, Steven G. Wise, Alexey Kondyurin, Marcela M. Bilek, Anthony Weiss, Martin Ng *Plasma Based Biofunctionalization of Cardiovascular Stents* **Heart Lung Circulation** (2013) 22 S46
- Thamarasee Jeewandara, Steven G. Wise, Alexey Kondyurin, Anthony Weiss, Marcela M. Bilek, Martin K.C.Ng *Bioengineering Stents With Proactive Biocompatibility* **Global Heart** (2014) 9 1 e70 - e71
- Thamarasee M. Jeewandara, Steven G. Wise, and Martin K.C.Ng *Biocompatibility of Coronary Stents* **Materials MDPI** (2014) 7 2 17
- Thamarasee Jeewandara, Steven G. Wise, Praveesuda L. Michael, Juichien Hung, Miguel Santos, Alexey Kondyurin, Anthony Weiss, Marcela M. Bilek and Martin K.C.Ng *Bioengineering L-605 Cobalt Chromium Cardiovascular Stent Biomaterial with Plasma Activated Coating, for Proactive Biocompatibility* **Arteriosclerosis, Thrombosis, and Vascular Biology** (2015) 35:A387
- S. Wise, P. Michael, E. Filipe, T. Jeewandara, J. Hung, A. Kondyurin, A. Weiss, M. Bilek, M. Ng *Non-thrombogenic, bioactive stent platform* **Heart Lung Circulation** (2015) 24:S286
- Thamarasee Jeewandara, *Bioengineering cobalt chromium cardiovascular stent biomaterial for surface enhancement and characterization* **The Winnower** (2016) DOI: 10.15200/winn.145619.92147
- Thamarasee M. Jeewandara, *Bioengineering cobalt chromium cardiovascular stent biomaterial for biofunctionalization* **Cold Spring Harbor Laboratory Press, bioRxiv** (2016) DOI: http://dx.doi.org/10.1101/042770

Conferences and presentation

- Thamarasee Jeewandara, Anna Waterhouse, Steven Wise, Yongbai Yin, Marcela Bilek, Anthony Weiss, Martin Ng. Oral presentation, 4th Sydney University Tissue Engineering Network (SUTEN), 2012. Sydney, Australia
- Thamarasee Jeewandara, Anna Waterhouse, Steven Wise, Yongbai Yin, Marcela Bilek, Anthony Weiss, Martin Ng. Poster presentation, 6th Annual Scientific Meeting of the Australian Health and Medical Research Congress 2012. Adelaide, Australia
- Thamarasee Jeewandara, Anna Waterhouse, Steven G. Wise, Alexey Kondyurin, Marcela M. Bilek, Anthony Weiss, Martin Ng. Poster presentation, 61st Annual Scientific meeting of the Cardiac Society of Australia and New Zealand (CSANZ) 2013, Gold Coast, Brisbane, Australia.
- Thamarasee Jeewandara, Anna Waterhouse, Steven Wise, Alexey Kondyurin, Marcela M Bilek, Anthony S Weiss, Martin Ng. Poster presentation, 2nd Annual NHMRC Symposium on Research Translation, 2013, Sydney Australia
- Thamarasee Jeewandara, Anna Waterhouse, Steven Wise, Alexey Kondyurin, Marcela M Bilek, Anthony S Weiss, Martin Ng. Poster presentation, American Heart Association, 2013, Dallas, Texas, USA.
- Thamarasee Jeewandara, Steven G. Wise, Alexey Kondyurin, Marcela M. Bilek, Anthony Weiss, Martin Ng. Poster presentation, World Heart Federation, World Congress of Cardiology Scientific Sessions, 2014, Melbourne, Australia
- Thamarasee Jeewandara, Steven G. Wise, Praveesuda L. Michael, Juichien Hung, Miguel Santos, Alexey Kondyurin, Anthony Weiss, Marcela M. Bilek and Martin K.C.Ng. Poster presentation, Arteriosclerosis, Thrombosis and Vascular Biology | Peripheral Vascular Disease (ATVB|PVD) Scientific Sessions, American Heart Association, 2015, San Francisco, California, USA.

Abbreviations

316L SS	316L stainless steel
AAMI	Association for the Advancement of Medical Instrumentation
ABTS	2,2'-azino-bis(3-ethylbenzothiazoline-6-sulfonic acid) diammonium salt
ACD	acid citrate dextrose
AFM	atomic force microscopy
ANOVA	analysis of variance
ASTM	American Society for Testing and Materials
β-TG	beta-thromboglobulin
BMS	bare metal stents
BSA	bovine serum albumin
CAD	coronary artery disease
CoCr	cobalt chromium
CPP	cyclic potentiodynamic polarization
DAB	3,3'-diaminobenzidine
DAPI	4,6'-diamidino-2-phenylindole
DES	drug-eluting stents
DPX	distyrene, plasticizer, xylene
DSA	drop shaped analysis
ECM	extracellular matrix
ECs	endothelial cells
EDTA	ethylenediaminetetraacetic acid

EDS	energy dispersive spectroscopy
EE	encapsulation efficacy
EELS	electron energy loss spectra
EFTEM	energy filtering transmission electron microscopy
EIA	enzyme immunoassay
ELISA	enzyme-linked immunoabsorbent assay
EPC	endothelial progenitor cell
ePTFE	expanded polytetrafluoroethylene
ESD	electron spectroscopic diffraction
ESR	electron spin resonance
F-actin	filamentous actin
FBS	foetal bovine serum
FDA	food and Drug Administration (USA)
FESEM	field emission scanning electron microscopy
FITC	fluorescein isothiocyanate
FN	fibronectin
FX	factor X
GPa	giga pascals
H&E	haematoxylin and eosin
HMWK	high molecular weight kininogen
HRP	horseradish peroxidase
HRTEM	high resolution transmission electron microscopy
HUVECs	human umbilical vein endothelial cells
IFFT	inverse fast fourier transform

ISO	international organization for standardization
kDa	kilo Dalton
L605	alloy for cobalt chromium
LST	late stent thrombosis
MACE	major adverse cardiac events
ML8	multi-link 8
mTOR	mammalian target of rapamycin
NIH	neointimal hyperplasia
NPs	polymeric nanoparticles
PAC	plasma activated coating
PB	phosphate buffer
PBS	phosphate-buffered saline
PCI	percutaneous coronary intervention
PECAM-1	platelet endothelial cell adhesion molecule-1
PIII	plasma immersion ion implantation
PLGA	poly (DL-lactide-co-glycolide)
PMN	polymorphonuclear
PRP	platelet rich plasma
PTCA	percutaneous transluminal coronary angioplasty
PVC	polyvinyl chloride
RMS	root mean square
rpm	revolutions per minute
SAED	selected area electron diffraction
SAM	self-assembled monolayers

SDS	sodium dodecyl sulfate
SE	standard error
SEM	scanning electron microscopy
SMC	smooth muscle cell
sP-selectin	soluble P-selectin
sC5b-9	soluble C5b-9 complex
TBST	tris buffered saline
TCC	terminal complement complex
TCP	tissue culture plastic
TE	recombinant human tropoelastin
TF	tissue factor
TIRF	total internal reflection fluorescence
TLR	target lesion revascularization
TPGS	d-α-tocopheryl polyethylene glycol 1000 succinate
Tris	tris (hydroxymethyl) isothiocyanate
vWF	von Willebrand Factor
WLI	white light interferometer
XPS	X-ray photoelectron spectroscopy
ZLP	zero loss peak

Table of Contents

List of Figures

List of Tables

Chapter 1 – Introduction and Literature Review

1.1 Biocompatibility of Coronary Stents

Cardiovascular disease continues to be the leading cause of mortality [1, 2], with a vast majority of these deaths attributed to obstructive coronary artery disease (CAD) [3]. Depending on the severity of the disease, the main interventional options for revascularisation include angioplasty, stent deployment and in severe, diffuse occlusions (more than 70%), bypass graft surgery [3]. Narrowed coronary arteries were originally treated percutaneously with balloon angioplasty alone [4]. However, clinical complications including abrupt vessel closure from elastic recoil in the short term and significant neointimal hyperplasia, limited the applicability of this intervention. Improved results were observed following the insertion of an additional intravascular mechanical support, cylindrical metal scaffolds known as stents [5]. The first balloon expandable stents were designed from surgical grade stainless steel, and aimed to provide additional mechanical support, limiting vessel recoil and preventing acute occlusion [6].

Stents were initially evaluated in a preclinical study relative to angioplasty alone, in canine coronaries to assess efficacy prior to human trials [5]. The extent of endothelial damage during angioplasty is proportional to the time of balloon inflation [5]. Since the balloon is immediately deflated after maximal inflation during stent implantation and 80% of the expandable wire mesh of the stent was open surface opposing elastic recoil, the process minimized endothelial damage compared to balloon angioplasty alone [5]. The first human clinical implantations indicated a high delivery success, low incidence of perioperative complications and a thrombosis incidence controllable with the use of anticoagulants [7, 8]. In

the absence of antiplatelet therapy, sub-acute thrombotic closure after stent implantation, was a notable risk [7].

Despite some benefits over angioplasty alone, stent deployment still results in significant injury to the vessel wall and disruption of the endothelium [9]. Disruption of endothelial monolayer integrity induces a cascade of pro-inflammatory events resulting in monocyte/neutrophil infiltration and smooth muscle cell proliferation; key contributing factors to neointimal hyperplasia. The rate of re-endothelialization following injury is a critical determinant of vascular lesion formation, and areas of injury that rapidly re-endothelialize have significantly less intimal thickening and restenosis [10], while also deterring thrombus formation [11]. In humans, bare metal stent struts are substantially endothelialized in 6–7 months, with significant coverage present after 2 months [12]. During reformation of the endothelium over stent struts, smooth muscle proliferation induced by injury contributes to neointimal formation and restenosis. The high rates of restenosis for bare metal stents are a significant drawback in their clinical application.

Preliminary drug-coated stents were engineered with surface anticoagulants, such as heparin or warfarin to prevent sub-acute thrombosis and bleeding complications [13]. Despite attenuating thrombosis, restenosis was unchanged, requiring a pharmacological approach for its inhibition. Drug eluting stents (DES) releasing anti-proliferative agents such as sirolimus and paclitaxel inhibit neointimal hyperplasia but also substantially delay healing and re-endothelialization [12]. Consequently, DES are not only susceptible to early thrombosis like bare metal stents (BMS), but are also prone to both late (30 days–1 year) and very late (>1 year) stent thrombosis [14]. In stable single vessel disease patients, late stent thrombosis (LST) occurs at a constant rate (0.6% per year) [15], with even higher rates reported (0.9%–3%/year) in real world studies[16]. Accordingly, the safety of DES remains in question [17]. Hence the advent of DES has further

exacerbated the biocompatibility issues of coronary stent implantation. The unsatisfactory performance of both BMS and DES has led to continued investigation of novel stent modifications, focusing on improving stent biocompatibility. The innovations discussed include surface tissue engineering, endothelial regeneration mechanisms, nanotechnology, and plasma physics for biofunctionalization of coronary stents.

1.2 Limitations of Bare Metal Stents (BMS)

The metal alloys used to produce bare metal stents are fundamentally incompatible with the vasculature, promoting thrombosis due to their inherent surface properties [18], while exerting no inhibitory effect on smooth muscle cell hyperproliferation. The dominant mode of early BMS failure is acute thrombosis, which can be as high as 24% in the absence of the dual anti-platelet therapy administered to stent recipients [8]. Stent thrombosis is defined as a composite 30-day endpoint, which can present as an abrupt vessel closure, large non-fatal myocardial infarction or death [19]. Deaths attributed to cardiac causes within the first 30 days of stent implantation are usually adjudicated as stent thrombosis [20]. Neointimal hyperplasia, or restenosis, is a major cause of bare metal stent failure after the early thrombosis risk has abated. In-stent restenosis is driven by an uncontrolled immune response, triggered by the disruption of the native endothelium and damage to the vessel wall. The re-modelling of the vessel post-injury is characterized by hyper-proliferative smooth muscle cells infiltrating into the vessel lumen and secreting extracellular matrix components [21].

BMS are made from surgical grade metal alloys, initially 316 L stainless steel (316 L SS), but more recently evolving to cobalt chromium and platinum alloys [22]. Stent strut thickness and alloy type play an integral role in the biological responses elicited. Changes to the metal alloy have facilitated thinner strut design while retaining sufficient radial strength, and led to the re-

design of stent structures for increased deliverability. The first Palmaz-Schatz crown stent designed for flexibility has evolved significantly to the malleable S-shaped velocity-stent, currently in development [23]. Stent design has further developed to include the Multilink stents with still thinner struts, Microstents and GFX stents [24] made of sinusoidal element of stainless steel. Sub-acute thrombosis rates post stent implantation, have greatly reduced over the course of stent evolution, although the rate of in-stent restenosis remained high [4].

1.3 Drug Eluting Stents (DES): An Imperfect Solution

Systemic drug administration post BMS implantation to reduce restenosis was ultimately unsuccessful due to low drug concentrations, non-specifically targeting the neointima [25]. DES locally releasing anti-proliferative agents were introduced in 2003 to reduce restenosis associated with stent implantation [26]. While DES have been highly effective in suppression of neointimal hyperplasia (up to 10-fold compared to BMS [27]) local vascular delivery of rampamycin analogues or paclitaxel is an untargeted approach, employing non-specific agents to inhibit all cell proliferation [28]. These drugs bind FK506 binding protein-12 (FKB12) which in turn blocks the cell-cycle specific kinase, mammalian target of rapamycin (mTOR), to halt mitotic progression in the juncture of G_1 and S phases in all cell types [29]. This in turn deregulates tissue factor in endothelial cells and monocytes [30, 31]. The elution of anti-proliferative agents is associated with a dramatic delay in healing and re-endothelialization at the stent deployment site; such that DES struts have less than 50% endothelial coverage at three years [12].

DES development has focused on the major failings of current devices and has included modifications to the metal alloys, coating polymers and eluted drugs [32]. For example, Abbott Vascular have developed a 2^{nd} generation everolimus-eluting XIENCE V stent, using a different stent alloy (cobalt chromium), polymer coating (fluoropolymer) and anti-restenotic

drug to its 1st generation counterparts. This resulted in enhanced endothelialization *in vitro* and *in vivo* compared to 1st generation DES [33]. In randomised clinical trials, the XIENCE V stent also exhibited improved safety outcomes compared to two iterations of first generation paclitaxel-eluting stents [16, 34]. Other approaches for second generation DES include the use of biodegradable polymers and selective coating of the anti-restenosis drugs solely on the abluminal surface of the stent [35]. Despite these innovations, significant rates of major adverse cardiac events persist, particularly in real world usage of DES incorporating a high proportion of patients with acute coronary syndromes [35].

The most recent innovations in DES development are combinations of existing technology; employing drug-elution from a resorbable stent platform [36], from an ultra-thin degradable polymer coating [37] or combined with endothelial cell capture [38]. These approaches are included in more detail, below.

1.4 Underlying Causes of Stent Incompatibility

The compatibility of bare metal stents is due both to the stent material and design, DES effectiveness is also affected by polymers used for coating, and the anti-proliferative drugs released. Design considerations such as strut thickness, stent design and mechanical properties have been steadily optimized, while polymer coatings and drug effects remain problematic, increasing inflammation [39], delaying re-endothelialization [12] and impairing endothelial cell function [40].

1.4.1 Inherent Thrombogenicity

Stents are inherently foreign bodies in the vessel wall, inducing platelet adhesion and activating coagulation, leading to thrombosis. Inhibition of platelet activation is required following stent delivery. The currently low rates of early stent thrombosis (1%–2%) are predicated on tolerance and adherence to dual antiplatelet therapy with aspirin and a thienopyridine [41]. This is not

feasible for an increasing number of patients with high bleeding risk, or those requiring surgery [42]and is associated with increased risk of significant morbidity including gastrointestinal bleeding [43]. There is also risk of antiplatelet hypo-responsiveness, which increases stent thrombosis [44]. In the case of DES, management of LST is additionally problematic. To reduce the incidence of late thrombotic events, extended dual anti-platelet therapy is now recommended following DES placement, though no consensus on the effectiveness of an extended regimen has been reached [45, 46].

In a recent large cohort study, new generation DES (n-DES) provided a modest improvement in clinical outcomes compared to old generation DES (o-DES) [47]. Old DES classified in the study, were first generation DES with bare metal platforms and sirolimus or paclitaxel drug elution [47]. New DES classified in the study diversely included; stents eluting non-inflammatory drug zotarolimus coupled with a biocompatible polymer system (bioLinx™) [48] designed to extend the duration of drug exposure in the vessel (Endeavor Resolute), multi-layer coating technology (Xience V) [49] and self-expanding stents designed for compression resistance (Promus Element) [50]. The study compared long-term outcomes of PCI with n-DES vs. o-DES and BMS to show comparatively lowered risk of restenosis, LST and mortality for n-DES, although no significant effect was observed for thrombosis [47]. The duration of recommended dual antiplatelet therapy to prevent thrombosis remains unchanged for both old and new generation DES in patients.

1.4.2 Delayed Re-Endothelialization

Following vascular injury, endothelial cells migrate from intact neighbouring coronary segments, or are recruited from circulating endothelial progenitor cells (EPC) [51] to re-endothelialize the injured artery. However, both rapamycin and paclitaxel actively suppress endothelial cell growth *in vitro* [31, 52, 53] and impede EPC homing and proliferation *in vitro*

[54, 55], actively impeding re-endothelialization. A morphological autopsy study conducted to compare coronary artery segments from patients after DES and BMS implantation revealed delayed arterial healing and poorer endothelialization after DES compared to BMS implantation of similar duration [12]. Within the 1st generation DES cohort, 60% of patients had evidence of LST and a 45% rate of death was reported for patients suffering from LST [12, 56]. Re-endothelialization was significantly higher in BMS compared to DES [40]. The impacts of 1st generation DES on vascular biology are schematically represented in figure 1.1.

Figure 1.1

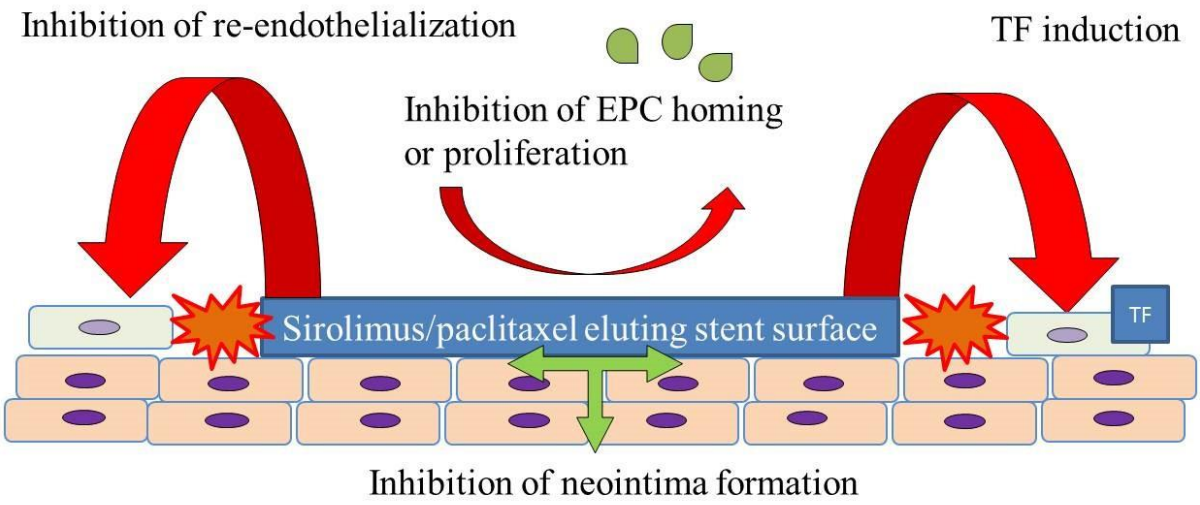

Coronary stent types, and their mechanism of action. First generation drug eluting stents (DES) impact on vascular biology: Modified from [40], reduced neointimal formation (green arrows) but increased thrombogenicity at stent bio-interface. Sirolimus/paclitaxel inhibition of endothelialization, tissue factor induction and endothelial progenitor cells (EPC) homing prevention (red arrows).

1.4.3 Metal and Polymer Coating Hypersensitivity

Hypersensitivity to metal alloys such as molybdenum and nickel has been previously observed in ~10% patients undergoing BMS implantation [57], although inflammatory response for stainless steel, is much less pronounced in comparison [58]. Hypersensitivity towards BMS alloys is associated with restenosis in the range of 15%–20% [40], with the extent of inflammation correlating to the degree of restenosis [59]. Marked hypersensitivity reactions have also been observed to the polymers coating DES. First generation DES coated with poly-ethylene vinyl acetate polymer are demonstrably pro-inflammatory [60]. This was further verified in a preclinical study when the copolymer, used as an antigen delivery matrix elicited an inflammatory response in ~25% of rabbits [61]. The inflammatory response in patients with spontaneous coronary dissection, post DES implantation was characterized primarily with eosinophilic infiltrations in the adventitia [59]. In severe cases DES related clinical complications exhibit necrotic core prolapse, in-stent restenosis and LST, preventing arterial healing [62]. A preclinical study in a porcine model showed progressive increases in the eosinophilic, granulomatous infiltrate, post first generation sirolimus (Cypher) stent implantation, starting at 28 days, increasing to 60% at 6 months [40].

1.4.4 Poor Coating Integrity

Another important, often overlooked aspect of stent safety is the coating integrity after crimping and expansion. Relatively few studies have evaluated the possibility of coating delamination [63, 64], despite it being widespread in commercially available DES and recognized as a safety concern by the Food and Drug Administration [65]. DES polymer coatings display widespread surface cracking, peeling and flaking at the polymer-metal interface [66-68]; exposing the underlying thrombogenic metallic substrate and contributing to chronic inflammatory and hypersensitivity reactions [39, 69]. Together, these failings highlight

the difficulty in simultaneously promoting re-endothelialization, while inhabiting neointimal hyperplasia and thrombosis. No current stent platform adequately achieves this goal, but some strategies are reviewed below and an updated summary is presented in chapter 6.

1.5 Novel Stent Modifications

Coatings aimed at increasing the inertness of metallic implants have been effective at reducing thrombogenicity but have generally failed to reduce restenosis rates. Examples of these coatings include gold [70]; diamond-like carbon [71, 72]; pyrolytic carbon [72] and phosphorylcholine (PC). PC; exemplifying the flaws of an inertness approach was observed to be non-thrombogenic *in vitro* [73]. However; *in vivo*; it failed to encourage endothelialization and ultimately had no effect on the rate of stent thrombosis [74]. In parallel; enhancement of stent biocompatibility has been pursued by actively influencing the host response. These coatings have failed because they only seek to address one aspect of vascular biocompatibility (e.g., thrombogenicity alone) at the expense of other aspects. Heparin-coated stents are one such example; designed to reduce thrombosis but not neointimal hyperplasia [75]. Below, we describe some of the most recent attempts to develop biocompatible stents.

1.5.1 Accelerating Endothelialization

Given that re-endothelialization plays an integral role in vascular healing after stent implantation, coating stent with substances to accelerate endothelial cell coverage is an important therapeutic approach [40]. Preliminary studies designed to capture endothelial progenitor cells (EPCs) by coating stents with a polysaccharide intermediate and murine monoclonal anti-human CD34-positive antibodies showed feasibility in human clinical trials [76]. The Genous Bio-engineered R stent, similarly coated with immobilized anti-CD34 antibodies aims to enhance endothelialization by capturing circulating endothelial progenitor cells (figure 1.2). The captured CD34-positive EPCs are proposed to differentiate into a mature endothelium, but the CD34-positive markers used are non-specifically shared by haematopoietic stem cells and immune complement cells. Circulating CD34-positive

mononuclear cells are also shown to differentiate into smooth muscle progenitor cells in patients with restenosis [77]. A higher rate of revascularization was observed in Genous stent compared to Taxus stent, in patients treated for coronary artery stenosis with a high risk of restenosis [78]. A recent proof-of-concept study shows some benefits for endothelialization and thrombogenicity, but leaves reduction of neointimal hyperplasia unaddressed and the platform reliant on drug-eluting technology [79]. A novel DES coated with integrin-binding cyclic Arg-Gly-Asp peptides was similarly utilized in a preclinical study to accelerate endothelialization via EPC attraction, using the same principles of EPC capture. In an initial porcine model evaluation, neointimal hyperplasia seems to be promisingly reduced [80, 81].

Figure 1.2

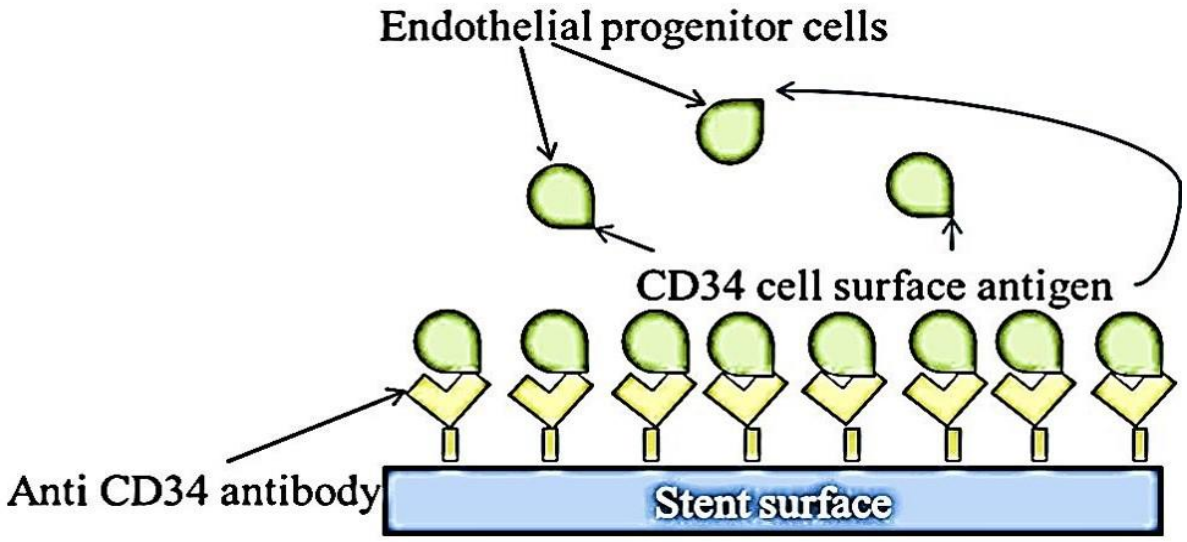

EPC capture stent mechanism of action: Modified from [82]. The CD-34 antibody immobilized on the stent surface polymer binds the CD-34 antigen on the EPC to promote rapid endothelialization.

1.5.2 Bioresorbable Stents

Bioresorbable stents are proposed to solve the problem of long-term stent biocompatibility by degrading over time [81]. The first bioabsorbable, balloon expandable stents implanted in humans were constructed from poly-L-lactic acid (PLLA) [83]. The bonds between the repeating lactide units of the bioabsorbable stent hydrolyze to produce lactic acid, metabolized to CO_2 and H_2O [81]. Absorption occurs via bulk erosion throughout the implant not just on the surface, allowing the stent strut to retain its shape, until the process is well advanced [83]. The Abbott Vascular bioresorbable vascular scaffold (BVS), a PLLA stent, has so far demonstrated restenosis similar to bare metal platforms, as well as late scaffold shrinkage and non-uniform vessel support, due to uneven scaffold degradation [84]. Alloys of magnesium have also been explored as bioabsorbable stent platforms [85]. Absorption by surface erosion reduces the strut thickness as the stent is absorbed within 4 months of implantation, leading to loss of radial support [85].

The latest generation bioabsorbable stents are designed for prolonged radial support coupled with drug elution [85]. A number of different materials have been utilized to manufacture these stents ranging from metal alloys to a variety of polymers, including tyrosine-derived polycarbonate polymer, salicylate and a linker, as well as metal-cobalt chromium with n-butyl methacrylate coating [86, 87]. The BioMatrix stent incorporates the thin S-stent platform with a reduced percentage metal surface area (16.3%–18.4%) to elute anti-proliferative drug biolimus A9 [37]; a highly lipophilic semi-synthetic analogue of sirolimus. Furthermore, the stent is completely bioabsorbable degrading *in vivo* to lactic acid in 6-9 months post implantation [36]. The JACTAX stent (Boston Scientific Corporation, Natick, MA, USA) was designed on similar principles, coated with an ultra-thin, mixture of biodegradable PLLA and paclitaxel drug applied as microdots, per 16-mm stent [88].

The stents were comparable to preceding paclitaxel eluting stent (TAXUS Liberté, Boston Scientific Corporation, Natick, MA, USA), although further studies are underway to evaluate their potential for improved vessel healing. As yet, none have FDA approval for humans use, but some clinical trials are underway [89, 90]. Current bioresorbable stents have markedly inferior mechanical properties in terms of device profile, flexibility, deliverability, and defined duration of vascular support to prevent recoil or radial strength, thereby dramatically limiting their capacity to be used for a large number of coronary lesion subsets, including bifurcation lesions, calcified lesions, tortuous coronaries and long lesions [90]. As a consequence of these profound limitations, metal alloy stents will remain the mainstay for endovascular stents in the foreseeable future.

1.5.3 Nanotechnology for Controlled Release of Drugs and Novel Stent Design.

Novel mechanisms of drug release include polymeric nanoparticles (NPs) to encapsulate pharmaceutical agents for targeted drug delivery to a tissue of interest [91-93]. For instance, d-α-tocopheryl polyethylene glycol 1000 succinate (TPGS) is used as an emulsifier in the formulation of the biomaterial matrix poly(DL-lactide-co-glycolide) (PLGA). The biodegradable PLGA/TPGS NPs deliver controlled paclitaxel release with high drug encapsulation efficiency (EE), for the treatment of restenosis. The higher drug EE improves cellular uptake and cytotoxicity against SMC proliferation, and is being considered in the development of third generation, nanoparticle coated DES [94]. The Nevo-sirolimus eluting stent is designed from L605 cobalt-chromium alloy with a drug delivery system based on PLGA. It utilizes a multi-channel reservoir system along the stent struts into which the drug-polymer (sirolimus/PLGA) matrix is loaded for elution [95] displaying superiority over traditional paclitaxel eluting stents (TAXUS Liberté) in clinical trials [96].

In patients with acute ST-segment elevation myocardial infarction (STEMI) undergoing PCI, sub-optimal myocardial reperfusion is common. Stents have therefore been specifically designed to prevent thrombus protrusion into the lumen after PCI, in acute myocardial infarction. The potential utility of a novel polyethylene terephthalate (PET) micronet mesh-covered thin-strut metal stent (MGaurd), was evaluated in this regard for its functional design to trap and exclude thrombus and atheromatous debris to prevent distal embolization [97]. The stent showed superior rates of epicardial coronary flow and complete ST-segment resolution, compared to conventional metal stents. Larger clinical studies are required to determine consistency of improved clinical outcomes.

1.5.4 Plasma polymerization

Applications of plasma modified materials are emerging in the fields of medicine, for drug delivery and tissue engineered biocompatibility of medical devices [98] . Plasma, the fourth state of matter is artificially generated when a dielectric gas ionized by free electrons is accelerated in a sufficiently strong electric field. The gas molecules separate on ion-impact, to create electrons and neutral gas atoms within a vacuum evacuated chamber. Subsequent collisions among these particles create more ions and electrons to interact with and modify the surfaces, including potential biomaterials [99, 100], modifying their surface energy, charge and surface chemistry, without altering bulk properties [101]. When argon and an increasing amount of acetylene are used in a plasma deposition system, a plasma activated coating (PAC) was created on a metallic biomaterial surface (figure 1.3) suitable for stent applications, utilized in this study. The thin carbon polymer layer on the biomaterial acts as a reservoir of free radicals, activating the surface for effective, covalent protein attachment (figure 1.4) [102, 103].

Pulse biased plasma polymerization has been adapted to metallic substrates, for one step covalent biomolecule immobilization, minimizing the otherwise complex process of chemical

linker based biofunctionalization discussed elsewhere [104]. The relationship between protein binding and biomolecule activity on PAC strongly adhered to stainless steel, has been demonstrated by direct covalent attachment of tropoelastin (TE), horseradish peroxidase (HRP) and catalase [104]. Surface characterization further elucidated the importance of surface free energy for effective biomolecule attachment [105]. Recent evidence suggests that PAC on a 316 L SS stent covalently binds a dense layer of human recombinant tropoelastin, facilitating the growth of endothelial cells [105]. Plasma modified surfaces coated with tropoelastin have shown improved blood biocompatibility, significantly reduced clot formation and improved endothelialization *in vitro* [105]. Pre-clinical studies of PAC stents demonstrate feasibility and deliverability with great potential as a carrier for local biomolecule delivery [106].

Figure 1.3

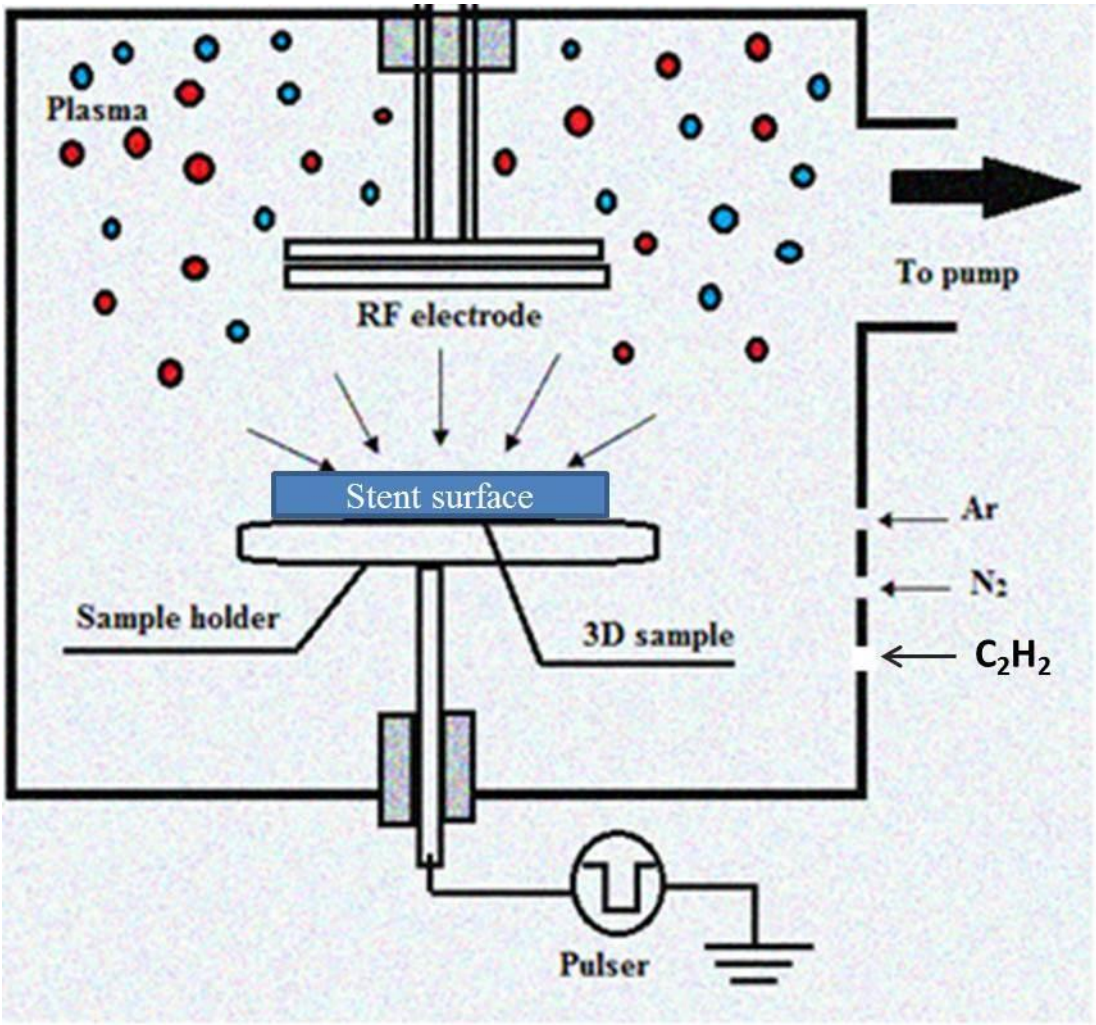

Plasma surface modification for coronary stents: from [101, 107]. Nitrogen, argon and acetylene plasma is introduced into a chamber under a vacuum and ionized by a power source such as an RF electrode. The charged ions in the chamber impact the substrate to modify the surface immersed in the plasma.

Figure 1.4

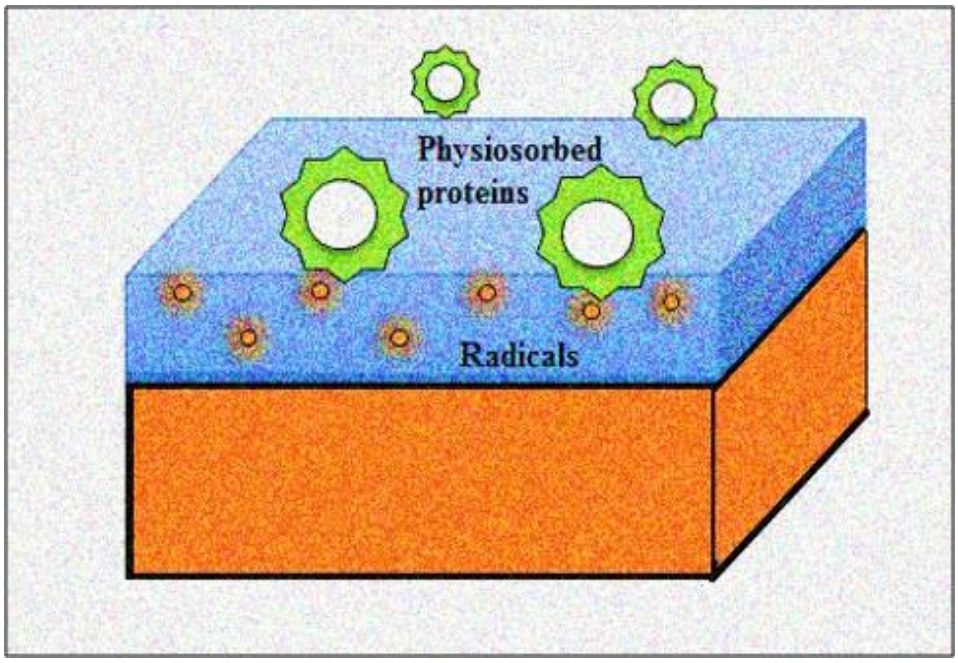

Illustration of predicted free radical surface functionalization (orange circles/precursors) of a modified biomaterial. The figure illustrates covalent, linker-free protein attachment (green) on PAC surface.

1.6 Conclusions and Future Perspectives

The development of coronary stents is an evolving process and a fundamental aspect of interventional therapy in the treatment of coronary artery disease (CAD). Stent biocompatibility is a multi-faceted process; having to be simultaneously hemocompatible, promote rapid re-endothelialization and suppress restenosis. BMS have evolved considerably since their first human use, but remains both thrombogenic and susceptible to restenosis. DES elute powerful cytotoxic drugs to inhibit SMC hyper-proliferation, but delay healing and induce inflammation, resulting in an increased risk of late thrombosis.

We have highlighted the latest strategies (updated in chapter 6) that appear to be most promising, including active promotion of re-endothelialization, bioresorbable stents, nanotechnology and plasma based modification. In light of the limitations still evident for each of these approaches, further development is required, with biofunctionalized combination devices and local biomolecule delivery (e.g., bioresorbable-drug-eluting stents and/or biocompatible stents underlying DES polymer), as the most likely to have success. Overall, many stent design innovations currently in development, promise to address the underlying lack of biointegration more directly, on the path to a truly biocompatible stent.

Chapter 2 – *In vivo* biocompatibility and efficacy of a plasma activated coronary stent coated with recombinant human tropoelastin.

2.1 Introduction

2.1.1 Translational animal models in cardiovascular disease studies

Cardiovascular disease and related conditions are at present the primary cause of death worldwide [108]. Animal models are used in an attempt to increase knowledge, provide new approaches for diagnostic, and treatment of pathologies [109]. Different methods have been associated to address cardiovascular disease, although no exclusive method perfectly recreates a human complication, depending on various associated factors. However, animal studies are essential for cardiovascular device evaluation, prior to evaluating their performance and safety in humans.

Clinically, failure of cardiovascular devices *in vivo*, are observed as thrombosis and restenosis [110]. Animal models used to evaluate cardiovascular devices should therefore include endpoints of endothelialization, thrombosis and restenosis. The next consideration is vessel location as this contributes to the endpoint measured. Additionally, the time course of experiment is critical to the specific endpoint [109]. The model can only predict the response in humans, based on specific endpoints chosen. Each device, and its specifications have multiple animal models, for preclinical evaluation *in vivo* [111].

Rabbit and porcine animal models are most commonly established to evaluate stents [112]. The classical porcine method is the preferred model to measure restenosis, although rabbit iliac artery stenting has become an accepted alternative [113]. When late stent thrombosis arose as an unforeseen clinical complication with first generation DES, data from animal studies were

used to help explain the phenomenon [113]. Delayed and incomplete vascular healing was detected as a toxicity/hypersensitivity reaction to polymer/drug matrix. Preliminary translational studies led to continued development of biocompatible drug carriers, absorbable polymers or fully bioeresorbable scaffolds to assist the re-endothelialization; healing process. Initial investigations of novel stent coating technologies in a translational model are therefore recommended, to assess preclinical safety of any new stenting technology developed.

2.1.2 Rabbit iliac artery model

Rabbits are useful in evaluating stent performance, since they have vessels with dimensions similar to human coronary arteries, allowing direct evaluation of human stents [111]. Arteries are denuded prior to implantation, to injure and stimulate a healing response, similar to the response after stenting a human vessel [114]. The model allows testing for endothelialization, early neointimal hyperplasia, and at longer time points restenosis. High blood flow through the arteries is maintained through administration of aspirin, to reduce acute thrombosis of the stents [33]. There are similarities drawn between the vascular healing responses following angioplasty for animal vessels, as seen in human studies [114].

The rabbit iliac artery model allows stent implantation into the common iliac arteries of rabbits, after injury was induced via endothelial denudation. The process entails removal of the luminal endothelial cell layer with an inflated balloon catheter, inserted into the artery, inflated and pulled back. The process intentionally damages the endothelial cells causing fragmentation and detachment of cells from the vessel lumen. The process is repeated twice for resulting denuded artery lacking an endothelium, with subendothelial matrix exposed to blood, as with injury occurring during PCI in human arteries with atherosclerotic plaques (figure 2.1). As seen on figure 2.1, following removal of endothelium, thrombosis at vascular sites leads to smooth muscle cell (SMC) migration, SMC proliferation and neointimal hyperplasia (NIH); i.e.

proliferation of cells in the inner most lining of the artery[115]. Ultimately this would lead to restenosis.

The bilateral iliac artery stenting model allows investigations in the left and right iliac arteries, allowing direct, controlled comparisons of different stent interaction with the vasculature. Previous studies have successfully utilized the translational animal model to test different stent materials [116], designs [117], drugs and DES [33], prior to clinical applications and commercial development.

Figure 2.1

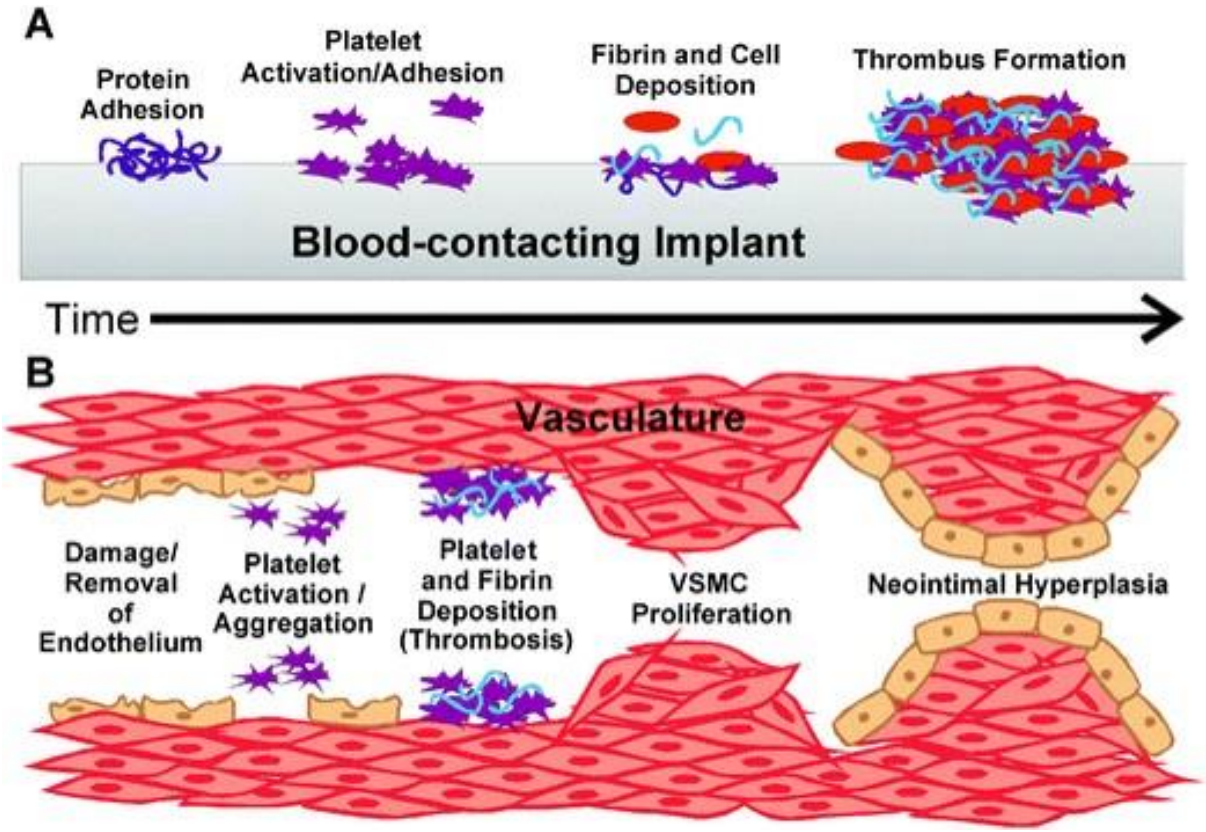

Implant induced removal of endothelium (endothelial denudation) to cause injury to vasculature. Followed by sequence of thrombotic, inflammatory events that contribute to vascular smooth muscle cell (VSMC) proliferation, neointimal hyperplasia, and restenosis in the long term. Image from [115].

2.1.3 Endothelialization

Incomplete endothelialization of strut surface drives late stent thrombosis (LST), an infrequent, life threatening complication, seen with FDA approved drug-eluting stents [118]. Mechanisms of late stent thrombosis are not well known. However endothelial cell growth is essential to maintain long-term luminal patency, since ECs provide structural and antithrombotic functions [33]. To assess for LST, large randomized clinical trials, statistically powered for LST endpoints, or indirect methods of endothelial dysfunction assessed via nitric oxide bioavailability assays in humans, can be conducted [119, 120]. However, preclinical studies allow for more effective initial safety and feasibility testing of a medical device. Arterial repair after stent placement in animals occur more rapidly than in humans, although they retain predictive value due to the sequence of biological responses elicited after stenting that show remarkable similarity to humans [114]. Interpretation of results pertaining to translational studies is highly contingent on the timeline after stent placement. Examination of DES implants in rabbit/swine models is often done at 28 days, although earlier time point may reveal more on the healing characteristics pertaining to a novel device modification [33]. A timeline of 28 days in a translational model is equivalent to 12-month coronary stent implants in humans [121].

Disparities in arterial healing among species are equally notable for rates of re-endothelialization after vascular injury [33]. Differences in shear stress, underlying atherosclerosis and use of juvenile animals may play a role in this regard. For instance, preclinical studies report complete endothelialization of DES at 28 and 90 days in the porcine model [122], but failed to predict complication of LST in humans after BMS implantation [123]. Relative to porcine studies, rabbits have slower endothelial regrowth, and are therefore a more desirable model to assess re-endothelialization of DES [121]. Aside from poor

endothelialization, several factors contribute to LST of DES, including malposition, overlapping stent placement, excessive stent length and bifurcation arterial lesions [121]. Commercially available comparator stents have little known rates of endothelialization and recovery, despite clinical applications worldwide [33].

2.1.4 Restenosis and thrombosis

Restenosis is the process in which a stented vessel becomes blocked again, usually 6 months after percutaneous coronary artery intervention (PTCA). This occurs as a result of neointimal thickening caused by smooth muscle cell hyperproliferation, extracellular matrix deposition and inflammation, known as neointimal hyperplasia (NIH), which also contributes to in-stent restenosis (ISR) [124]. Based on the length of restenosis in relation to stented length, ISR is defined as 1) focal, 2) diffuse 3) proliferative or 4) occlusive [125]. Thrombosis occurs as a result of the stent geometry, material, and coating, activating platelets and initiating coagulation [126, 127]. Based on severity, stent thrombosis (ST) is defined as 1) acute ST (thrombosis occurring 0-24 hours after PTCA) 2) subacute ST (1-30 days), 3) late ST (30 days to 1 year) and 4) very late stent thrombosis (VLST), >1year after stent implantation. Restoration of an intact endothelium by progressive endothelialization after implantation is integral to the stent biointegration process, and reduction of thrombosis and restenosis [128]. Clinically, bare metal stents (BMS) are limited by susceptibility to high rates of restenosis and drug-eluting stents (DES) are susceptible to high rates of very late-stent thrombosis as well as thrombus related in-stent restenosis [18, 129, 130].

Although the primary aim of DES is to inhibit restenosis via attenuation of vascular smooth muscle cell migration and proliferation [131], common complications include inhibition of endothelial cell proliferation by DES drugs, signal transduction pathway activation, and impairment of the healing process up to 3 years after implantation compared to BMS [132].

Generally, four key factors contribute to increased risk of stent thrombosis and restenosis, these include; device malposition [133], patient and lesion related factors [134], time course of dual antiplatelet therapy (DAPT) administration [135], and poor biocompatibility of stent material or polymer used for BMS and drug-loading in DES, *in vivo* [40]. Whilst interventional procedure-related risk factors can be minimized in conjunction with advanced imaging systems [133], and DAPT timeline-related risks minimized via clinical decisions individualized to each patient [135], the in-stent thrombosis and restenosis risk owing to incompatibility of stent material or DES polymer, largely remains to be addressed [105, 107].

2.1.4.1 Assisted endothelialization

Efforts to improve surface biocompatibility of stents, for vascular compatibility focus on reducing early markers of ISR, and late-stent thrombosis (LST) [105]. We have previously demonstrated a strategy to modulate desired physiological responses at the implant-tissue interface by covalent linker-free immobilization of proteins. The plasma activated coating (PAC) with covalently bound human tropoelastin (TE) (a major regulator of vascular cells *in vivo*), has been applied to 316L stainless steel flat surfaces, demonstrating enhanced hemocompatibility and endothelialization *in vitro* [136-138]. Studies have also shown the ability of tropoelastin to stimulate increased endothelial cell migration and adhesion compared to smooth muscle cells (SMC) [139]. Given the unique ability of TE to modulate cellular response, coating intravascular stents with tropoelastin may stimulate *in vivo* endothelialization, reduce neointimal hyperplasia (NIH) to attenuate vascular remodelling, and improve device performance. We had previously applied PAC to 316L SS BMS, demonstrating its feasibility as a stent coating technology for 7 days *in vivo* [106].

2.1.5 Histopathology – Resin histology methods for stented arteries

Comparative preclinical histological studies remain the most effective means of evaluating healing of vascular stent implants, after explanting them post euthanasia [33]. However, technical challenges precede histopathological evaluation at the stent-artery interface; including preservation of cellular morphology and arterial architecture [140]. For adequate histopathological staining, sections require a thickness of ~5-7 µm, with an intact tissue stent interface. Methacrylate resin methodologies offer adequate preservation of tissue-material although subsequent sectioning/processing methods remain largely obscure [141]. Previous studies have investigated technical challenges in resin histology, with different sectioning and visualizing methodologies [140, 141]. Conventional paraffin embedding and sectioning procedures demonstrated limitations in their application to the histological study of

endovascular stent implants [141]. Most embedding procedures that evaluate stent-artery interface require complete removal of the metal stent prior to tissue processing, which damages vascular architecture. At present therefore standard stent embedding procedures employ methacrylate resin media for stented arteries [141, 142]. Currently glycol methacrylate, methyl methacrylate (MMA), and a combination of MMA and n-butyl methacrylate (BMA) are widely used resins to process stented-tissue, or bone material [141]. Exact formulations of embedding procedure that serves preservation, sectioning, staining of stented-arteries differ among studies, and procedures are not definite.

A number of technical requirements precede stent-artery evaluation *in vitro*. The embedding media should allow histological staining, immunohistology and immunofluorescence, with or without deplasticization (resin removal). The sections should be within a specific thickness range, to uptake stain and evaluate cellular reactions immediately surrounding stents [140]. The tissue immunoreactivity and histopathology should be similar to that of paraffin embedded sections.

The aim of this study was to assess re-endothelialization with a focus on surface coverage, and relevant histological/immunohistochemical markers of thrombosis, and coagulation. We translated PAC+TE to a stent platform to perform a pilot endothelialization study by implantation of stents in denuded rabbit common iliac arteries; a well-established model of endothelialization. The study is a follow-up to our previous investigation with PAC vs. BMS [106]. Feasibility of PAC+TE implantation, coating integrity, rate of endothelialization, early markers of neointimal hyperplasia (NIH), thrombosis and inflammation will be investigated. Furthermore, embedding procedures, resin-artery sectioning procedures and arterial preparation for histological, immunohistochemical and microscopy will be described and optimized.

2.2 Materials and Methods

2.2.1 Materials, Equipment, Suppliers and Facilities

A list of chemicals, reagents, materials and their suppliers are presented in Table 2.1

Table 2.1 Materials and their suppliers

Chemical/Reagent/Material	Supplier/Facility
0.014" Route PTCA guide wire	ASAHI INTECC, Aichi, Japan
3.25 mm RX Sprinter Legend balloon dilation catheter	Medtronic, Minneapolis, Minnesota, U.S.A
5F Radiofocus Introducer (sheath)	Terumo, Tokyo, Japan
Acetylpromazine	Lyppards, NSW, Australia
Albumin powder (egg white protein)	Chemist Warehouse, Newtown, NSW, Australia
Anti-Rabbit IgG CD31 raised in mouse	Abcam, Cambridge, MA, USA
Aniline Blue	Electron Microscopy Sciences, ProSciTech, QLD, Australia
Aspirin (Aspro)	Bayer, Pymble, NSW, Australia
Buprenorphine	Royal Prince Alfred Hospital, Sydney, NSW, Australia
CD31/PECAM1 antibody JC/70A	Novus Biologicals, Littleton, CO, USA
DPX Mountant for Microscopy-10	BDH Chemicals, Kilsyth, VIC, Australia
Electropolished customized 316LSS stent	Laserage, Waukegan, Illinois, USA
EnVision™ G|2 System/AP, Rabbit/Mouse (permanent red)	Dako Australia, North Sydeny, NSW, Australia
EnVision™ K4011 HRP, Rabbit (DAB+)	Dako Australia, North Sydeny, NSW, Australia
Eosin (alcoholic)	Fronine, Taren Point, NSW, Australia
Mayer Hematoxylin	Fronine, Taren Point, NSW, Australia
Ferric Ammonium Sulfate 5%	Electron Microscopy Sciences, ProSciTech, QLD, Australia

Gelatin Powder	Chemist Warehouse, Newtown, NSW, Australia
Goat serum	Sigma-Aldrich, St. Louis, MO, USA
Hoechst trihydrochloride, trihydrate, FluroPure™ grade (MW 615.99)	Sigma-Aldrich, St. Louis, MO, USA
Image-Pro Premier 9.1 analysis software	Media Cybernetics, Rockville, MD, USA
Iodine	Livingston International, Roseberry, NSW, Australia
Isofluorane	Lyppards, NSW, Australia
Lethabarb	Lyppards, NSW, Australia
MAC387	Abcam, Cambridge, MA, USA
Methyl methacrylate	Sigma-Aldrich, St. Louis, MO, USA
Microm HM355S (rotary microtome)	Thermo Fisher Scientific, Walldorf, Germany
Monoclonal anti-actin α-smooth muscle antibody produced in mouse	Sigma-Aldrich, St. Louis, MO, USA
New Zealand White Rabbits	IMVS, Adelaide, SA, Australia
Normal goat serum (NGS)	Sigma-Aldrich, St. Louis, MO, USA
Omnipaque 240 mg I/mL (contrast)	GE Healthcare, Rydalmere, NSW, Australia
Papaverine	Sigma-Aldrich, St. Louis, MO, USA
Paraformaldehyde	Sigma-Aldrich, St. Louis, MO, USA
Picric Acid-Orange G Solution	Electron Microscopy Sciences, ProSciTech, QLD, Australia
Ponceau Fuchsin Solution	Electron Microscopy Sciences, ProSciTech, QLD, Australia
Proteinase K stock	Sigma-Aldrich, St. Louis, MO, USA
Sodium Azide (NaN_3) 99.99%	Sigma-Aldrich, St. Louis, MO, USA
Sterile saline	Pfizer, Perth, WA, Australia
SuperFrost®Plus	Menzel-Glaser; ProSciTech, QLD, Australia
Taxus Liberte Stent	Boston Scientific, Natick, MA, USA
Triton X-100	Sigma-Aldrich, St. Louis, MO, USA
Tungsten carbide knife, profile D (16 cm)	Leica Biosystems, Nussloch, Germany

Xylene	LabTech Services & Supplies, Windsor, NSW, Australia

2.2.2 Stent design

The stent design was based on the dimensions of commercially available stents. The stents were laser cut from slotted tubes of 316L vacuum melted stainless steel and electropolished to remove surface contaminants (Laserage, Waukegan, Illinois, USA).

2.2.3 Production of tropoelastin, stent design and synthesis of plasma activated coating

Recombinant TE was expressed and purified from *Escherichia coli* as described previously [143, 144]. Plasma-activated coating (PAC) was made by graded deposition, from 100% stainless steel to 100% PAC, using reactive magnetron sputtering with sample rotation (sputtering voltage of 800 V, cathode current of 3 A) [106, 145], followed by pure stainless steel deposition and increasing fractions of the plasma polymer in the presence of acetylene (10 sccm), argon (4 sccm) and nitrogen (4 sccm) plasma until a pure plasma polymer layer was formed [106, 145]. Two plasma sources were included in the pulsed plasma deposition system 1) radio frequency (RF) electrode at 13.56 Mhz and 2) pulsed direct current voltage source. An ENI-6B RF generator was used to power the RF plasma through an ENI Matchwork matching network. The pulsed DC voltage was generated using a RUP-3 pulse generator from GVS-Elektonik (Dresden, Germany). The grounded plasma chamber acted as an anode electrode. The plasma energy and magnetron settings sputtering were altered to ensure PAC deposition on all surfaces of the stent to obtain homogenous coverage of the 3D stent sample. The stent PAC deposition had column like structures to prevent delamination.

2.2.4 ^{125}I-Radiolabelling tropoelastin

Sterile filtered TE (2 mg/mL) in PBS was labelled with ^{125}I using iodination beads (Pierce) as previously described [146]. Briefly, iodobeads with Na^{125}I were used to label tropoelastin according to the manufacturer's instructions. The labelled solution was desalted, to remove unreacted $^{125}I^-$. A scintillation counter (Cobra II Auto Gamma, Packard Bioscience) was used to quantify radioactivity of the protein, before and after desalting. (The experiments were done by Dr. Anna Waterhouse – A.W).

2.2.5 Surface coating with $^{125}I^-$ Radiolabeled tropoelastin to detect covalent binding

The PAC+TE stents and BMS were incubated overnight at 4^{o}C, with 50 µg/mL ^{125}I-labeled TE. Samples were washed with sodium dodecyl sulfate (SDS), then blocked with 3% BSA. The radioactivity of the samples were measured before and after SDS, using a scintillation counter (Cobra II Auto-Gamma, Packard BioScience) to quantify level of covalently bound protein (Dr. A.W.)

2.2.6 Rabbit endothelialization model

Study approval was obtained from Sydney South West Area Health Animal Ethics Committee (protocol number 2008/036) and the University of Sydney Animal Ethics Committee (protocol number K00/12-2009/3/5243). Experiments were conducted in accordance with the Australian Code of Practice for the Care and Use of Animals for Scientific Purpose.

2.2.6.1 Animal housing

The stent implantation procedure was performed as described previously [106]. Adult New Zealand White Rabbits were housed in cages (1x1 m wide and 1.6 m high) with bedding straw and environmental enrichment. The room was temperature controlled with a 12 h light-dark

cycle. The animals were fed standard rabbit chow *ad libitum* with free access to sterilized drinking water.

2.2.6.2 Stent preparation

The 316LSS bare metal stents (BMS) were sterilized by plasma etching, then transferred to a sterile container, immediately after treatment in a sterile environment. The PAC-316LSS stents were also transferred to a sterile container immediately after treatment in a sterile environment. The PAC-316LSS-TE stents were incubated with sterile filtered TE (100 µg/mL in PBS) for 16 hours at 4^{o}C and rinsed in saline prior to procedure.

2.2.6.3 Stent implantation

Fourteen animals underwent iliac artery intervention in total. The control group received denudation of 1 iliac artery with no manipulation of the bilateral artery (n=4), and the experimental group received denudation and implantation of a BMS and PAC+TE stent in bilateral iliac arteries (n=10). Briefly, rabbits weighing 3-4 kg were sedated, anesthetized and endothelial denudation was performed via a 5 F sheath catheter placed in the femoral artery by cut down. A 3.25 mm x 10 mm angioplasty balloon catheter (Sprinter®Legend RX) was placed into the aorta over a 0.014" guide wire, inflated to nominal pressure and withdrawn retrograde three times to the external iliac artery. The control animals received no further manipulation (n=4). A BMS or PAC+TE stent hand crimped onto a 3.25 mm balloon catheter, was placed in the common iliac artery (confirmed by angiography) and expanded (to a diameter of 3.1 mm). The procedure was repeated for the bilateral iliac artery, randomizing the type of stent, order and side of implantation. A single dose of heparin was administered at the time of surgery (100 U/kg) and aspirin was administered orally 24 hours before surgery (40 mg/day) and maintained throughout the study [117, 147]. After 7 days, anaesthetized rabbits were exsanguinated by left ventricular puncture, perfused with lactated Ringer's solution and given a lethal injection of

lethabarb (130 mg/kg). Stents were explanted, flushed with lactated Ringer's solution and fixated in 4% (v/v) formaldehyde [106]. Scanning electron microscopy (SEM) and immunofluorescence analysis were carried out on 4 stent pairs and histology was carried out on 6 stent pairs.

2.2.7 Scanning electron microscopy

Biological sample processing for SEM was carried out on denuded and stented vessels. Samples were longitudinally bisected and half of each stent fixed in 2.5% glutaraldehyde for 2 hours. Samples were fixed with 1% (v/v) osmium tetroxide, dehydrated with ethanol, mounted and coated with 20 nm gold. Stents were imaged with a Philips XL-30 CP scanning electron microscope (SEM). The percent cell coverage was quantified with Image J (MA, USA). (Dr. A. W)

2.2.8 Immunofluorescence

A longitudinally bisected stent half or artery segment, was fixed in 4% paraformaldehyde for 16 h for immunofluorescence as previously described (24). Briefly, samples were incubated with 0.2 M glycine to quench fixative fluorescence (24 h at 4 ºC) and blocked for 2 h at room temperature with 10% (v/v) goat serum in TBST (0.5% Tween in Tris buffered saline). Samples were incubated with rabbit anti-CD31 antibody raised in mouse (Abcam, 1:25 in TBS) or with mouse $IgG1_k$ (Abcam, 1:25 in TBS) for 16 h at 4 ºC, washed 4 times in TBS, stained with phalloidin-TRITC (0.1 μg/ml) in TBS for 45 min, then washed 3 times with TBS. Stent sections were stained with 0.1 μg/ml Hoechst in TBS for 10 min and imaged using a 10x objective (HC PL FL 10x/0.3 PH1, free working distance, 11 mm) on a Leica TCS SPII Multi-Photon Microscope. Multipoint positioning with wide field Z-stacks was used to image stents due to sample thickness. Projections from each channel were automatically generated and stacks were merged by mosaic stitching (Leica Microsystems, Germany) (Dr. A. W).

2.2.9 Histology: tissue collection and fixation

For histological processes stented and denuded arteries were incubated in 4% paraformaldehyde for 24 h, then stored in 70% ethanol and embedded in methyl methacrylate (MMA) resin (all resin solutions were kept at 4^{o}C and polymerized at -18 ^{o}C to -20 ^{o}C). For methacrylate embedding three separate solutions were prepared as the resin mixture. The reagents mentioned below were provided by the biomaterials and tissue engineering research unit at the University of Sydney (Dr. Hala Zreiqat, Tissue Engineering). Solution 1 infiltrate (4^{o}C); and unwashed MMA. Solution 2a infiltrate (4^{o}C); unwashed MMA (90 mL), dibutylphthalate (10 mL), and benzoyl peroxidase (0.25 g). Solution 2b (room temperature); unwashed MMA (95 mL), dibutylphthalate (5 mL), and benzoyl peroxidase (0.5 g). Tissue samples were first dehydrated through alcohol: 95% ethanol x 2 (4 hours apart), followed by 100% alcohol. The samples were processed in solution 1 and 2a, at 4^{o}C. Infiltrated stented segments were left in an upright glass vial, completely filled with the polymerization mixture 2b at room temperature (exclude air). The samples were tightly capped and polymerized at -18 to -20^{o}C. Time of polymerization was dependent on sample size. Following adequate polymerization (~2 weeks), the specimen were removed by breaking the glass vials and pushing specimens out. The polymerized blocks were then shaped and trimmed off excess plastic with a grinder and sandpaper prior to sectioning (Polymerization was conducted by Miss Barbara James, research assistant, school of mechanical and aerospace engineering.)

2.2.10 Histology: Sectioning of stented arteries

The polymerized blocks were trimmed off excess resin with a linear precision saw (Buehler Isomet 5000) and polished with synthetic diamond paper (1200 μm) (Struers Inc. OH, USA) to smoothen surface prior to sectioning with an automated microtome (Thermo Scientific, HM

355S). Transverse sections, 7-10 μm in thickness were made using a D-profile tungsten carbide (TC) knife (Leica Microsystems, 16 cm). We investigated two different microtomes; Reichert-Jung Polycut S microtome (Leica Microsystems) available at Anzac Institute, Concord Hospital, and the HM355S automated microtome. Since resin is hydrophobic, sectioning was facilitated with 30% methanol. Sections were adhered to 3% gelatin coated slides (ProSciTech super-frost plus adhesion slides). The sections were covered with thin plastic film and stacked together with a spring clamp, left overnight at 42 ^{o}C prior to staining.

2.2.11 Histology: Slides

Initially uncoated glass slides were investigated to adhere hydrophobic resin sections. The adherence was comparatively increased when glass slides were coated with aminopropyltriethoxysilane (AES), provided by the Anzac Institute, Concord hospital. Next we used albumin (egg white protein) with sodium azide on glass slides. After these trials, we used 3% gelatin (PBS) as our coating of choice on Superfrost Plus glass slides, for long term adherence of hydrophobic resin sections.

2.2.12 Histology: Staining

Sections were de-plasticized with 2-Methoxyethyl acetate (Sigma-Aldrich) for 1 h, cleared in 2 washes of xylene for 20 mins, followed by hydration in descending grades of ethanol prior to staining with hematoxylin/eosin (H&E) for NIH and Carstairs' stain for early markers of thrombosis, using the manufacture's protocol [148]. Images were captured with bright field microscopy (Zeiss Imager 2.0, USA). To assess early NIH from H&E stained sections; the neointimal thickness between stent struts and lamina were calculated within cross sections (n=5 per animal), and neointimal area between the lamina and internal elastic lamina (IEL) (inclusive of stent struts) was calculated using computerized morphometry (n=5 per animal, 5x magnification, Image J and Image Pro Plus Media Cybernetics, USA). When stained with

Carstairs' stain, the fibrin, red blood cell and collagen content appeared red, yellow and blue respectively. The individual content of each component was quantified as a percent area within the NIH surrounding each stent strut (20x magnification), compared to the total NIH area (n=10 struts, within 5 cross sections per stent); with the 'smart segmentation' analytical tool on Image Pro Premier version 9.0.3 (Media Cybernetics, USA).

2.2.13 Immunohistochemistry (IHC)

Resin-artery segments were trialled to identify presence of 3 biomarkers; CD31 (luminal endothelialization), α smooth muscle actin - α-SMA (smooth muscle cell (SMC) proliferation) and MAC 387 (neutrophil/macrophage infiltration). Sections were deplasticized as mentioned in 2.2.12. Two methods were trialled for antigen retrieval; heat induced epitope retrieval (HIER) and proteinase induced epitope retrieval (PIER). Since tissue sections disintegrated during HIER, we selected PIER as the antigen retrieval step, prior to immunostaining for all 3 biomarkers. Proteinase K was prepared in TE buffer (50 mM Tris base, 1 mM EDTA, 0.5% Triton x-100, pH 8.0) at room temperature and stored at -20^{o}C (Proteinase K was kindly provided by Dr. Hamish Prosser, Immunobiology Group, HRI). Resin-artery sections of interest were incubated for 1 hour in proteinase K (1:125, with TE buffer), and blocked in NGS for 30 min. Depending on tissue thickness and size, we chose the following dilutions for primary antibodies: CD 31 (1:50 in TBST, 45 min), α smooth muscle actin (1:100 in TBST, overnight at 4^{o}C), and MAC387 (1:50 in PBS, 1 hour). We used two secondary antibody kits; 1) HRP-Rabbit (DAB+) for CD31 and MAC387 (brown dye), 2) rabbit-mouse linker with AP chromogen kit for α-SMA (red dye) (kits used in accordance to manufacturer's instructions).

2.2.14 Microscopy

Sections were imaged with transmitted light microscope, Olympus BX61 Microscope (SIS software), and Olympus IX70 inverted microscope (bright field microscopy).

2.2.15 Statistics

Data are expressed as mean ± standard error of the mean and indicated in figures as (*p<0.05, ** p<0.01 and *** p<0.001). After *in vivo* experiments, compiled stent SEM images were scored for percentage cell coverage of stent struts and intersections and divided by the number counted. Stents were also analyzed for the area of CD31 positive labelling, neointimal hyperplasia and fibrin deposition (Image J and Image Pro Plus software respectively). The data were analyzed by paired t-test for statistical significance, using GraphPad Prism version 6.00 (GraphPad Software, San Diego, California) for Mac OS X.

2.3 Results

2.3.1 Covalent attachment of tropoelastin (TE) to PAC stents *in vitro*

Covalent binding of TE to PAC stents was assessed by radioactively labelling tropoelastin with ^{125}I, measuring the amount bound to the surface, before and after SDS washes at 95^{o}C [18]. The PAC stents bound 20617±42% cpm of radiolabelled TE which was reduced by 32.23% to 13971.75±41% cpm after SDS treatment (Fig. 2.2). In contrast, BMS had 6887.75±8.8% cpm of ^{125}I TE physiosorbed to the surface, this reduced by 79.82% to 1389.75±3% cpm after SDS treatment. The PAC stents bound more TE, retaining 67.77% on surface after SDS washing to indicate covalent attachment of protein to stent surface.

2.3.2 *In vivo* assessment of stents: Feasibility of PAC+TE bioengineered stent

We had previously established biocompatibility of PAC+TE surfaces *in vitro* [145, 146] and biocompatibility of PAC stents alone *in vivo* [106]. The present *in vivo* feasibility study was carried out with a total of 10 animals, each receiving a control BMS (316L SS stent) and a treated stent (PAC+TE) implanted in bilateral common iliac arteries for a period of 7 days. We aimed to comparatively quantify progressive response to bilateral artery stenting with a 7-day follow up study, to evaluate initial response as illustrated for BMS (Fig. 2.3). The vessel position, stent deployment and post-implant patency were confirmed for each animal via angiography [106]. All animals survived the in-life phase of the study. There was no infection or gross inflammatory response observed post-surgery or on explant of the stents. Animals were euthanized 7 days after stent implantation, and longitudinal and cross-sectional samples of the stent-artery interface of PAC+TE stents and BMS prepared for investigation.

2.3.3 Cellular coverage of stents after 7 days

Experimental animals received a BMS in one common iliac artery and a PAC+TE stent in the bilateral common iliac artery for 7 days. Stent pairs from 4 animals were longitudinally bisected and analyzed by SEM. Seven days post implantation, all stents had cells partially covering the struts (Fig. 2.4 A). The percentage of strut cell coverage showed no significant difference between paired BMS and PAC+TE stents, 79±5% vs. 51±13% respectively (Fig. 2.4 B).

2.3.4 Detection of endothelium

Image analysis of stent sections stained with CD31, TRITC Phalloidin and Hoechst showed CD31 immunolabelling at cell peripheries on the intima, between struts and in some cases covering the struts in all samples (Fig. 2.5A and Fig. 2.5B). Increased CD31 positive cells were observed at the end of the stents compared to the middle of the stents, however, there was no significant difference detected in the percent of CD31 staining between matched pairs of BMS and PAC+TE stents, 83% vs. 75% respectively (Fig. 2.5C). Additionally, there were areas of struts in all samples in which the cells covering them were CD31 negative.

2.3.5 Neointima formation

Five cross sections each of the stent pairs from the 7 day study randomly chosen along the length of the stents were H&E stained to assess neointimal thickness and neointimal area. A schematic cross section of the stented arterial wall represents the stented vessel and area of interest used for analysis (Fig. 2.6). The thickness and total area between the stent/internal elastic lamina and the lumen at 7-day follow up was quantified for early neointimal proliferation/NIH. Representative images from the middle sections of stents are shown (Fig. 2.7 A). Stent struts were observed as black-square shapes in the histological analysis. There

was no visible inflammatory response caused by either BMS or PAC+TE stents in the H&E stained sections and positive remodelling was not seen at day 7. Thickening of tissue on the luminal side of internal elastic lamina (IEL, indicated with white arrows), shows the presence of early NIH (Fig. 2.7 A). Neointimal thickness of images quantified with Image J, indicate lower thickness in PAC+TE stents (22.73±6.52 μm) compared to BMS (31.77±6.95 μm) ($P<0.05$) (Fig. 2.7 B). Total neointimal area was lower for PAC+TE (377.97±40.19 μm^2) vs. BMS (433.69±62.39 μm^2) ($P<0.05$) (Fig. 2.7 C).

2.3.6 Early Markers of Thrombosis

The sum of fibrin, red blood cell (RBC) and collagen content detected with Carstairs' stain were used as markers of early in-stent thrombogenicity (Fig. 2.8 A). The fibrin content (red) within the neointima (indicated by black arrow) was higher in BMS (25.23±2.25%) vs. PAC+TE stents (18.32±1.94%) ($P<0.05$) (Fig. 2.8 B). There was no significant difference in the RBC content (yellow) in BMS (26.40±9.82%) vs. PAC+TE (23.52±8.43%) (Fig. 2.8 C) or collagen content (blue) for BMS (22.2±8.2%) vs. PAC+TE (28.82±10.9%) (Fig. 2.8 D), although a trend towards decreased RBC content and increased collagen content, was observed in PAC+TE vs. BMS respectively. The overall key morphological features at 7 day follow up, were schematically illustrated to compare BMS vs. PAC+TE stents (Fig. 2.9)

2.3.6 Immunohistochemistry trials

The IHC results were visualized to indicate positive antigen retrieval, and immunostaining uptake for MAC 387 (markers for macrophage/neutrophil) and CD31 (luminal endothelialization) (2.10 A, B respectively). Results for α SMA (smooth muscle actin) showed

non-specific staining uptake compared to the negative control (2.10 C). Results were not quantified due to limited number of sections.

Figure 2.2

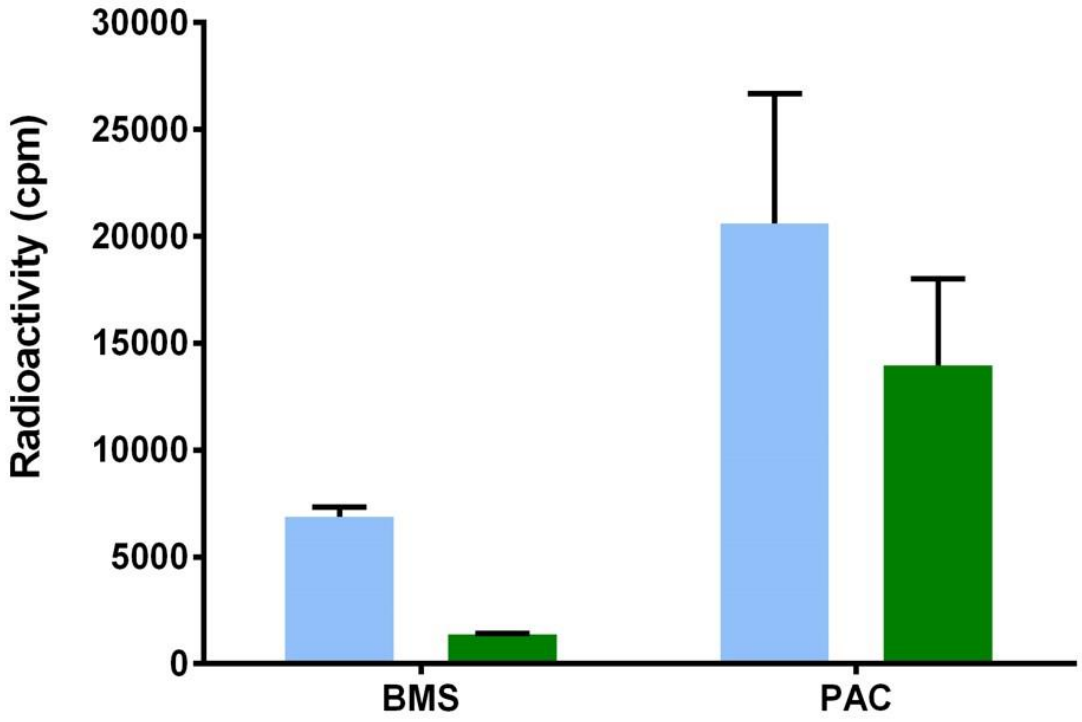

Covalent binding of ^{125}I Tropoelastin (TE), Radioactivity count of ^{125}I TE bound to PAC and BMS before (blue) and after (green) SDS treatment for 10 min at 95^{o}C.

Figure 2.3

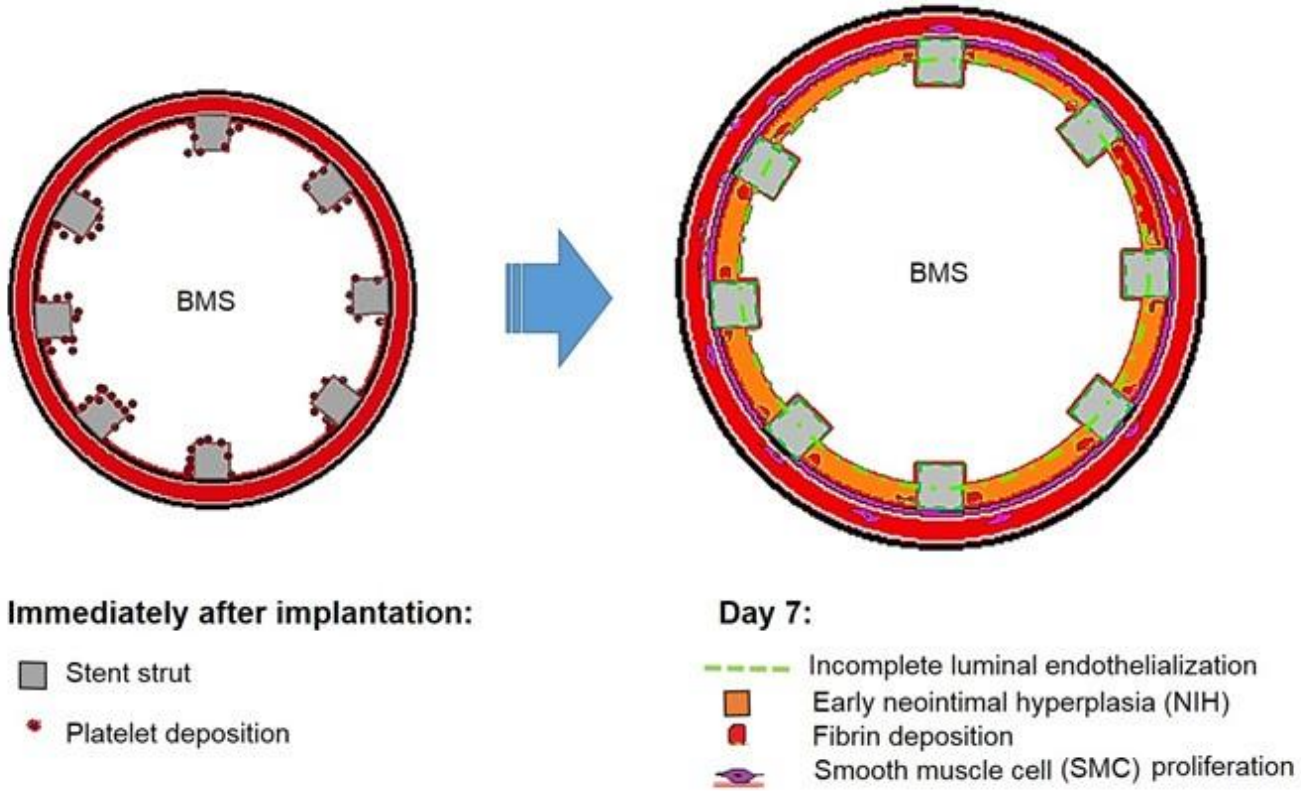

Illustration of key morphological features observed after stent implantation in BMS, immediately after implantation and at 7-day follow up. Early response is characterized by luminal endothelialization, in-stent platelet/fibrin deposition, smooth muscle cell (SMC) proliferation/migration and characteristic neointimal thickening. Illustration modified from Virmani et al [114].

Figure 2.4

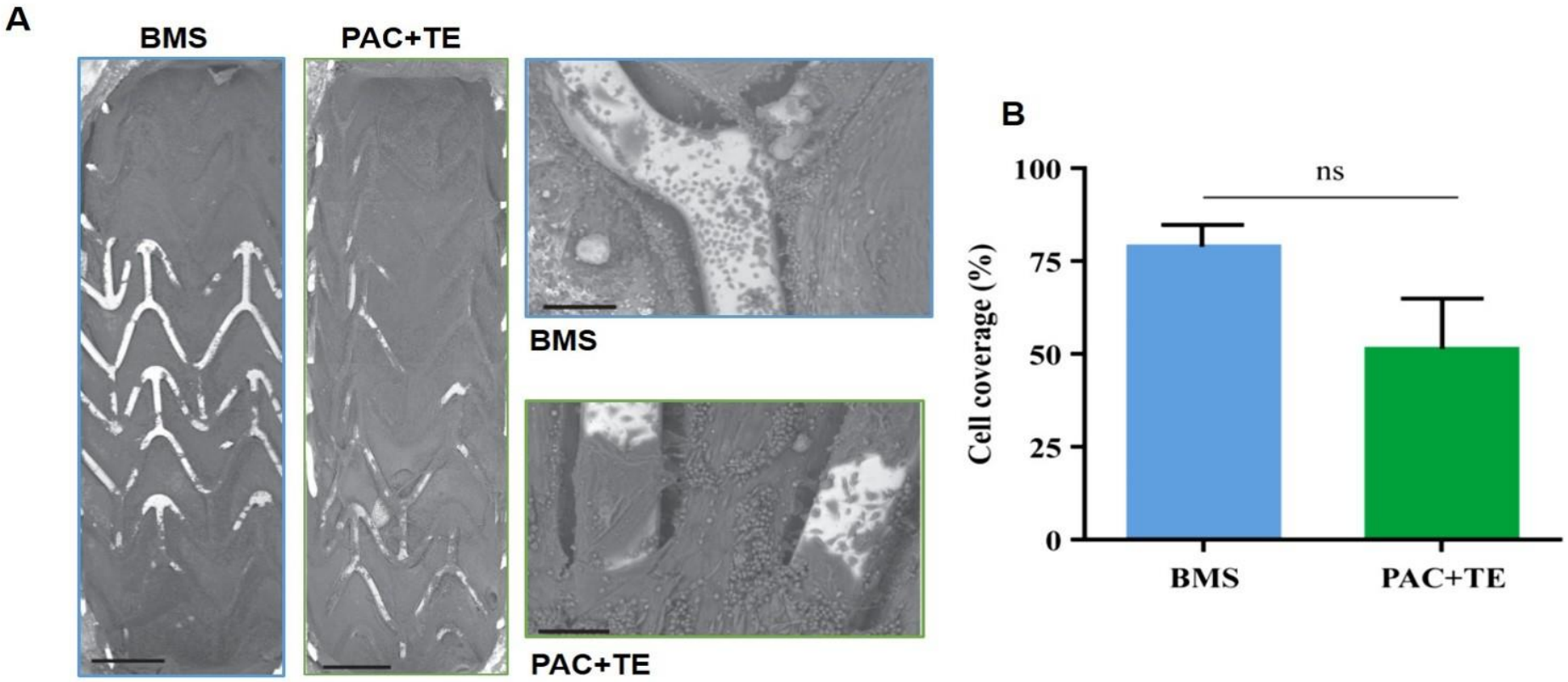

Cell coverage of paired implanted stents. A. Representative SEM images of cell coverage on paired stents, BMS (blue), PAC+TE (green), 7 days post stent implantation. Scale bars in low magnification images indicate 1 mm and scale bars in the high magnification images indicate 100 μm. B. Percentage of cell coverage on stent struts.

Figure 2.5

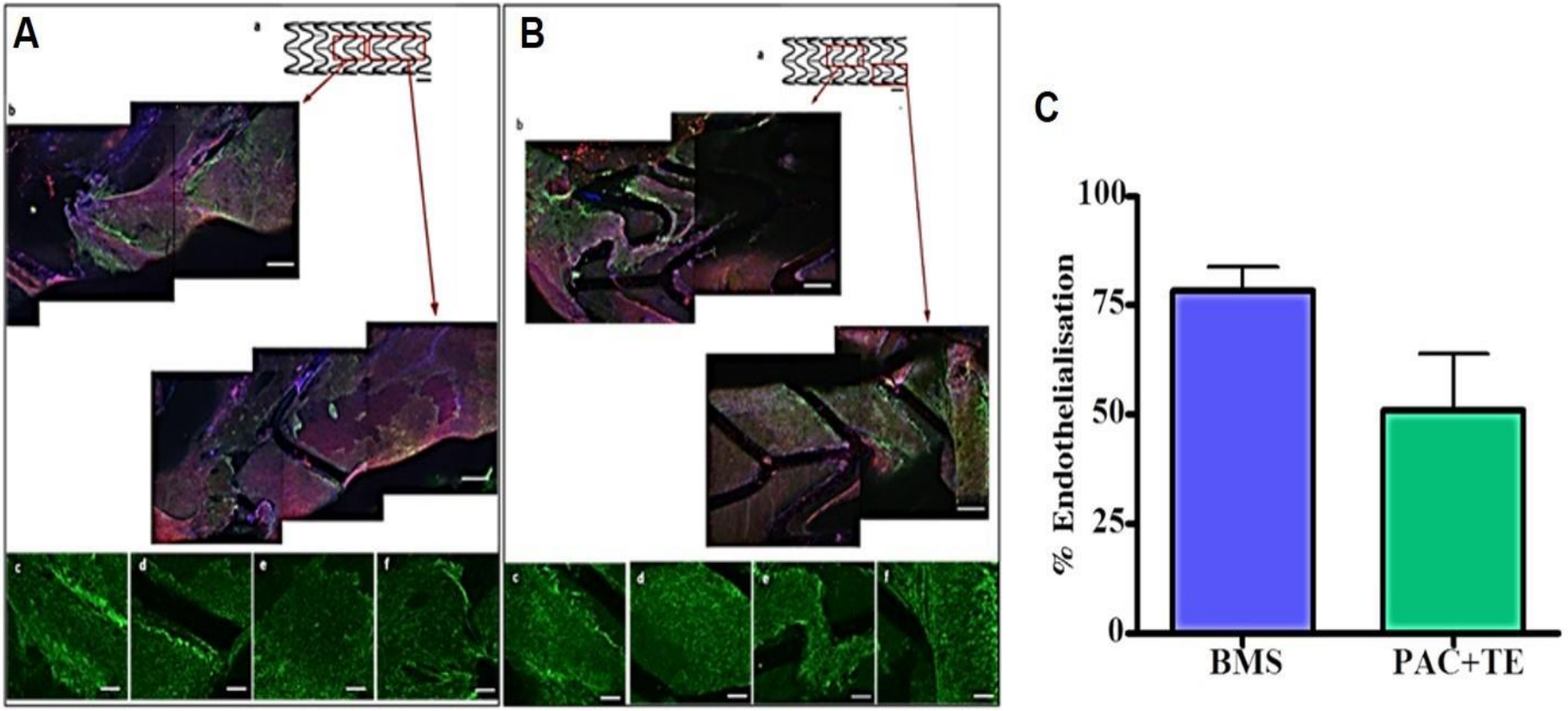

Representation of the stents: (A) merged projections of longitudinally sectioned BMS, (B) merged projections of longitudinally sectioned PAC+TE, and (C) percent endothelialization quantified with CD31 immunofluorescence for both stent types. Stents were immunofluorescently labelled for CD31 (green), phalloidin TRITC for actin (red), and Hoeschst for nuclei (blue) (b). Stent sections labelled with CD31 for endothelialization are magnified and imaged for each stent type (c-f)

Figure 2.6

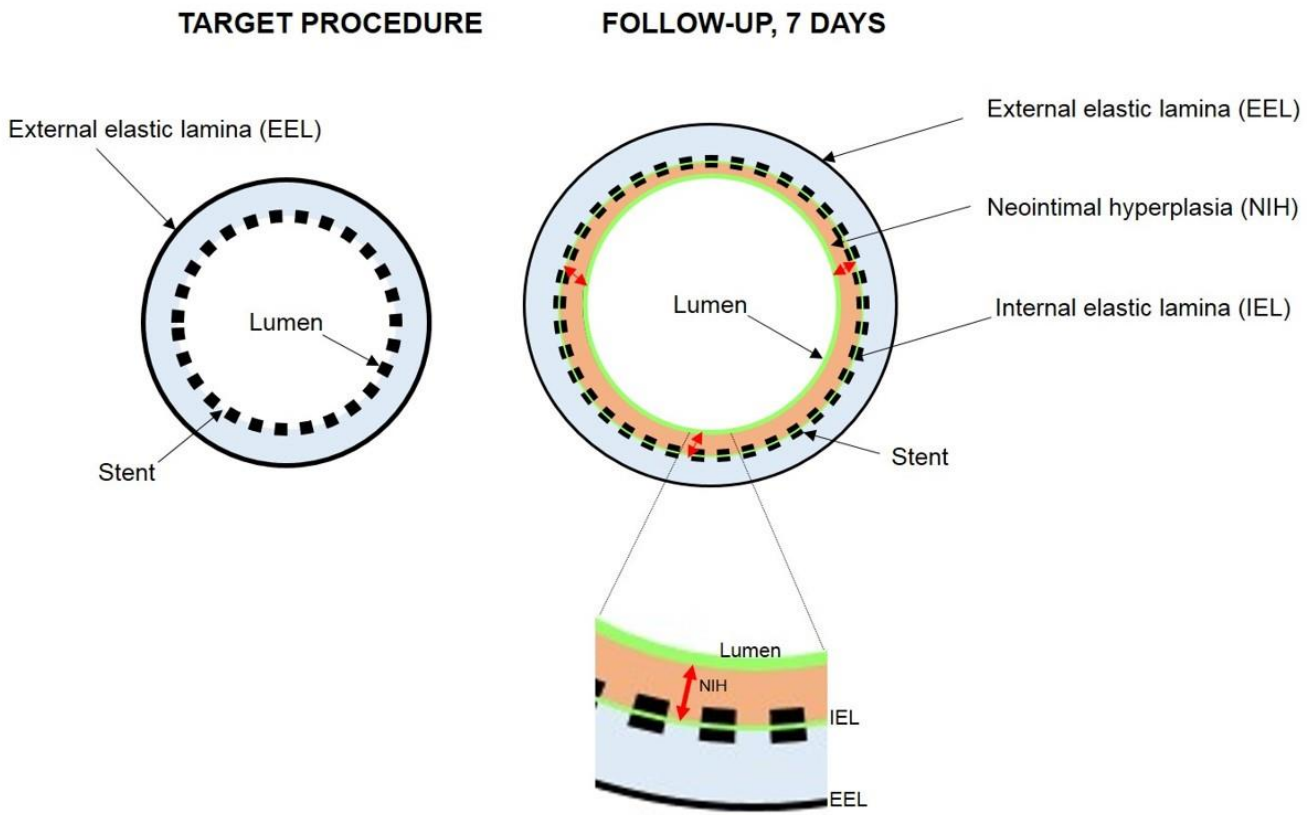

Representation of a stent-artery cross section, denuded at target procedure and 7-day follow-up with no observable positive arterial remodeling. At day 7, the site of interest for early neointimal hyperplasia (NIH) (red arrow, explained in detail inset) is the thickness between the lumen and the internal elastic lamina (IEL) inclusive of stent struts. The neointimal area of total vessel calculated is highlighted in green. Respective calculations were done with Image J and Image pro premier, results were compared between stent types. Image modified from Farooq et al [149]

Figure 2.7

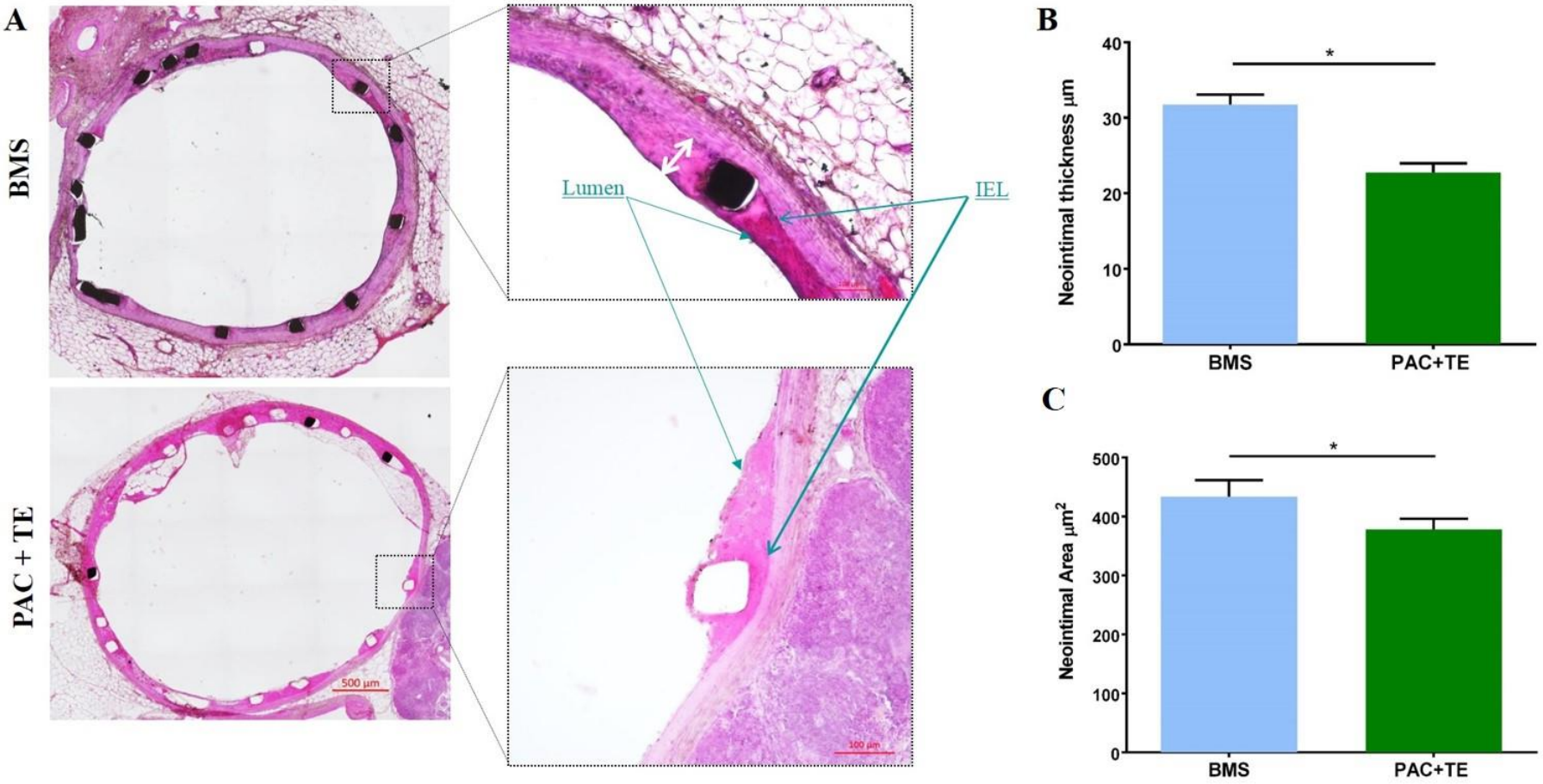

A. H&E staining for the degree of early neointimal hyperplasia (NIH). B. Significantly lowered neointimal thickness BMS (31.77±6.95 µm) vs. PAC+TE (22.73±6.52 µm) and C. Significantly lowered neointimal area PAC+TE (377.98±40.19 μm^2) vs. BMS (433.69±62.39 μm^2) was observed.

Figure 2.8

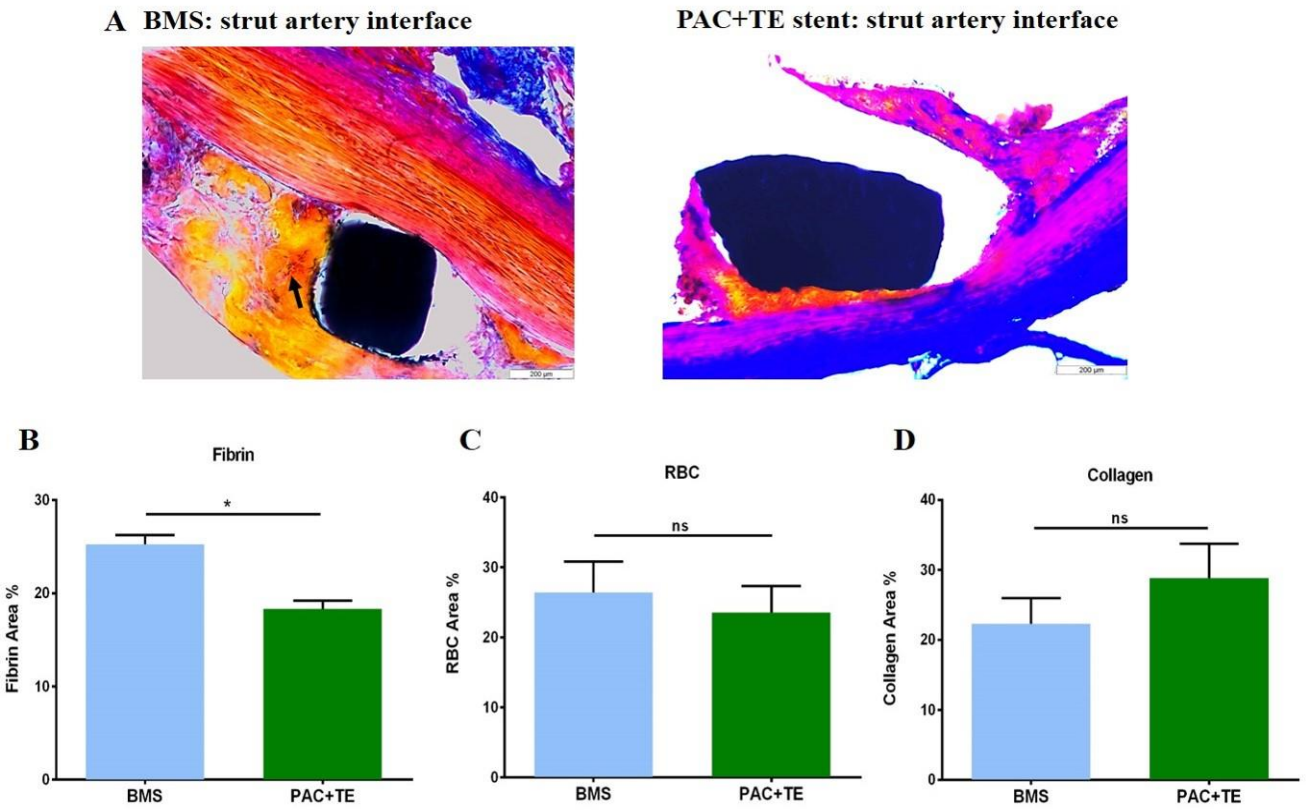

Carstairs' staining for degree of fibrin, RBC and collagen deposition in stented rabbit iliac arteries. For accuracy, only the content of fibrin in the neointima surrounding the stent struts was quantified (20x magnification). Arrow indicates fibrin deposition (red), among the RBC (yellow) in the neointima for BMS. Collagen deposition (blue) dominant in the adventitia. Calculations of the media, were exempted from the study. Percent fibrin content was significantly higher in BMS (25.23±2.25 %) vs. PAC+TE stents (18.32±1.94 %). There was no significant difference in the RBC and collagen content in stented arteries.

Figure 2.9

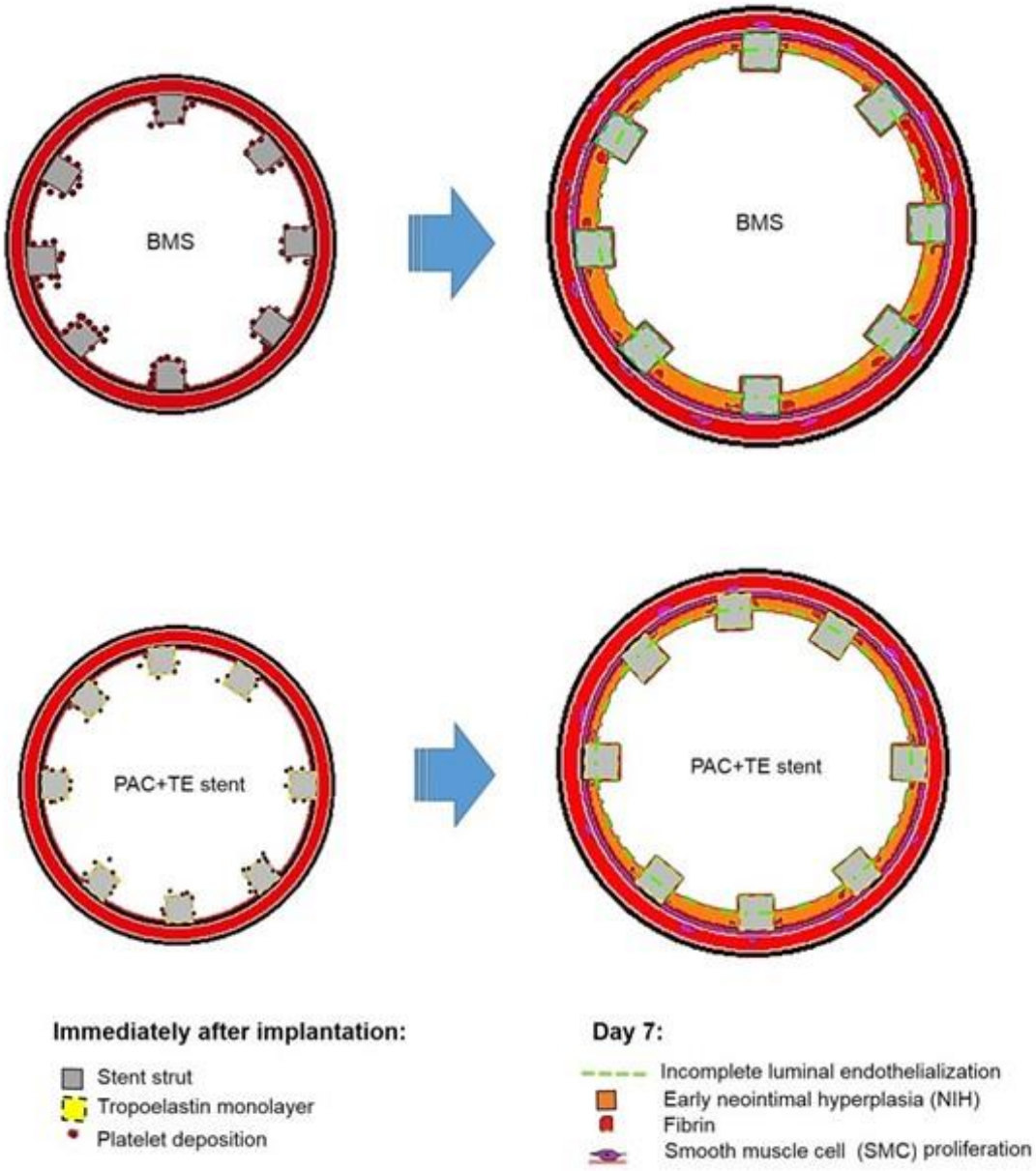

Illustration of the key morphological features after stent implantation for BMS vs. PAC+TE, immediately after implantation and at 7-day follow up. Early response at 7 day is characterized by luminal endothelialization, in-stent platelet/fibrin deposition, smooth muscle cell (SMC) proliferation/migration and characteristic neointimal thickening. Positive arterial remodelling is not observed for either stent type at 7 day follow up. Illustration modified from [114]

Figure 2.10

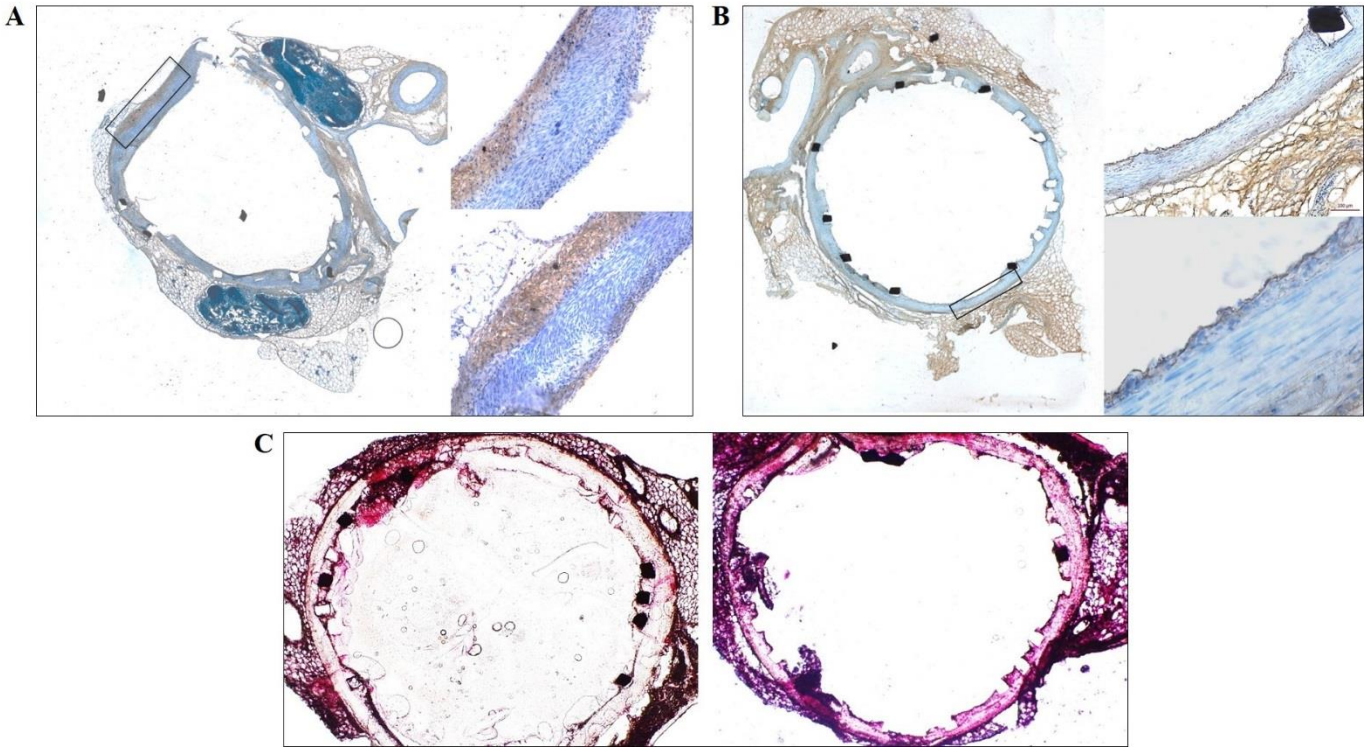

Cross sections were stained after antigen retrieval with PIER. A) MAC 387 antibody, marker of neutrophil activation was positive for both PAC+TE and BMS (BMS represented) (4x mag, 10x, 20x mag inset). B) CD31 antibody, marker of luminal endothelialization was positive for PAC+TE not BMS (PAC+TE represented) (4x mag, 10x, 20x mag inset). C) Non-selective staining seen for α SMA positive stented artery cross-section (right), compared to negative control (left) (10x mag).

2.4 Discussion

This is the first investigation of a covalently immobilized monolayer of recombinant human tropoelastin on a PAC stent surface, to assess biocompatibility in an established rabbit bilateral iliac artery stenting model. The key outcomes of the study demonstrate strong covalent protein binding to a PAC stent, reduced early neointimal area, reduced neointimal thickness, reduced fibrin deposition, equivalent cell coverage and equal early endothelialization, compared to 316LSS BMS, after 7 days *in vivo*. The pilot study was feasible *in vivo*.

2.4.1 *In vitro* evaluation of stent PAC

Similar to original PAC previously analyzed, stent-PAC was able to retain covalently bound tropoelastin (TE), demonstrated by radioactively-labelled tropoelastin retention, after SDS washes *in vitro* (figure 2.2). We used radioactive iodination of tropoelastin; an established method [146, 150], to label and quantify covalent attachment of proteins to the modified surface. The linker-free covalent binding observed, is consistent with previous studies [136, 151], providing the robust surface adhesion required for *in vivo* application on cardiovascular stents. In the novel plasma-based coating process discussed, the biomaterial is completely covered by the thin layer of deposited plasma polymer, ensuring the chemical status of the stent surface is determined by the deposited material and not underlying bare metal alloy [106],[151]. Animal studies are necessary to fully evaluate medical device safety. Stent endothelialization is often investigated with porcine or rabbit, animal models. This study demonstrates implantation of PAC+TE stents and BMS into balloon denuded rabbit common bilateral iliac arteries. Endothelialization of this model would be at a slower rate compared to porcine model, allowing differences to be observed at 7 days [33].

2.4.2 *In vivo* evaluation of PAC+TE stent

2.4.2.1 Pilot study

The pilot animal experiment was designed to establish feasibility and safety of a PAC+TE stent compared to BMS *in vivo*. Stents were implanted in bilateral iliac arteries of rabbits for 7 days to assess endothelialization and PAC+TE integrity at primary endpoints. The model was chosen since its commonly used to assess healing response following arterial denudation and stent implantation [33], with results comparable to humans at chosen endpoints [114].

Both stent types were sterilized during the deposition and cleaning process, to result in a homogenous surface. This is a common method of surface sterilization with plasma modified materials in medicine [98]. A diameter of 3.1 mm was chosen for balloon expansion during stent implantation, since rabbit common iliac arteries were approximately 2.5-2.75 mm in diameter, to result in a stent to artery ration of 1.13:1-1.24:1. This method is equivalent to overexpansion of stents during human implantation, although at a value below the ration of 1.3:1, which can cause chronic vessel injury [152]. Animals were maintained on aspirin received daily in their drinking water, starting 24 hours prior to the procedure, and maintained throughout duration of the experiment, to prevent acute stent thrombosis [33, 117]. Animals were sacrificed at 7 days, the endpoints chosen based on literature showing near complete percent endothelialization for BMS by 14 days [33]. Earlier time points were chosen to detect a possible increase in endothelialization on PAC+TE compared to BMS.

The control animals with one denuded iliac artery without stent implantation, and the bilateral iliac artery with no manipulation were chosen to assess success of the balloon denudation procedure. Denudation of the artery with a balloon catheter as a control, was successful resulting in comparable vessel healing response, as in literature [153]. Furthermore, each experimental animal had one BMS implanted in an iliac artery and PAC+TE in the bilateral

iliac artery. The order and side of stent implantation was randomized. No animals died as a consequence of either stent type and no observable infection was seen at the endpoint, owing to sterility of the stents. By day 7, stents were well tolerated, without fracture post-implantation.

2.4.2.2 Addressing endothelialization and thrombogenicity.

Our strategy to mitigate restenosis and thrombosis was to exploit the attributes of recombinant human tropoelastin (TE). TE is the monomer of the biopolymer elastin, which clinically regulates vascular cells. Elastin and TE have been shown to have low thrombogenicity, promote endothelialization and inhibit SMC proliferation [138, 139, 154] making it an ideal coating candidate to enhance biointegration of stents. Recombinant human tropoelastin has been produced from *E. coli* (36) and successfully used in a range of biomaterials [155]. Tropoelastin has potential advantages for vascular biocompatibility in comparison to other intravascular device coatings such as vascular endothelial growth factor (VEGF) and anti-CD34 antibodies, shown to have adverse effects in clinical studies [139, 156]. To robustly immobilize TE to stents *in vivo*, we utilized covalent protein binding capability of PAC (38). We had previously angiographically established coating integrity of PAC stents *in vivo* [106] .

2.4.3 Histopathology evaluation of PAC+TE stent

Histopathological assessment after BMS and DES implantation in human arteries allowed evaluation of the arterial-stent interface, and has been well documented [114, 157]. The local response to 316L SS BMS implantation follows a similar pattern of arterial injury and repair, accompanied with neointimal formation and endothelialization in animals, and in humans [114]. However, timeline for healing response after BMS placement in a human is 5-6 times longer than in rabbit iliac arteries, and pig coronary arteries. In animals, peak neointimal growth is reached at 28 days, compared to 6-12 months in humans. Of note, the precise time course for

neointimal growth and healing in human coronary arteries with DES is unknown due to prolonged inhibition of neointima [114]. The rate of neointimal expansion is greatest between 7-14 days in animal models.

2.4.3.1 Early markers of neointimal hyperplasia and thrombosis

The study shows increased early neointimal thickening and neointimal area, with H&E staining, for BMS compared to PAC+TE (figure 2.7). Although a characteristic peak in early neointimal growth is observed, as expected, neither stent type exhibited positive arterial remodelling or luminal compromise at 7 days [158]. In the early response, platelet and fibrin deposition occurs around the stent struts and scattered neutrophils within mural thrombi extend between struts [114, 128]. Excessive mural thrombogenic response was prevented by anti-coagulation with aspirin.

Histopathological results with Carstairs' [148] showed lower fibrin deposition surrounding struts for PAC+TE stents compared to BMS, indicating comparatively improved arterial response at 7 days (figure 2.8). At 7 days, percent content of red blood cells and adventitial collagen between stent struts did not vary significantly. The RBC area percentage in the stent-strut/artery interface showed trends towards reduction in PAC+TE compared to BMS, whilst collagen content showed an increase in PAC+TE compared to BMS, following a distinct pattern of local arterial injury and repair, in response to stenting [114]. At 28 days, fibrin is expected to be absent, while neointima may gain a larger number of SMC, proteoglycans, type III collagen, and majority of inflammatory cells around stent struts, incrementally (figure 2.1). Extended studies would allow further evaluation of thrombosis and remodelling.

Preliminary luminal endothelialization is expected to occur at the artery/stent interface by day 7 [33]. Immunofluorescence analysis of CD31, and endothelial specific marker, on surface of longitudinal sections of PAC+TE showed equivalent cell coverage compared to BMS at 7 days,

at the proximal and distal ends of stents, as seen in previous studies of endothelialization [147, 159] (figures 2.4 and 2.5). The expression of CD31 was concentrated at endothelial cell borders, where it engages in cell-cell binding, and is seen between and covering struts on BMS and PAC+TE stents. The presence of tropoelastin did not show an improved benefit for endothelial cell interaction *in vivo*. The CD31 negative areas observed could be due to uncovered struts, thrombus formation or early SMC proliferation and migration from the arterial lining.

Documented timeline for cell proliferation peaks at seven days reducing in half at 14 days, to return to low baseline levels at one month [114]. A longer study time point of 14 or 28 days will be more conclusive of the arterial response *in vivo,* to assess impact of PAC+TE vs. BMS on endothelialization. The arterial wall was injured via denudation prior to stent deployment, for comparable arterial healing as seen in humans. This is a generalized estimation of arterial repair, given that most human arteries for stent implantation are associated with extensive local trauma [160]. However, arterial remodelling termed 'Glagov's phenomenon' occurs regardless of atherosclerotic plaques in the arteries, since blood flow properties mediate remodelling after angioplasty, hypertension, flow diversion as well as atherosclerotic plaque progression [161].

2.4.3.2 Immunostaining of PAC+TE

Immunostaining was conducted on resin stent-artery cross sections to visualize markers of endothelialization (CD31), smooth muscle hyperproliferation (α SMA), and neutrophil infiltration (MAC 387). For the purpose of antigen retrieval and antibody uptake, the resin had to be completely deplasticized. However, MMA resin posed several technical challenges, including incomplete deplasticization, which compromised complete antigen retrieval (figure 2.10). By day 7, most biomarkers of endothelialization, neutrophil infiltration and smooth muscle cell proliferation, were at early stages of expression. Previous investigations showed

absence of macrophage expression at 3-14 days, although neutrophil, not macrophage infiltration is shown to occur after endothelial denudation [162]. The antibody marker of inflammation MAC 387 used in this study, recognizes tissue macrophage as well as intracytoplasmic antigen expressed by day 7, which includes granulocytes and monocytes abundant during this timeline. We observed staining up take with MAC 387 on BMS and PAC+TE by day 7, on a few sections, although inconsistently (figure 2.10 A). Virmani et al [114] have shown stent struts contain smooth muscle cells, macrophages with scattered lymphocytes, red cells, and luminal endothelial cells by day 7. Endothelialization is usually complete between 14-28 days [33], we observed partial luminal endothelialization with PAC+TE stent cross-sections at day 7 in agreement (figure 2.10 B). Rate of neointimal expansion is greatest between 7-14 days [114], since H&E staining indicated thickening of neointima in our study, we investigated smooth muscle cell hyperproliferation with α-smooth muscle actin (α SMA) antibody. Nonspecific staining uptake was observed for resin-stent artery cross sections, in comparison to negative controls (figure 2.10 C). The IHC limitations in this chapter, could be owing to resin type (MMA), incomplete deplasticization, lack of PIER optimization thereof, and lack of antigen retrieved for staining. Extensive trials were limited in this study, due to limited number of sections available. Furthermore, at day 7, antigens for endothelialization (CD31), neutrophil (MAC 387) and smooth muscle actin (α SMA), are likely to be at early stages of expression, or not available at all. Biomarkers of IHC staining, are likelier to be expressed completely during investigations with extended timeframes, as well as within different embedding media to minimize practical and technical limitations.

2.4.3.3 Study Limitations

The main limitations of the present study is the short 7-day time frame. This time point was chosen to primarily address feasibility and safety of a stent surface bioengineered with a bioactive monolayer of tropoelastin. Positively remodelled vessels predict increased likelihood

of restenosis, and were not observed at this earlier time point either. Complete evaluation of the morphological features mentioned, can be investigated with an extended timeline and larger cohort, given that feasibility of technique and stents have been confirmed herein. To minimize technical limitations discussed, different embedding media can be used, and techniques of antigen-retrieval optimized.

2.5 Conclusion

The PAC+TE stents showed covalent binding capacity for recombinant human tropoelastin *in vitro* compared to BMS. This is the first study to investigate the effect of PAC+TE stents in a rabbit bilateral iliac artery model of endothelialization *in vivo*. The PAC+TE stents showed equivalent cell coverage, equivalent endothelialization, reduced early neointimal thickness, neointimal area, and reduced early fibrin deposition compared to commercial BMS. The study of covalently immobilized tropoelastin on a PAC stent *in vivo* was feasible, showing no adverse early inflammatory or thrombogenic effects. A larger cohort, within an extended 14-28 day study timeline, is essential to verify long-term impact of PAC+TE stents vs. BMS *in vivo*. The results presented demonstrate PAC+TE stent coating as a promising approach to improve biocompatibility of coronary stents *in vivo*.

Chapter 3 – Bioengineering alloy L605 cobalt chromium cardiovascular stent biomaterial for surface enhancement and characterization

3.1 Introduction

3.1.1 Cobalt chromium material for surgical implant applications

A principal requirement for biomedical alloys in device implantation is *in vivo* corrosion resistance, combined with optimal mechanical properties at implant interface. The ideal metal alloy would have "the elastic modulus of magnesium, strength of cobalt chromium, corrosion resistance of titanium and formability of stainless steel"[163]. Biocompatibility has been re-defined in the material context, as the ability of a material to perform with an appropriate response in a specific application [164]; the definition highlights device response variation is probable in varied biological conditions.

The stiffness of a material, also known as its elastic modulus, is an important concern during *in vivo* applications of biomaterials. Implanted alloys take a disproportionate share of the load (stress), to cause stress shielding; as a result in orthopaedic applications of biomaterials, the bone associated with implant becomes comparatively stronger [163]. Cobalt chromium also exhibits improved corrosion resistance; for example, hip implants originally made of stainless steel were replaced with cobalt-chromium alloys as the material of choice for long-term safety and associated durability [165].

At present, cobalt chromium alloys are commonly incorporated as implant materials in dentistry, orthopaedics and cardiology [166]. The alloys have found applications with blood contact in pacing leads, AAA stent grafts and self-expanding stents for over a decade [163]. The driving force to select these super alloys as laser-cut commercially available

cardiovascular stents is due in parts to, reduced strut thickness for improved deliverability and reduced total stent volume (without compromising radial strength or radiopacity), combined with acceptable biological response *in vivo*. As outlined in chapter 2, four key factors contribute to implant device performance *in vivo*, including device position, patient lesion-related factors, time course of DAPT and device material characteristics. Device characteristics are directly linked to material composition. Biocompatibility, X-ray/MRI visibility, radial strength, arterial recoil mechanisms, axial/radial flexibility, deliverability, profile and long term durability of an implant device are dependent on overall physical, chemical and mechanical properties of material used for implant device manufacture [167]. Cobalt-chromium based biomaterials are covered by several ASTM (American Society for Testing and Materials) approved specifications, with ASTM F75 Co-28-6-Mo and **ASTM F90** Co-20Cr-10Ni, predominant for cast alloys and wrought alloys respectively [168].

The ideal stent material will be fully corrosion resistant, biocompatible, fatigue resistant, and visible with X-ray/MRI methodology.

3.1.1.1 Microstructure of Cobalt Chromium Alloy L605

Investigating the microstructure of metal alloys used as biomaterials, predominantly examines the physical and chemical composition at the elemental, supramolecular and atomic levels of the material of interest. The ASTM F90 wrought alloy Co-20Cr-10Ni utilized in this study is comprised of the chemicals seen in table 3.1. The metal L605 alloy used in this study meets ASTM F90 and UNS R30605 specifications; i.e. chemical, mechanical and metallurgical requirements for wrought cobalt chromium alloy, for use in surgical implants. Several alloys of cobalt chromium are used in commercial CoCr stent production, including MP35N, Phynox/Elgiloy and L605. Selected physical and mechanical properties of the 3 CoCr alloys and stainless steel alloy 316L are comparatively represented in table 3.2, replicated from [166].

Table 3.1 Chemical Analysis of wrought Co50-Cr20-W15-Ni10 Alloy for Surgical Implant Applications [utilized in this study].

Element	**Percent Weight (Wt%)**
Carbon (C)	0.112
Chromium (Cr)	20.10
Cobalt (Co)	BAL
Iron (Fe)	2.40
Manganese (Mn)	1.51
Nickel (Ni)	10.70
Tungsten (W)	14.70
Phosphate (P)	0.010
Sulphur (S)	<0.002
Silicon (Si)	0.20
Specifications: AMS 5537, H; ASTM F90-09 Chemistry only, UNS# R30605	

Table 3.2 Comparing physical and mechanical properties of annealed CoCr alloys vs. 316L stainless steel alloy [table from [166]]

Alloys	**Specific Mass (g/cm^3)**	**Elastic Modulus (GPa)**	**UTS (MPa)**	**Yield Strength (MPa)**	**Tensile Elongation (%)**
316 L SS	7.95	193	670	340	48
Phynox / Elgiloy	8.30	221	950	450	45
MP35N	8.43	233	930	414	45
L605	9.1	243	1000	500	50

Cold work and annealing conditions contribute to the typical mechanical properties observed for the metal alloys, a small grain size of ASTM 7 or finer obtained in manufacture. The requirement for small grain size is imperative in stent production with thinner strut size requiring a minimum of 3 grains through the strut as a rule of thumb [166]. Alloy L605 utilized within the present study has a fine grain size of ASTM 5 within material microstructure, twinning grain boundary, and a material thickness of 250 µm. The microstructure of alloy L605 has been studied via transmission electron microscopy (TEM), energy filtering transmission electron microscopy (EFTEM), electron spectroscopic diffraction (ESD) for surface analyses, and selected area electron diffraction (SAED) to display twinning boundary microstructure in the CoCr material matrix herein. Among the 3 CoCr alloys mentioned, alloy L605 stands out as the most favourable material for stent production due to higher density, stronger elastic modulus, radiopacity and recoil. The underlying stent material for commercially available drug-eluting coronary stent system Xience Prime^{TM} is a medical grade L605 CoCr alloy (FDA summary of safety and effectiveness data, 2011). Of note, new generation innovative bare metal stent Multi-Link8 coronary stent system (Abbott Vasculature) is also manufactured with cobalt chromium technology for thin struts and improved deliverability [169].

Previous studies conducted on the manufacture of cobalt chromium alloy L605 have shown the variability of material based on cold work and final anneal temperatures, with a described cold work range of 0-45% and temperature window of 900-1175^{o}C, allowing stent designers a selection of optimal material properties for their device [166]. Studies investigating the link between stent design and its performance conclude that optimized material properties are overall dependent on device design [170, 171].

3.1.2 Impact of stent design on restenosis and intimal hyperplasia:

Several practical considerations are made during applications of a material in a coronary stent system. Commercially available stents are either balloon expandable or self-expanding during implantation. The ideal stent material for balloon expandable stents, would have an infinite elastic modulus to prevent recoil, a low yield strength to allow crimping/expansion of the stent delivery system, high ductility to withstand deformation during expansion, and high tensile properties (ultimate tensile strength -UTS) to permit thinner struts for an overall lower volume/profile [167]. Thinner strut size and lower profile, alloy L605 stents improves flexibility, and access to smaller vessels. Stent strut size is also associated with greater clinical benefits as discussed below. The material properties outlined above are interrelated; therefore require careful compromise to prevent contradictions. For example, materials with higher tensile strength permit thinner struts but typically also have higher yield strengths, and the latter may result in acute recoil during balloon deflation. Whilst alloy 316L SS, is a reference material for successful stent applications despite weak radiopacity, the cobalt based alloy L605 exhibits comparatively higher density, elastic modulus, strength and difference between yield and UTS, with similar ductility compared to stainless steel. Alloy L605 has therefore received much interest as a stent material. However, no available material at present is known to demonstrate ideal features, therefore compromises have been made to sacrifice some material properties over others during practical applications of the alloys in cardiovascular stents.

The main benefit of stenting compared to balloon angioplasty alone is the ability to comparatively reduce restenosis [4]. However, in-stent restenosis is a major limitation of stent therapy, predominantly in bare metal stents, with intimal hyperplasia being the mechanism of stent restenosis, as seen mainly with stainless steel stents within multivariate study models [172, 173]. Simple, cost-effective strategies have been rigorously employed to address clinical

complications and understand mechanisms of in-stent restenosis [174, 175]. Although relation between strut thickness and vascular wall reaction seems intuitive, very little attention has been paid to the phenomenon. The effect of strut thickness on restenosis has been investigated within clinical trials with stents of similar design and material composition, but reduced strut size (ISAR-STEREO trials) [176]. The primary endpoint of the trial - angiographic restenosis showed a 42% risk reduction for thin strut patients (15%) compared to patients with 2x strut size (25.8%) [176].

The usefulness of cobalt chromium coronary stent alloy, investigated during its first clinical experience after deployment further exemplifies that novel thin strut stents maintain radiopacity and radial strength, without compromising long-term results, as seen with thicker strut stainless steel or gold-coated stents [177]. The effect of strut thickness on restenosis outcome and neointimal hyperplasia has been further investigated within several other clinical studies, comparing various stent types including cobalt chromium stents [176, 178]. At 6 month follow-up a comparative intravascular ultrasound study investigating intimal hyperplasia among 3 types of commercial stents show stent type as the only independent predictor of intimal hyperplasia thickness within human atherosclerotic coronary arteries [178]. Among the stents compared, cobalt chromium stent Multi-Link proved to result in less tissue proliferation at 6-month follow-up, compared to 316-L stainless steel Palmaz-Schatz and InFlow stents [178].

The acceptable biocompatibility and reduced adverse proliferative response has made cobalt chromium alloy a suitable stent platform for drug eluting stents as well. Clinically, after drug-elution the residual polymer matrix and stent should maintain biocompatibility in patients, to prevent restenosis and device failure. Based on this rationale, thin-strut cobalt chromium is often utilized as the underlying biomaterial for drug eluting stents [95, 179]. Clinical trials

comparing two types of DES have shown NEVO sirolimus eluting stent (NEVO SES) with a cobalt chromium backbone more superior to TAXUS Liberte paclitaxel-eluting stent with 316L SS backbone (TAXUS Liberte PES); in relation to neointimal hyperplasia suppression, less positive remodelling and decreased morphometric abnormalities surrounding stent or at stent margins [95].

3.1.3 Clinical effects of drug eluting stents and cobalt chromium stents:

A broad spectrum of clinical trials have demonstrated that restenosis, in-stent neointimal hyperplasia and major adverse cardiac events (MACE; death, myocardial infarction, stroke and target lesion revascularization (TLR)) were significantly reduced with the use of DES compared to BMS [27, 180]. While the clinical benefits of DES reported are entirely due to the highly significant reduction in repeat revascularizations, concerns about late events associated with DES have surfaced, suggesting discriminate usage of DES [181, 182]. The incidence of late stent thrombosis, a potentially fatal complication, is associated with an increased risk post DES implantation, compared to restenosis predominant in BMS, as illustrated in figure 3.1 [183]. Parallel to the variation in vascular disease severity within patients undergoing stent implantation, the role of adjunctive antiplatelet therapy is also integral to stent bio-integration. Although originally a science advisory including the American Heart Association, American College of Cardiology and Society for Cardiovascular Angiography and Interventions et al, recommended a 12 month regime of dual antiplatelet therapy, as published in 2007 [184], recent investigations still debate the optimal duration of DAPT, which has not yet been precisely determined [135, 185]. While patients with coronary artery disease worldwide have received immense health benefits via coronary-artery stent implantation, potentially serious albeit uncommon complications such as stent thrombosis and internal bleeding need aggressive examination, risk assessment and development of preventative measures [183].

Whilst DES successfully addressed the issue of in-stent restenosis predominant to early BMS, the stent type is held back by late stent thrombosis (LST). The use of DAPT was recommended for a period of 6-12 months after implantation of DES to combat LST, although adherence to therapy beyond 12 months [135], or non-adherence to therapy prior to 6 months [185], result in adverse bleeding risks. The clinical outcome for DES requires patient-based individualized decisions, and indiscriminate administration of stent type. In contrast, clinically, thin-strut cobalt chromium stents (CCS) have shown superiority to thick-strut BMS via reduced restenosis [176], is cost-effective, and bears similarity to DES in relation to MACE as well as rates of stent thrombosis [186], therefore increasingly incorporated as the underlying biomaterial for new-generation DES [179]. As a result we chose cobalt chromium alloy L605 (ASTM F90), as our biomaterial of interest for plasma modification and investigation in this study.

Figure 3.1:

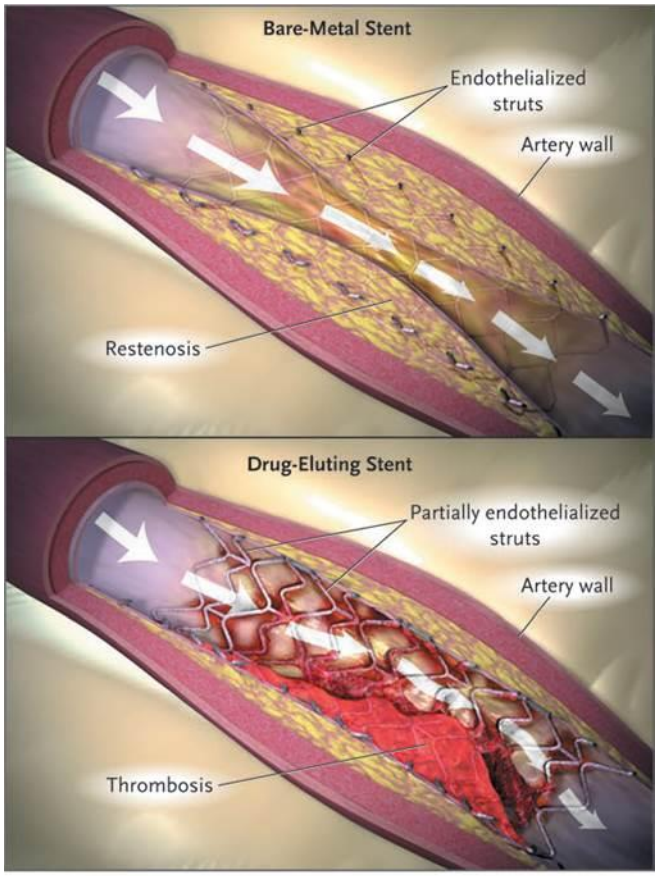

COLOR FIGURE

Rev 1	02/07/07
Author	Curfman
Fig #	1
Title	Drug-eluting stent thrombosis
ME	Lamont
DE	Curfman
Artist	Williams

AUTHOR PLEASE NOTE:
Figure has been redrawn and type has been reset
Please check carefully

Potential complications of coronary stenting: Restenosis observed in a traditional bare metal stent and late stent thrombosis observed in a drug eluting stent. Arrows indicate blood flow. Image is from www.nejm.org. An animation showing restenosis and stent thrombosis can also be viewed on the same site.

3.1.4 Plasma activated coating on cobalt chromium alloy L605:

3.1.4.1 Mechanism of PAC – Applied Physics for Material Modification:

An energetic ion-assisted plasma process that can make any surface hydrophilic, enables covalent immobilization of biological molecules in their native conformation (without chemical linkers), as demonstrated on an alloy 316L stainless steel platform [103, 187]. The proprietary plasma activated coating [172], introduced in chapter 1 and 2, is a unique material modification method [107]. The applied plasma physics technique creates free radicals that migrate to the surface from a reservoir beneath, the radicals bind biomolecules, via covalent bonds with amine groups, to form a full protein monolayer [103]. The process is illustrated schematically in figure 3.2. Applications of PAC with a monolayer of covalently bound protein on a 316L SS coronary stent, within an *in vivo* translational study, was extensively discussed in chapter 2 (Manuscript in preparation for Biomaterials). The kinetics and number densities of free radicals in the reservoir govern the shelf life of the modified biomaterial and its' covalent binding capacity [103]. The reservoir can be formed on any solid material (polymer and metal included) activating the surface for biocompatibility, this approach has various medical applications, as seen with a cardiovascular stent surface [101, 106].

The ion treatment creates a free radical reservoir on the surface of a material. Surface modification can be quantified with plasma kinetics for hydrophilicity and surface energy. Chemically, free radicals have an unpaired electron and an associated electron spin. The electron spin density created via plasma modification has been quantified previously - immediately after deposition and over 8 weeks with electron spin resonance (ESR), in both ion-implanted and plasma deposited low-density polyethylene (LDPE) polymer surfaces [103]. Kinetic studies have already shown the number of unpaired electrons within the reservoir migrating to the surface decrease over-time, either due to migration internally or due to

quenching in the bulk/via surface oxidation reactions to environmental exposure. Previous studies also show that annealing modified surfaces in a vacuum after ageing restored free radical density to its original EPR (electron paramagnetic resonance) intensity within pulse-biased polymers [145]. Radical density, thickness of plasma coating and covalent binding capacity are correlated, furthermore high levels of covalent immobilization of surface biomolecules have been observed after a period of 1 year shelf storage [145]. The ability to retain an attached biomolecule on the surface of a modified biomaterial is conventionally tested after vigorous washing with a detergent - sodium dodecyl sulphate (SDS), and enzyme linked immunoabsorbent assays (ELISA) [187]; discussed further alongside surface biocompatibility in chapter 4.

3.1.4.2 Surface coating characterization after plasma modification of biomaterial – polymer biocompatibility:

The microstructure of plasma modified alloy 316L stainless steel surfaces have been characterized previously, to investigate surface coating integrity [103], coating composition [106] and plasma polymer adhesion to a material surface [145], prior to its applications on a metallic coronary stent platform and investigations *in vivo* [106]. As discussed within this chapter, drug eluting stents have several short-comings, DES consist of three major components; 1) the drug, 2) the polymer coating and 3) the stent. Generally polymer coatings are necessary for drug adherence to stents, with multiple layers to dictate drug kinetics and optimal release over time [188]. The polymer coating is consistently optimized after being a major limiting factor for DES, owing to *in vivo* incompatibility; inflammation, and correlating neointimal proliferation [188]. Polymer damage/delamination may predispose to in-stent restenosis (ISR) due to altered drug kinetics and be potential nidus to sub-acute stent thrombosis [175] [189, 190].

Several experimental studies have reported problems with coating delamination [191], including recent reports on abluminal biodegradable polymer delamination of a biolimus-eluting stent, delivered through a calcified coronary artery, figure 3.3 [192]. It appears that the high levels of deformation developed at the plastic hinge of a stent during its deployment create a significant mechanical challenge to achieve an intact bond between the coating and the DES [193]. Computational studies in biomedical engineering have investigated the stent-coating interface to understand de-bonding during stent deployment, revealing that coatings de-bond from the stent surface in tensile regions, during deployment [193, 194]. The process of coating delamination is a critical challenge for commercially available DES, as such *in vitro* compression experiments (stent crimping/expansion) show webbing effects, revealing bare metal underneath with commercially available Cypher and Taxus (early-generation DES), figure 3.4 [190]. The coating delamination simulated in computational studies closely correlate to experimental images seen [193]. Investigations conclude the following parameters initiate stent coating delamination: 1) coating thickness and stiffness, 2) interface strength between coating and stent surface, 3) curvature of DES plastic hinge [193], these parameters must therefore be governed during the engineering process of manufacturing coated stents/biomaterial surfaces.

The aims of this work are to 1), modify commercially available ASTM F90 alloy L605 material with PAC 2), physical and chemical characterization of modified surface 3), nanotechnological characterization of surface coating at an atomic and supramolecular level (nanoindentation) to analyse coating roughness, thickness and stiffness i.e. coating integrity 4) Investigate microstructure of the cross-sectional interface between coating and stent surface to affirm its application in cobalt chromium stent technology.

Figure 3.2

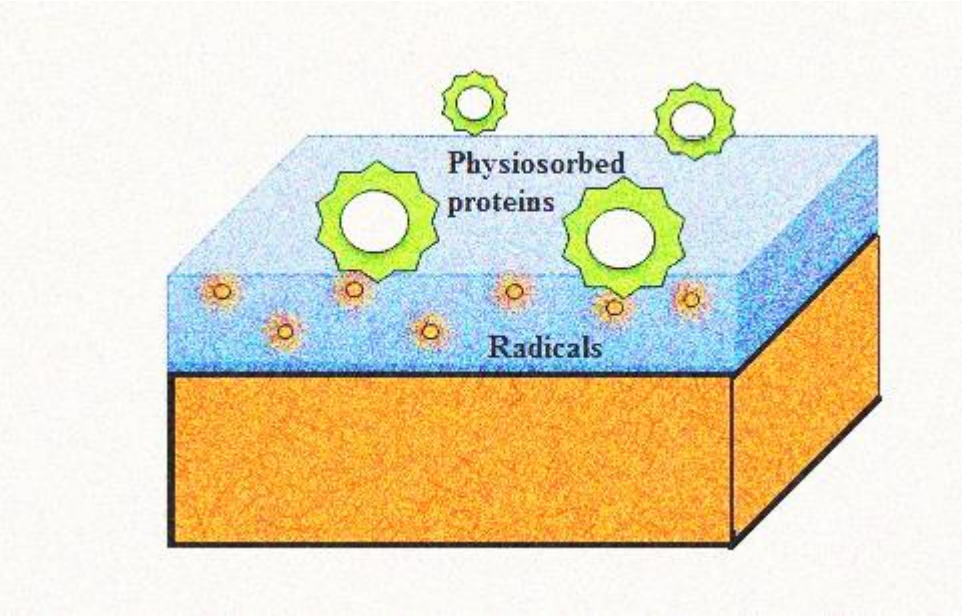

Free radicals diffuse to the surface and form covalent bonds with physiosorbed proteins. First step is the physisorption of a protein to the surface, second step is the direct, linker-free covalent bond formation. Imaged modified from Bilek et al [103]

Figure 3.3

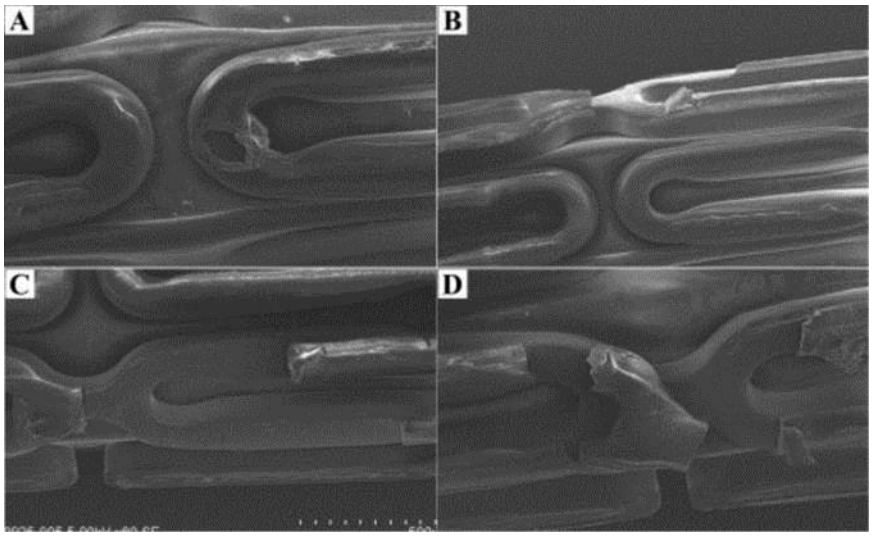

Scanning electron microscopy shows damage to polymer of the biolimus-eluting stent that would not advance to the lesion (A to D). Note that most of the damage to the polymer is delamination of abluminal polymer (B to D). Image from [195]

Figure 3.4

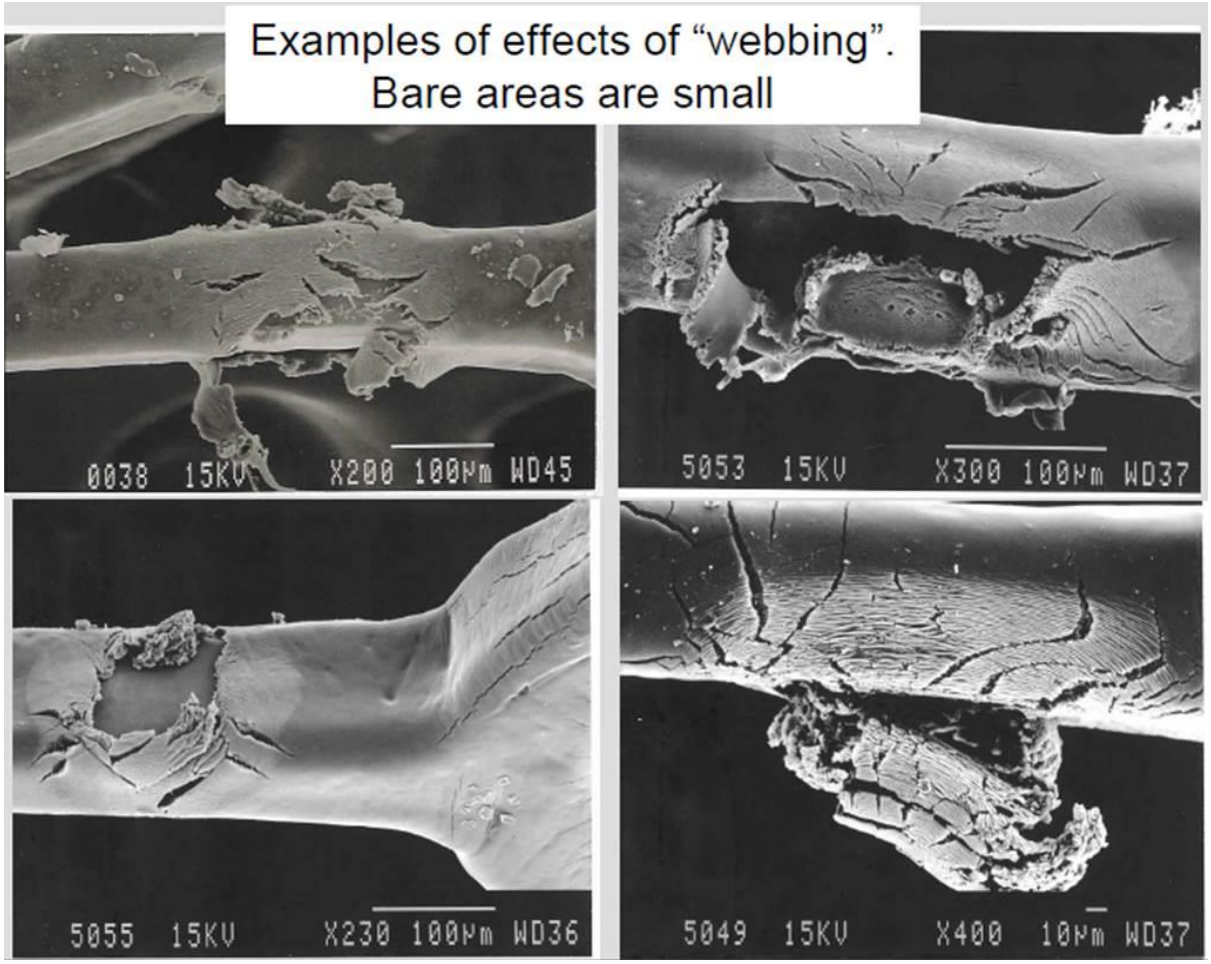

Taxus Express deployment separates struts and draws the in-continuity polymer out to form ‘webs’ after *in vitro* compression experiments. Polymer is pulled off the stent leaving areas of bare metal exposed. Image from Ormiston et al, TCTMD conference 2005 [190]

3.2 Materials and Methods

3.2.1 Materials, Equipment, Suppliers and Facilities

A list of chemicals, reagents, materials and their suppliers are presented in Table 3.3

Table 3.3 Materials and their suppliers

Material/Equipment	**Supplier/Facility**
Agilent Nano Indenter G200	Civil Engineering, University of Sydney, Australia
Atomic Force Microscopy - Pico scanning probe microscope (SPM)	Australian Center for Microscopy and Microanalysis, University of Sydney, Australia
Cobalt chromium alloy L605 sheets (ASTM F90, AMS 5537, 250 µm)	High Temp Metals, Inc. Sylmar, California 91342, USA
JEM-2200FS - Transmission Electron Micrsocope	Australian Center for Microscopy and Microanalysis, University of Sydney, Australia
Kruss contact angle goniometer (DSA10-Kruss GmbH)	Applied Physics, University of Sydney, Australia
NanoMap 1000WLI Interferometry	Civil Engineering, University of Sydney, Australia
Plasma Activated Coating (PAC) technology	Applied Physics, University of Sydney, Australia
Point Probe® Plus Force Modulation Mode [PPP-FM], Model A	Nanosensors, Neuchatel, Switzerland / Nucletron Pty. Ltd, Newtown, Sydney, Australia
Surface profilometer	Applied Physics, University of Sydney, Australia
Zeiss Ultra - Field Emission Scanning Electron Microscope	Australian Center for Microscopy and Microanalysis, University of Sydney, Australia
Zeiss Auriga - Focussed Ion Beam – Scanning Electron Microscope	Australian Center for Microscopy and Microanalysis, University of Sydney, Australia

3.2.2 Surface coating metallic samples

3.2.2.1 Preparation of cobalt chromium alloy L605

Samples of alloy L605 and alloy 316L SS (10 cm x 8 cm x 0.025 cm) were washed in 3 reagents; 70% ethanol, acetone, and phosphate buffered saline (PBS) for 15 minutes each, prior to PAC deposition. All experiments were carried out with freshly made PAC (used within 2 weeks) unless stated otherwise.

3.2.2.2 Synthesis of plasma-activated coating

The pulsed plasma deposition process described in chapter 2 was slightly altered and optimized for PAC deposition in this chapter. Fused silica (10 cm x 8 cm x 0.05 cm) was also coated with the same PAC recipe, as a reference material. The cleaned substrates were mounted onto a stainless steel cylindrical ccrf reactor. Base pressure of the system was pumped down to 10^{-6}-10^{-5} Torr, a reactive mixture of argon, nitrogen and acetylene plasma introduced in the upper part of the reactor. The flow, Q, of each gas for alloy L605 surface; Q_{Argon} = 3 sccm, $Q_{Acetylene}$ = 1 sccm and $Q_{Nitrogen}$ = 10 sccm (500 v, t = 20mins), is controlled individually, using mass flow controllers and maintained constant during deposition (PAC1 recipe). We also trialled a second recipe for PAC deposition on alloy L605 sample of similar dimensions (10 cm x 8 cm x 0.025 cm) Q_{Argon} = 3 sccm, $Q_{Acetylene}$ = 2 sccm and $Q_{Nitrogen}$ = 10 sccm (1000 V, t = 10 mins) (PAC2-recipe). Plasma was sustained at a total pressure of 80 mTorr, rf power 50 W and deposition time of 10-20 mins. The time of deposition correlated to thickness as specified prior to characterization.

3.2.2.3 Surface Profilometry

The thickness of the PAC recipe deposited on L605 and reference Si wafer surface was measured on the reference material with surface profiler Dektak 3030 (Bruker, Germany).

3.2.3 Plasma kinetics – Contact angle goniometry and surface energy

The sessile drop technique was used for contact angle measurements with DS10 Kruss contact angle goniometer (Kruss GmbH, Germany). Within a time-frame of 15 mins post PAC deposition (hitherto refered as PAC-L605); the PAC-L605 (0.5 cm x 3 cm, thin strip) was placed on the goniometer platform, a water drop was introduced to the surface through a microsyringe. The three phase contact line of the drop was made with drop shape analysis software (DSA), and measured with a microscope at room temperature, for three liquids; water, diiodomethane and formaldehyde respectively. Measurements were conducted within a 15 min time-frame post PAC-L605 modification, upto 40,320 mins (4 weeks). For drop shapes that were > 90^{o} and < 90^{o} we used equations 3.1 and 3.2 respectively from ref [196], to manually compute the contact angles.

$$\tan\theta = \frac{\sqrt{2rh-h^2}}{r-h} \qquad \text{for } \theta > 90^{o} \qquad 3.1$$

or

$$\tan\theta = \frac{2rh}{r^2-h^2} \qquad \text{for } \theta < 90^{o} \qquad 3.2$$

The average contact angle for 5 measurements, at each time point, of two liquids (water and diiodomethane) were used to compute correlating surface energy and its components (polar and dispersic parts) with regression method/Owens-Wendt-Rabel-Ström kinetic model (DSA software), within the same timelines (15 mins – 40,320 mins). Results were compared with a similar PAC recipe deposited on alloy 316L SS within a 15 min – 20,160 min (2 week) time-frame.

3.2.4 Electron Dispersive X-ray Spectroscopy – Surface Chemistry Characterization

Samples of PAC-L605 (recipe 1 and 2) were comparatively imaged alongside alloy L605 bare metal (0.8 cm x 0.8 cm), using a Zeiss-Ultra field emission scanning electron microscope (Zeiss, Germany). The surface chemistry at the nanoscale was analysed with Aztec software (Oxford Instruments, UK) at an acceleration voltage of 2 kV, working distance of 11 mm and 2000 X-ray cps. The percent weights of the elements predominant on the three different sample surfaces were quantified independently for an average of 3 sites on the 3 surfaces.

3.2.5 Scanning Probe Microscopy (SPM) – Atomic Force Microscopy (AFM)

The multi-purpose scanning probe microscope PicoSPM (Molecular Imaging, Agilent Technologies, AZ, USA) was operated in the atomic force microscopy (AFM) mode. Force modulation mode AFM was first operated with multipurpose scanner, MAC mode and MAC III controller to obtain an AC tune plot for point probe plus –force modulation (PPP-FM) for silicon nitride SPM cantilever (225 µm length x 28 µm width x 3µm thickness)(Nanosensors, Switzerland). The cantilever was tuned to its resonance frequency (ranged between 45-115 kHz) to ensure calibration, prior to conducting AFM trace/retrace plots of the modified PAC-L605 (0.8 x 0.8 cm) metal surface; for surface imaging and roughness measurements. Using the plot of resonant frequency, the quality factor (Q) was computed for the cantilevers at half power-bandwidth, via equation 3.3 modified from [197], where f_r is the resonant frequency and Δf is the half-power bandwidth.

$$Q = \frac{f_r}{\Delta f} \qquad 3.3$$

The Sader method [198] was used to calibrate the spring constant *K* of the rectangular cantilever. The parameter was computed via equation 4 on Ref [198], using an online calibrator [199]; i.e no code was written by the user. After cantilever calibration, the surface roughness of a PAC-L605 modified material (0.8 x 0.8 cm) was computed with Nanoscope AFM instrument (Molecular Imaging, Agilent Technologies, AZ, USA) in the contact force modulation mode, with a 20 µm scanner for imaging in air. Surface topographical 3D images and raw deflection images of PAC surfaces, obtained by AFM were constructed using the image processing software Nanotec Lab WSxM version 4.0 Beta 8.0 (Nanotec Electronica) [200]. The nanoscale surface roughness (RMS) of PAC-L605 surface at 20 x 20 um areas, were computed via equation 5 in [201], using automated WSxM version 4.0 nanotechnology app [200]. Frequency distribution of the surface roughness was also simulated using same software. Images of the surface were obtained at five different locations of PAC L605 material via which the average RMS roughness was determined automatically for the modified material.

3.2.6 Nanoindentation – Surface Stiffness

Surface stiffness of a modified PAC L605 sample surface was calculated and compared to a sample of bare cobalt chromium alloy L605 (2 x 1 x 0.05 cm) by force-controlled nanoindentation, using a Hysitron Triboindenter (G200, Agilent) fitted with a Berkovich diamond indenter (TB22122, m0 24.7772) with a radius of curvature R. Nanoindentation was conducted at a maximum load of 50 mN for 100 indents, at randomly chosen positions, for each surface. The indentations were made under the same conditions to confirm uniformity of mechanical properties of the entire coating. Surface stiffness was measured as a log function of the unload depth (D) (nm) vs. load, as a function of force (F) mN, equation 3.4 from [202]

$$S = \frac{\Delta F}{\Delta D} \qquad 3.4$$

The unloading displacement for 21 indentations were batch processed using a Matlab Mathworks version 8.5 (MA, USA) algorithm to calculate surface stiffness; developed by Dr. Yixiang Gan's group, Civil Engineering, University of Sydney (Appendix A).

3.2.7 NanoMap White Light Interferometer (WLI) – Surface Roughness

A second method was trialled for surface roughness measurements of a modified PAC-L605 surface using NanoMap-1000WLI 3D optical profilometer (AEP technology, Santa Clara, CA, USA). The PAC-L605 sample (0.6 cm x 0.6 cm) was mounted to computer controlled sample stage, located on a vibration isolated table (air pressure controlled at 1 atm). The sample was magnified with a 10 x objective, optical microscope. Field of view was chosen using the computer controlled motorized NanoMap Optical software (serial #500226), for a 100 μm Z range, and 1 mm x 1 mm scanning area of sample at a 1 x scan speed run. The optical image obtained was opened in image software PIPS 6.0.14, to generate a 3D image of topographical data with Zero background and global levelling. The optical image was next opened in Gwyddion 2.41 software for SPM data analysis (Dept. of Nanometrology, Czech Metrology Institute), using the automated 'Statistical quantities' tool, the roughness measurements (RMS) for sample surface at 5 different surfaces were calculated and averaged.

3.2.8 Tripod Polishing and Focussed Ion Beam (FIB) milling – preparation of thin metal PAC-L605 lamellae

A cross-section of the modified PACL605 metal was prepared for TEM using tripod polishing and focussed ion beam milling (FIB). The metal was sectioned to obtain a small sample (approx. 3mm x 3 mm x 2 mm), progressively thinned down to 5-10 µm and 20 nm using the two techniques. For tripod polishing, the metal sample was fixed to a Pyrex tripod stage, with a piece of Si wafer (5 mm x 5 mm x 0.5 mm) attached to cover the modified surface. The sample was initially ground in turn on 30, 9, 3 µm diamond films (approx. 60 mins in total). The specimen was removed from the Pyrex stage and cleaned carefully in acetone to remove the thin sample of interest with a 5-10 µm thickness. The sample was mounted to a copper half-grid for focussed ion beam (FIB) milling.

The sample material mounted on a half-grid was inserted vertically to the FIB chamber (Zeiss, Auriga). Before milling, a platinum (Pt) line was deposited over the area of interest, marking position of target area. An initial incidence angle of ± 4^{o} was used in perpendicular exposure of the sample at a 30 kV milling voltage and 25 pA current, for sample milling down to about 150 nm thickness. The incidence angle was increased to ± 6^{o} at a voltage of 5 kV and 10 pA, until a further thickness of 80 nm was achieved. Residual milling to obtain a cross-section of 20 nm thickness was conducted at ± 8^{o}, 5 kV for remaining material. The final electron transparent lamellae seen from top looks like a cross bar in the letter 'H', referred to as the H-bar technique during lift out and transfer to HRTEM. The electron transparent 20 nm PAC-L605 sample lamellae cross-section prepared within FIB was lifted out, and attached to a copper half-grid for high resolution transmission electron microscopy (HRTEM).

3.2.9 High Resolution Transmission Electron Microscopy (HRTEM) – Metal Coating Interface Analysis

The FIB sample was placed on the JEOL double tilt high background TEM sample holder, for JEM-2200 FS HRTEM - (JEOL, San Francisco, CA, USA). The 20 nm thin PAC-L605 lamellae cross-section was imaged at 200 kV field emission gun acceleration voltage, 95.5 µA (dark current), and 52.0 µA (Emission current) up to 1.1 Å atomic resolution and 1.2 M magnification. The alloy L605 bare metal, beneath the PAC deposition was imaged separately to visualize the alloy microstructure with selected area electron diffraction (SAED). We obtained an inverse fast Fourier transform (IFFT) pseudo colour image of the interface imaged for PAC-L605 cross section, and conducted an electron energy loss spectrum (EELS) with zero-loss peak (ZLP) omega filter, for quick reliable measurement of local thickness to verify interface chemical composition. The thickness was calculated as $mfp*In(I/I_0)$, where mfp is the mean free path of electron inelastic scattering, tabulated for most elemental solids and oxides (Gatan Inc, Japan) [203], and I/ I_0 are integrals under the whole spectrum and under the ZLP, respectively.

3.2.10 Statistics

Data were analyzed for statistical significance as described in Chapter 2.2.15.

3.3 Results

3.3.1 Surface coating thickness

The surface coating profilometer trace for PAC-L605 modification, indicated a 20 nm surface thickness (details provided by PhD candidate Mr. Miguel Santos, Applied and Plasma Physics, University of Sydney).

3.3.2 Plasma Kinetics

The initial water contact angle, 15 mins post PAC-L605 modification was 44.4^{o}±3.41, by 2 weeks the contact angle increased to 89.98 ^{o}±3.78, by 4 weeks to 92.96^{o}±1.38 (figure 3.5 A). Correlating surface energy calculated 15 mins post PAC deposition was 62.35±2.43 mJ/m^2, by 2 weeks 32.22±2.88 mJ/m^2, and by 4 weeks 28.96±1.20 mJ/m^2. Results were compared with a similar PAC recipe deposited on alloy 316L SS within a 15 min – 20,160 min (2 week) time-frame (figure 3.5B). The water contact angle for PAC-316LSS was 57.86 ^{o}±0.48, by two weeks the contact angle increased to 84.66 ^{o} ±0.33. Correlating surface energy calculated 15 mins post PAC-316LSS deposition was 52.02±0.05 mJ/m^2 and decreased to 37.68±0.01 mJ/m^2 at two weeks, summarized in Table 3.4. Figure 3.6 illustrates wetting angles for both water and diiodomethane, used to calculate surface energy of PAC-L605, initially very low at 15 mins post PAC deposition (44.5^{o} and 39.48^{o} respectively), increasing up to 89.98^{o} for water and 58.9^{o} for diiodomethane within 2 weeks. Figure 3.7 illustrates variation of the components of surface energy (polar+dispersive) summing up total surface energy. The polar energy decreased significantly over time from 22.62 mJ/m^2 to 3.15 mJ/m^2, although the dispersive part did not change much from 39.622 mJ/m^2 to 29.11 mJ/m^2.

3.3.3 Surface Chemical Composition

Initially the chemical composition of stainless steel alloy 316L was compared to cobalt chromium alloy L605 (ASTM F90). Alloy 316L SS had a predominant Iron (Fe) percentage weight (48.50%), in contrast alloy L605 had reduced Fe content (1.77%) and significantly high percent weight Cobalt (Co) (34.96%). In this chapter, we compared the surface chemistry of PAC recipe 1 (C-1, N-10, 500 V, t – 20 mins), PAC recipe 2 (C-2, N-10, 1000 V, t - 10 mins) and L605. The PAC-L605 modified surface of our choice had a predominant Nitrogen (N) (3.033%) and Carbon (C) peak (9.20%) compared to the alloy L605 surface, Figure 3.8.

3.3.4 Surface roughness – Atomic Force Microscopy and NanoMap white light interferometer (WLI) technique

Surface roughness was measured for 5 separate positions on PAC-L605 modified surfaces at 20 x 20 µm areas. Prior to imaging the Si_3N_4 (silicon nitride) cantilevers were calibrated, the Q factor calculated as 383, from the resonant frequency peak of 76.5 kHz obtained from the AC tune plot, shown in figure 3.9. The force constant K of the cantilever was computed as 5.04 N/m, using the online Sader method. The AFM 3D surface topography and corresponding deflection images are seen in figure 3.10. The frequency profile simulated for surface roughness via WxSM Nanotec software fitted Gaussian function, the average roughness is 69.19 nm for RMS roughness measured for modified surfaces at a 20 µm x 20 µm areas, figure 3.10.

Similarly surface roughness was measured for 5-10 separate positions on the PAC-L605 modified surface at 100 µm x 100 µm areas with NanoMap WLI technique. The NanoMap 3D topography images constructed are seen in figure 3.11. The average roughness RMS computed with the WLI mechanical profiler Gwyddion software was 0.272 µm.

Figure 3.5

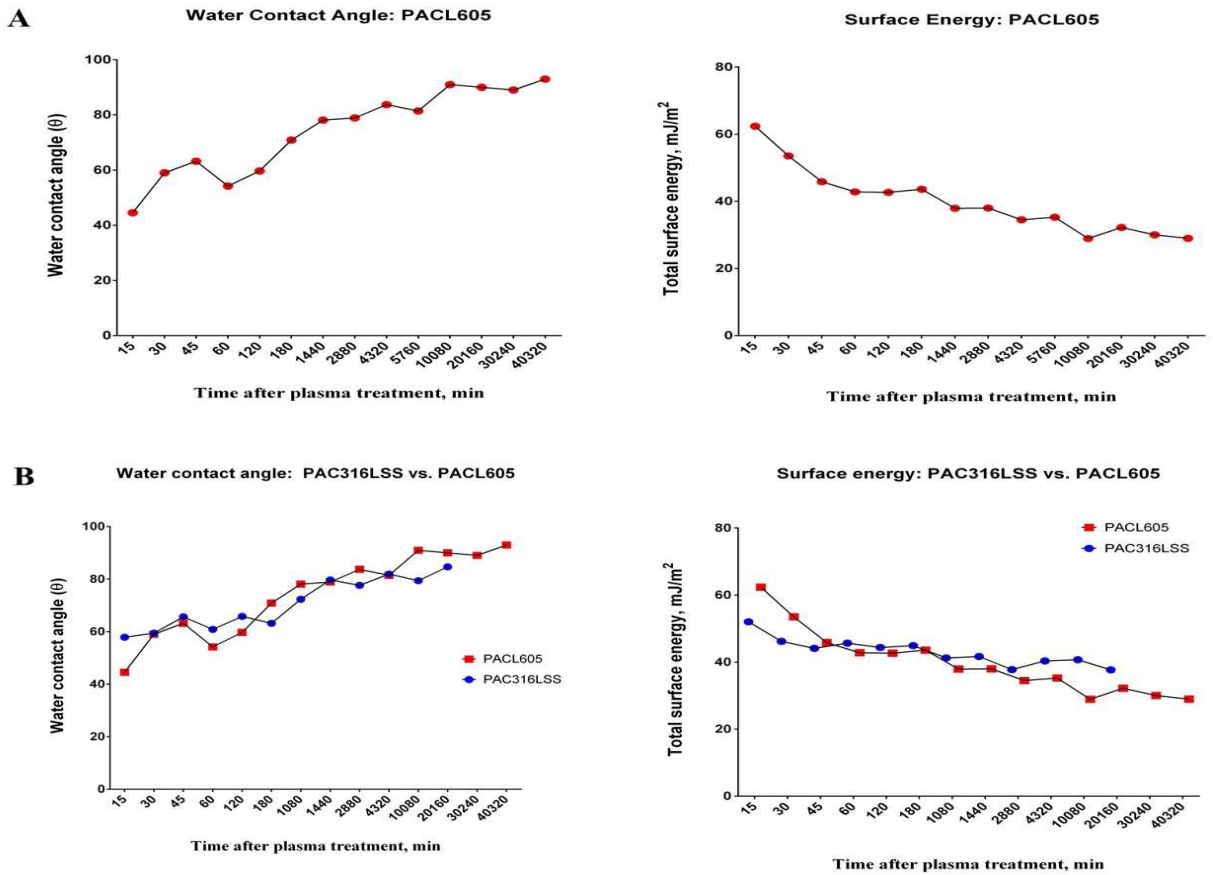

(A) Water contact angle for PAC-L605, increased over a time-frame of 15 mins - 40,320 mins to plateau, correlating surface energy decreased over a time-frame of 15 mins – 40,320 mins to plateau.

(B) The PAC-L605 results were compared with PAC-316LSS, to indicate similar trends for both plasma modified biomaterials, over a time-frame of 15 mins – 20,160 mins for water contact angle and surface energy respectively.

Figure 3.6

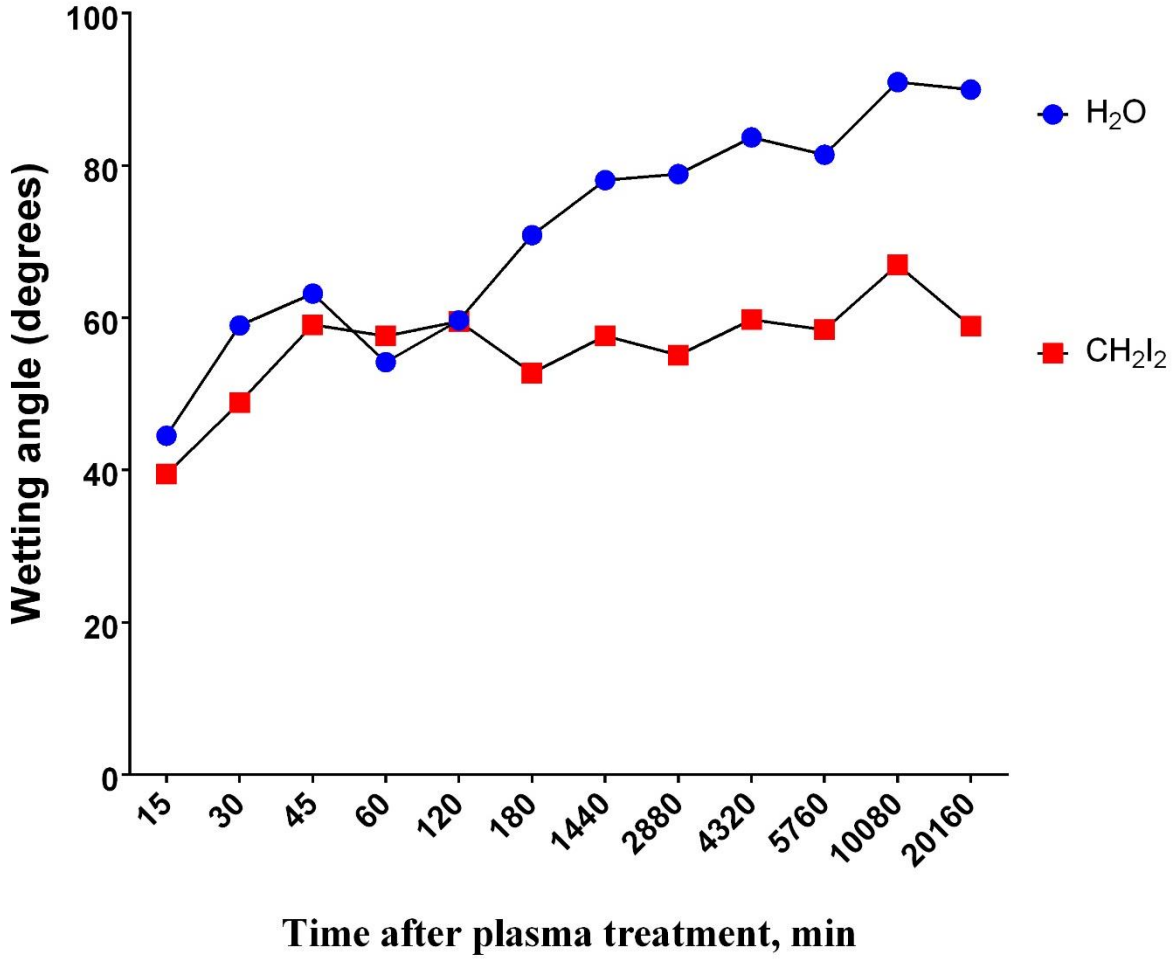

Water (H_2O) and diiodomethane (CH_2I_2) of PAC-L605 with time after plasma treatment, until 2 weeks (20,160 mins). Contact angle recovers shortly after plasma treatment.

Figure 3.7

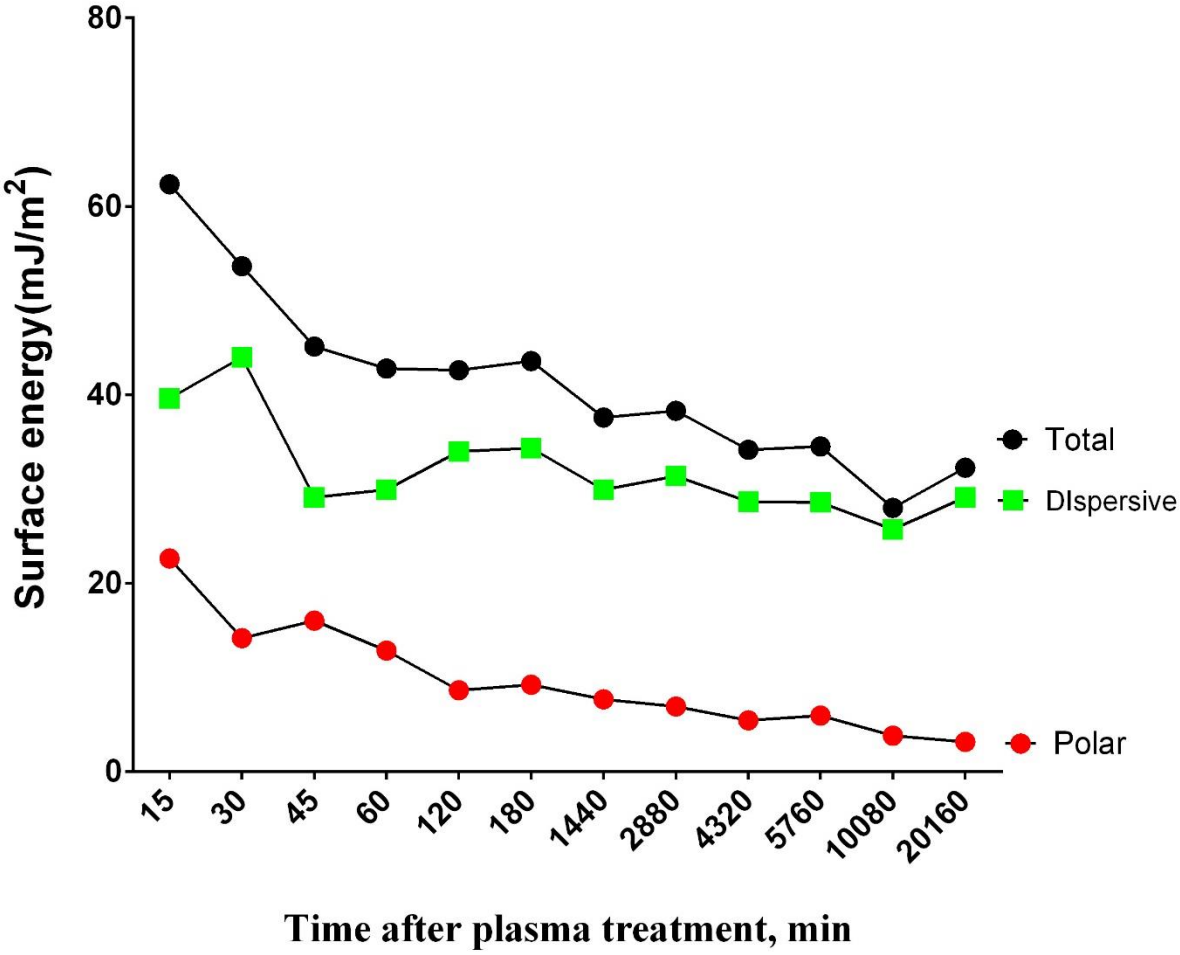

Variation of total surface energy and its parts (polar and dispersive) - 2 weeks after plasma treatment (20,160 mins) for PAC-L605.

Table 3.4 Comparative water contact angle and surface energy for PAC modified biomaterial alloys L605 and 316LSS within a time-frame of 15 min – 20,160 mins (2 weeks) and/or 40,320 mins (4 weeks).

	Surface hydrophilicity			Surface energy mJ/m^2		
Biomaterial	15 mins	20,160 mins	40,320 mins	15 mins	20,160 mins	40,320 mins
PAC-L605	44.4^{o}±3.41	89.98^{o}±3.78	92.96^{o}±1.38	62.35±2.43	32.22±2.88	28.96±1.20
PAC-316L SS	57.86^{o}±0.48	84.66^{o}±0.33		52.02±0.05	37.68±0.01	

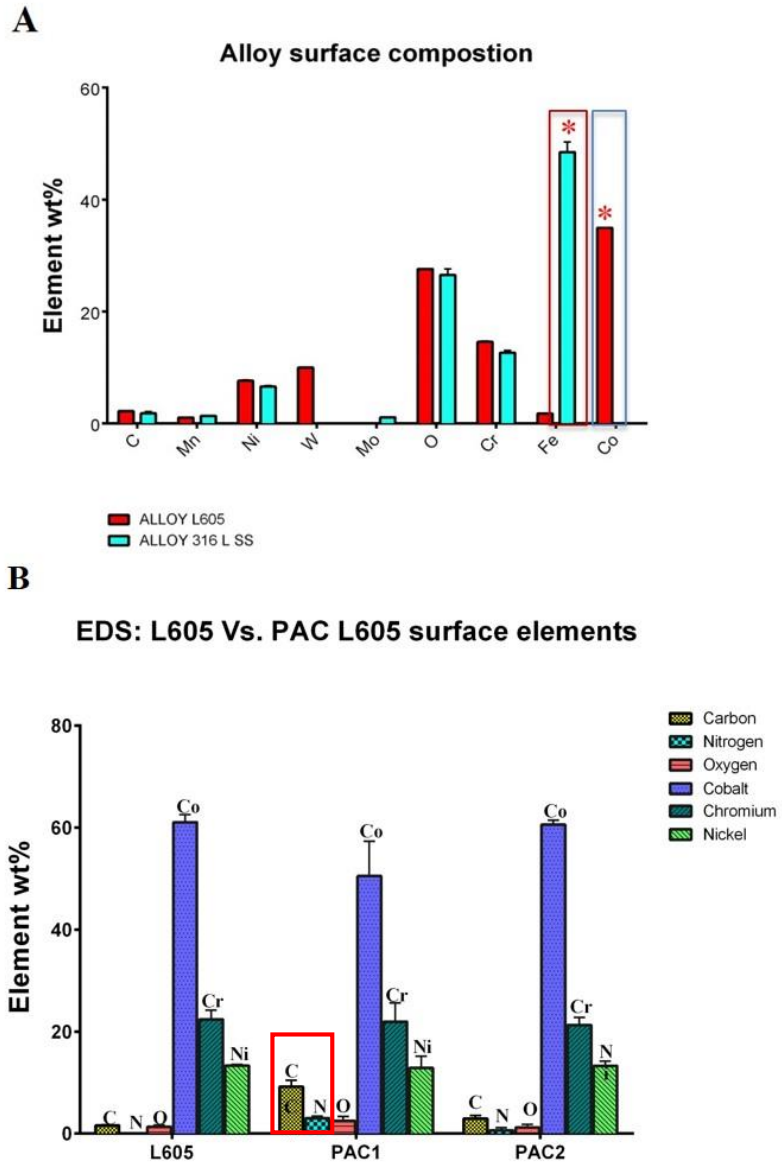

Figure 3.8

(A) Surface composition of cobalt chromium alloy L605 (ASTM F90) and stainless steel alloy 316LSS (ASTM F138) – showing predominant Co and Fe peaks respectively.

(B) Plasma recipe 1 (C-1, N-10, t=20 mins, 500 V), modified PAC-L605 surfaces show predominant C and N peaks, compared to bare metal alloy L605 and PAC-2 (C-2, N-10, t=10 mins, 1000 V).

Figure 3.9

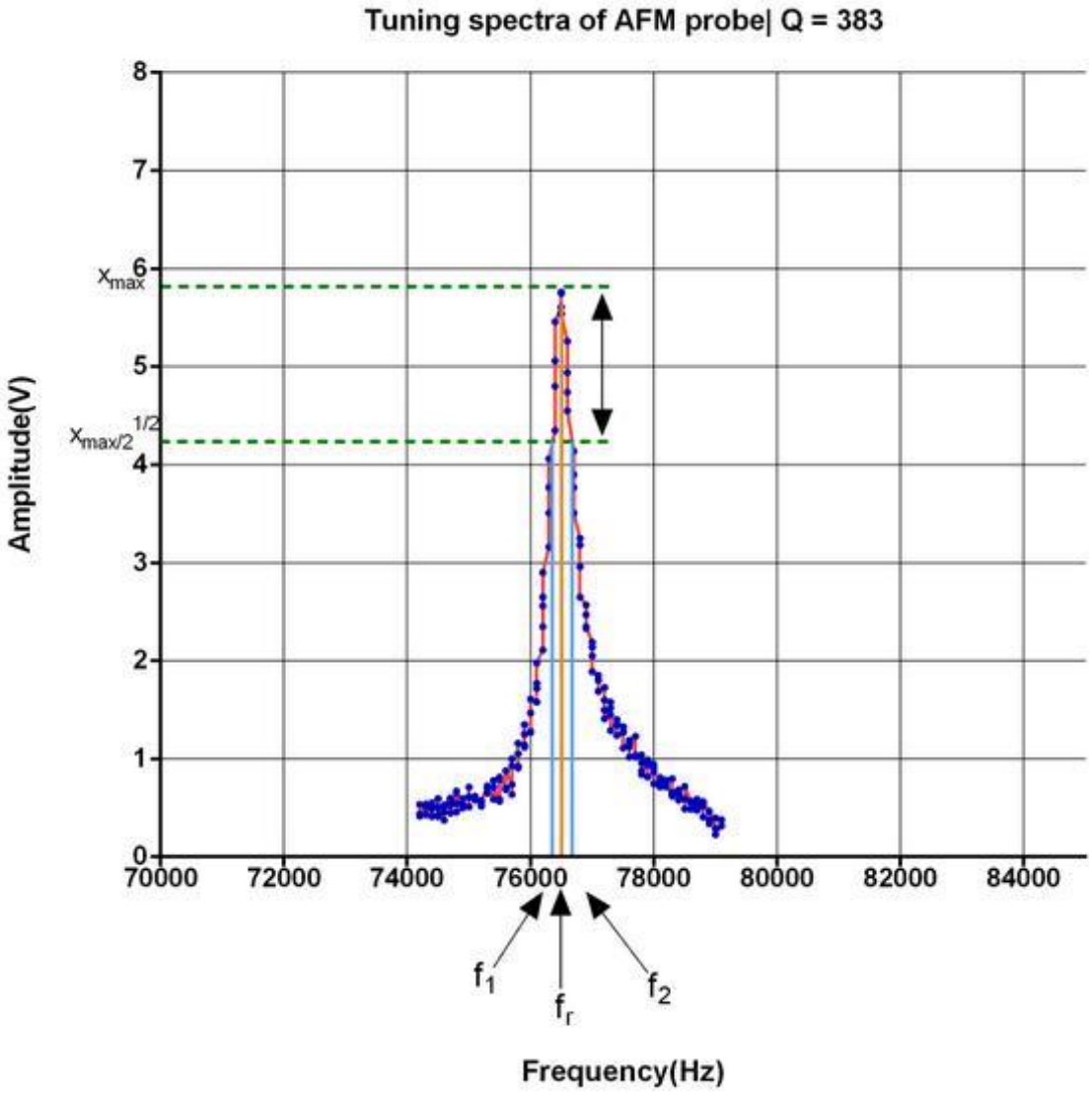

The AC tune plot for PPP-FM Silicon nitride cantilever indicate a resonance frequency of 76.5 kHz. The Q factor was calculated as 383, representative of the sharp peak. The force constant K was calculated as 5.04 N/m (Sader method).

Figure 3.10

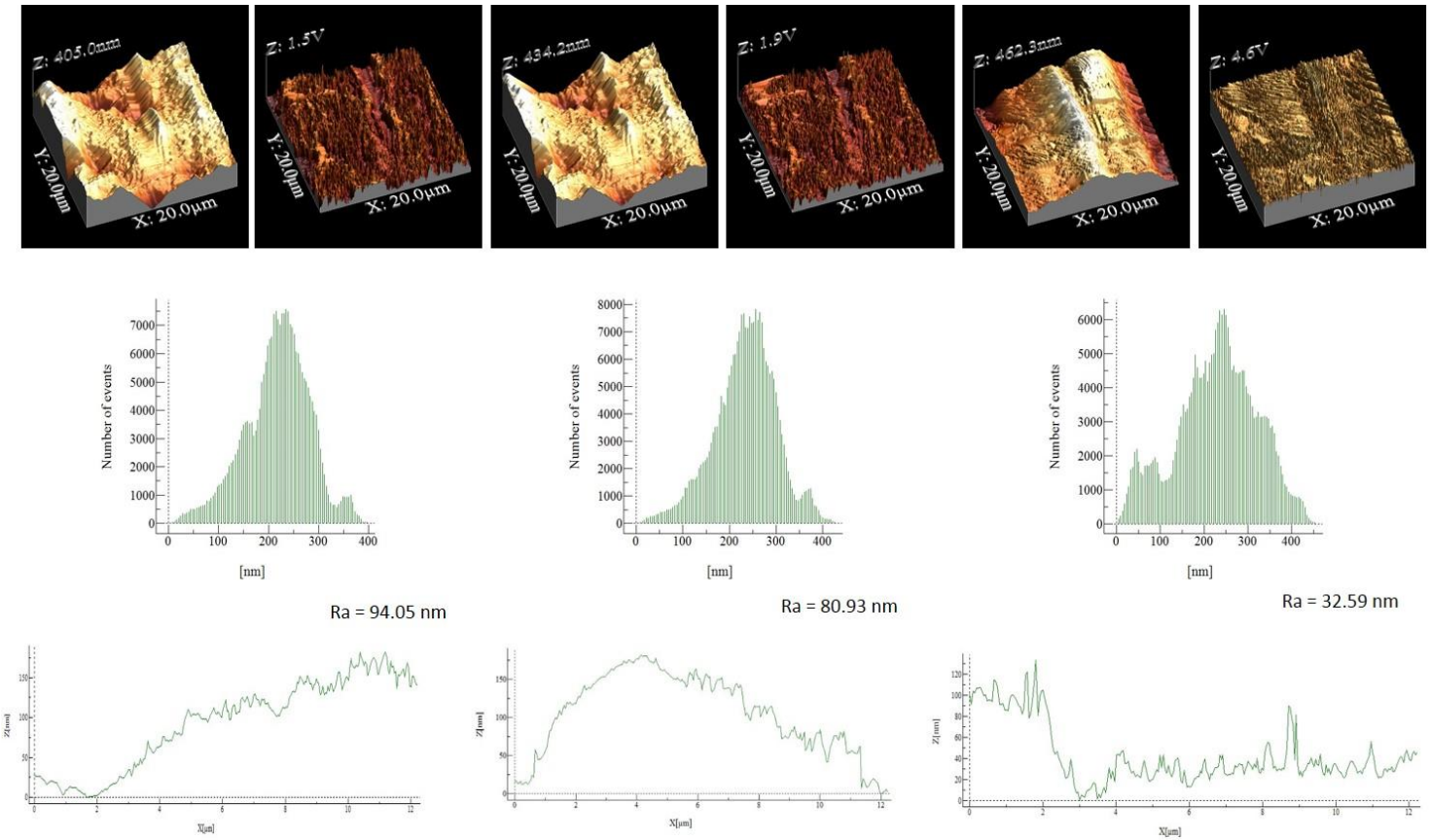

The AFM images were traced/retraced within a 20 um x 20 um area, converted to 3 D images of surface topography. Frequency distribution simulated for surface roughness measurements, fitted a Gaussian function, representative of isotropic surface engineering. The average roughness for each surface topography is represented with roughness profile (WSxM software, Nanotec Electronic).

Figure 3.11

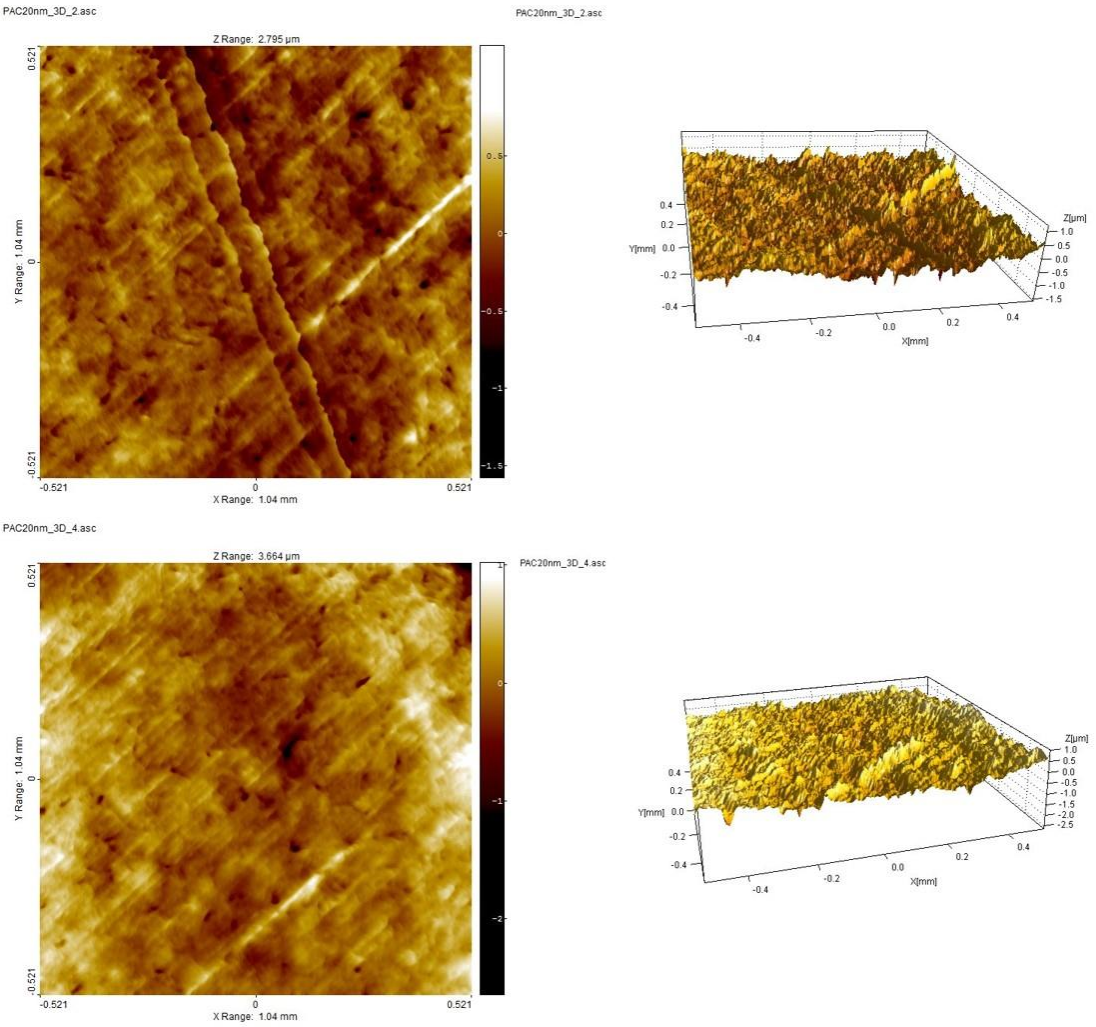

The NanoMapWLI images of PAC-L605 were imaged at 10 x objective, within a 100 µm x 100 µm scanning area, the images were converted to 3D topographical surface representations (Gwyddion software) and roughness measured with statistical tool (measurements not shown).

3.3.5 Nanoindentation – Surface stiffness

The surface stiffness of a 20 nm PAC-L605 coating was compared to the surface of an alloy L605 bare metal. The maximum load indentation was 50 mN. Figure 3.12 shows the surface stiffness at lowest indentation load 0.19 mN (~2 mN), to be 0.0036 mN/nm for PAC, and the comparative surface stiffness at lowest load indentation for bare metal alloy L605 to be 0.051 mN/nm. With increasing indentation load, surface stiffness increased similarly for both surfaces. At maximum load 50 mN, surface stiffness for PAC-L605 was 0.013 (0.012492) mN/nm and 0.013 (0.012652) mN/nm for L605.

3.3.6 The PAC-L605 coating interface preparation for HRTEM analysis

The tripod polished sample resulted in a smooth, 5-10 μm thick cross section of PAC-L605 interface. Further milling of the sample via FIB resulted in a 20 nm thick cross section of PAC-L605, creating an electron transparent lamellae suitable for interface imaging with HRTEM, figure 3.13 A, B. Figure 3.14 A shows HRTEM image at the cross-sectional interface of a plasma polymer deposited on a crystalline cobalt chromium material. The white (electron transparent) layer is PAC, which was capped with a thin platinum layer during TEM cross-section preparation via FIB (not shown). The inverse fast Fourier transform (IFFT) image of the PAC-L605 interface showed a distinct buffer layer/ion stitching at PAC-metal interface (green), as described in theory for PAC deposition and free radical surface functionalization [103]in figure 3.14 B. The plasma coating (yellow) adheres to alloy L605 (blue) via ionic stitching/buffer layer (green), at the metal-plasma interface. Figure 3.15 shows the bare, crystalline cobalt chromium selectively imaged via electron diffraction to show twinning between grain boundaries in the material matrix, previously only described via SEM imaging [166]. The EELS indicated overall thickness of 47.84 nm for platinum (Pt), 35 nm for carbon (C), and 66.67 nm for cobalt (Co), confirming surface elemental thickness/composition as seen

on TEM image, figure 3.16. For simplicity of presentation we colour segregated three regions of the material interface to represent the materials on a TEM image identified via EELS (spectra not included for simplicity).

Figure 3.12

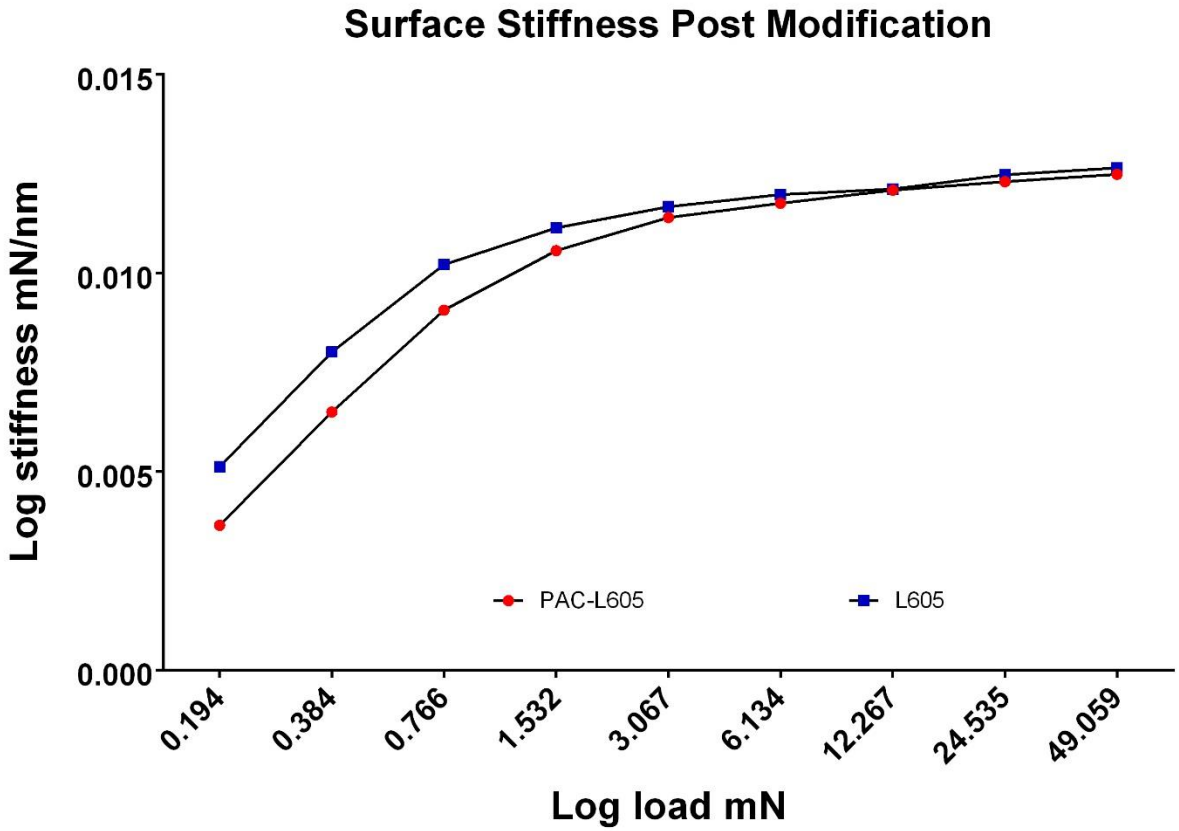

Nanoindentation for surface stiffness conducted on a 20 nm PAC L605 coating vs. alloy L605 surface, for 20/100 indents each. The maximum load was 50 mN, minimum load 0.19 mN. The surface stiffness computed for an average 20 indents show PAC-L605 surface stiffness is lesser than bare metal alloy L605 stiffness at first (at 0.19 mN PAC L605 is 0.0036 mN/nm vs bare alloy L605 0.051 mN/nm). With increasing load, stiffness of the coating remains the same as metal alloy, confirming integrity and coating non-delamination at a force of 50 mN.

Figure 3.13

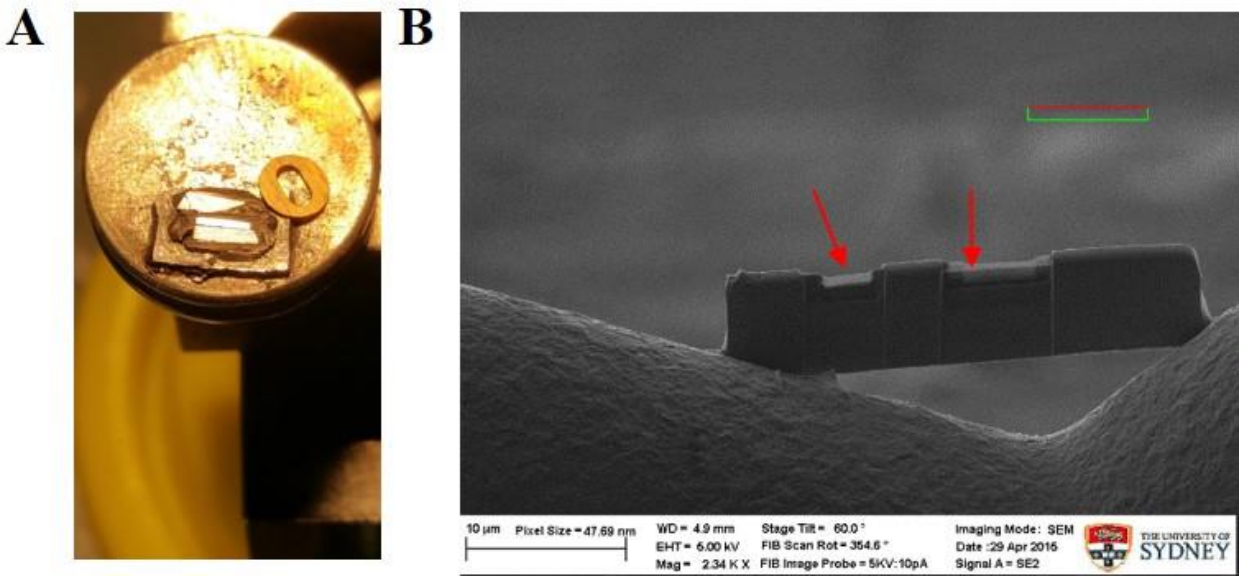

A) Sample preparation for HRTEM: Smoothly polished PAC-L605 sample on Pyrex stage of tripod (10 x mag), between two Si wafers, with copper grid (O) for thickness approximation.

B) The FIB milled PAC-L605 sample, with two regions at the modified material interface, milled to 20 nm thickness (red arrows, 2.3 K x mag, 5 kV).

Figure 3.14

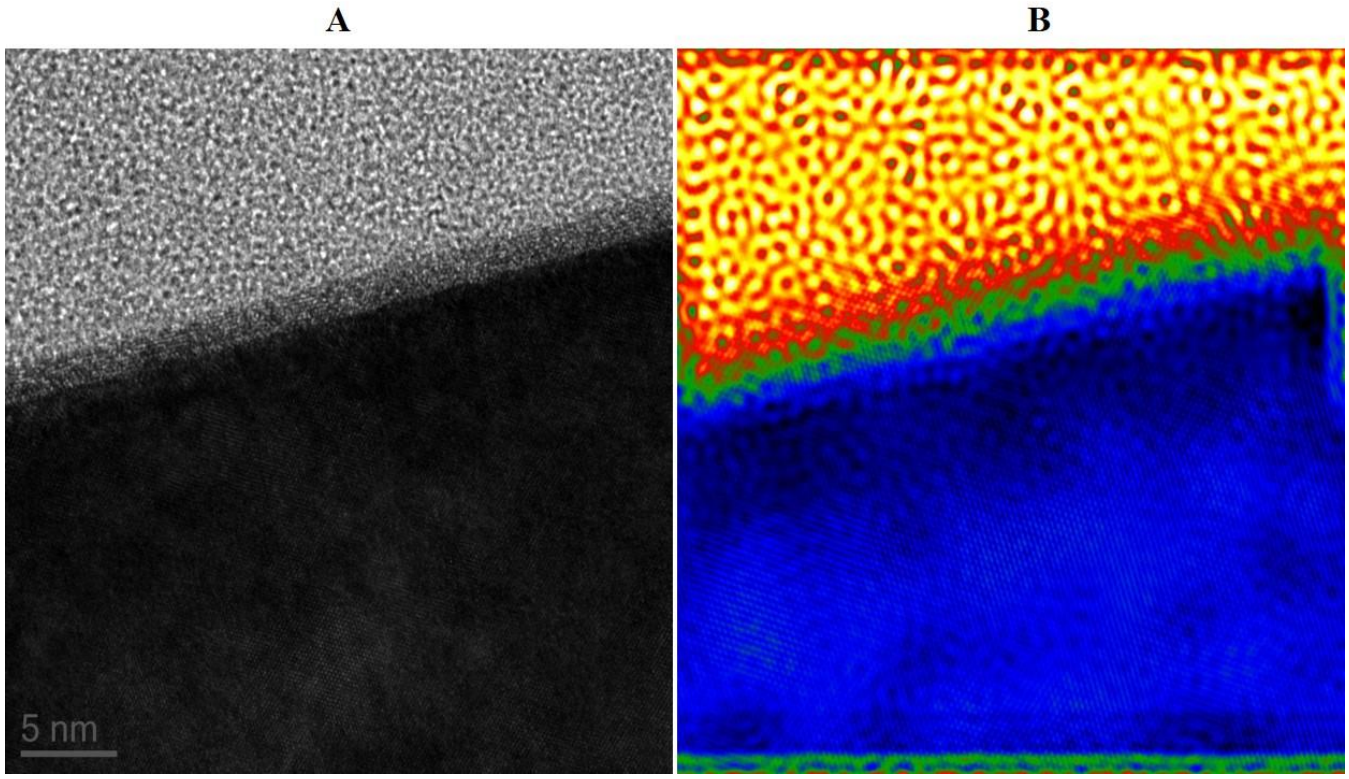

A) Cross section of PAC-L605 surface: HRTEM image with white (electron transparent) polymer deposit, crystal metal alloy (black) and ionic stitching at interface (grey).

B) Corresponding IFFT image shows plasma coating (yellow) adheres to alloy L605 (blue) via ionic stitching buffer layer (green) at metal-interface (1.2 M x mag, 1.1 Å resolution, 200 kV)

Figure 3.15

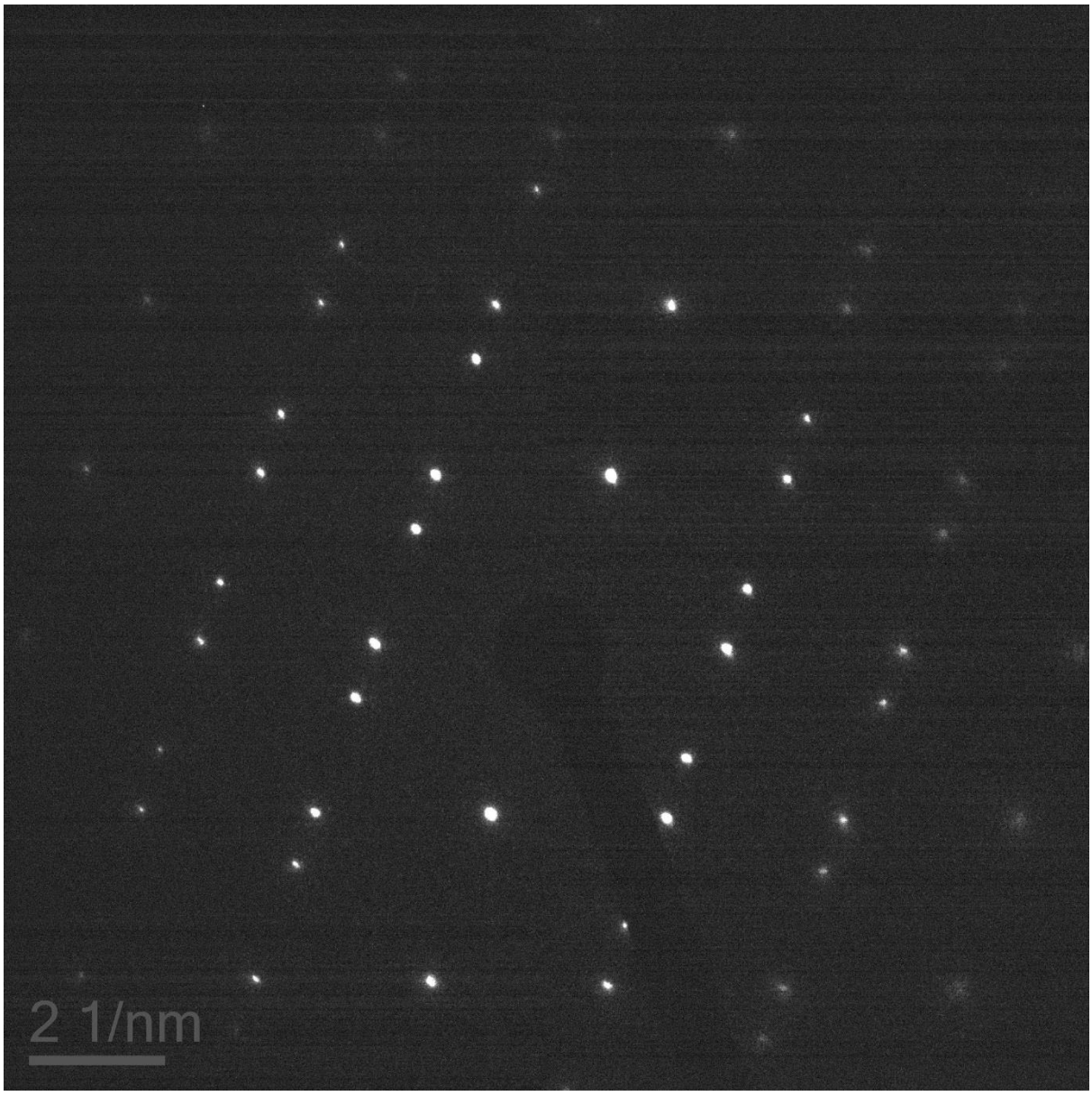

Selected area electron diffraction of the alloy L605 cobalt chromium metal matrix; i.e. region below the thin cross-section of PAC-L605 interface. The material matrix shows presence of crystal twinning as predicted for metal alloy microstructure.

Figure 3.16

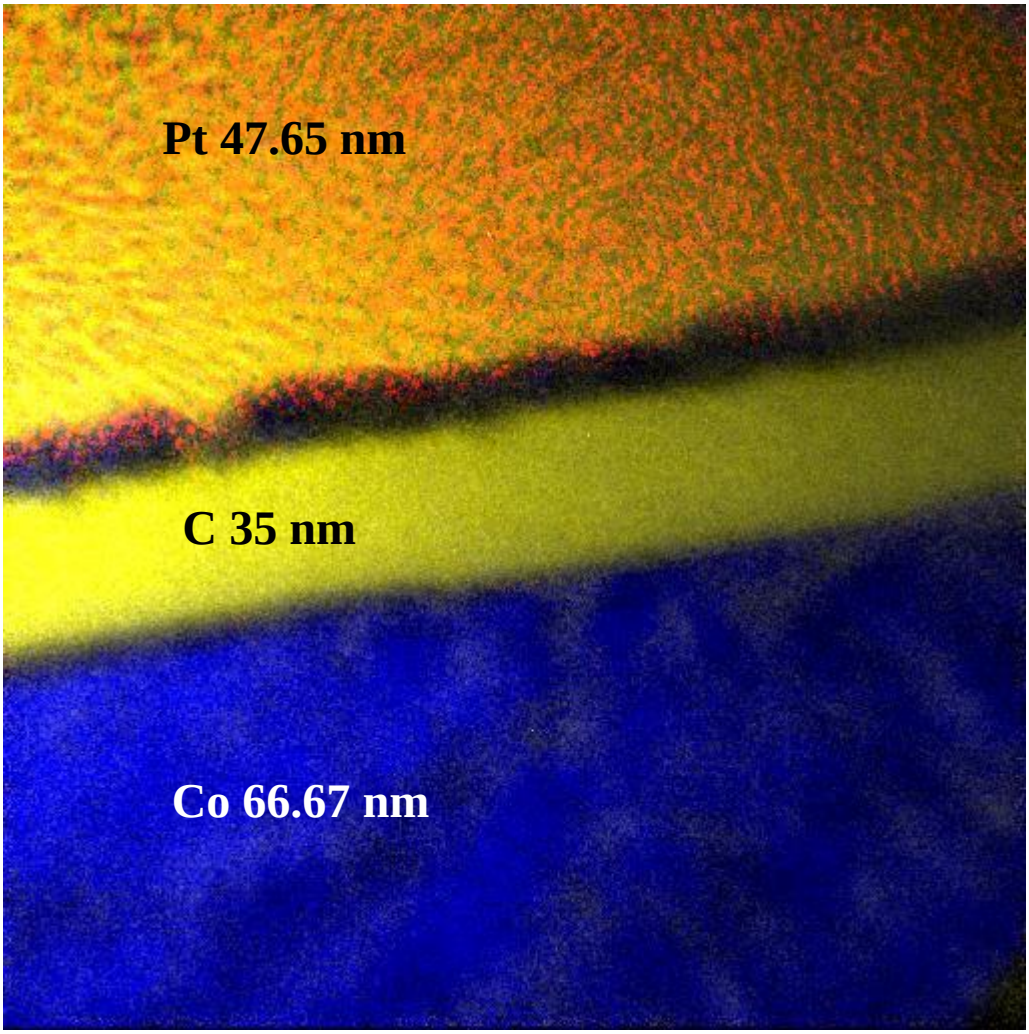

Chemical composition of the PAC-L605 cross sectional interface represented via colour segregation on a TEM image (2.3 K x Mag). Thickness of elements were confirmed with electron energy loss spectra EELS (spectra not represented).

3.4 Discussion

Several aspects of the plasma activated coating for use on alloy L605 cobalt chromium stent were characterized within this chapter. These include physical and chemical characterization of the surface coating, micro/nanoscale assessment of surface roughness and stiffness, mechanical stability of modified material, and coating integrity at PAC-L605 interface to prevent delamination; as necessary for a robust coronary stent coating. Biofunctionalization of the surface coating will be addressed in chapter 4. This is a first study investigating PAC as a surface coating on cobalt chromium flat metal alloy L605. Key outcomes of this study include physical, chemical characterization to confirm surface modification at the microscale, characterization of PAC-L605 interface via nanotechnology to explain unique PAC technology, support non-delaminating coating technique, and its suitability for alloy L605 coronary stent applications.

3.4.1 Investigating PAC properties on alloy L605.

The plasma chemical composition was similar to the coating deposited on an alloy 316L stainless steel and coronary stent platform, discussed in chapter 2, although a coating time of 20 min was utilized, for a 20 nm coating, at a deposition rate of 1 nm/min. Electron Dispersive X-ray spectroscopy (EDS) is a surface specific technique, allowing analysis of the chemical composition with a penetration depth of as little as 5 Å [204]. The qualitative and quantitative microanalytical X-ray technique provides information on the chemical composition of a sample, for elements with atomic number (Z). The electron beam of 2 keV was focussed on the sample surface in field emission scanning electron microscopy (FESEM). We used a very low accelerating voltage of 2 kV to ensure electrons from the primary beam only penetrated the modified surface of material, to interact with atoms of the surface and not underlying biomaterial - to obtain X-ray intensities specific to surface coating chemical composition. The interaction volume of a low acceleration voltage provided information of the surface coating

alone, indicating a higher peak for percent element weight of both carbon and nitrogen on the modified PAC-L605 surfaces compared to bare alloy L605. The purpose of plasma assisted surface modification is to change the physical, chemical or biological properties of a material for biocompatibility. Physical properties of the surface modification include variation to surface texture, roughness and wettability, which significantly influence the behaviour of material with fluids and vasculature, *in vivo*. Chemical and biological surface properties influence the process of absorption and biomedical reaction investigated in chapters 4-5.

We focused on the physical and mechanical characteristic changes of a modified metal alloy surface at micro scale, including surface roughness and surface hydrophilicity. Earlier studies indicate high surface roughness decreased spreading of a liquid on low energy solids [201, 205]. Emerging technologies on surface engineering technology for MEMS and lab-on-chip devices have led to a rapid growth of mechanical and electrical fabricating systems at the microscopic and nanoscale levels [206]. Roughness change of a solid material substrate is usually realized by material removal and adding processes, i.e. simultaneous etching and thin film deposition, as well as energetic ion implantation [145, 207]. When viewed at the nanoscale via AFM and WLI optical profilometry, surface roughness of PAC was immediately apparent. The inconsistent, isotropic micro-scale surface coating is attributed to the proprietary plasma polymerization process of deposition and consecutive etching [145]. The PAC-L605 surface developed in our study, enhance favourable mechanical adhesion properties for *in vivo* applications, and increase overall amount of surface area for bearing loads.

Of the two techniques trialled, NanoMap WLI technique resulted in faster, more accurate surface imaging within a larger surface area. The roughness analyses were computed in the nano/micro scale for AFM and NanoMap respectively. Additionally, surface imaging with AFM required calibration of Si_3N_4 cantilevers, which showed a sharp resonant peak at 76.5 Hz and a correspondingly high Q factor, these parameters were used to compute force constant of

the cantilevers, for accurate calibration prior to imaging. NanoMap ensured complete noise elimination for high sensitivity imaging, which was a significant limitation with AFM. The maximum possible scanning area with AFM was only within the 20 μm x 20 μm range, which did not allow for wide-range surface mapping, while NanoMap allowed larger scanning area of 100 μm x 100 μm utilized (up to 150 mm). AFM images limited the ability to accurately estimate surface roughness of PAC-L605, which was higher. It was also visually apparent that PAC surface coating of 20 nm thickness, had a micro scale average roughness, as imaged in figures 3.10-11. For most engineering surfaces contact type instruments such as optical profilometry based on the physical principle of the wave properties of light, is widely used. We therefore chose NanoMap WLI for future roughness measurements of plasma modified biomaterial.

Surface roughness has a strong influence on wetting characteristics of a modified material. Water contact angles as high as 150^{o} have been observed on hydrophobic polymer surfaces such as PTFE (polytetrafluoroethylene) and PE (polyethylene) [201]. The untreated alloy L605 is also strongly hydrophobic with a water drop wetting angle approximating >100^{o}. Immediately after plasma treatment, the water contact angle decreased significantly, near 45^{o}, indicative of a hydrophilic surface modification. The same sharp changes were observed for wetting angles of formamide and diiodomethane. In correlation, the total surface energy increased to ~65 mJ/m^2 immediately after PAC deposition (figure 3.5 A). Similar trends were observed within a 2 week time-frame for PAC-316LSS surfaces - compared to PACL605; in relation to both parameters of surface hydrophilicity measured (figure 3.5 B). The initial variation for wetting angles of water and diiodomethane were similar, although by 2 weeks, values changed significantly (figure 3.6). Random variation in wetting angle for the two liquids at comparatively similar early time-frames, is due to inconsistent surface roughness. Most realistic engineering surfaces are random, either isotropic or anisotropic; since roughness of

our PAC-L605 engineered surfaces fit a gaussian profile (figure 3.10), they are isotropic [208]. Furthermore, contributions of polar and dispersive components to total surface energy also varied with time; whilst the polar energy decreased significantly, the dispersive part did not vary similarly with time (figure 3.7). The random variations observed, could also be due in part to isotropic surface engineering. The dispersive component of surface energy represents surface oxidation, and polar component represents surface free radicals, with time of exposure to air [103]. The plasma kinetics study had a similar time-line and experimental set up to Kondyurin et al [209].

Chemical reactions are a common process in surface engineering, with ability to change surface roughness of materials by removing or generating a new material layer on the substrate via microfabrication [210, 211]. The decrease in wetting angle and increased surface free energy, post PAC modification of alloy L605, is caused by chemical transformations on the plasma coated surface, as verified with EDS surface chemistry analysis, and visualized via imaging with AFM/NanoMap at the Nano/micro scale. With time, surface hydrophilicity decreases, in response to changes to surface chemistry of the coating [103]. As Bilek et al explains with previous electron spin resonance (ESR) studies; surface free radicals are quenched by oxidation during exposure to air, resulting in a plateau of the oxygen group. As observed herein with dispersive surface energy calculations. The ageing surface chemistry can be verified further with EDS as before, or with X-ray photoelectron spectroscopy on a metal. Surface energy values for PAC-L605 stabilize at a higher value than the hydrophobic untreated alloy L605.

Surface hydrophilicity is important to biofunctionalize a stent coating, since hydrophobicity influences blood viscosity [212] and interaction of blood/protein components on surfaces, whilst extreme hydrophilicity interacts poorly with proteins and cells [213]. Mildly hydrophilic surfaces are therefore at an advantage *in vivo*, as they display favourable interactions with proteins, cells and blood, and decrease platelet adhesion as seen with polymer/surface

modifications of stainless steel stents [106, 214]. Several commercially available stent surfaces such as PBMA (Cypher), SIBS (Taxus) PVDF-HFP (Xience V) are comprised of hydrophobic polymers with contact angles in the range of 112^{o}, 118^{o}, and 129^{o} respectively. Even the commercially available stents termed to have 'hydrophilic' polymer surfaces, such PC (Endeavor) and BioLinx (Resolute) have contact angles in the range of 81^{o} and 94^{o} respectively [215]; well above surface hydrophilicity observed on PAC-L605 or PAC-316LSS surfaces herein. Polymer biocompatibility for DES is essential; for example the vascular response to inflammation induced by residual polymer can overwhelm biological effects of drug elution, resulting in late formation of neointima, as seen with Cypher^{TM} sirolimus eluting stents [216]. Although BioLinx stent polymer has slightly higher hydrophilicity in comparison to Cypher and shows lower inflammation scores, the effects could be due to extended period of drug elution (180 days), than polymer biocompatibility [215]. Despite hydrophobic PVD-HPF copolymer, Xience V^{TM} stents have shown safety for over 2 years in preclinical [217] and clinical assessments [218]. Of note, the coronary stent system has an underlying thin-strut cobalt chromium coronary stent, which as mentioned on introduction and seen in assessments [217, 218], may have contributed to maintain lowered restenosis outcomes after the first 120 days of everolimus drug elution.

3.4.2 Unique features of proprietary plasma technology suited for a stent coating

Atherosclerotic vessels treated via vascular stents, commonly involve fatty lipid deposits, plaques and arterial calcification. For revascularization, stents are expanded *in vivo*, and commonly undergo a process of crimping and expansion. Polymer coatings on DES undergo large strains and must remain as a permanent scaffold, these mechanical challenges must be taken into account to ensure long-term safety during DES device development and deployment [219]. Clinically, new generation biolimus-eluting stents have displayed inability to withstand

certain complications/challenges; resulting in damage to the abluminal polymer and stent replacement [192]. Polymer layer integrity has been a persistent concern with commercially available stents, as has been observed with BiodivYsio, Taxus and Cypher stents via SEM analysis [189, 190]. Several negative clinical complications can result from stent coating failure *in vivo*, including increased risk of thrombosis, interruptions to pharmacokinetics of a drug dose released by the polymer coating, inflammatory response as well as micro embolisms [193, 220]. To adequately design stent coating that withstand large deformations; mechanisms underlying delamination must be understood. Parameters governing delamination initiation include; coating thickness, stiffness and interface strength/integrity between the coating and stent surface [193].

Indentation, a traditional method is used to quantify mechanical properties of materials as well as thin films or coatings [221, 222]. The phenomena allows to diagnose surface cracking/delamination of hard, brittle surfaces, since they cause jumps, or kinks in the raw data of load vs. depth [223]. Complexities are also generated since investigated systems are usually composed of at least two materials with different mechanical properties. Failure of integrating different systems include plastic deformation, cracking of the coating, or failure of the interface [221]. The main emphasis in this investigation was to extract quantitative data of the surface stiffness post PAC modification in comparison to bare metal alloy L605. The PAC stiffness was lower than alloy L605, at initial minimum load (0.20 mN), since it is composed of a 20 nm thick, soft coating. However, with increasing load, the coating does not delaminate or crack; instead the PAC-L605 vs. L605 surface stiffness shows similarity from 3 mN onwards to 50 mN, indicating the coating is well adhered to underlying metal surface. There were no jumps, plateaus or kinks in the load-displacement raw data, used to compute surface stiffness (figure 3.12).

We chose to include unloading displacement (nm) for 21 indentations only (100-79; equally for both surfaces) for stiffness calculations, since they provided sufficient detail of surface overall. Incidentally, for unloading displacement data at ~60 indents, the Matlab indentation code generated negative values of surface stiffness, for both alloy L605 and PAC-L605 surfaces. We ruled out coating delamination as a cause of the occurrence since the phenomenon was common to both surfaces. It appears that, since our original sample is a 0.8 cm x 0.8 cm x 0.025 cm flat metal for nanoindentation tests, the surface may have bent after the berkovich tip passed the 60^{th} indentation, along both PAC-L605 and alloy L605 surfaces. Resulting in negative values, not incorporated herein. Since stiffness is directly proportional to young's modulus (E), this parameter E, can be calculated, according to the Oliver-Pharr method [202].

To observe cross-sectional microstructure, and reconfirm individual layer thickness of deposited coating at interface, we characterized the PAC-L605 interface with high resolution transmission electron microscopy (HRTEM) and electron energy loss spectroscopy (EELS). The cross-sectional TEM sample was methodically prepared by grinding down a 250 µm thick PAC-L605 material to 10-15 µm via tripod polishing, the remainder milled with FIB to create a 20 nm thick electron transparent metal lamellae for HRTEM (figure 3.13). The TEM image of the PAC-L605 interface at high magnification and high resolution, showed presence of a distinct ionic buffer layer at the interface, detailing ionic stitching attachment of PAC to the metal surface, also clearly seen with the fast inverse Fourier transform (IFFT) image, in colour, (figure 3.14 A, B). This explains in visual detail the non-delaminating nature of PAC, as theorized in applied/plasma physics [187, 224] and computed via nanoindentation in this study.

Further, we characterized the alloy L605 material, just beneath the cross-section of PAC-L605 interface/lamellae, with selected area electron diffraction (SAED), to obtain atomic level detail of the cobalt chromium metal matrix. Figure 3.15 is representative of the characteristic twinning between grain boundaries of cobalt chromium crystals, with similarity to SEM images

of grain boundary microstructure previously observed for alloy L605 [166]. The metal alloy remains unchanged post-surface modification. Finally, we used electron energy loss spectroscopy (EELS) to reconfirm individual layer thickness, and chemical elements present in the cross-section of PAC-L605 interface. The thickness calculated via electron inelastic scattering (mean free path – MFP), and interface elements at the PAC-L605 cross-section were re-confirmed as platinum (deposited during FIB milling), carbon (acetylene plasma polymerization), cobalt (bare metal alloy, underlying material) (figure 3.16).

The combined results for 1) PAC surface stiffness preventing delamination and 2) integrity of coating interface observed with HRTEM, also in support of (1), re-establish the suitability of PAC as a non-delaminating, robust stent coating on alloy L605 cobalt chromium.

3.5 Conclusion

Overall, these results demonstrate that modification of a commercially available alloy L605 material with PAC, alters surface chemistry and improves surface hydrophilicity. Micro/nanostructured surfaces were developed with the intention of improving biomimicry during interactions with micro/nanoscale living tissue *in vivo*. Isotropic roughness at the microscale observed imparts surface ability to bear loads, and interact favourably with biological molecules (investigated *in vitro* in chapters 4-5). We showed here for the first time via coating stiffness, the surface modification is non-brittle, soft and strongly adhered to underlying metal alloy L605. The interface HRTEM cross-section, also detailed for the first time in this study, showed robust adhesion of PAC to alloy L605, via ionic stitching. This PAC will be used for all further experiments.

Chapter 4 – Plasma based biofunctionalization of alloy L605

4.1 Introduction

4.1.1 Micro and Nanotechnology in Tissue Engineering Materials

The rationale to develop micro/nanostructured biomaterials for tissue engineering is for improved interaction with natural tissues. Natural tissues and associated extra cellular matrix are fundamentally nanostructures in composition themselves (cells are in the microscale, compared to nanoscale proteins) [225]. A complex set of interactions control cell proliferation, differentiation and apoptosis pathways, resulting in cell fates [226]. Evaluating biological design from an engineering perspective aid researchers develop surfaces for improved biomimicry and biocompatibility, for clinical applications.

4.1.1.1 Biomaterial – Cell interactions

Intracellular structural architecture of the cell or the cell cytoskeleton, modulates cellular responses at the microscale, including transport and binding-reactions. Generally structural behaviour of cardiovascular, endothelial, smooth muscle cells (SMC) as well as neural and osteoclast cells on a biomaterial, are heavily influenced by the filament systems of the cytoskeleton [227]. The initial anchorage between cell and biomaterial involves extracellular matrix proteins, intracellular cytoskeleton and cell membrane proteins [228]. Successful cell-material interaction is represented by cell attachment, proliferation and spreading, to evaluate biocompatibility of materials for tissue-engineering applications [229].

4.1.1.2 Biomaterial – Protein interactions

Proteins are the first biological entities to interact with a biomaterial surface post-implantation, and adsorb on hydrophobic surfaces, as seen with fibrinogen and fibronectin [230]. Protein-

surface interactions are fundamentally responsible for the biocompatibility or lack thereof of implant surfaces, *in vivo*. Mechanistically, proteins absorb rapidly to implant materials; saturating surfaces to prevent healthy interactions with living cells. The key to controlling positive cellular responses lie in the ability to control the orientation, and conformation of proteins attached on a biomaterial; a challenging issue in tissue engineering, given synthetic biomaterials are not generally biocompatible in composition [231]. The adsorptive behaviour of proteins highly depend on surface properties of a biomaterial, including topography, hydrophilicity, surface energy, charge and surface chemistry, characterized in chapter 3 (for PAC-L605). A core limitation at present of protein-biomaterial anchorage is the inability to control the amount, conformation and type of protein adsorbed *in vivo*. A vascular device such as a stent, capable of immobilizing proteins, should have a biocompatible surface, bind a high concentration of candidate protein - in their native conformation, and retain protein functionality as seen with PAC-316LSS stents *in vivo*, in chapter 2.

4.1.1.3 Biomaterial – Blood interactions

Surface bioengineering and roughness parameters regulate material/device hemocompatibility [212]. The immediate biological response after medical device implantation is blood coagulation, which precedes wound healing, *in vivo*. However, a synthetic material surface can activate intrinsic/extrinsic coagulation as well as complement system, resulting in unnecessary coagulation and inflammation at the implant/tissue interface, schematically represented in figure 4.1 [232]. The adverse thrombogenic effects after device implantation although prevented with aggressive dual antiplatelet and/or anticoagulation therapy, increases susceptibility to inconsistent bleeding risks [135, 185]. Fundamentally, surface bound fibrinogen and platelet activation are markers of coagulation cascade initiation [232]. Surfaces inert to platelet adhesion and activation of coagulation achieved through surface engineering, may potentially avert an adverse biological response [233].

A biofunctionalized material facilitates bioactive attachment of proteins, promotes cell proliferation and thromboresistance. Surface engineered materials are investigated *in vitro*, prior to transferring modification technique to an implantable device for pre-clinical testing, to decide suitability for clinical applications. Practically, basic biological responses of a modified biomaterial are evaluated by simulating clinical conditions *in vitro* [234, 235].

Figure 4.1

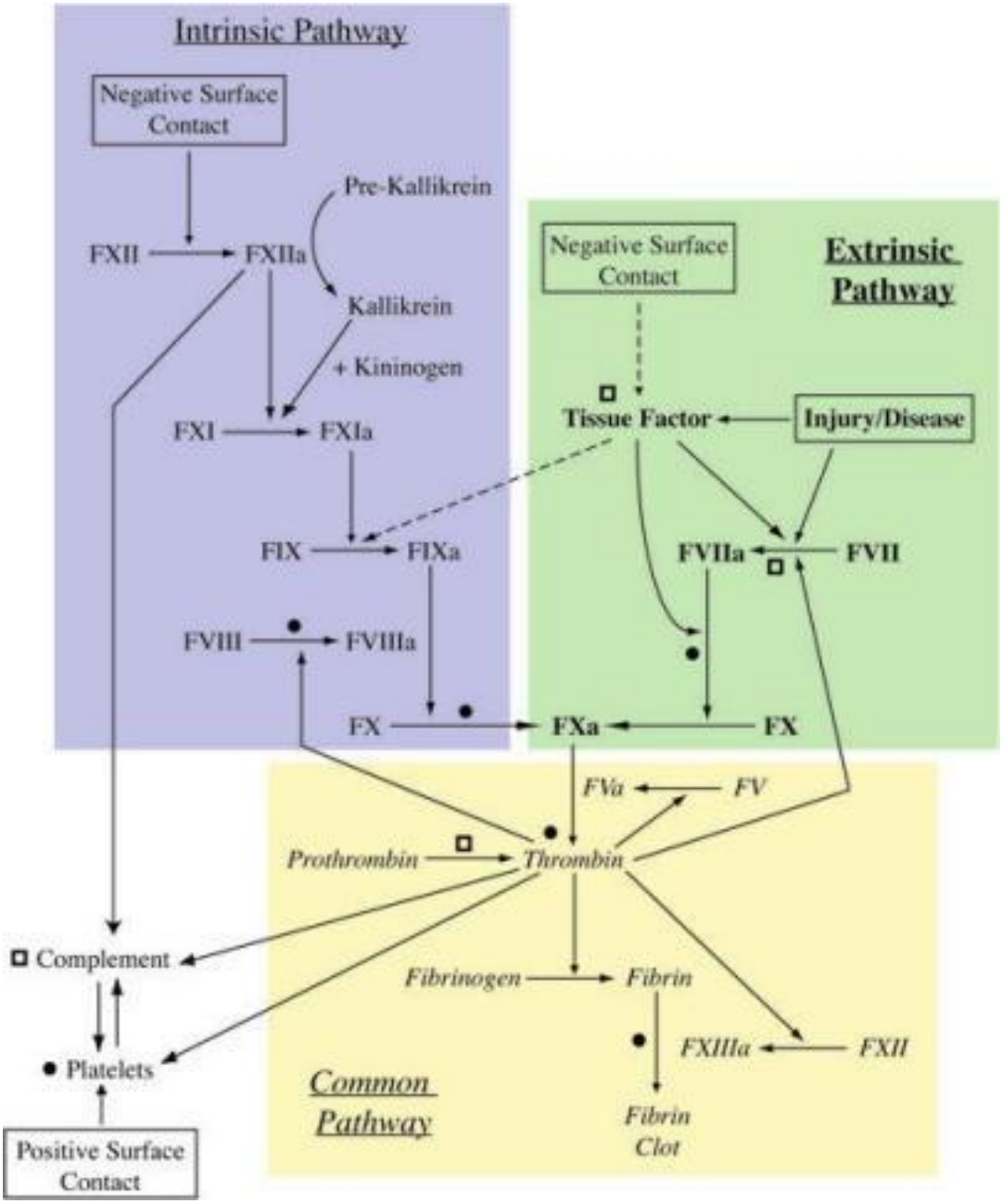

Coagulation cascade: an overview of the intrinsic, extrinsic and common coagulation pathways. Factors activated via platelets are denoted by circles ●, factors activated via complement proteins denoted by open squares □ (Image from Waterhouse et al [232]).

4.1.2 Facilitating stent endothelialization

A single layer of endothelial cells (ECs) known as the endothelium, line the vascular wall lumen and maintain vascular homeostasis [236]. Stent implantation causes significant injury to the endothelium and vascular wall, resulting in inflammation, as well as neointimal hyperplasia (NIH), detailed in chapter 2 [237]. The process of endothelium repair depends on migration of surrounding mature ECs, and circulating endothelial progenitor cells (EPCs) to site of injury for endothelialization. DES therapy attenuates the natural response to damage; causing acute inflammation and subsequent NIH at site of implantation Accelerating re-endothelialization post stent implantation is a suitable strategy to assist natural process of repair, as it reduces NIH and late stent thrombosis (LST) exhibited [114, 183, 237]. Many clinical investigations have therefore examined assisted endothelialization at the host-implant interface for cardiovascular stents [76].

Cultured cells are regularly used *in vitro,* to investigate cell-biomaterial interactions such as cell adhesion and proliferation [105, 238]. The choice of human umbilical vein endothelial cells (HUVECs) and human coronary artery endothelial cells (HCAECs) have been verified previously for biomaterial testing [239], as ECs play a fundamental role *in vivo* at the host-implant surface. Endothelialization assists 3 key processes of device biointegration including; 1) formation of neointima, 2) reduced thrombogenicity and 3) device patency [239]. Specific *in vitro* studies for enhanced biomaterial-cell interactions include; HUVEC culture on titanium oxide films modified via plasma immersion ion implantation (PIII) [240], plasma treated PET (polyethylene terephthalate) and PTFE (polytetrafluoroethylene) with human ECs [241], surface-modified titanium alloys with passage2/3 HUVECs [239] and studies with plasma modified alloy 316LSS for assisted endothelialization [138]. Overall, surface-engineered biomaterials show superior cell-interactions, compared to their original (pre-modified), hydrophobic state. Protein adsorption on a hydrophobic material surface may enhance EC

adhesion, but the process requires controlled protein adsorption with their bioactive sites exposed, and is therefore tedious [242].

4.1.3 Stent thrombosis / blood biocompatibility

Stent thrombosis is a rare but catastrophic event, predominantly associated with DES as late/very late stent thrombosis (VLST) [183]. Meaningful comparisons between clinical trials were conducted to form standardized definitions of clinical thrombosis based on time elapsed after device implantation - proposed by the Academic Research Consortium (ARC) [243] (chapter 1). The frequency of stent thrombosis is similar in the first year post-implantation for both BMS and DES, with recommended DAPT continuation. The risk of thrombosis is however longer for DES, requiring prolonged DAPT administration due to delayed neointimal coverage [40]. Investigations on clinical VLST for both DES and BMS, conclude that different biological mechanisms underlie the phenomenon depending on stent type [244].

Mechanistically both DES and BMS surface polymer/metal alloy induce platelet adhesion, activation and thrombus formation, requiring mandatory antiplatelet therapy effective for an unknown period of time (individualized for patients, usually 6-12 months) [135]. Platelets play a pivotal role in thrombus formation and coagulation [232]. High platelet activity is a risk factor for many thrombotic events (figure 4.1), with involvement in the conversion of fibrin to fibrin clot deposition; the final step in blood coagulation [245], and clinically increased platelet turnover is seen in patients with previous definite thrombosis [246]. Several clinical studies including a recently concluded five year follow up, indicate direct correlation of stent thrombosis to associated cumulative incidence of stent thrombosis elevation and myocardial infarction (STEMIs) [247], and a correlation was also seen between DAPT dose (high not low), and mitigation of acute stent thrombosis [248].

Since formation of fibrin clots is directly influenced by platelet activation and vice versa, implication of fibrinogen and fibrin structure is investigated in treatment of thrombosis [245]. Biomaterial surface-related fibrinogen and fibrin deposition plays a role in stent/vascular implant thrombosis, investigated *in vitro* for novel biomaterials, alongside surface-platelet deposition, and surface-whole blood interaction. Factors underlying stent thrombosis and related multiple adverse reactions are categorized in Table 4.1 [249]

Table 4.1. *In vivo* clinical mechanisms and factors leading to adverse reactions of coronary stents. Factors tabulated are related to DES and BMS, from Kristensen et al [250]. Highlighted components are factors directly related to stent-material induced adverse reactions.

CLINICAL FACTORS			
Procedure-related parameters	**Patient characteristics**	**Stent characteristics**	**Anti-platelet therapy**
Use of multiple stents	Diabetes	Metal/polymer incompatibility	Inadequate intensity of therapy: time/dose
Small vessel diameter	Acute coronary syndromes such as STEMI	Polymer defects: non-uniform drug release	Non-compliance
Coronary dissection/long lesions	Left ventricular dysfunction	Hypersensitivity inflammation	Premature cessation of DAPT
Geographic miss	Renal failure	Time course of drug elution	
Stent malapposition	Advanced age		
Underexpansion of the stent/slow flow	High platelet reactivity		
Stent design – strut thickness, polymer/alloy type			
Bifurcation lesions			

4.1.3.1 *In vitro* biocompatibility investigation

During the initial investigation of complex biological systems *in vitro*, biomaterial-blood interactions are investigated via static and/or flow assays within simulated physiological parameters. The chandler loop model used in flow studies determine hemocompatibility [105] [251] for *in vitro* coronary flow investigations [105, 252]. The model is appropriate due to geometric/fluid mechanics characteristics, flow rate to simulate coronary blood flow, and loop configurations similar to arterial curvatures, approximating curved flow [253]. The model is simple, clinically relevant, forms physiologically similar thrombi, and supported by previous investigations (with both biomaterials and stents) [252, 254, 255]. Figure 4.2 is a schematic depiction of the modified circulating loop as a theoretical and experimental model [252].

Blood anticoagulation is integral prior to any *in vitro* experiment to prevent air-induced thrombosis. The most commonly used anticoagulants are citrate and heparin, with heparin the lesser-potent anticoagulant, only partially inhibiting platelet activation [256].

Figure 4.2

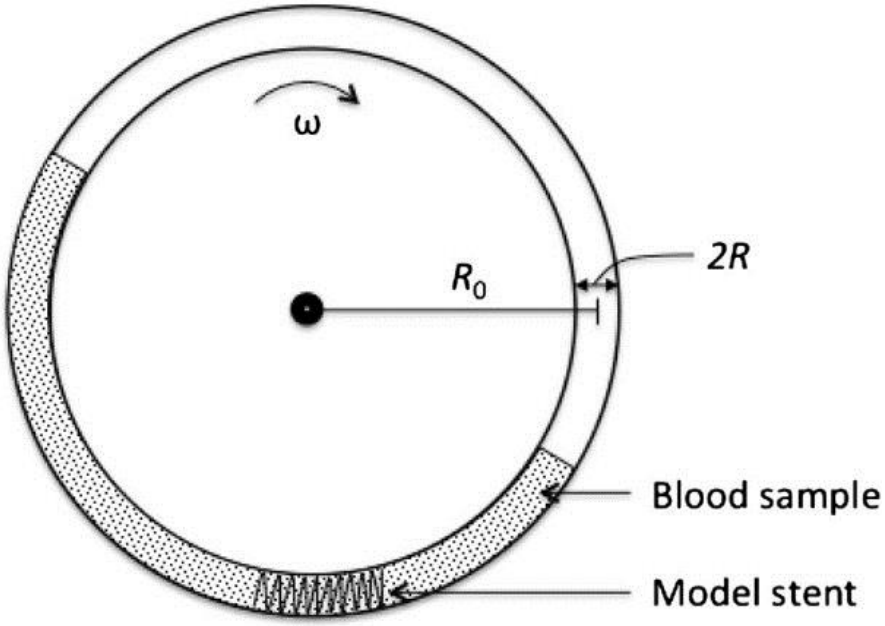

Theoretical model for modified experimental chandler loop with blood sample and model stent. Image from [252].

4.1.4 Protein-biomaterial interaction dynamics

Theoretically an ideal biomaterial will show absolute protein resistance. However, this is impractical, therefore applications of biomaterials require simultaneous anticoagulative therapy [257]. A key aim of bioengineering surfaces is to prevent nonspecific protein adsorption to improve biocompatibility [257]. In order to design and develop rationale strategies for biocompatible materials, theoretical understanding of surface kinetics and protein binding dynamics is essential [258]. Major players in protein-biomaterial surface adsorption are water mediated hydrophobic and hydration forces, culminated in a concept known as "Berg's law" or "Berg's limit". Berg's limit is a quantitative definition of surface hydrophilicity/hydrophobicity, in relation to protein adsorption [257, 259]. According to Berg's limit, surfaces with $\theta < 65^0$ are hydrophilic, have repulsive forces and prevent long-range attractive forces with proteins (as opposed to hydrophobic surfaces with $\theta > 65^0$). However the same principles don't apply to bioinert surfaces, discussed elsewhere [257]. In brief, mechanism of surface protein adsorption is energetically favoured on hydrophobic surfaces, whereas the mechanism is energetically unfavourable for hydrophilic surfaces. Mammalian cell attachment process, is distinct from protein adsorption, and occurs efficiently on hydrophilic, but not on hydrophobic surfaces [259].

Whilst non-selective protein adsorption to a surface results in adverse effects *in vivo,* controlled covalent attachment of a specific protein candidate (available in the subendothelial ECM) to a modified material, can increasingly influence its biocompatibility [187]. Successful completion of a specific biomedical task as a result of protein surface retention, should allow a quantitative measure between material chemistry and biological response *in vitro* and *in vivo* [259]. The structure-reactivity relationship is the foundation of biomaterials research [259]. Plasma based methods generate linker free protein binding sites for medical applications [103, 187] .

4.1.5 Tissue Engineering Biomaterials

Different strategies are utilized in tissue-engineering to form 2-dimensional, micro and nanofeatured polymer materials [225]. Responsive polymer surfaces adapt to environmental stimuli in relation to surface wettability, species adherence, protein binding and convert chemical/biochemical signals into optical, electrical and mechanical signals [260]. Applications of modified nanomaterials include, drug delivery, diagnostics, tissue engineering, and surface coatings [260]. Polymer surfaces on DES manufactured for controlled drug delivery and release systems, must also interact positively with environmental stimuli [261]. Surfaces that can modulate biomolecule activity, facilitate protein immobilization, cell adhesion and migration at the aqueous-material interface of medical devices and stents [262]. Fabrication of thin polymer films are mediated via several deposition techniques with varying degrees of complexity. Techniques such as spin-coating, plasma deposition, chemical vapour deposition, and polymer brushes are currently employed for surface modification, with diverse medical applications [262, 263].

Bioengineering a stent surface for biocompatibility aims to attenuate three clinical complications; 1) inflammation, 2) thrombogenicity and 3) neointima formation/in-stent restenosis (ISR), while promoting surface endothelialization [264]. For surface modification of cardiovascular metal stents, constructing a buffer layer at the interface of organic and inorganic materials (as observed in our study), is very important to obtain a robust surface with long-term biocompatibility [244]. Table 4.2 outlines tissue engineering techniques for cardiovascular stent surfaces, to address specific clinical complications, commonly encountered during PCI.

Table 4.2 Cardiovascular stent materials, modifications and applications. Anti-thrombosis modifications are shaded in orange, anti-restenosis modifications shaded in green.

Cardiovascular stent material	Modification Technique	Application
Titanium oxide film (Ti-O) on titanium metal.	Phosphorous ion implantation and vacuum annealing [265]	Anti-thrombosis
	Plasma immersion ionization (PIII) [266]	Anti-thrombosis
	Substrate nanocrystalization [267]	Anti-thrombosis
Stainless steel (316L SS)	Cyclic potentiodynamic polarization (CPP) [268]	Anti-thrombosis
Allylamine film on 316LSS	Pulsed plasma polymerization followed by heparin bonding [269]	Anti-thrombosis
Tantalum oxide film (Ta-O) on 316L SS	RF magnetron sputtering [270]	Anti-thrombosis
Gold stent	Biotinylated boophilin (B-boophilin) immobilized on SAM via neutravidin [271]	Direct thrombin inactivation for anti-thrombosis
Stainless steel wafers	Glow discharge plasma mixed N_2 and O_2 at different molar ratios [272]	Apoptosis to limit ISR Anti-restenosis
Micropatterned Nitinol surface	Plasma nanocoating between 40-50 nm [273]	Cell adhesion and endothelialization. Anti-restenosis
Nitinol and Teflon (for radioactive stents)	Plasma modification and covalent immobilization of HA-DTPA with yttrium/indium radionuclide [274]	Anti-restenosis
Bioeresorbable polymers on Nitinol stent	Bioabsorbable abluminal layer of polyactic acid and biolimus A9 [275]	Anti-restenosis

4.1.5.1 PAC-L605 biofunctionalization

The proprietary plasma based technology on polymer/metal surfaces biofunctionalize a material to 1) covalently bind a protein, 2) reduce surface thrombogenicity, and 3) facilitate cell proliferation *in vitro* and *in vivo* [106], with or without surface protein tropoelastin [103, 187]

The N-terminal segment of tropoelastin in a buffer solution is theorized to facilitate its integration to a surface/scaffold [276], while the exposed C-terminal allows cell adhesion via integrins [277]. Previous investigations have proven this with adherence of HUVECs and HCAECs (human coronary artery endothelial cells) to recombinant fragments of tropoelastin for cell proliferation [278]. Tropoelastin is a cell-adhesive, subendothelial, extracellular matrix (ECM) protein [277], which can specifically promote endothelial cell adhesion, and proliferation, to form a cell monolayer on a biomaterial [279, 280]. The same investigations, have also accounted for its ability to inhibit smooth muscle cell growth/recruitment from intima [280]. Tissue-engineered surfaces with endothelial cells adhered to small-diameter vascular grafts, risk *in vivo* detachment during coronary flow, to cause thrombosis and graft failure [280]. For *in vivo* applications therefore, natural recruitment of endothelial cells to an ECM surface, is a desirable option at the site of implant.

Most surface modifications discussed above (table 4.2), have addressed one of the two clinical complications; either thrombosis or restenosis. The PAC modification allows simultaneous anti-thrombotic applications, facilitates endothelialization to minimize restenosis, and promotes covalent binding of a desired protein in its native conformation [276].

The aims of this work are to 1) determine covalent binding capacity of tropoelastin (TE) to PAC-L605 surfaces 2) visualize cell proliferation on PAC-L605, PAC-L605/TE and alloy L605 surfaces *in vitro,* 3) investigate plasma based biofunctionalization on thrombogenicity

for PAC-L605, PAC-L605/TE and alloy L605 *in vitro;* with or without surface immobilized tropoelastin (TE).

4.2 Materials and Methods

4.2.1 Materials, Equipment, Suppliers and Facilities

A list of chemicals, reagents, materials and their suppliers are presented in Table 4.3

Table 4.3 Materials and their suppliers

Chemical/Reagent/Material	Supplier/Facility
4',6-Diamidino-2-phenylindole (DAPI)	Sigma-Aldrich, St. Louis, MO, USA
6 mm Tygon tubing ND-100-65, Class VI (ID 6.35 mm, O.D. 7.93, 50 FT)	Saint-Gobain Performance Plastics, PA, USA
Absolute ethanol	Sigma-Aldrich, St. Louis, MO, USA
Anti-elastin antibody (BA-4) raised in mouse	Sigma-Aldrich, St. Louis, MO, USA
Anti-mouse IgG-fluorescein isothiocyanate (FITC) raised in goat	Sigma-Aldrich, St. Louis, MO, USA
Bovine Serum Albumin (BSA)	Sigma-Aldrich, St. Louis, MO, USA
Crystal Violet	Sigma-Aldrich, St. Louis, MO, USA
Culture flasks	Greiner Bio One (Cell Star) Kremsunster, Austria
Culture plates	Greiner Bio One (Cell Star) Kremunster, Austria
Diammonium 2,2-azino-bis(3-ethylbenzothiazoline-6-sulfonate) (ABTS)	Sigma-Aldrich, St. Louis, MO, USA
Fibrinogen from Human Plasma, Alexa Fluor 488 Conjugate (F13191)	Life Technologies Australia, Victoria, Australia
Foetal Bovine Serum (FBS)	Sigma-Aldrich, St. Louis, MO, USA
Formaldehyde 37% v/v	Sigma-Aldrich, St. Louis, MO, USA
Glutaraldehyde (25%)	Sigma-Aldrich, St. Louis, MO, USA
Glycine	Sigma-Aldrich, St. Louis, MO, USA
Goat Anti-Rabbit IgG Fc (Alexa Fluor® 488) (ab150089)	Abcam, Cambridge, MA, USA
Graduated pipettes	Greiner Bio One (Cell Star) Kremunster, Austria
Heparin sodium salt (porcine intestinal mucosa, H3393, 180 U/mg)	Sigma-Aldrich, St. Louis, MO, USA
Hexamethyldisilazane (HMDS)	Sigma-Aldrich, St. Louis, MO, USA
Hydrogen peroxide	ThermoFisher Scientific (BDH), Scoersby, VIC, Australia
MesoEndo medium	Cell Applications, Inc, San Diego, CA, USA
Osmium tetraoxide (OsO_4)	ProSciTech, Thuringowa, QLD, Australia

Phalloidin-TRITC (Tetramethyl Rhodamine Iso-Thiocyanate)	Sigma-Aldrich, St. Louis, MO, USA
Phosphate Buffered Saline (PBS)	Tissue Culture, Heart Research Institute
Polyclonal swine Anti-Rabbit Immunoglobin-G/FITC (F0205)	Dako Australia, Pty. Ltd, Victoria, Australia
Polyclonal Rabbit Anti-Human vWF (A008229)	Dako Australia, Pty. Ltd, Victoria, Australia
Sodium dodecyl sulphate (SDS)	Sigma-Aldrich, St. Louis, MO, USA
Silicon tubing (ID 10 mm, 10 FT) Masterflex	John Morris Scientific Pty Ltd, NSW, Australia
Trypsin/EDTA	Sigma-Aldrich, St. Louis, MO, USA
Triton X-100	Sigma-Aldrich, St. Louis, MO, USA

4.2.2 Preparation of PAC-L605

Preparation of alloy L605 and PAC deposition was carried out as described in chapter 3.2.2, for PAC1-L605 (C-1, N-10, 500 V, t = 20 min) and PAC2-L605 (C-2, N-10, 1000 V, t = 10 min) surfaces respectively. Prior to all experiments, metallic samples (with or without PAC) were sterilized by washing 3x with 70% ethanol, acetylene, and PBS sequentially for 15 min each. Unless specified, two recipes of PAC (PAC1/PAC2) were investigated simultaneously to detect optimum biofunctionalization in cell culture and hemocompatibility assays.

4.2.3 TE coating for SDS-ELISA

Recombinant human tropoelastin (TE) was expressed and purified from an E.coli expression system [281]. The PAC-L605 and alloy L605 samples (0.8 x 0.8 cm) were incubated overnight with 250 µl of 50 µg/mL tropoelastin in phosphate buffered saline (PBS), at 4^{o}C, within a 24 well plate.

4.2.4 ELISA detection of TE

An enzyme-linked immunoabsorbent assay (ELISA), using an anti-elastin primary antibody was employed to detect tropoelastin bound on non-modified alloy L605 and PAC1-L605, with and without SDS treatment. The samples were placed into the wells of a 24-well plate. Tropoelastin was incubated with samples as described in section 4.2.3. Unbound tropoelastin was removed by aspiration and samples washed thrice with PBS. The samples were transferred to 5% SDS (w/v) in PBS and incubated at 90^{o}C for 10 min. Non SDS-treated samples were washed in PBS alone. Following SDS treatment, samples were returned to the 24-well plate and washed thrice with PBS. Non-specific binding was blocked with 3% (w/v) BSA in PBS for 1 hour at room temperature (RT). Following BSA blocking samples were incubated with the anti-elastin antibody BA-4 raised in mouse (1:2000) for 1 hour at RT [282]. The primary antibody was removed and samples washed 3x with PBS and incubated with anti-mouse IgG-

HRP conjugated secondary antibody raised in goat (1:5000) for 1 hour at RT. The secondary antibody was removed and samples washed three times with PBS. The samples were transferred to a new 24-well plate, ABTS solution (40 mM ABTS in 0.1 M NaOAc, 0.05 M NaH_2PO_4, pH 5, containing 0.01% (v/v) H_2O_2) was added and incubated at RT for 45 mins. The plates were agitated and 100 µl aliquots of the ABTS transferred to a 96-well plate, absorbance was read at 405 nm using a microplate reader (Biorad) [138]. Surfaces without tropoelastin were used as blank controls for both PAC-L605 and alloy L605.

4.2.5 Cell culture

Human coronary artery endothelial cells (HCAECs) were provided at the tissue culture lab, HRI. Endothelial cells (passages 2 to 5) were grown to 90% confluence in a humidified 37^{o}C incubator with 5% carbon dioxide. The medium was aspirated and cells washed twice with PBS. Cells were lifted from the surface by incubation with trypsin/EDTA (0.0025% (v/v) trypsin, 0.02% (v/v) EDTA) for 4 min at 37^{o}C, with gentle tapping to dislodge cells. Once cells were lifted, trypsin/EDTA was inhibited with the addition of mesoendothelium media (10 mL). The cell suspension was centrifuged for 5 min at 1500 rpm then cells resuspended and plated for growth in Mesoendo medium or counted for experimental work.

4.2.6 Cell attachment assay on metallic samples

Cell assays were performed in triplicate in tissue culture plastic (TCP), 24 well plates containing 0.6 x 0.6 cm samples of L605, PAC-L605 and PAC-L605-TE respectively (PAC1 recipe). The PAC-L605 with TE were incubated with TE (50µg/mL) in a volume of 0.25 mL overnight at 4^{o}C. Prior to cell seeding, wells were washed 3 times with PBS and blocked with heat denatured (80^{o}C, 10 min) BSA (10 mg/mL) for 30 min, then washed 3 times with PBS again. HCAECs were lifted as described in 4.2.5 and counted using a haemocytometer. The cell density was adjusted, 5 x 10^4 cells seeded into each well and left to attach for 1 hour at

37°C. Wells were washed 3 times with PBS and fixed in 3.7% (v/v) formaldehyde for 30 min. All samples were washed 3 times with PBS and stained with crystal violet (0.1% for 1 hour). After staining all samples were washed 3 times with RO water, the stain was solubilized with 10% (v/v) acetic acid, and absorbance determined with a spectrophotometric plate reader (BioRad) at 570 nm.

In parallel, cells were cultured on alloy L605 and alloy 316L SS for 1 hour cell attachment, for visualization with DAPI. Samples were washed 3 times with PBS and treated with 0.2 M glycine for 20 mins and 0.2% Triton X-100 for 10 min before staining nuclei with 0.15 µg/mL DAPI for 15 mins. Images from 5 random fields per sample were obtained with an Olympus IX70 inverted microscope using a filter set for excitation between 350-380 nm. Cell nuclei were counted using Image J [283].

4.2.7 Cell proliferation assay

Wells with L605, PAC-L605 and PAC-L605-TE (PAC1 recipe) were set up as described in section 4.2.6. HCAECs were seeded in 24-well plates at a density of $2x10^4$ or $5x10^4$ based on cell count as described in section 4.2.6, and left to proliferate for 3 or 5 days. Medium was changed on day 3. At each time point, cells were fixed with formaldehyde and quantified with crystal violet as described in section 4.2.6.

4.2.8 Immunofluoroscent detection of vWF and filamentous actin (F-actin)

Metallic samples with or without TE (50 µg/mL) were seeded with cells as described in section 4.2.7. For F-actin visualization 5 biomaterial surfaces were investigated: 1) PAC1 recipe 2) PAC2 recipe, 3) PAC1 recipe with tropoelastin, 4) PAC2 recipe with tropoelastin, 5) cobalt chromium bare alloy L605. After 5 days of culture, cells were washed thrice with PBS and fixed for 30 min in 3.7%-4% formaldehyde in PBS. Formaldehyde was aspirated, cells washed 3 times in PBS and subsequently treated with 0.2 M glycine for 20 min. The samples were

washed thrice in PBS and incubated with 0.2% (v/v) Triton X-100 for 10 min. The cells were blocked with 5% (w/v) BSA in PBS for 1 hour, incubated sequentially with human anti-vWF antibody (1:400) for 30 min. The primary antibody was removed, samples washed 3 times in PBS, and incubated with goat anti-rabbit IgG Fc (Alexa Fluor® 488) (1:90) for 1 hour. The secondary antibody was removed, cells stained with phalloidin-TRITC (0.1 µg/mL) in 3% BSA for 45 min, washed thrice with PBS and stained with 0.15 µg/mL of DAPI in PBS for 15 min. Samples were mounted onto glass slides with DAPI fluoroshield and coverslipped for imaging. The cells stained with phalloidin-TRITC and DAPI were merged and visualized first on all 5 biomaterials, followed by vWF (IgG Fc Alexa Fluor), phalloidin-TRITC and DAPI staining. Fluorescent staining uptake was imaged with an Olympus IX70 inverted microscope, using a mercury lamp. For DAPI visualization, an excitation between 350-380 nm, and emission of 470 nm was used. For Alexa Fluor 488 visualization, an excitation between 450-490 nm and emission of 525 nm was used. For phalloidin-TRITC visualization, an excitation between 557-560 nm and emission of 576 nm was used. Sequential imaging eliminated potential bleed-through fluroscence from other channels, allowing convergence of images to visualize all 3 stains merged.

4.2.9 Scanning Electron Microscopy

HCAECs were cultured for 2 days on L605, PAC-L605 and PAC-L605-TE as described in section 4.2.7 (optimum PAC recipe chosen after 4.2.8 results). Samples were washed thrice in PBS and fixed in 4% formaldehyde in 0.1 M phosphate buffer (PB) for half hour at RT. Cells were dehydrated in ascending grades of ethanol (from 30% (v/v) to 100 % (v/v)) before chemical drying with hexamethyldisilazine (HMDS). The samples were mounted to stubs using carbon tape, sputter coated with 20 nm gold and imaged with Zeiss Ultra field emission scanning electron microscope (FESEM).

4.2.10 Thrombogenicity analysis

4.2.10.1 Blood sampling

Whole blood was obtained from healthy, non-smoking, male volunteers with informed consent in accordance to the Declaration of Helsinki. Volunteers had not taken aspirin or any anticoagulant 2 weeks prior to donation. Blood was taken by a trained phlebotomist using a 21 G butterfly needle to prevent platelet activation and a 20 mL syringe. Donated blood was anti-coagulated with 0.5 U/mL heparin (180 units/mg). Approval of this work was granted by the University of Sydney, Human Research Ethics Committee (2012-2015). All experiments were conducted in triplicate samples at least thrice with different donor's blood.

4.2.10.2 Platelet rich plasma (PRP) isolation

Samples of L605, PAC-L605 and PAC-L605-TE (0.8 x 0.8 cm) were placed in a 24 well plate previously blocked with 3% BSA in PBS for 1 hour, at RT and washed thrice with PBS. Blood was anti-coagulated with 0.5 U/ml heparin and centrifuged for 15 min at 1000 rpm. The supernatant was removed and 250-500 µl was incubated with each sample for 60 min at 37^{o}C while rocking. Samples were processed for SEM as described in 4.2.9. An additional step was included during biological preparation of blood/platelet/fibrinogen surfaces for SEM. The surfaces were post fixed with 0.1 % OsO_4 in 0.1 M PB for 1 hour, prior to dehydration.

4.2.10.3 Ageing study on thrombogenicity

An ageing study was conducted on different samples, with PRP assay to analyse thrombogenicity over time. The samples were 1) 1-month old PAC-L605, 2) 1 month old PAC-L605 incubated with TE stored for 2 weeks at -20^{o}C, 3) 1 month old PAC-L605 incubated with TE stored overnight at 4^{o}C 4) bare alloy L605 (control). Samples were placed in a 24 well plate and incubated with PRP isolated as mentioned in 4.2.10.2 incubated at 37^{o}C for 60 min. Samples were processed for SEM as described in 4.2.10.2

4.2.10.4 Whole blood adhesion analysis

A 24 well plate was blocked with 3% BSA in PBS for 1 hour at room temperature and washed thrice with PBS. 0.8 x 0.8 samples of L605, 316L SS, PAC-L605 were incubated with 500 µl of heparinized whole blood (0.5 U/mL) for 60 mins at 37^{o}C, while rocking, to observe variation of hemocompatibility on different biomaterials. In parallel, 0.8 x 0.8 samples for L605 and PAC-L605 were similarly incubated with 500 µl of heparinized whole blood for a period of 30, 60, 90 mins at 37^{o}C to observe time variation effects on surface hemocompatibility. Samples were processed for SEM as described in 4.2.10.2

4.2.10.5 Modified Chandler loop

Coagulation under flow conditions were investigated using a modified chandler loop [105, 251, 252]. The sample dimensions for L605 biomaterial inserted to the model were calculated to achieve an area-to-volume ratio between 0.5-6 cm^2/mL to meet ISO10993-12 requirements. The corresponding blood sample volume per loop, for the finalized dimensions of the biomaterial were calculated according to the volume constraint $A/6 \leq V \leq 2A$ presented in Gaamangwe et al [252] (A is sample area, V is volume of blood). To implement the chandler loop model, a rotor was used to drive a turntable, and the rotor speed set at 34 rpm. The turn table had a holder attached vertically, approximately 60 mm from its centre to hold sample tube loops (Biochemistry, University of Sydney). The blood sample loops were made of medical grade Tygon silicon tubes (Internal diameter (ID) 6.35 mm, outer diameter (O.D) 7.93 mm). The length of the spliced sample tubes were 300 mm, with a 20 mm silicon connector (MasterFlex, ID 10 mm) used to hold the two ends of the medical grade tubing together, forming a loop. The wall shear rate for the model was previously defined by Gardner [284], and converted to wall shear stress by considering blood as a Newtonian fluid, seen in equation 4.1 [252].

$$\tau_W = \frac{2\pi R_0 \omega \mu}{15R} \quad 4.1$$

Where τ_w is wall shear stress, R_0 loop curvature radius, R tube internal radius, ω angular velocity in RPM, and μ is blood dynamic viscosity. Wall shear stress derived earlier was applied to our model, to assess shear stress on alloy L605 sample biomaterial, compared to shear stress on the tube wall.

The tubes were randomized and filled with the appropriate volume of heparinized whole blood. Heparin concentration of 0.5 U/mL was used (Anna Waterhouse, Dissertation 2011). The loops were placed on the sample holder and rotated at 34 rpm at 37ºC for 60 min. The blood, thrombus and metal from each loop were removed, the metal + any thrombus washed twice in PBS, blot dried for imaging and weighing. Initially, we assessed thrombogenicity between PAC-L605 recipe 1 (500 V), PAC recipe 2 (1000 V) and alloy L605 at 60 mins, 37ºC. Based on initial results, the next flow assay investigated thrombogenicity of 1 week old PAC, PAC with tropoelastin (overnight, 4ºC) and alloy L605. Flow assays were repeated with 5-month aged PAC-L605 vs. L605, to assess effects of ageing on thrombogenicity.

4.2.10.6 Surface fibrinogen deposition – Flow assay

Fibrinogen staining assay was done to visualize surface fibrin on biomaterials after flow assay in a chandler loop. A 24 well plate was blocked with 3% BSA/PBS for 1 hour at RT. The plate was washed thrice with PBS. A stock solution of fibrinogen was prepared (5 mg fibrinogen in 3.3 mL of 0.1 M $NaHCO_3$, pH 8.3 at RT), and gently agitated for 1 hour. Samples of PAC-L605 and L605 were removed from chandler loop after 1 hour flow assay at 37ºC, weighed and imaged. These samples were incubated in a 24 well plate with a volume of 250 µL fibrinogen-Alexa Fluor 488 (F-13191), per well, for 15 mins. Working solution was prepared

in distilled water (1:60 dilution). The solution was removed, washed once with PBS and the biomaterials in wells were incubated with DAPI (0.15 µg/mL) for 15 mins, without light exposure. The samples were imaged with an Olympus IX70 inverted microscope using a mercury lamp and a filter set for excitation between 500-524 nm.

4.2.11 Statistics

Statistical analysis was carried out as described in Chapter 2.2.15

4.3 Results

4.3.1 SDS resistant binding of TE to PAC

Tropoelastin (TE) was bound to PAC-L605 (500 V) and L605 surfaces to comparatively assess theory of covalent protein binding on modified surfaces for enhanced biomimicry; as seen previously on PAC-316LSS [105]. In the absence of TE, the background levels of absorbance were 0.012±0.009 on PAC-L605 control and 0.010±0.014 on alloy L605 respectively, figure 4.3. In the presence of TE without SDS treatment, both PAC-L605 and L605 had increased absorbance readings at 0.202±0.01 and 0.138±0.005 respectively, indicative of TE binding, figure 4.3. After SDS treatment, absorbance readings decreased to 0.142±0.011 for PAC-L605 (31.40% reduction) and 0.041±0.009 for L605 (70.04%). The PAC-L605 surfaces displayed covalent binding by retaining 68.6% of the bound tropoelastin after SDS detergent washing, figure 4.3.

4.3.2 HCAEC count on alloy L605 and alloy 316 L SS

Cell attachment on alloys L605 and 316LSS were conducted in parallel to HCAEC attachment visualized with DAPI staining for Image J quantification. Five random fields of the imaged surfaces were quantified. Within 1 hour the cell count on alloy L605 surfaces was 269.1±28.53 and on alloy 316LSS was 299.4±40.36, the values were not significantly different, figure 4.4. DAPI staining showed that cells homogenously covered a large proportion of both 316LSS and L605 surfaces.

4.3.3 HCAEC attachment on biomaterials

To comparatively determine cell adhesive and proliferative capacity of L605, PAC-L605 and PAC-L605-TE respectively with HCAECs at passage 3, cell attachment and proliferation at 1 hour, 3 days and 5 days respectively were quantified by crystal violet staining. The crystal violet assay has been previously validated for ECs (Anna Waterhouse, Dissertation 2011).

Human coronary artery endothelial cell (HCAEC) attachment on L605, PAC-L605 and PAC-L605-TE were quantified by crystal violet staining after BSA blocking relative to the positive control tissue culture plastic (TCP). After 60 min, the absorbances for TCP vs. L605, PAC-L605 and PAC+TE at 507 nm were 0.215±0.01, 0.111±0.009, 0.113±0.009 and 0.126±0.015 respectively, figure 4.5. Cell culture density was not significantly different between the biomaterials, although significantly different from positive control tissue culture plastic.

4.3.4 HCAEC proliferation on biomaterials

HCAEC proliferation at day 3 and day 5 were quantified on L605, PAC-L605, and PAC-L605-TE surfaces, relative to positive control TCP. Results presented in figure 4.6A and graphed in 4.6B are relative to cell growth on biomaterials of interest only (positive control TCP, was higher and not shown). At 3 days of cell culture, the absorbances for TCP vs. L605, PAC-L605 and PAC+TE at 507 nm were 0.272±0.034, 0.126±0.012, 0.135±0.013, and 0.119±0.009 respectively (figures 4.6A and B). By day 5 of cell culture, the absorbance for TCP vs. L605, PAC-L605 and PAC+TE at 507 nm were 0.535±0.017, 0.194±0.014, 0.271±0.016 and 0.304±0.048 respectively. Similar to 1 hour attachment assays in 4.3.3, the growth of cells were significantly higher for TCP (positive control), and not significant among the biomaterials at 3 or 5 day culture (figures 4.6A, B).

4.3.5 Visualizing HCAEC morphology

4.3.5.1 F-actin distribution in HCAECs on biomaterial: DAPI/Phalloidin-TRITC

Filamentous actin distribution and cell nuclei of HCAECs were visualized first with inverted fluorescent microscopy on 5 different biomaterial surfaces at day 5 proliferation. Autofluorescence of PAC surface did not interfere with the fluorescent dyes, as seen in figure 4.7. At 40x magnification, homogenous distribution of F-actin was observed on PAC2 surfaces compared to PAC1, similar trends were also observed for PAC2 surfaces with TE. PAC2 recipe

was chosen for further cell experiments, and termed PAC-L605 throughout the chapter for interaction with cells.

4.3.5.2 Fluorescence microscopy detection of f-actin, vWF and nuclei: triple stain

Distribution of f-actin, vWF and cell nuclei (triple stain) were visualized for HCAECs on PAC-L605 and L605. At 10x magnification, cells on both surfaces appeared well spread and flattened, with vWF visualized in cell cytoplasm as an endothelial cell marker, with well-defined cell alignment of cytoskeleton on both surfaces, figure 4.8A. At higher magnification (40x), images indicated a more confluent, homogenous, distribution of the actin cytoskeleton for endothelial phenotypes on PAC-L605 compared to alloy L605, figure 4.8B. There was no difference in the vWF staining uptake between cells cultured on PAC-L605 and bare alloy L605, at 40x magnification, figure 4.8B.

4.3.5.3 SEM detection of cell morphology

Scanning electron microscopy (SEM) images of HCAECs were cultured and fixed after 2 days. The morphology of cells on PAC+TE surfaces were confluent and spread out overall compared to PAC-L605 and alloy L605. Similarly, HCAECs on PAC+TE surfaces also had the least spindle projections compared to PAC-L605 and L605. SEM allowed higher magnification for detailed morphology of cells on biomaterial surfaces, figure 4.8C.

4.3.6 Detection of alloy L605 and PAC-L605 thrombogenicity – static assays

4.3.6.1 Platelet rich plasma (PRP) assay

Static blood assays with platelet rich plasma, isolated from heparinized whole blood were incubated for 1 hour at 37^{o}C and observed with SEM, on PAC-L605, PAC-L605-TE compared to L605, Figure 4.9. The presence of protein in platelet rich plasma prevents platelets and fibrin

adherence to the modified, hydrophilic PAC-L605 and PAC-L605-TE surfaces (A, B), while fibrin and platelets adhered to alloy L605 cobalt chromium surface (C) (1.27 Kx Magnification)

4.3.6.2 Ageing study with platelet rich plasma (PRP)

The ageing study was conducted to assess variation of surface hemocompatibility on modified surfaces with or without protein, over time. The SEM images post PRP assay (60 mins at 37^{o}C) showed hemocompatibility sustained on PAC-L605-TE surfaces, incubated with proteins for 2 weeks at -20^{o}C, figure 4.10 A. Similar hemocompatibility was observed on PAC-L605-TE surfaces, incubated with protein overnight at 4^{o}C, figure 4.10 B. Likewise hemocompatibility is retained on PAC-L605 surfaces stored airtight for 1 month, figure 4.10 C. As before, surface platelet adhesion and fibrin clot formation is observed on alloy L605 bare metal surfaces, figure 4.10 D.

4.3.6.3 Whole blood adhesion assay

Whole blood adhesion compared PAC-L605, L605 and 316L SS surfaces at 60 mins to show superior hemocompatibility on plasma modified surfaces compared to thrombogenicity of both alloy L605 and 316LSS surfaces, figure 4.11 A. Whole blood adhesion assays on PAC-L605 vs. L605 at 30, 60, 90 min show comparatively lower thrombogenicity on the plasma modified surfaces at each time point, figure 4.11 B. Representative SEM images for thrombogenicity at 30, 60, 90 min time points, are seen in figure 4.11 C. For optimum thrombogenicity and blood flow assays, the 60 min time point was chosen.

4.3.7 Detection of alloy L605 and PAC-L605 thrombogenicity – Flow assays

4.3.7.1 Modified chandler loop optimization

Sample dimensions for alloy L605 and PAC-L605 surfaces were optimized as 1.33 cm^2 (area). To meet the ISO requirements, we used a blood volume range utilized by other investigators [252], the volume constraint was finalized at 2.5 mL/cm^2 for flow assays. The wall shear rate

for the model was previously defined by Gardner and Gaamangwe et al [252, 284]. We showed shear rate on sample surface is twice the shear rate on wall (equation 4.1), schematically depicted on figure 4.12. The samples were aligned perpendicular to the direction of flow. We used a heparin concentration of 0.5 U/mL previously optimized for PAC-316LSS flow assays (Anna Waterhouse, Dissertation 2011).

4.3.7.2 Comparative thrombus formation for PAC-L605 vs L605 surfaces

Thrombus formation at a time course of 60 min was investigated with a modified chandler loop flow assay, at 37^{o}C. Initially, two PAC-L605 recipes [PAC-1 (500 V) and PAC-2 (1000 V)] were compared with alloy L605, lowered clot formation was observed for PAC-1 compared to PAC-2 and L605 surfaces; 2.5±1.1 mg, 8.63±2.5 mg and 22.2±11.4 mg respectively ($p = 0.06$, not significant), figure 4.13 A. Flow assays were repeated with PAC-1 recipe (referred to as PAC-L605, in reference to blood work henceforth) vs. PAC-L605-TE vs. L605, 1 week post modification. Significantly lowered thrombogenicity was observed with PAC-L605 and PAC-L605-TE compared to L605; 2.26±1.0 mg, 3.56±3.6 mg and 10.33±3.3 mg respectively ($p=0.005$), figure 4.13B. Comparative flow assays were repeated with PAC-L605 vs. L605 surfaces, five months post modification, hemocompatibility was retained with aging, PAC-L605 surfaces had lower clot formation compared to the bare metal alloy; 7.16±3.5 mg and 25.16±6.66 mg respectively ($p=0.02$), figure 4.13C.

4.3.7.3 Surface fibrinogen deposition for PAC-L605 vs L605 surfaces.

The amount of surface fibrinogen was visualized for n=3 samples each after modified chandler loop flow assay, on alloy L605 and PAC-L605 surfaces. The L605 surfaces had predominant fibrinogen staining uptake compared to the modified PAC-L605 surfaces, after 60 min. Surface fibrin clot area was quantified with image pro premier (Media Cybernetics, USA) for 5 different areas on n=3 samples each. The PAC-L605 surfaces had significantly low fibrin area,

481.40±263.92 μm^2 compared to bare L605 alloy surfaces 1451.82±867.83 μm^2, figure 4.14. Results are in correlation to clot weights of the 2 surfaces after 60 min flow assay (seen in 4.3.7.2).

Figure 4.3

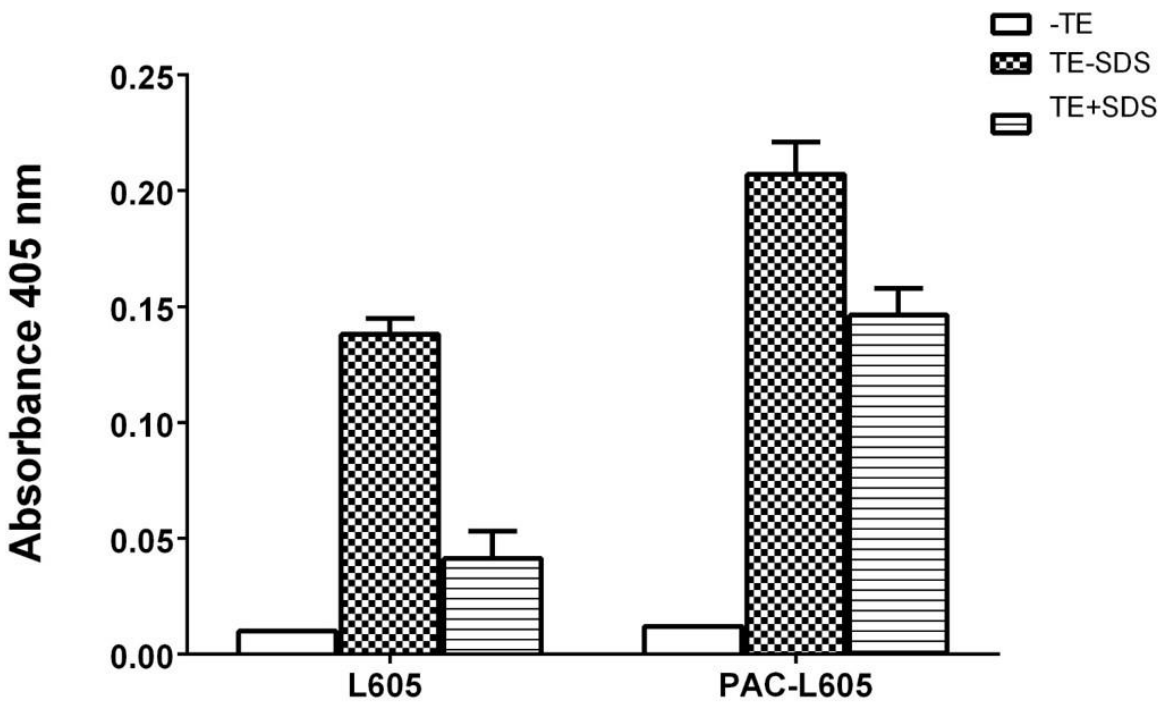

Enzyme Linked Immunoabsorbent assay (ELISA) with anti-elastin antibody to detect covalent binding capacity of tropoelastin to PAC-L605 surfaces compared to L605. The TE-SDS samples (checked) are indicative of those not subjected to SDS detergent treatment, whereas TE+SDS samples (stripes) indicate surfaces subject to SDS detergent treatment. The blanks are negative controls (no TE).

Figure 4.4

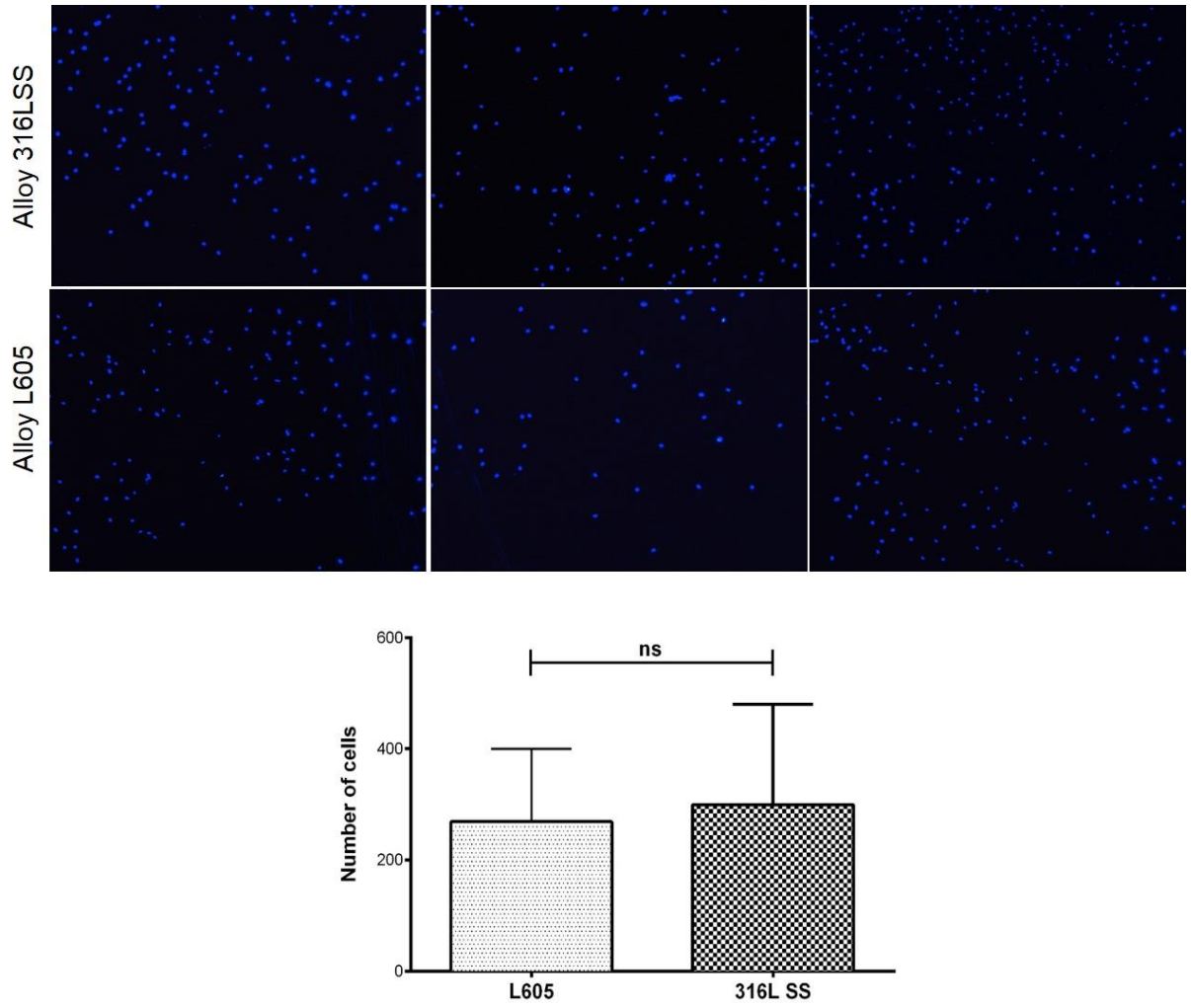

Human coronary artery endothelial cell (HCAEC) count, visualized with DAPI after 1 hour attachment on alloy L605 and alloy 316L SS surfaces, and quantified with Image J. Cell attachment at 1 hour is not significantly different between the two material alloys of interest.

Figure 4.5

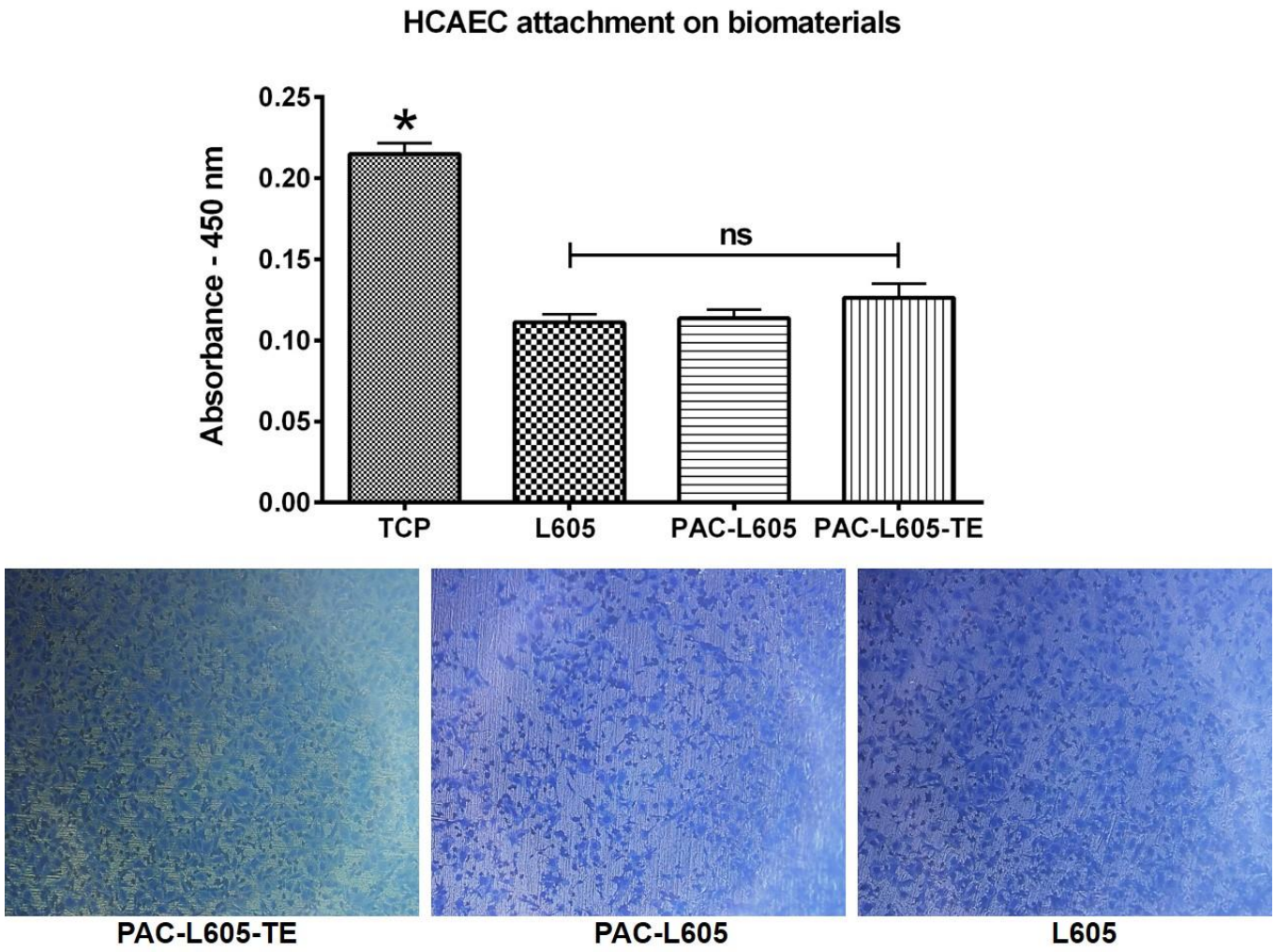

HCAEC attachment (1 hour) quantified and visualized with crystal violet absorbance after 1 hour at 37ºC on PAC-L605-TE, PAC-L605, and cobalt chromium alloy L605 surfaces. Representative inverted microscopy images of crystal violet stained cells on biomaterials to visualize variability of surface cell attachment.

Figure 4.6 A

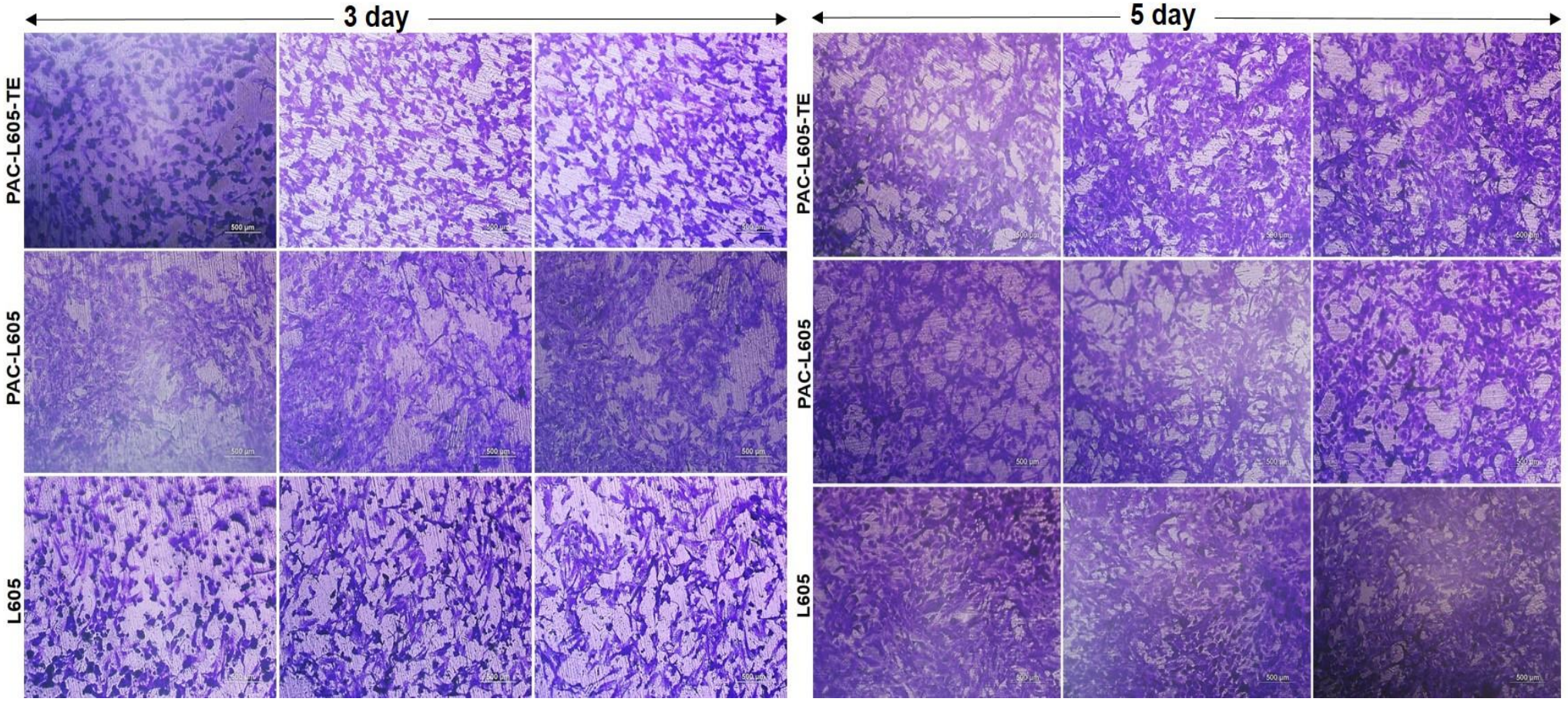

A) Human coronary artery endothelial cells (HCAECs) cultured on PAC-L605-TE, PAC-L605 and cobalt chromium alloy L605 surfaces, visualized with crystal violet after 3 days and 5 days respectively (10x magnification, scale bar 500 µm, Olympus inverted microscope). Absorbance quantified next in figure 4.6B

Figure 4.6 B

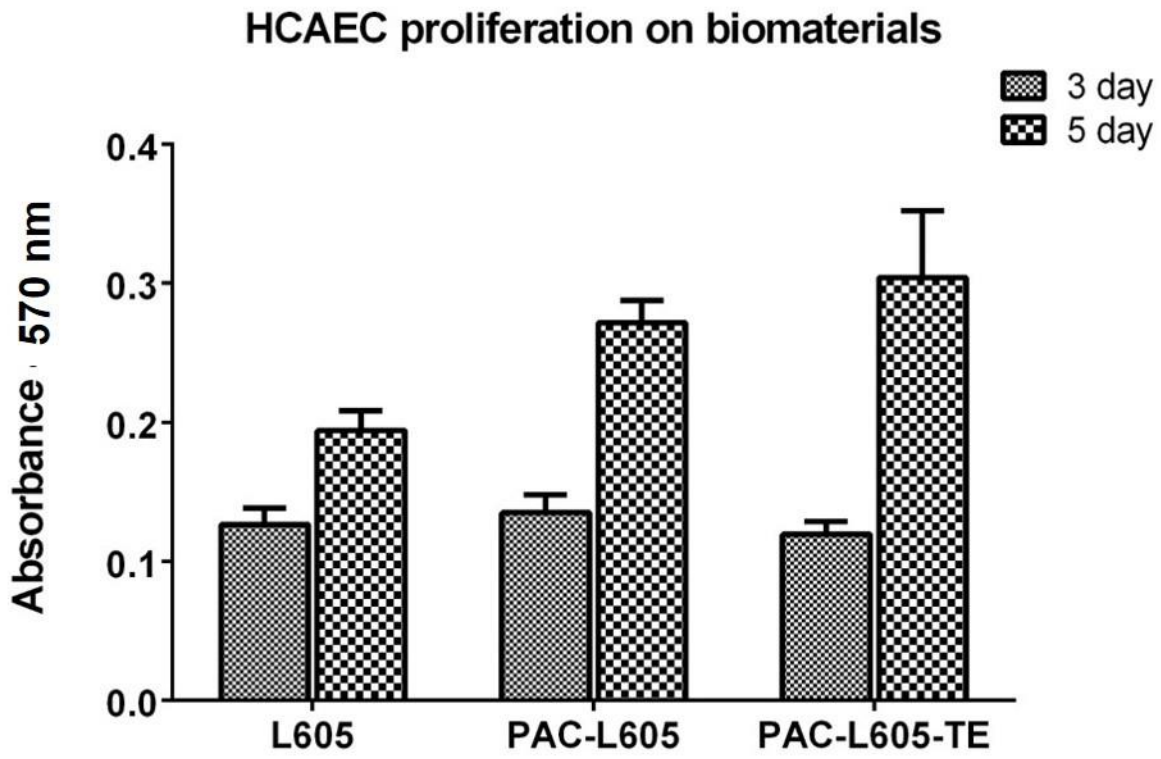

B) Absorbance of crystal violet stained biomaterial surfaces visualized in figure 4.6A above, quantified for L605, PAC-L605 and PAC-L605-TE respectively. The density of cells on surface increased progressively from 3-5 days. The results were not significantly different among the biomaterial surfaces at 3 days or 5 days.

Figure 4.7

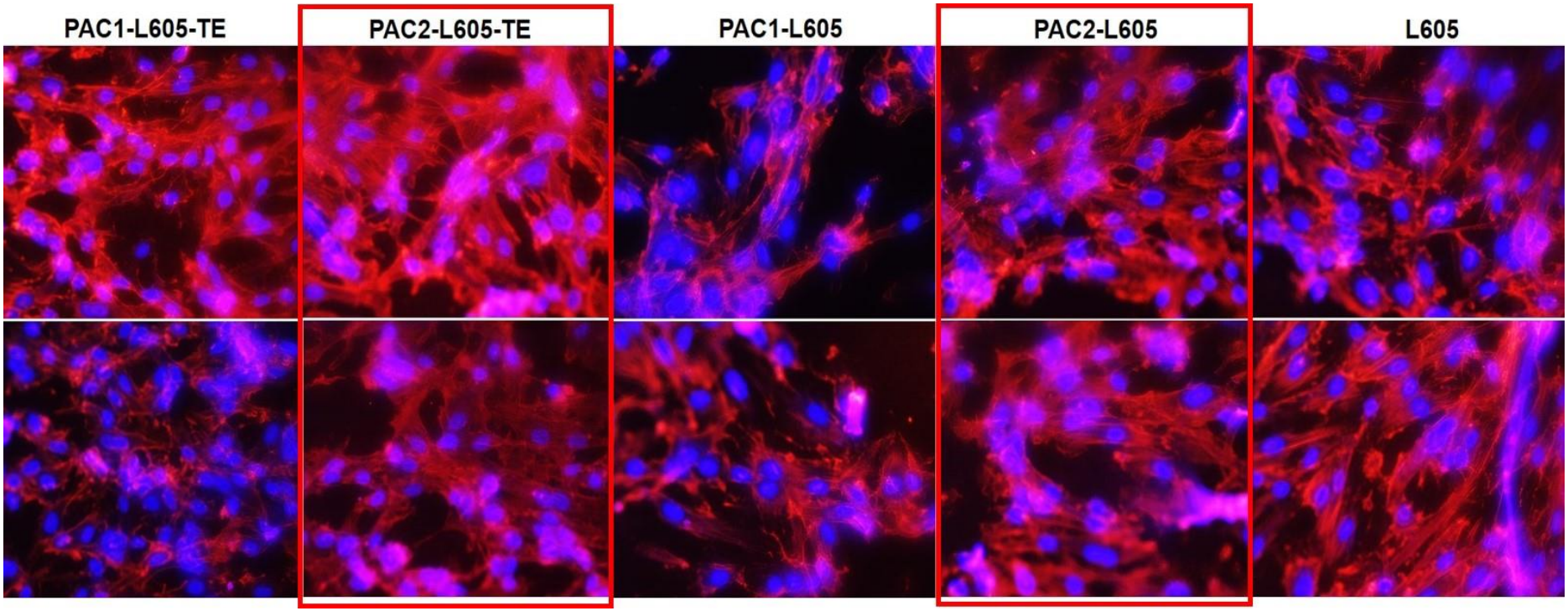

Filamentous actin (F-actin) on biomaterials were identified and visualized with phalloidin-TRITC at 40x magnification (inverted fluorescent microscope). HCAECs were cultured for 5 days on PAC 1 and PAC 2 recipe surfaces with or without tropoelastin, and on bare cobalt chromium alloy L605. F-actin were more homogenously spread on PAC2 surfaces compared to PAC1 (highlighted in red, with and without tropoelastin) and chosen for further experiments in cell culture.

Figure 4.8A

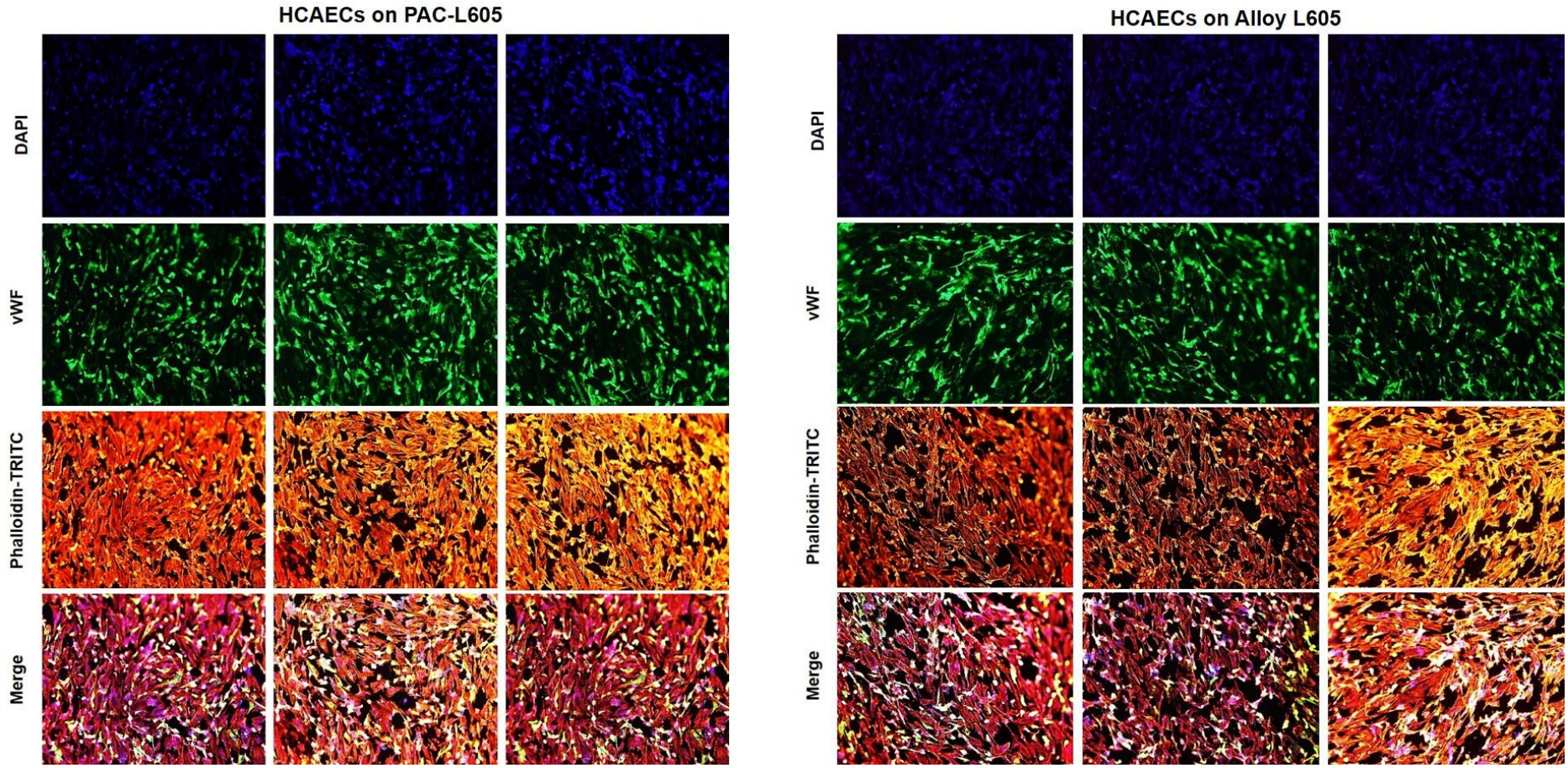

Triple stain with DAPI, vWF and Phalloidin-TRITC (merged in the final panel) to detect the nuclei, Weibel-Palade bodies and cytoskeleton respectively of HCAECs at day 5 proliferation on PAC-L605 and L605 surfaces. By day 5, at 10x magnification there was no visible difference on cell growth between the two surfaces (Olympus inverted fluorescence microscope).

Figure 4.8B

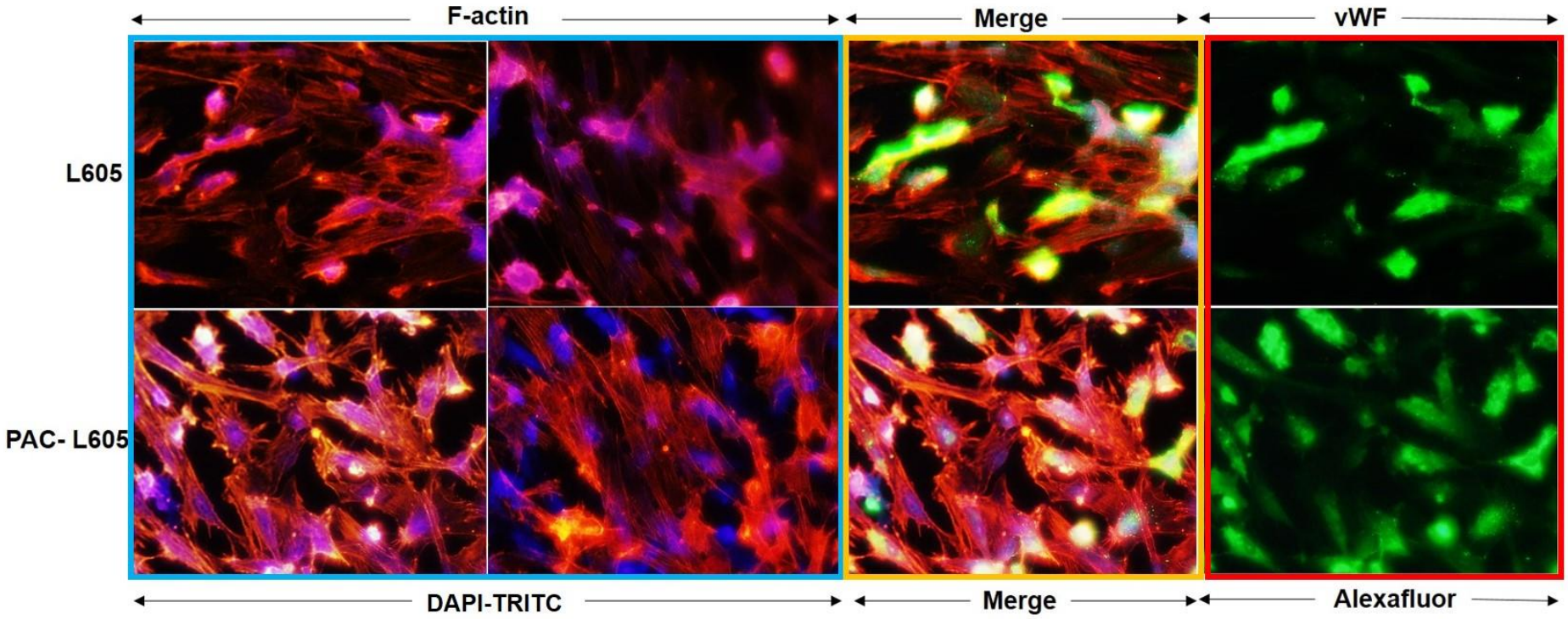

Filamentous actin visualized on PAC-L605 and L605 surfaces at high magnification (40x) with phalloidin-TRITC and DAPI after 5 day culture (blue box). Well defined f-actin cytoskeleton observed on PAC-L605 surfaces compared to alloy L605. Merged triple immunofluoroscent stain (yellow box). There was no visible variation to the morphology of vWF in Weibel-Palade bodies, visualized on the 2 surfaces with Alexafluor 488 (red box). Images were visualized at 40x magnification, inverted fluorescence microscope.

Figure 4.8C

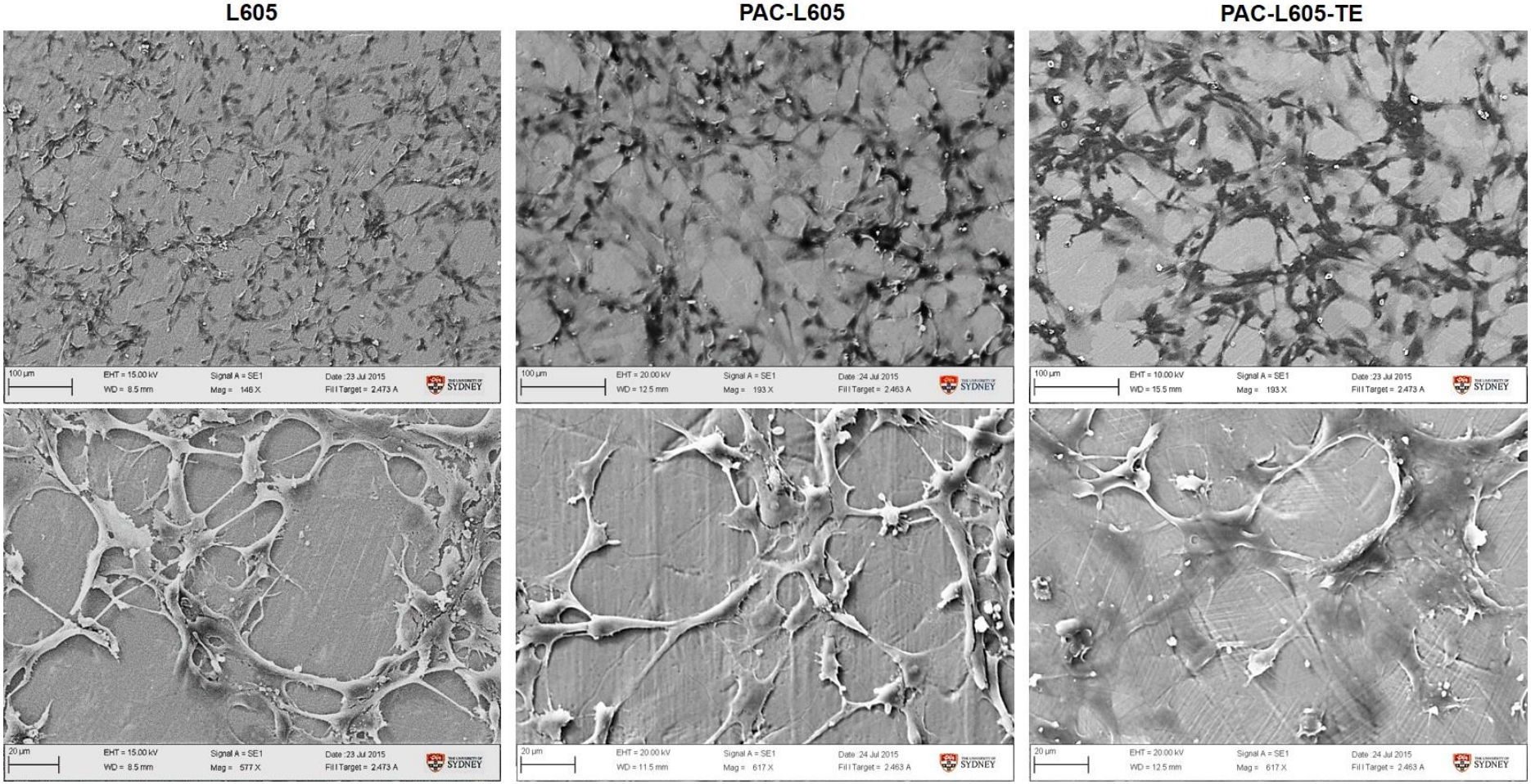

HCAECs on alloy L605 and PAC-L605 indicate more spindle projections compared to PAC+TE surfaces (ECM protein). PAC+TE surfaces also had more confluent HCAEC growth with better surface attachment (FESEM: top panel 140x/190x magnification, second panel 500x/600x magnification).

Figure 4.9

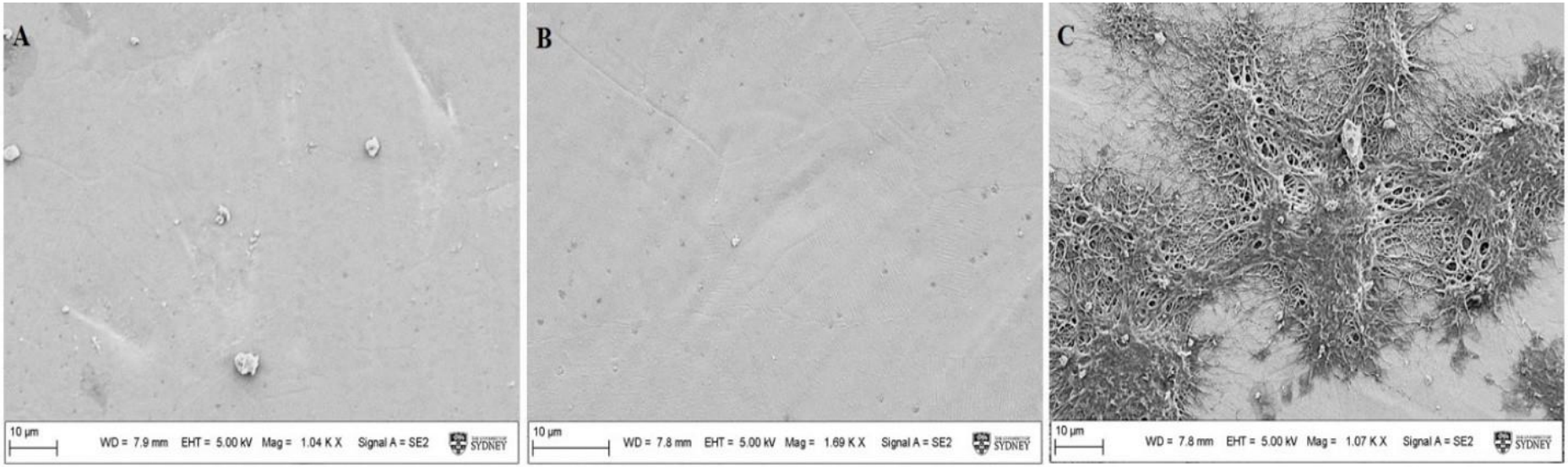

Platelet rich plasma (PRP) assay (37^{o}C, 60 mins), SEM images: Presence of protein in platelet rich plasma prevents platelets and fibrins adhering to the modified hydrophilic PAC-L605 and PAC-L605-TE surfaces (A, B). Fibrin and platelets adhere to alloy L605 bare cobalt chromium surface (C). Images were acquired with FESEM, 1.2 K magnification.

Figure 4.10

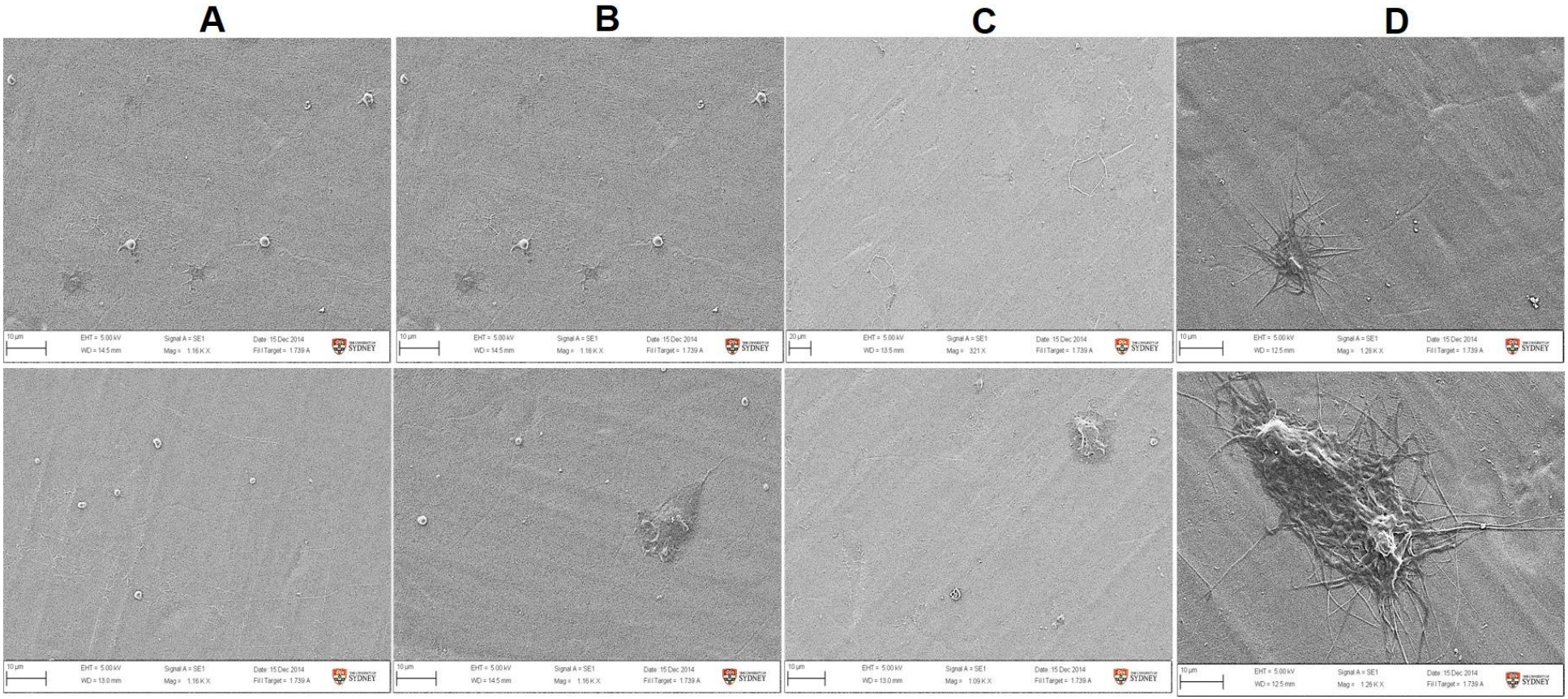

Ageing study with platelet rich plasma (PRP) assay, 60 mins, 37^{o}C; Sustained hemocompatibility seen on A) PAC-L605-TE surfaces incubated for 2 weeks at -20^{o}C, B) PAC-L605-TE surfaces incubated overnight at 4^{o}C, C) PAC-L605 surfaces stored airtight for 1 month, and surface platelet/fibrin clot deposition on alloy L605 bare metal surfaces (Magnification 1.08 K x).

Figure 4.11

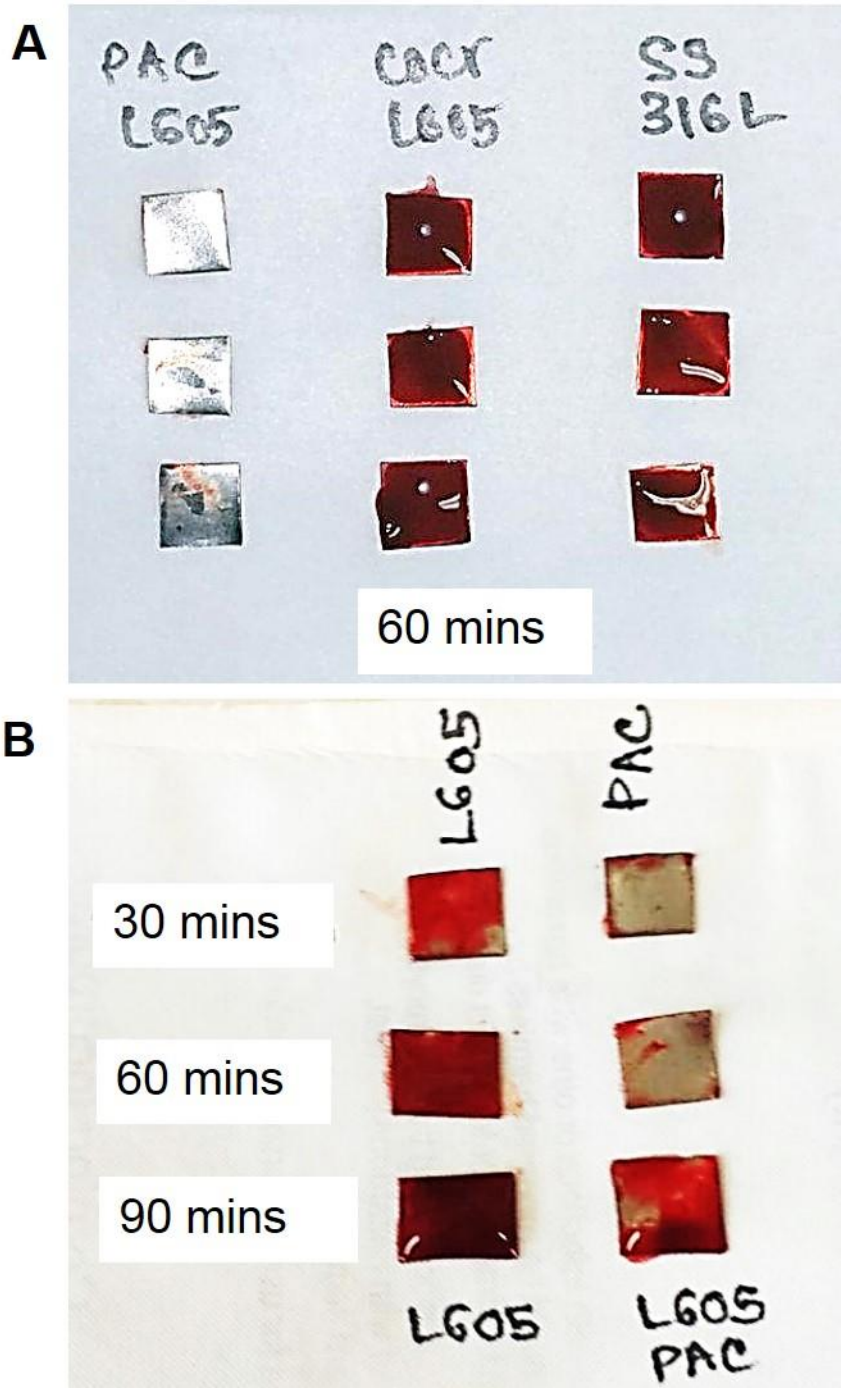

Static assay: whole blood adhesion comparing A) PAC-L605 vs. L605 and 316LSS at 60 mins, 37^{o}C. PAC shows superior hemocompatibility compared to both bare metal alloys. B) Comparing L605 vs. PAC-L605 at 30, 60, 90 mins show comparatively lower thrombogenicity at each time point for PAC.

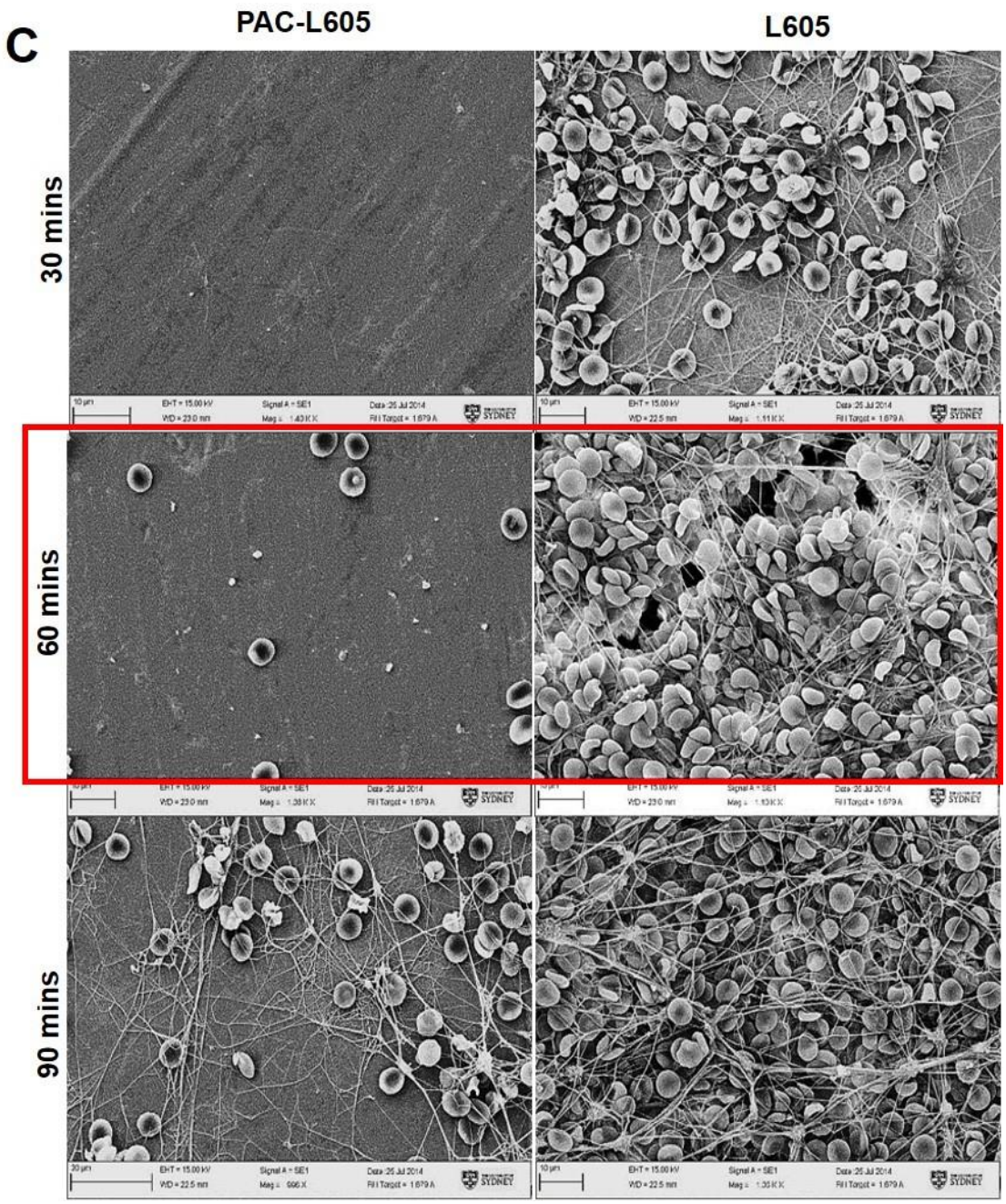

Static assay: C) SEM representation of PAC-L605 vs. L605 surfaces at 30, 60, and 90 mins after whole blood adhesion. Modified surfaces show hemocompatibility at all 3 time points compared to the bare metal alloy. For optimum thrombogenicity 60 min time point (red highlight) was chosen for assays.

Figure 4.12

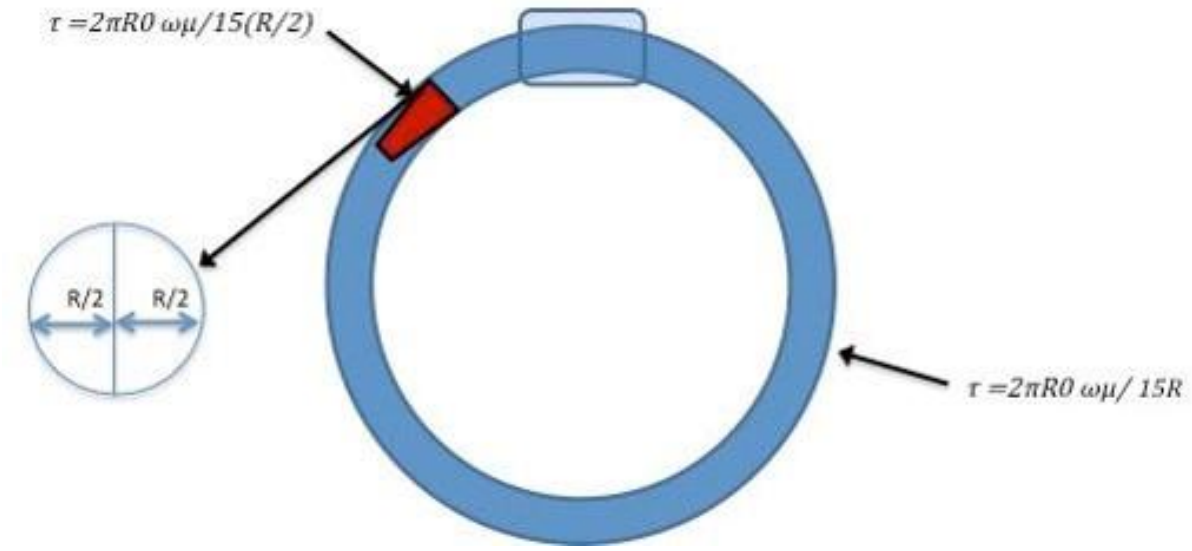

Representation of the rotating loop with biomaterial immobilized on the wall of the medical tubing. Since material is immobilized at the radius of tube, the shear rate on sample surface will be twice the shear rate present on medical tubing for our model, as theorized in Gaamangwe et al [252].

Figure 4.13 A

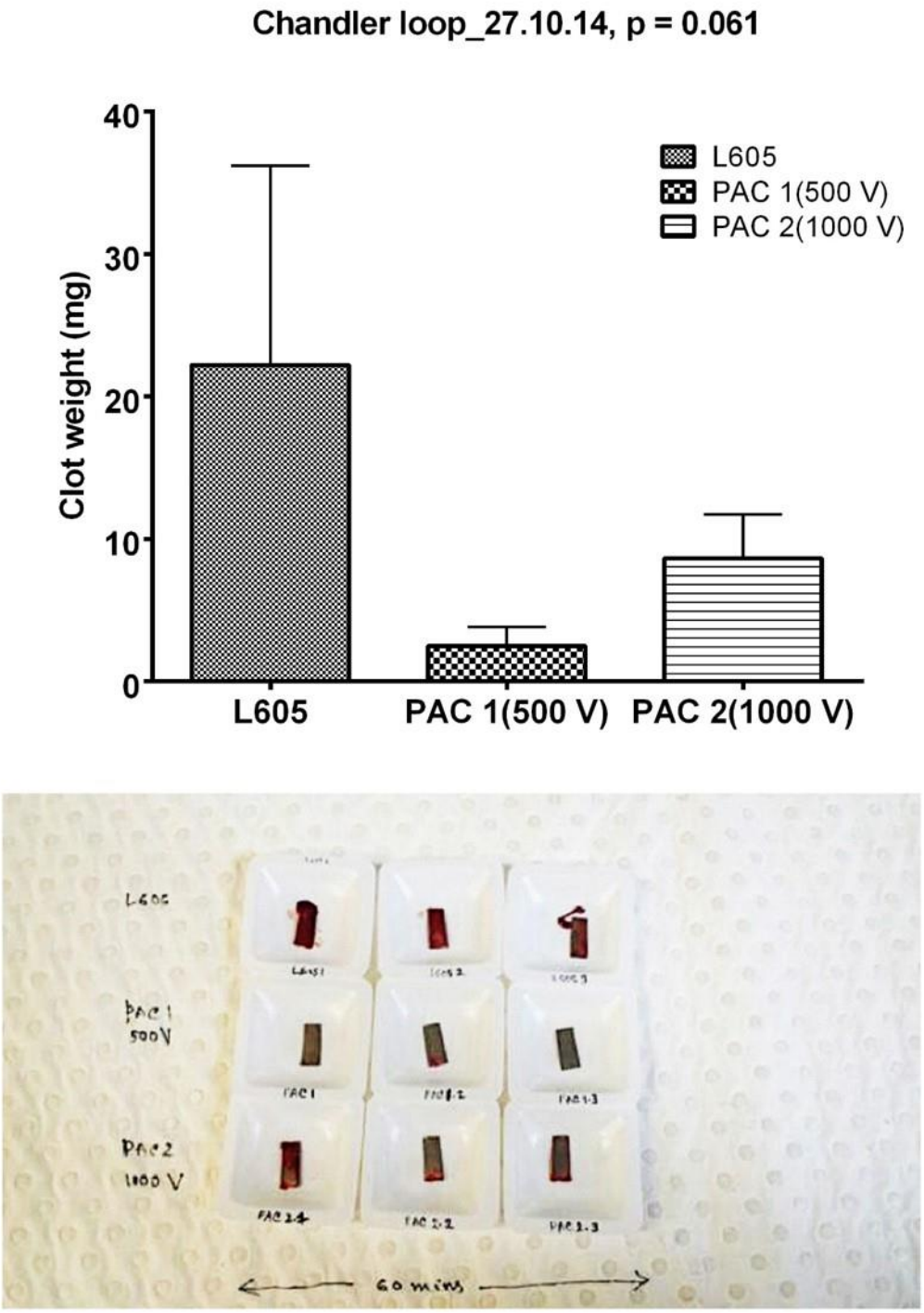

Flow assays for thrombogenicity, modified chandler loop 60 mins, 37ºC: A) Clot formation lower for PAC-1 recipe compared to PAC-2 and alloy L605 (p=0.06, ns).

Figure 4.13 B

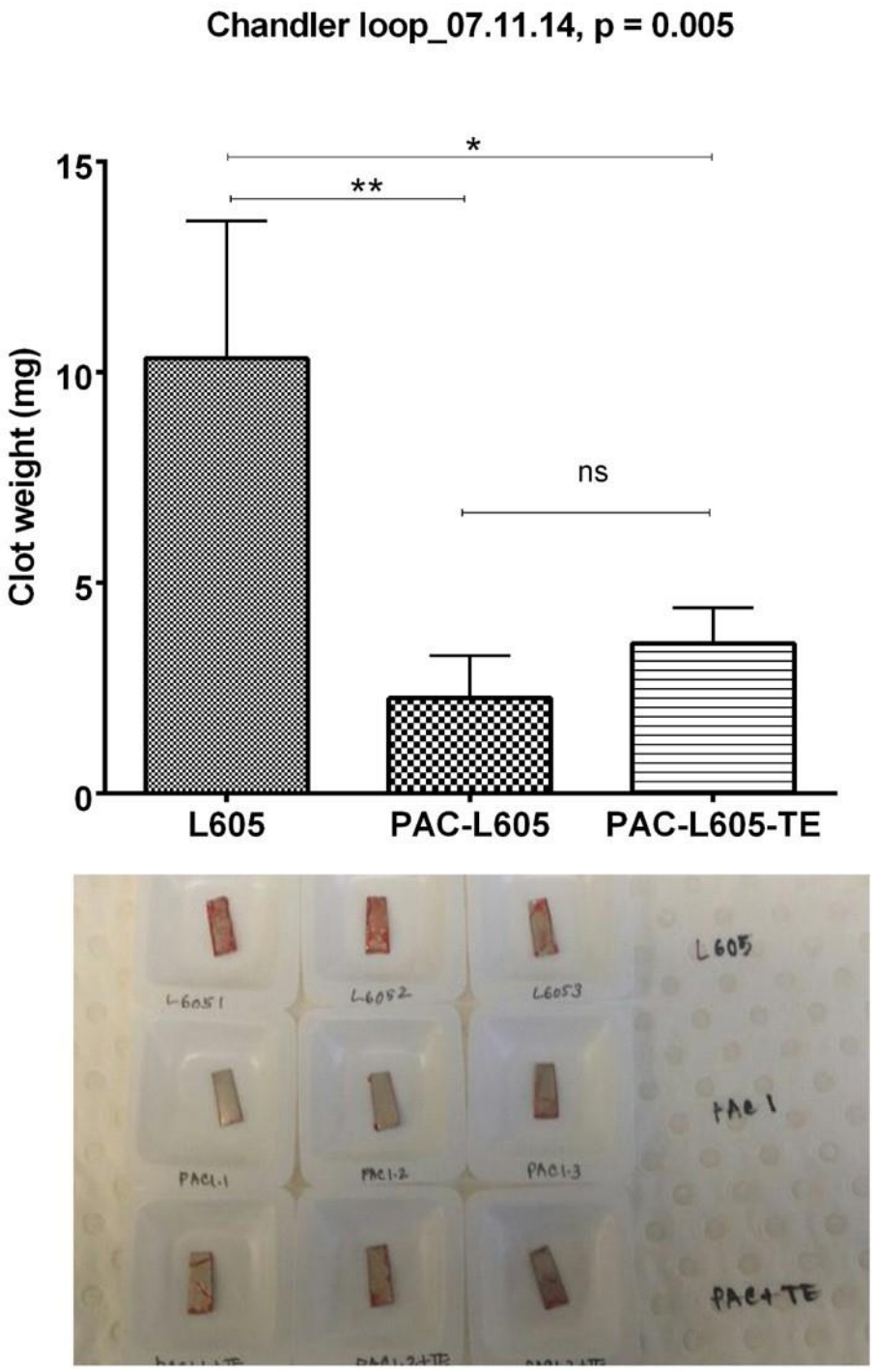

After 1 week, clot formation was significantly lower for PAC-L605 and PAC-L605-TE (tropoelastin incubated at 4^{o}C, overnight) surfaces compared to L605 (p=0.005).

Figure 4.13 C

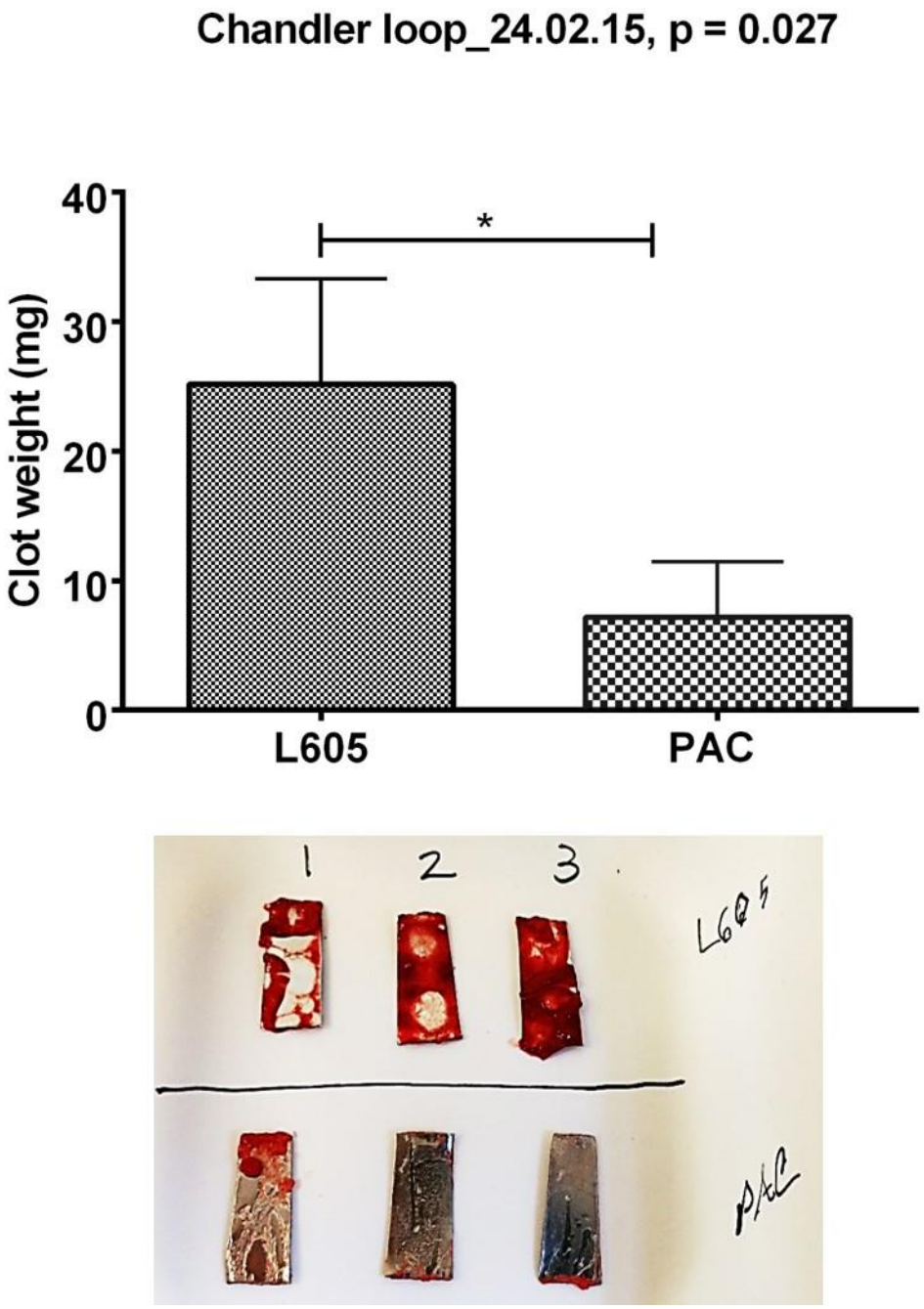

After 5 months clot formation still significantly lower for PAC-L605 compared to L605 (p=0.02); hemocompatibility is retained.

Figure 4.14

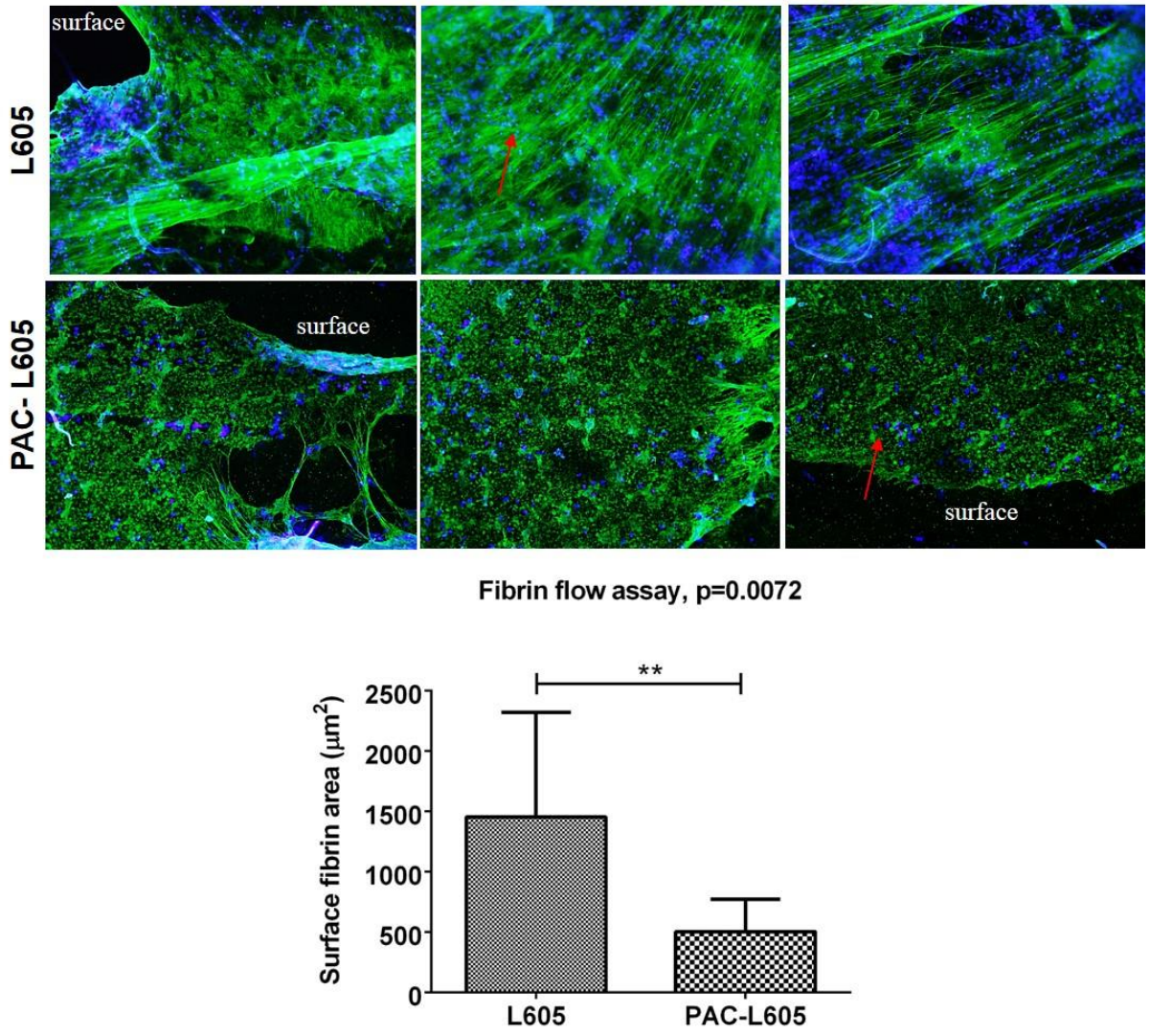

Surface fibrinogen clot deposition visualized with fibrinogen Alexa Fluor 488 and DAPI, on alloy L605 and PAC-L605 samples, after 60 min flow assay at 37ºC. Fibrin clot deposition (green) is indicated with red arrows, nuclei stained with DAPI is seen in blue. The scale bar of the images is 200 µm (10 x magnification). Surface fibrin area was calculated with image pro premier (Media Cybernetics, USA) on 5 different areas for n=3 samples each for L605 and PAC-L605.

4.4 Discussion

Biofunctionalization of PAC-L605 surface was comparatively assessed with alloy L605 bare material, *in vitro*. Surface modifications via proprietary plasma technology confer specific traits including; covalent attachment of a protein candidate of interest, improved hemocompatibility and assisted cell attachment/proliferation *in vitro*. Testing biofunctionalization of materials is crucial prior to *in vivo* applications for anticipated biointegration. Thrombogenicity of biomaterials *in vivo* has proven to be complex and fatal. In this chapter, biocompatibility of stent coatings were assessed under ISO10993-12 standards, in the lab prior to intended translation *in vivo*.

4.4.1 Covalent binding capacity of a plasma modified biomaterial

4.4.1.1 ELISA

Covalent binding of bioactive protein molecules is required for persistent biomimicry of a PAC surface. We demonstrated the covalent attachment of a protein to a modified surface via SDS washing and ELISA treatment. Sodium dodecyl sulfate (SDS) is commonly used as a research tool in protein biochemistry [285, 286]; the compound works by disrupting non-covalent bonds in the proteins, denaturing them and causing molecules to lose their conformation or native shape. The detergent wash is a valid indicator to assess covalent binding capacity of a biomaterial, with a surface bound protein of interest. The presence of TE before and after SDS-wash was detected with a monoclonal antibody, BA-4 anti-elastin, and a secondary HRP conjugated antibody in an ELISA. The BA-4 monoclonal antibody is specific to the valine-glycine-valine-alanine-proline-glycine (VGVAPG) repeating sequence in elastin and tropoelastin molecules, recognizing sequence regardless of protein conformation [287]; therefore suited for protein detection on biomaterials. The negative control showed low levels of absorbance. Higher absorbance was observed on PAC surfaces after SDS washes, compared to bare alloy L605, indicating covalent surface attachment on PAC-L605 (figure 4.3).

The covalent binding capacity of PAC surfaces, is due to the presence of surface free radicals on PAC, investigated in depth with PAC-316LSS [103] and characterized with PAC-L605, in chapter 3. The reservoir of free radicals migrate through the PAC interface, binding with the N-terminal region of proteins via a variety of amino acids [276]. Previously with alloy 316LSS a surface thickness of 200 nm was utilized (Anna Waterhouse, Dissertation 2011). In this study, in contrast, a 20 nm surface coating and different PAC recipe was incorporated. The difference in surface polymer thickness may account for the lower absorbance values observed at 450 nm (OD 0.15-0.20), compared to previous PAC-316LSS surfaces with higher absorbances in the range of OD 0.4-0.5 (Anna Waterhouse, Dissertation 2011). Initial investigations on covalent binding assessment of plasma technology [145], showed a full monolayer of tropoelastin achieved approximately at 72 nm, for a correlating absorbance of OD 0.3-0.5 (450 nm), also in support of the present observation [145]. The 20 nm PAC-L605 coating used throughout this study, shows potential to bind a surface protein, although for applications on a cobalt chromium stent surface (alloy L605), it would be ideal to trial various PAC surface thicknesses, ranging from 20 nm-200 nm, prior to translational studies.

4.4.2 Cell attachment and proliferation on biomaterials

Initially we investigated the interaction of endothelial cells on two biomaterials, alloy L605 and alloy 316LSS, prior to surface modification. The attachment of passage 3 HCAECs at 37^{o}C was visualized with DAPI, and cell nuclei counted with Image J software. Similar cell attachment was detected on the two material surfaces. Although largely spread-out, both surfaces support cell attachment, as visualized, and quantified after 1 hour of incubation (figure 4.4).

4.4.2.1 Tropoelastin assists EC attachment and proliferation

We had previously established tropoelastin (ECM protein) to support human umbilical vein endothelial cell (HUVEC) attachment and proliferation *in vitro* on PAC-316LSS surfaces [105, 138]. Based on similar principles and methods, we investigated the effect of tropoelastin on PAC-L605, for *in vitro* HCAEC attachment and proliferation. Crystal violet staining, a well-established methodology [288], was used to visualize and quantify EC attachment and proliferation, on PAC-L605-TE, PAC-L605 and L605 surfaces. The attachment of EC visualized with crystal violet, was established to linearly correlate with the number of cells present on a surface. Using crystal violet we observed similar cell attachment for PAC-L605 and L605 surfaces (figure 4.5), increased cell proliferation was observed for PAC-TE surfaces at 3/5 days, although values were not significantly different (figure 4.6 A, B).

4.4.2.2 Cell proliferation and actin cytoskeleton in endothelial cell phenotypes

Cells are capable of mechanosensing topography of a biomaterial for effective orientation and homogenous surface proliferation [225]. Studies reveal a preference of cell adherence to randomly organized surfaces within µm ranges of roughness to facilitate cellular anchorage and growth [289]. The interaction between modified biomaterials and biological elements are dictated by two phases at the material interface. The cell-biomaterial interaction is optimized via surface micro/nanofabrication to create biomimetic microsystems [290], that aid tissue repair after injury during medical device implantation [289].

In the present study, we investigated two different PAC recipes with/without tropoelastin to visualize cellular anchorage and cell spreading in HCAECs cultured for 5 days, via phalloidin TRITC (f-actin marker) and DAPI (nuclei) (figure 4.7). In total 5 types of biomaterial surfaces were investigated at high magnification (40x) (figure 4.7). Based on cell-biomaterial surface

interactions, PAC 2 surfaces favoured improved cellular anchorage, and were selected for further cell proliferation studies. The final response of cells to biomaterial topography is reflected in the organization of the actin cytoskeleton, observed with f-actin specific immunostaining, after proliferation. Actin cytoskeleton provides a strong, dynamic intracellular scaffold to organize integral membrane proteins within the cell's interior, respond to environmental cues, and assist proliferation [289] .

To establish cell support and culture exclusively between PAC-L605 and L605, multiple immunolabelling or triple staining was used. At 10x magnification, by day 5, cells showed equal expression for vWF (Weibel-Palade bodies, endothelial cell specific marker), phalloidin-TRITC (f-actin), and DAPI (nuclei) staining seen in figure 4.8A. At higher magnification (40x), a well-defined alignment of cell cytoskeleton is observed for PAC-L605 surfaces, compared to the alignment on bare metal alloy L605, figure 4.8B. There was no difference to vWF expression on either surface at a higher magnification.

As theorized by Ingber in 1993, change in cell shape in response to an applied pressure or due to interaction with substrates, is based on the cell's cytoskeleton [291]. Internal tension and lack of cell-substrate attachment generates round/symmetrical cell and nuclei shapes, whereas when attached to a substratum, cytoskeleton mechanically stabilizes the cell in a coordinated fashion [291]. To design optimized biomaterials for tissue engineering applications, it is important to understand cellular cytoskeleton, for efficient tissue regeneration and assisted healing, while avoiding an undesirable immunological or inflammatory response [226]. Biomimicry is the end result of surface nano/micro fabrication, allowing surfaces to mimic the physiological nano/micro environment.

4.4.2.3 EC phenotype on different biomaterial surfaces

Endothelial cell phenotype was investigated on three different surfaces; L605, PAC-L605 and PAC-L605-TE after 2 day proliferation with SEM (figure 4.8C). SEM allows higher magnification and detailed surface morphology of cells cultured on a non-transparent surface. The images reveal enhanced cell spreading and cell processes on PAC+TE surfaces, followed by PAC, whilst L605 surfaces show a higher consistency of spindle like projections and alteration to cell shape. During biological preparation for SEM, we eliminated the usual osmium tetroxide (OsO_4) fixation on all 3 surfaces, to prevent alterations to cell morphology. The altered cellular structure of ECs grown on alloy L605 could be due to surface kinetics; i.e. hydrophobicity and low surface energy. Results suggest that the selected PAC-L605 composition (PAC2 recipe) with covalently bound ECM tropoelastin protein, is best suited for EC growth and survival.

Overall, PAC- L605 (PAC2 recipe) with or without tropoelastin, assists anchorage dependant cell functions such as cell spreading and proliferation. The effects are enhanced with surface ECM protein, tropoelastin. Modifications to the biomaterial coupled with adhesive protein is suited for cardiovascular tissue engineering, which requires prior *in vitro* cell culture.

4.4.3 Thrombogenicity under adhesion and flow conditions

The *in vitro* model for hemocompatibility is already an over simplification of a very complex physiological system [252, 290]. We chose the modified chandler loop model for whole blood flow assays based on several previous studies and experimental standardization. To assess initial thrombogenicity of surfaces under static conditions, we utilized platelet rich plasma (PRP) incubation, and whole blood static adhesion. We chose heparin the lesser potent anticoagulant (section 4.1.3), as utilized previously for blood flow and static adhesion assays.

4.4.3.1 Platelet activation and surface fibrin clot formation

Platelet activity, conversion of fibrinogen to fibrin clot deposition (final step in blood coagulation), and whole blood adhesion were investigated under static conditions [105]. As seen with PRP and whole blood adhesion assays (figure 4.9 and 4.11 A,B,C), PAC-L605 surfaces with or without TE, bound fewer platelets, had less surface fibrin deposition and markedly lower coagulation, compared to alloy L605 and alloy 316LSS surfaces. The observation is rationalized as presence of protein in PRP preventing platelet/fibrin adherence to the modified hydrophilic PAC-L605 and PAC-L605-TE surfaces, whilst fibrin and platelets adhere to hydrophobic cobalt chromium and stainless steel alloys. Under physiological conditions, arterial thrombi formed are mainly composed of platelet aggregates bound together by thin fibrin strands, as observed on L605 surfaces with SEM images (figure 4.9).

4.4.3.2 Thrombogenicity of PAC with aging

During surface characterization investigated in chapter 3, we noted changing plasma kinetics of PAC-L605 surface within a period of 2 weeks. The variation was explained as a result of surface oxidation with time [103]. To assess impact of time/oxidation on surface thrombogenicity, we investigated hemocompatibility of PAC-L605 with PRP. The samples 1) PAC-L605-TE after 2 weeks of storage with TE (-20^{o}C) compared to TE overnight (4^{o}C), and 2) 1 month airtight storage of PAC-L605 without protein were compared with alloy L605. The SEM images of resultant PRP assays (figure 4.10) were similar to previous observations with fresh PAC, with/without surface protein (figure 4.9); indicating no significant changes to surface hemocompatibility with time. The ability to store protein bound surfaces for an extended period of time at -20^{o}C, while retaining protein conformation and surface hemocompatibility, is a feasible concept for tissue engineering and future clinical applications with a cardiovascular stent platform. We also investigated effects of surface ageing, within a blood flow model, discussed in 4.4.4 next.

4.4.4 Thrombogenicity under flow conditions

Fluid dynamics affect parameters of flow, to determine rates of cell and protein transport to the surface *in vivo* [292, 293]. Conflicting results have been observed for shear rates on different substrates (relative to platelets, thrombin, fibrin, and leukocyte deposition) due to differences in experimental conditions; i.e. varying degrees of blood components present, properties of the material studied and the state of inflammatory activation [292].

We had previously investigated thrombogenicity of a PAC-316LSS biomaterial, within a modified chandler loop, *in vitro* [105]. Thrombogenicity of PAC-L605 was investigated for the first time in this study. The modified biomaterial was 10x thicker (250 µm alloy L605, compared to 20 µm 316LSS foil), positioned vertically within the Tygon tube (instead of in contact with the wall), and had a 20 nm PAC surface compared to the 200 nm coating on 316LSS (Anna Waterhouse, Dissertation 2011) (figure 4.12). To justify novel inclusions in our current model, we utilized selection criterion for sample volume per surface area, and wall-shear stress equation, theorized elsewhere [252]. The sample volume was 2.5 mL per Tygon tube, and wall shear rate on sample twice the value on tube wall (figure 4.12). *In vitro* fluid dynamics relate to physiological conditions, where *in vivo* shear rate on the stent/implant surface is higher than flow shear rate on arterial wall. Hemodynamics play a quantitative role between stent implantation and thrombosis, detailed *in vivo* using computer fluid dynamics (CFD) simulation [294]. In future, a similar biomechanical study may be conducted first *in vitro* to quantitatively measure hemodynamics for stent-blood contact with CFD software [295].

4.4.4.1 Fibrinogen deposition

Surface fibrinogen deposition after flow assays were investigated via modified chandler loop and fluorescent microscopy, with fibrinogen antigen attached to a fluorescent dye Alexa Fluor

488. After 60 min chandler loop flow, fluorescein-labelled fibrinogen were quantified in higher densities on alloy L605 surfaces compared to PAC-L605; in correlation to higher thrombus formation on L605 compared to PAC-L605. Clinically, fibrinogen adsorption onto implant surfaces, is known to render biomaterials into thrombogenic surfaces. The critical effect of fibrinogen adsorption impacts overall bio-integration of an implantable material and therefore investigated in biomedical and materials research [296]. Fibrinogen protein possess amphiphilic properties (hydrophobic and hydrophilic) allowing adsorbance on any surface, and facilitates platelet aggregation [297]. Fibrinogen is a precursor of the blood coagulation complex, converted via thrombin and factor XIIIa to fibrin, and the final product of the coagulation cascade, fibrin clot (figure 4.1). Highly branched networks of thin fibrin fibres, cross-linked by activated factor (F)XIII, improves fibrin elastic properties and resistance to lysis [298]. Additionally, fibrinogen adsorption leads to formation of conditioning film on implant surfaces *in vivo,* potentially resulting in problematic bacterial attachment [297]. Mechanisms in bioengineering employed improved material hemocompatibility, conferring resistance to surface fibrinogen deposition, as well as platelet aggregation, although exact mechanisms of action are yet unknown.

4.5 Conclusion

We investigated biocompatibility of two different PAC recipes, with or without surface bound tropoelastin, in comparison to bare metal alloy L605. The proprietary plasma technology allowed covalent immobilization of a protein candidate of interest, enhanced surface endothelialization and lowered thrombogenicity compared to alloy L605. The PAC 2 recipe enhanced endothelial cell proliferation compared to PAC 1 recipe, this was applicable to PAC2 +TE surfaces as well. Overall, PAC2+TE showed best surface cytocompatibility in terms of cell spreading. In terms of hemocompatibility, PAC 1 recipe with higher nitrogen content appeared to enhance surface hemocompatibility compared to PAC 2 recipe, with or without surface tropoelastin. Tropoelastin did not appear to markedly increase hemocompatibility of PAC, compared to PAC alone. Therefore the ideal PAC recipe for a stent platform should be optimized between the two recipes. Ideally PAC1 (C-1, N-10) with a longer deposition time (t>20 min) or t=10 min, may result in an optimized polymer surface for equal cell proliferation and hemocompatibility. The surfaces maintained biocompatibility with age. Studies conducted herein on modified alloy L605 flat surfaces, assessed compatibility of the coating technology prior to its translation to a cobalt chromium stent platform.

Chapter 5 – Biological evaluation of medical devices: Selection of tests for interactions with blood.

5.1 Introduction

5.1.1 Objectives and Regulations of Standards in Medical Device Evaluation

The ISO (International Organization for Standardization) is a worldwide federation of national standards bodies [299]. A voluntary standard for a medical device is a recommendation provided to the manufacturer, detailing information of the product, basic safety and performance criteria, qualifying the device for clinical use. The standard further represents techniques that can be used to measure if device conforms to a safety or performance criteria; in comparison to performance characteristics of different products [299]. Recommending disclosure of the performance characteristics of a medical device necessitates development of specialized tests methods for uniform assessment and reporting. Reaching consensus on these tests is considerable part of committee work; including Association for the Advancement of Medical Instrumentation (AAMI), and the food and drug administration (FDA)[300].

All standards and recommended practices are voluntary, i.e. within discretion and professional judgment of the user of the document, unless adopted by government regulatory or procedural authorities [299]. Despite periodic review and revision, a standard or recommended practice is a static document, applied to a dynamic technology. Particular care should therefore be taken in applying a product or standard to an existing device, equipment, procedure or practice. A standard or recommended practice is only an important reference, and not a replacement to responsible decision making [299].

Professional judgment should be exercised in applying these criteria to existing equipment/devices. However, no single source of standardized information will serve to identify a particular product as "unsafe" [299]. In a preclinical setting, a standard or recommended practice should only be exercised in conjunction with other policies/guidelines and professional judgment.

5.1.1.1 Selection of tests for ISO 10993-4: FDA modifications

The ISO 10993-4 criterion was originally prepared by a technical committee for biological evaluation of medical devices [301], and revised last in 2013. The selection of test methods for the interaction of medical devices with blood should specify; device design, materials, usage environment and risk benefit [299]. The scope of the updated, FDA-modified, ISO-10993-4 (2013) utilized herein is for the biological evaluation of medical device materials in contact with blood. However, it should be ***emphasized***, the FDA guidelines only apply to the evaluation of a final, finished medical device [300]. As a result, any preliminary tests conducted and optimized in accordance to the International Standards on a modified biomaterial, while beneficial for optimization prior to stent translation, will need to be repeated with a modified stent in its final form; prior to preclinical testing [300].

In general, recommended tests for medical devices include assessments on; *in vitro* cytotoxicity, acute, sub chronic and chronic toxicity, hemocompatibility, irritation, genotoxicity, carcinogenicity and effects on reproduction. Evaluation of any device intended for human use requires systemic data, ensuring that benefits provided by the final product exceed any potential risks of the device. The FDA's perspective on cardiovascular devices extends to high risk ventricular assist devices (VADs), mechanical heart valves, stents, pacemakers, cardiac resynchronization therapy (CRT), and defibrillators [302]. Determination for clinical application of cardiovascular devices are based on FDA's review of extensive

preclinical bench and animal testing, followed by data from device used in a human clinical trial.

With the advancement of scientific knowledge in relation to basic mechanisms of tissue responses, the number and exposure of test animals is minimized with preference to chemical constituent testing of devices, and *in vitro* models [290].

5.1.1.2 Hemocompatibility tests according to ISO 10993-4:

The interaction of material surfaces with human blood is investigated with selected ISO 10993-4 tests. The tests predominantly represent two biological cascades resulting in clinical complications during blood-material interaction; 1) hemostasis (in relation to coagulation and platelets) and 2) inflammation (in relation to complement and leukocytes). In the modified chandler loop, diverse conditions of blood circulation can be simulated to investigate hemostatic/inflammatory markers in plasma; including complement, platelets, leukocyte activation, and generation of thrombin as well as formation of fibrin [303, 304]. After chandler loop assay, enzyme linked immunoabsorbent assays (ELISA), were used to investigate coagulation and inflammatory activation markers in plasma, listed in table 5.1.

Table 5.1. Selected tests for interaction with blood in accordance to ISO 10993-4.

ELISA test	**Molecular marker/cascade investigated**
Thrombin-Antithrombin complex (TAT)	Thrombosis/Coagulation
Beta-thromboglobulin (β-TG)	Platelet activation
sP-selectin	Platelet activation
SC5b-9 complex	Complement activation (immunology)
PMN-elastase	Leukocyte activation (hematology)

5.1.2 Thrombin Anti-Thrombin Complex (TAT): Critical role of thrombin

In vivo coagulation cascade is a response to vessel injury, as schematically shown in figure 5.1 A. Vessel injury occurs during PTCA (percutaneous transluminal coronary angioplasty), stent implantation, as well as atherosclerotic plaque rupture. Mechanistically, disruption of the vessel surface exposes subendothelial collagen and Von Willebrand factor, to which platelets adhere and become activated. Subendothelium exposure results in cells that constitutively express tissue factor; i.e. trigger the coagulation cascade [305]. A series of reactions cascade as a result, to form thrombin. Thrombin is the link between injury, trigger, coagulation process, platelet activation and inflammation [306].

Schematic details of the laboratory coagulation cascade mimics *in vivo* cascade depicted in figure 5.1A. Tissue factor (factor Xa) generated due to vessel injury [via collagen, vWF and fibroblasts] converts prothrombin to thrombin. Thrombin amplifies the process, acts as a potent platelet agonist, and converts fibrinogen to fibrin. Once platelets are activated they aggregate to form platelet-fibrin-thrombus that plugs the site of injury. Within an artery (coronary or cerebral) this formation can fill the vessel lumen, obstruct blood flow leading to myocardial infarct, or in the brain, to a stroke.

However, the cell-based model of coagulation proposed by Hoffman-Monroe [307] (figure 5.1B), shows *in vivo* coagulation is regulated via cell surface properties, and occurs as three overlapping stages; not as a simplified laboratory-based coagulation cascade (figure 5.1A) [307]. The 3 stages include initiation, amplification and propagation [307]. Since we investigated the proportion of thrombin formed, relative to blood-material contact *in vitro* in this chapter, we focus on the laboratory-based coagulation cascade (figure 5.1A).

The human thrombin-antithrombin *in vitro* ELISA is designed for quantitative measurement of thrombin-antithrombin complex (TAT) concentrations in plasma, isolated after whole blood

flow. Thrombin is a multifunctional serine protease generated at sites of vascular injury, and antithrombin a serine protease inhibitor; regulating the blood coagulation cascade [306]. The inhibitory activity of antithrombin is greatly enhanced in the presence of heparin. Heparinized whole blood is used prior to blood-material contact investigations, under static and flow conditions *in vitro* (chapter 4). TAT complex formation is assisted during heparinized blood-material contact assays. The *in vitro* ELISA quantifies TAT complex, while indirectly displaying proportion of thrombin generated and correlating proportions of antithrombin produced. The analysis is an important integer to measure activation of the coagulation cascade, and biocompatibility of materials in contact with blood, *in vitro*; [higher the concentration of TAT, higher the thrombin and antithrombin generated].

Figure 5.1

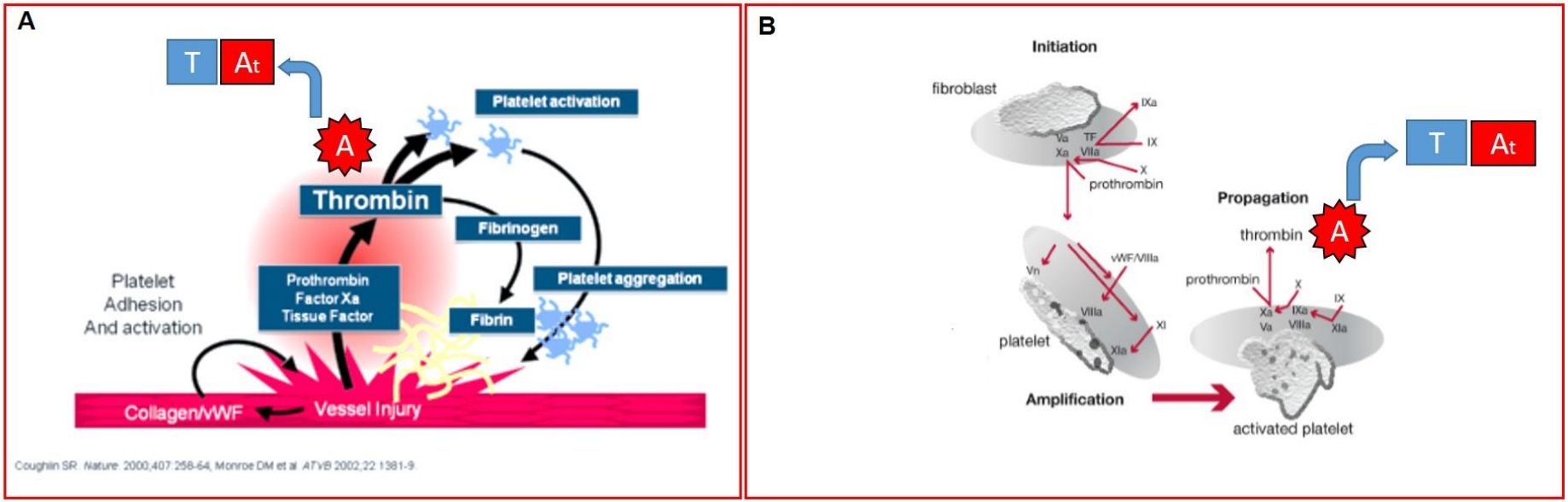

A) The cascade model of coagulation, schematically depicted in an *in vivo* environment, to explain the laboratory coagulation cascade. The red star with integer A indicates antithrombin, a serine protease inhibitor, forming thrombin-antithrombin complex (represented as TAt). B) In the cell-based model of haemostasis, coagulation is regulated by the cell surface receptors, to explain aspects of haemostasis that the cascade protein-centric model cannot explain. Images modified from [305],[306] and [307] respectively.

5.1.3 Beta-Thromboglobulin (β-TG): Platelet Release Reaction

Beta-thromboglobulin (β-TG) is a platelet specific protein (molecular weight 35 kDa), composed of 4 identical subunits [308]. The protein is synthesized in the cells as a biologically inactive precursor - platelet basic protein (PBP), stored in alpha-granules and released in large amounts after platelet activation. The released protein stimulates various processes including synthesis of plasminogen activator [308]. Measurement of plasma levels of secreted platelet protein β-TG, is suggested as an effective means of detecting increased platelet activation *in vivo* and *in vitro* [309].

The clinical measurement of platelet materials released, provide a better index of platelet activation in atherosclerotic vascular disease and arterial thrombosis [309]. A high plasma level of β-TG is equated with increased platelet release both *in vitro* and *in vivo.* Heparin infusion does not usually change the level of β-TG in laboratory tests [309]. *In vivo,* patients with abnormal coronary angiograms without previous myocardial infarction (MI) did not show elevated levels of β-TG, although values were significantly elevated in whom MI had occurred 6 months previously [310]. In patients with ischemic heart disease, platelet release is attributed to prior occurrence of MI, than to patients with atherosclerotic coronary arteries [310, 311].

Platelet adhesion and aggregation form important features of blood-material interaction [312], and platelet release reactions occur during this process. The release of platelet contents is also induced by thrombin during the coagulation cascade [312]. Quantifying platelet release factors after blood-material contact is therefore an index of biomaterial hemocompatibility. Assessments of material hemocompatibility have also previously been quantified, with platelet specific protein β-TG *in vitro* [312]. The *in vitro* ELISA assay uses an antibody specific to β-TG to enable quantification of platelet release using a standard curve, in plasma isolated after whole blood flow assay. *In vitro* β-TG assessment is further supported by previous

investigations in cardiovascular disease *in vivo* [310, 311], and material/cardiovascular stent hemocompatibility investigations *in vitro* [313, 314].

5.1.4 Soluble P-selectin: Platelet Activation

The glycoprotein P-selectin is localized in α-granules of platelets and Weibel-Palade bodies of endothelial cells [315]. The P-selectin protein expressed at 10x higher concentration on platelets than on ECs, is clinically defined as a marker of platelet activation *in vivo*. P-selectin has been evaluated in patients with coronary symptoms; at elevated levels with unstable angina [316], acute coronary syndrome [317] and coronary stenting [318]. P-selectin is also elevated in patients with congestive heart failure, stroke and peripheral artery disease [315]. Notably, increased levels of soluble P-selectin predict major cardiovascular events in patients with existing peripheral or coronary artery disease [319], and future risk of cardiovascular events in apparently healthy women with mean levels of P-selectin significantly higher at base level [320].

As mentioned previously in 5.1.3, plasma markers such as beta thromboglobulin and platelet factor 4, also secreted from α-granules define platelet activation. However, P-selectin remains activated for 1 hour on platelet surface, while other plasma markers such as β-TG and platelet factor 4 have a comparatively shorter half-life [315]. Soluble form of P-selectin is thought to be directly secreted from platelet cells into plasma [321].

Mice engineered to have high levels of soluble P-selectin, exhibit a pro-coagulant state [322], while P-selectin deficient mice show prolonged bleeding [323], highlighting its central role in hemostasis. Further studies indicate the molecule's association as a direct inducer of procoagulant activity in vascular and thrombotic diseases [315]. However, 3 independent

studies have shown platelets that have already shed their P-selectin, continue to circulate; therefore not all functional platelets are defined by P-selectin positivity [324]. Further, platelet leukocyte aggregates, mediated in part by P-selectin, are a more positive marker of platelet activation, compared to P-selectin-positive platelets, because of their longer duration in blood circulation [324], investigated via the complementary and leukocyte activation pathways, introduced next.

5.1.5 SC5b-9 Complex: Soluble terminal complement complex

Inflammation plays a key role in cardiovascular disease, contributing to the development of atherosclerotic lesions, plaque rupture and thrombosis [325]. The primary role of soluble terminal complement complex (TCC, SC5b-9) formed via activation of the complement system, is pathogen cell lysis and foreign body elimination [326]. An inflammatory response is elicited via formation of the membrane attack complex (MAC). The soluble terminal complement complex TCC, SC5b-9, seen in figure 5.2 (circled in red) [327], is generated by solubilization of C5 to C9 proteins of the membrane attack complex (MAC). The physiological role of complement system, as a rapid effector after vessel injury, contributes to its involvement in inflammation and thrombosis, in cardiovascular disease (CVD).

Three established mechanisms of complement activation exist, namely; classical, lectin and alternative pathways, leading to formation of the membrane attack complex (MAC) for effector responses on pathogen's membrane (highlighted orange, figure 5.2) [327]. Functional effects of complement activation are implemented by TCC (SC5b-9 complex). This quantifiable complex forms via another multistep process, that includes initiation (C5-C7 molecules), polymerization (C8-C9 molecules) for SC5b-9 formation, and its inhibition with CD59 present on healthy body cells (not shown), to prevent an autoimmune response [326]. The intended

biological outcome of the systematically regulated cascade is membrane perturbation of invading pathogens/foreign particles (figure 5.2) [327].

In vitro investigation of TCC, is an ISO recommended test after blood-material contact to assess biocompatibility of a material [252]. Clinically, increased complement activation after cardiopulmonary bypass intervention represent post-operative organ dysfunction [328]. Reduced complement activation is a marker of biocompatibility, as observed with heparin-coated cardiopulmonary bypass devices, *in vitro* [328]. Complement activity is therefore a common clinical complication that contributes to cardiovascular disease. Its role in the development of atherosclerosis, ST segment elevation, as well as non ST segment elevation acute coronary syndrome, and coronary bypass graft surgery has been investigated to understand molecular basis, for new therapeutic interventions that modulate complement activity [329]. *In vitro* investigation of an activated complement system is represented by terminal complement cascade (TCC, SC5b-9) ELISA quantification - after blood-material contact, to allow assessment of material biocompatibility.

5.1.6 Polymorphonuclear neutrophil (PMN) elastase: Leukocyte Activation

Angioplasty/stent implantation provoke local vascular injury during endothelial denudation, and plaque crushing, to promote leukocyte recruitment for local inflammation [330]. Recruitment and activation of polymorphonuclear neutrophils (PMN) following endothelial damage is observed after percutaneous coronary interventions (PCI), and plays a role in pathophysiology of acute coronary syndromes (ACS) [331]. Polymorphonuclear neutrophils (PMNs) are abundant blood circulating leukocytes, secreting proteolytic enzyme neutrophil elastase; activated during inflammation to destroy bacteria and host tissue [332]. Resulting chronic inflammation has direct cytotoxic effects, with ability to destroy human endothelial cells during neointimal hyperplasia [330]. Neutrophils potentiate platelet activation, and amplify endothelial damage, to play a significant role in the pathogenesis of restenosis after PCI [330, 331]. Activated inflammatory cells are present in atherosclerotic plaques, as well as in peripheral circulation [331]. Activated inflammatory cells also initiate production and expression of acute phase inflammatory proteins such as interleukin (IL)-6, and β_2 integrin MAC-1 on the surface of PMNs to regulate firm leukocyte adhesion to platelets, and to fibrinogen at site of injury [332]. These in turn have been linked to plaque formation and rupture, support neointimal thickening, clinical restenosis after stenting, as well as subsequent cardiovascular events in patients already suffering from acute coronary syndrome (ACS) [332, 333].

Contact with biomaterials *in vivo,* activates both monocytes and neutrophils. Degranulation leads to release of elastase, resulting in extracorporeal circulation due to leukocyte activation [334]. Material-induced leukocyte activation is dependent on exposed surface area, protein ligands present on the interface, and the presence of adherent platelets [334]. Hydrophobic surfaces tend to promote leukocyte adhesion and activation, compared to hydrophilic surfaces. *In vivo* studies have shown activated leukocyte adherence to stents, oxygenators and

hemodialysis membranes [331]. The primary aim of leukocyte activation is to engulf a pathogen/infiltrating foreign particle. Since a biomaterial cannot be engulfed by leukocytes, surface adhering neutrophils and monocytes attempt phagocytosis [334]. This results in extracellular release of proteolytic enzymes, reactive oxygen intermediates which potentiate injury, promote smooth muscle cell proliferation, migration and extracellular matrix deposition [335]. Down-regulation of leukocyte activation may therefore reduce inflammation-associated neointimal thickening, platelet adhesion and clinical restenosis commonly observed post PCI.

Material-induced leukocyte activation is mediated via several factors; including thrombin formation, platelet activation and complement activation already introduced within the chapter. Inhibition of one pathway alone is therefore insufficient to inhibit leukocytes [334]. *In vitro* investigation of material-induced leukocyte activation is quantified via PMN elastase released after degranulation. Comparative studies with *in vitro* ELISA allow PMN elastase quantification to estimate surface induced inflammation, and thereby estimate biocompatibility.

The study aimed at establishing an *in vitro* model foremost, to test hemocompatibility of PAC-L605 surfaces, in accordance with ISO 10993-4. The tests were performed with heparinized human whole blood. After flow assays in a modified chandler loop, blood plasma was analyzed for coagulation, platelet activation, complement activation and leukocyte activation with relevant enzyme linked immunosorbent assays (ELISAs). The ISO recommended tests allow a robust criterion to determine clinical markers *in vitro*, prior to translating PAC technology to an ML8 commercial stent (alloy L605, cobalt chromium), and subsequent translational studies *in vivo*.

Figure 5.2

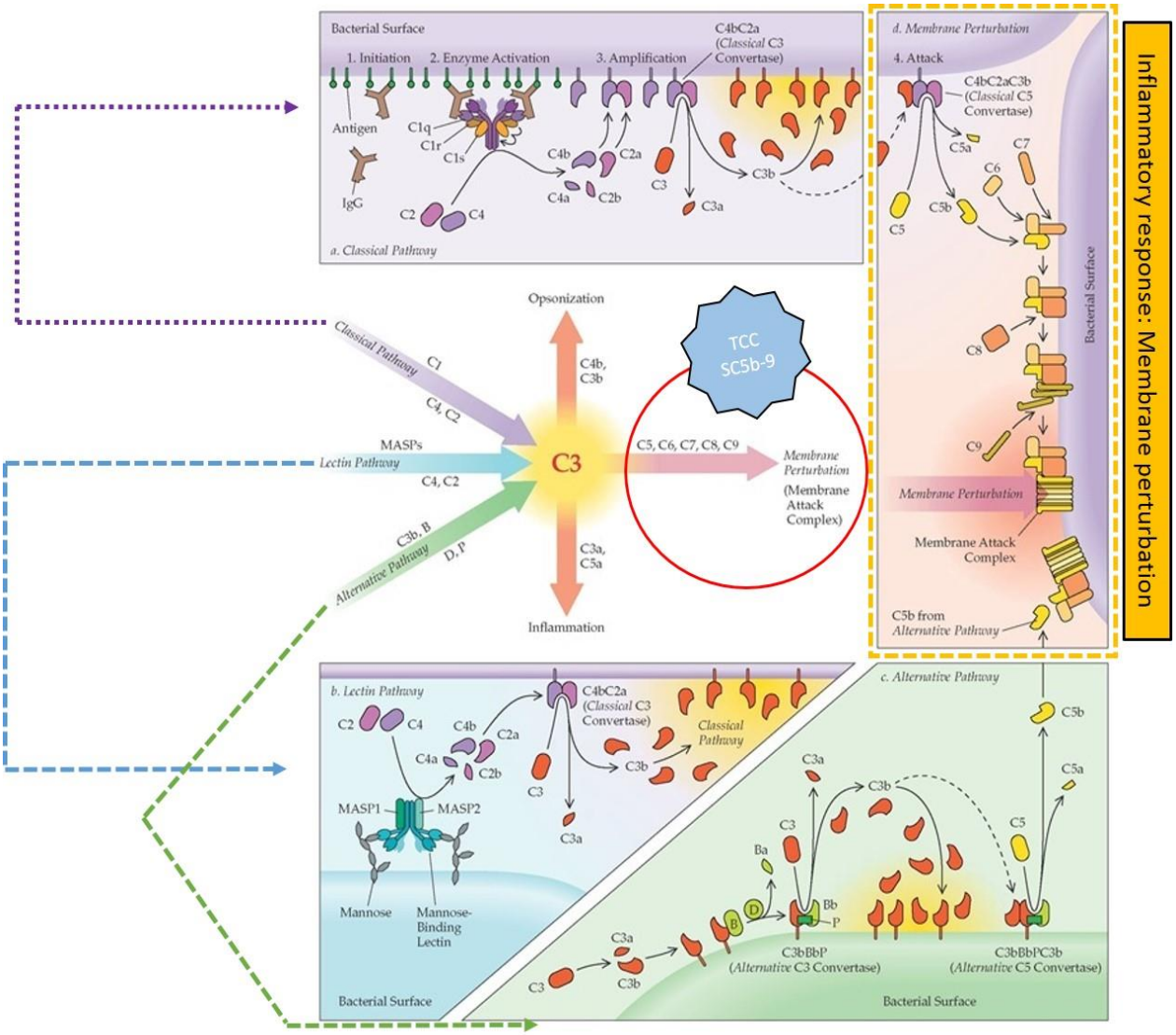

Soluble terminal complement complex (TCC, SC5b-9), is generated by the solubilization of the C5 through C9 membrane attack complex (MAC): circled in red. Formation of MAC is a consequence of activation of the complement system, by the classical pathway (seen in purple), lectin pathway (blue) or alternative pathway (green). The final outcome of MAC formation, is an inflammatory response resulting in membrane perturbation of invading pathogens, to disrupt target cells, cell lysis and death (highlighted in orange). Measurement of SC5b-9 complex after blood-material contact, comparatively quantifies initiation of biomaterial induced inflammatory response via all the complement pathways. Image is modified from [327] and what-when-how.com/acp-medicine/innate-immunity-part-2/ website.

5.2 Materials and Methods

5.2.1 Materials, Equipment, Suppliers and Facilities

A list of chemicals, reagents, materials and their suppliers are presented in Table 5.2

Table 5.2 Materials and their suppliers

Chemical/Reagent/Material	Supplier/Facility
6 mm Tygon tubing ND-100-65, Class VI (ID 6.35 mm, O.D. 7.93, 50 FT)	Saint-Gobain Performance Plastics, PA, USA
Beta-Thromboglobulin (β-TG) ELISA kit	MyBioSource Inc. San Diego, CA, USA
Citrate (CTAD) 4.5 mL, 0.109M (blue cap)	BD vacutainer, Macquarie University Research Park, NSW, Australia
EDTA (K_3EDTA), 3 mL (lavender cap)	BD vacutainer, Macquarie University Research Park, NSW, Australia
Heparin sodium salt (porcine intestinal mucosa, H3393, 180 U/mg)	Sigma-Aldrich, St. Louis, MO, USA
Polymorphonuclear elastase (PMN elastase) ELISA kit	Abcam, Cambridge, MA, USA
Silicon tubing (ID 10 mm, 10 FT) Masterflex	John Morris Scientific Pty Ltd, NSW, Australia
Soluble P-selectin (sP-selectin) ELISA kit	Life Technologies Australia, Victoria, Australia
Soluble terminal complement complex – SC5b-9 (plus EIA) ELISA kit	MicroVue Quidel, San Diego, CA, USA
Thrombin-Antithrombin (TAT) ELISA kit	Abcam, Cambridge, MA, USA

5.2.2 Preparation of alloy L605 and PAC-L605

Preparation of alloy L605 and PAC deposition was carried out as described in chapter 3.2.2. For the blood-material contact experiments in this chapter, we chose **PAC1**-L605 recipe (C-1, N-10, 500 V, t=20 min), referred throughout as PAC-L605. Prior to all experiments the two materials were cleaned and sterilized.

5.2.3 Modified Chandler Loop: Flow Assay

Prior to plasma isolation for each enzyme immunoassay (EIA), modified chandler loop flow tests were conducted, to investigate clot formation as described in section 4.2.10.5. Plasma was isolated after 60 min flow, for each EIA at different centrifugation speed and time limits, as recommended in commercial kits and previous literature. After flow assay, 1000 µL of heparinized whole blood was added to microcentrifuge tubes with $1/10^{th}$ volume of citrate/EDTA for plasma isolation (100 µL). The varied plasma isolation conditions for each ELISA is shown in table 5.3. All aliquots were stored at -20^{o}C overnight, for each ISO recommended ELISA. Each experiment was conducted in duplicate.

Table 5.3 Specific conditions of plasma isolation after 60 min chandler loop flow assay for individual ELISAs.

	Plasma Isolation Conditions		
ELISA test	**Centrifugation speed**	**Time (mins)**	**Anticoagulant**
Thrombin-Antithrombin complex (TAT)	3000 x g	10	10% citrate
Beta-thromboglobulin (β-TG)	1000 x g	20	10% citrate
sP-selectin	1000 x g	15	10% citrate
SC5b-9 complex	10,000 x g	5	10% K_2EDTA
PMN-elastase	1500 x g	10	10% K_2EDTA

5.2.4 Thrombin-Antithrombin Complex (TAT) Human ELISA

The Thrombin-Antithrombin complex (TAT) concentrations in plasma isolated from 60 min flow (stored at -20ºC), was quantified according to manufacturer's instructions (abcam, Cambridge, MA, USA). Plasma samples were not diluted prior to ELISA, 50 µL of the sample and standards were added to the wells in duplicates. The standard range was from 1.48 ng/mL-120 ng/mL with a sensitivity of 1.5 ng/mL. Standards were prepared according to protocol. Samples were subsequently incubated with TAT-specific biotinylated detection antibody, followed by wash buffer, as recommended. Biotinylation was followed by streptavidin peroxidase conjugation, and TMB (tetramethylbenzidine) to visualize enzymatic reaction (Streptavidin-Peroxidase). The density of the colour compound formed after stopping the reaction was representative of the TAT concentration captured within the plate; corresponding to the biomaterial of interest. Reading was performed in a 96 well plate at 450 nm with a 570 nm wavelength correction.

5.2.5 Beta Thromboglobulin (β-TG) Human ELISA

The human Beta-Thromboglobulin (β-TG) concentration in plasma isolated from 60 min flow (stored at -20^{o}C), was quantified according to manufacturer's instructions (MyBioSource, San Diego, CA, USA). Plasma samples were not diluted prior to ELISA, 50 µL of the sample and standards were added to the wells in duplicates. The standard range was from 100 ng/mL to 3.12 ng/mL, prepared at manufacture, with a sensitivity of 1.0 ng/mL. To increase sensitivity, we prepared a 7th standard of 1.57 ng/mL [250 µL of standard 6 (3.12 ng/mL) in 250 µL standard diluent]. The assay was carried out according to the manufacturer's instructions. Optical density, representative of the β-TG concentration captured within the 96 well plate was measured at 450 nm.

5.2.6 Soluble P-selectin (sP-selectin) Human ELISA

The soluble P-selectin (sP-selectin) concentration in plasma isolated from 60 min flow (stored at -20^{o}C), was quantified according to manufacturer's instructions (Life Technologies, Victoria, Australia). In the initial experiment, the plasma samples were diluted 1/10th in assay buffer as recommended in the protocol, in repeat experiments the plasma samples were diluted 1/30th with assay buffer. The sP-selectin stock standard was reconstituted by addition of 360 µL of distilled water. The homogenized standard was diluted sequentially in assay buffer as instructed, to prepare a standard range from 40 ng/mL to 0.63 ng/mL, with a sensitivity of 0.2 ng/mL. The assay was carried out according to manufacturer's instructions. Optical density, representative of sP-selectin concentration captured within the 96 well plate was measured at 450 nm with a 620 nm reference wavelength.

5.2.7 Terminal Complement Complex (TCC, SC5b-9) Human ELISA

The soluble C5b-9 complex/TCC concentration in plasma isolated from two separate flow assays at 10 min and 60 min (stored at -20^{o}C), was quantified according to manufacturers' instructions (MicroVue, Quidel, San Diego, CA, USA). The plasma samples were diluted 1/10th with specimen diluent as recommended in the protocol. The SC5b-9 complex standard range was from 185 ng/mL to 0 ng/mL, prepared at manufacture. High controls (106-156 ng/mL) and low controls (15-33 ng/mL) were also provided for the assay, and used in similar dilution to the samples. The assay was carried out according to the manufacturer's protocol. Optical density, representative of SC5b-9 concentration, captured within the 96 well plate was measured at 450 nm.

5.2.8 Polymorphonuclear Elastase (PMN-elastase) Human ELISA

The PMN-elastase concentration in plasma isolated from 60 min flow (stored at -20^{o}C), was quantified according to manufacturer's instructions (abcam, Cambridge, MA, USA). The plasma samples were diluted 1/10th with sample diluent as recommended in the protocol, in trial experiments the plasma samples were diluted 1/100th (1:100) with sample diluent. The 10 ng/mL stock standard was prepared by reconstituting PMN elastase standard with 2700 µL sample diluent, and held at room temperature for 30 min. The PMN elastase standard range was from 10 ng/mL to 0 ng/mL, with a sensitivity of 1.98 pg/mL. High controls and low controls were provided for the assay, used in similar dilution to the samples. The assay was carried out according to manufacturer's protocol. Optical density representative of PMN-elastase concentration within the 96 well plate was measured at 450 nm with a 620 nm reference wavelength.

5.2.9 Statistics

For flow results and ELISA data, the averages, statistical significance and unknown concentration of 6 pairs of variables, were calculated with Microsoft Excel (Office 2013, DC, USA) and GraphPad PRISM 6 for Mac OS X software (Version 6a; GraphPad Software, La Jolla, CA, USA). Unknown concentrations were calculated with nonlinear regression (curve fit). Standard curves to interpolate hyperbola (X is concentration) were selected with fitting method (least squares ordinary fit), to interpolate unknowns from the standard curve. Statistical significance was estimated with paired t-tests for grouped data between two variables, and ordinary one-way ANOVA with multiple comparisons for >2 variables, as appropriate. All results corresponding to ELISA concentrations are presented in figures in their ***experimental dilution***. The interpolated concentration for unknown variables is multiplied by appropriate dilution factor, within context describing results, as appropriate.

5.3 Results

5.3.1 Comparative flow and EIA for PAC-L605 vs. L605 surfaces

Five consecutive flow assays were conducted for each plasma isolation event for ELISA. Depending on conditions of centrifugation (table 5.3), 200-500 µL of plasma was isolated and stored at -20^{o}C for utilization in ELISAs. All results corresponding to EIA concentrations, are presented in figures in their initial experimental dilution. The interpolated concentration is multiplied by appropriate dilution factor, within context.

5.3.2 Quantification of Thrombin Antithrombin (TAT) complex for PAC-L605 vs L605 surfaces: [TAT complex] is lower on PAC

Thrombus formation at a time course of 60 min was investigated with a modified chandler loop flow assay prior to plasma isolation for TAT. Significantly lowered clot formation was observed for PAC-L605 compared to alloy L605 surfaces; 8.36±4.38 mg and 35.9±7.88 mg respectively ($p=0.001$), figure 5.3 A. The TAT complex was identified and quantified with a standard curve to derive test results, figure 5.3 B. Significantly lowered concentration of TAT was observed with plasma isolated after contact with PAC-L605 surfaces compared to L605; 7.22±1.33 ng/mL vs. 15.93±2.55 ng/mL respectively ($p=0.002$), figure 5.3 C.

5.3.3 Quantification of Beta-Thromboglobulin (β-TG) for PAC-L605 vs. L605 surfaces: [β-TG] is lower on PAC

Thrombus formation at a time course of 60 min was investigated with a modified chandler loop flow assay prior to plasma isolation for β-TG. Plasma was isolated from the 60 min flow assay for SC5b-9 ELISA as well, investigated next (5.3.5). Significantly lowered clot formation

observed for PAC-L605 vs L605; 3.93±2.86 mg vs. 30.70±1 mg respectively (p=0.025), figure 5.4 A. The β-TG complex was identified and quantified with a standard curve to derive test results, figure 5.4B. Significantly lowered concentration of β-TG observed with plasma isolated after contact with PAC-L605 surfaces compared to L605; 16.61±3.33 ng/mL vs. 27.16±3.75 ng/mL respectively (p=0.025), figure 5.4C.

5.3.4 Quantification of soluble P selectin (sP-selectin) for PAC-L605 vs L605 surfaces: [sP-selectin] lower on PAC

Thrombus formation at a time course of 60 min was investigated with a modified chandler loop flow assay, prior to plasma isolation for sP-selectin. Significantly lowered clot formation was observed for PAC-L605 vs. L605 surfaces; 4.56±3.65 mg vs. 43.95±9.95 mg respectively (p=0.014), figure 5.5 A. The sP-selectin complex was identified and quantified with a standard curve to derive test results, seen in figure 5.5B. A dilution of 1:10 yielded absorbances higher than the standard curve, therefore the experiment was repeated with a 1:30 dilution. The sP-selectin concentration was quantified after contact with PAC-L605 surfaces compared to L605. Due to variability of results, only the average absorbance was used to calculate concentration, presented in figure 5.5C. Concentration interpolated from the standard curve was multiplied by a dilution factor (x30) presented in parentheses. The average sP-selectin after PAC-L605 contact was 4.87±0.07 ng/mL (146.19±2.1 ng/mL), and the average concentration after L605 contact was 10.575±020 ng/mL (317.25±6 ng/mL) (p=0.0138). Absorbances for the high control was above the standard curve, concentration could not be interpolated at 1:30 dilution. Concentration of the low control was 2.078 ng/mL±0.090 (62.34±2.7 ng/mL) (not included in graph). Experiments should be repeated at higher dilution, to interpolate concentration for high control and minimize unknown concentration variability.

5.3.5 Quantification of soluble terminal complement complex (SC5b-9) for PAC-L605 vs L605 surfaces: at 60 mins [SC5b-9] lower on PAC

Thrombus formation at a time course of 60 min was investigated with a modified chandler loop assay - prior to plasma isolation for SC5b-9. Significantly lowered clot formation was observed for PAC-L605 vs. L605 surfaces at 60 min, figure 5.6 A (results are the same as those for 5.3.3, since flow assay was common to both. Conditions of plasma isolation were different – see table 5.3). Clot formation at 10 min was very low, as expected, and not significantly different between the two surfaces. Although trends show lower clot formation for PAC-L605 compared to alloy L605; 0.6±0.35 mg vs. 2.5±1.04 mg respectively, figure 5.6A. The SC5b-9 complex was identified and quantified with a standard curve to interpolate test results, figure 5.6B. Concentration interpolated from the standard curve was multiplied by a dilution factor (x10) presented in parentheses. Concentration of SC5b-9 at 60 min was significantly lower for PAC-L605 surfaces compared to alloy L605; 98.18±21.88 ng/mL (981.91±218.84 ng/mL) vs. 120.27±15.05 ng/mL (1202.77±150.53 ng/mL) respectively ($p=0.032$). The high control yielded a concentration of 113.66±1.41 ng/mL (1136.6±14.16) and the low control yielded a concentration of 34.20±1.98 ng/mL, (342.0±19.80) figure 5.6C. Concentration of SC5b-9 at 10 min was not significantly different between PAC-L605 and L605 surfaces; 42.06±0.38 ng/mL (420.66±3.8 ng/mL) vs. 43.51±1.93 ng/mL (435.19±19.33 ng/mL) respectively ($p=0.444$), figure 5.6C.

5.3.6 Quantification of Polymorphonuclear elastase (PMN elastase) for PAC-L605 vs L605 surfaces:

Thrombus formation at time course of 60 min was investigated with a modified chandler loop assay prior to plasma isolation for PMN-elastase. Significantly lowered clot formation was

observed for PAC-L605 vs. L605 surfaces at 60 min; 1.8±0.48 mg vs. 9.4±1.65 mg respectively (p=0.015), figure 5.7A. The PMN elastase enzyme was identified and quantified with a standard curve to interpolate test results, seen in figure 5.7B. Concentration interpolated from the standard curve were multiplied by a dilution factor (x100) presented in parentheses. Concentration of PMN elastase at 60 min was not significantly different between L605 and PAC-L605 surfaces; 2.72±0.45 ng/mL (272.75±45.17 ng/mL) vs. 3.26±0.26 ng/mL (326.84±26.03 ng/mL) (p=0.149) respectively. The high control yielded a concentration of 10.67±2.9 ng/mL (1067.52±296.83 ng/mL) and low control yielded a concentration of 1.19±0.41 (119.66±40.82 ng/mL), figure 5.7C.

Figure 5.3

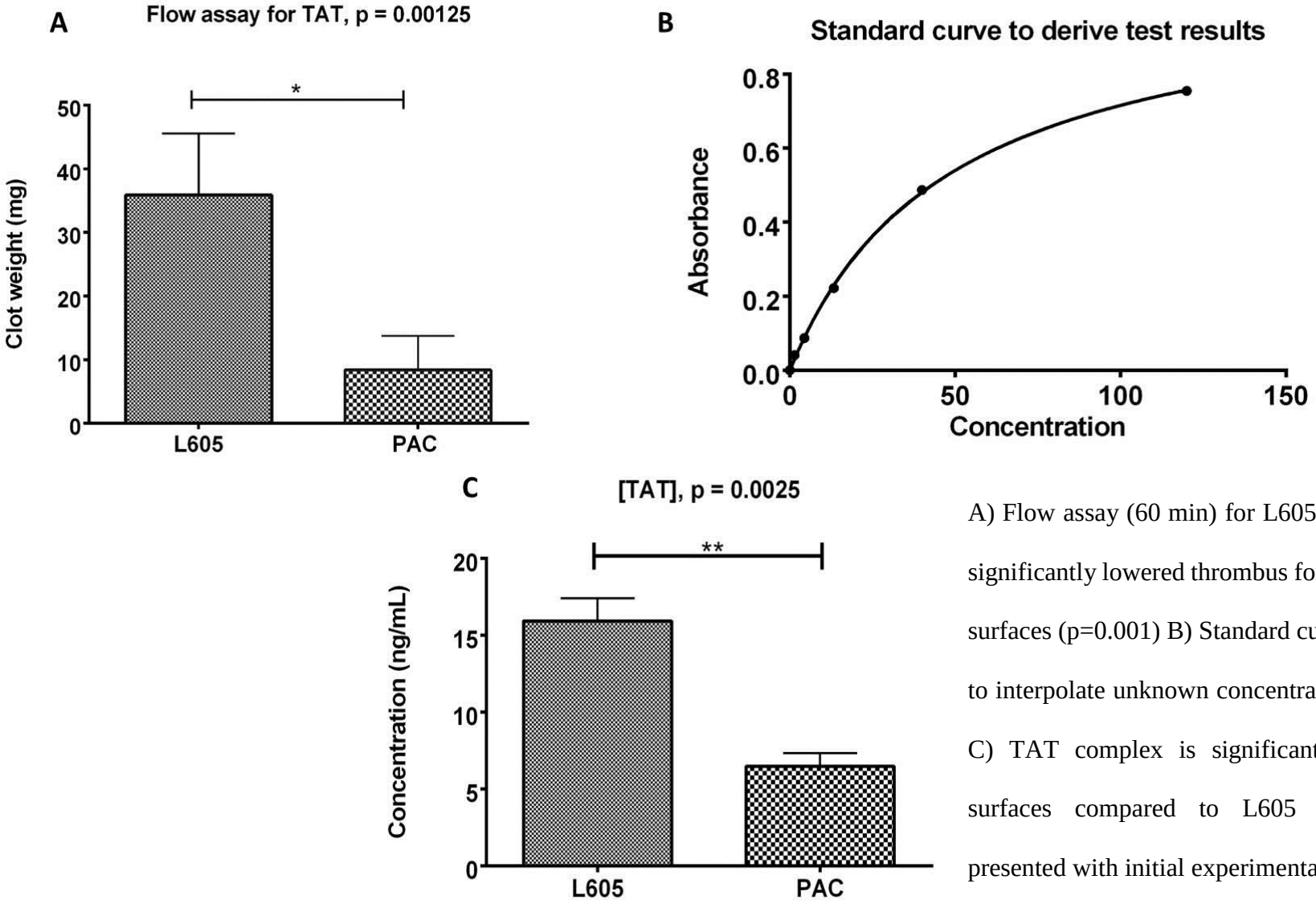

A) Flow assay (60 min) for L605 vs. PACL05 shows significantly lowered thrombus formation on modified surfaces (p=0.001) B) Standard curve for TAT ELISA to interpolate unknown concentrations at 450/570 nm C) TAT complex is significantly lower for PAC surfaces compared to L605 (p=0.002). Graphs presented with initial experimental dilution.

Figure 5.4

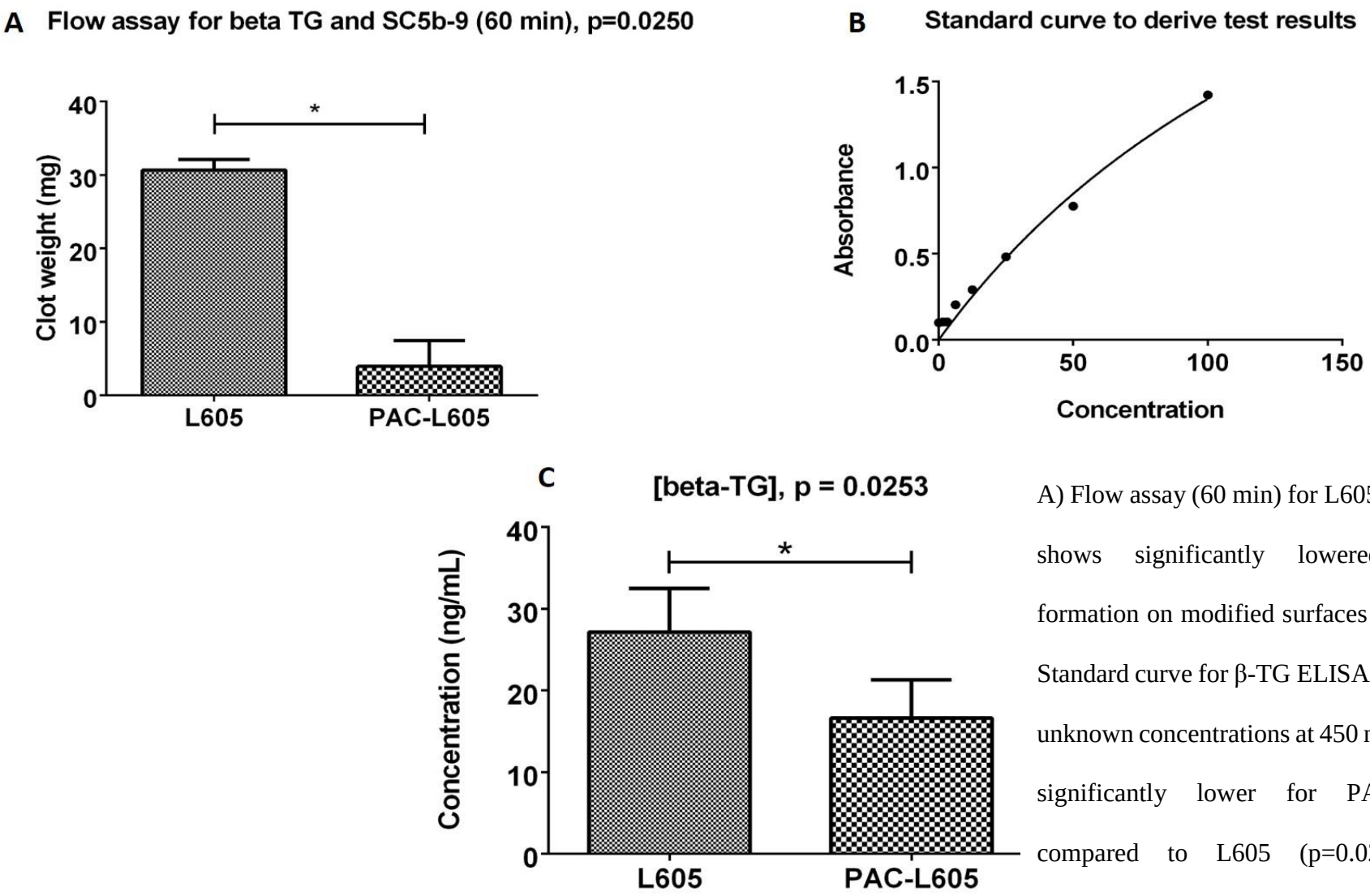

A) Flow assay (60 min) for L605 vs. PACL05 shows significantly lowered thrombus formation on modified surfaces (p=0.025) B) Standard curve for β-TG ELISA to interpolate unknown concentrations at 450 nm C) β-TG is significantly lower for PAC surfaces compared to L605 (p=0.025). Graphs presented with initial experimental dilution.

Figure 5.5

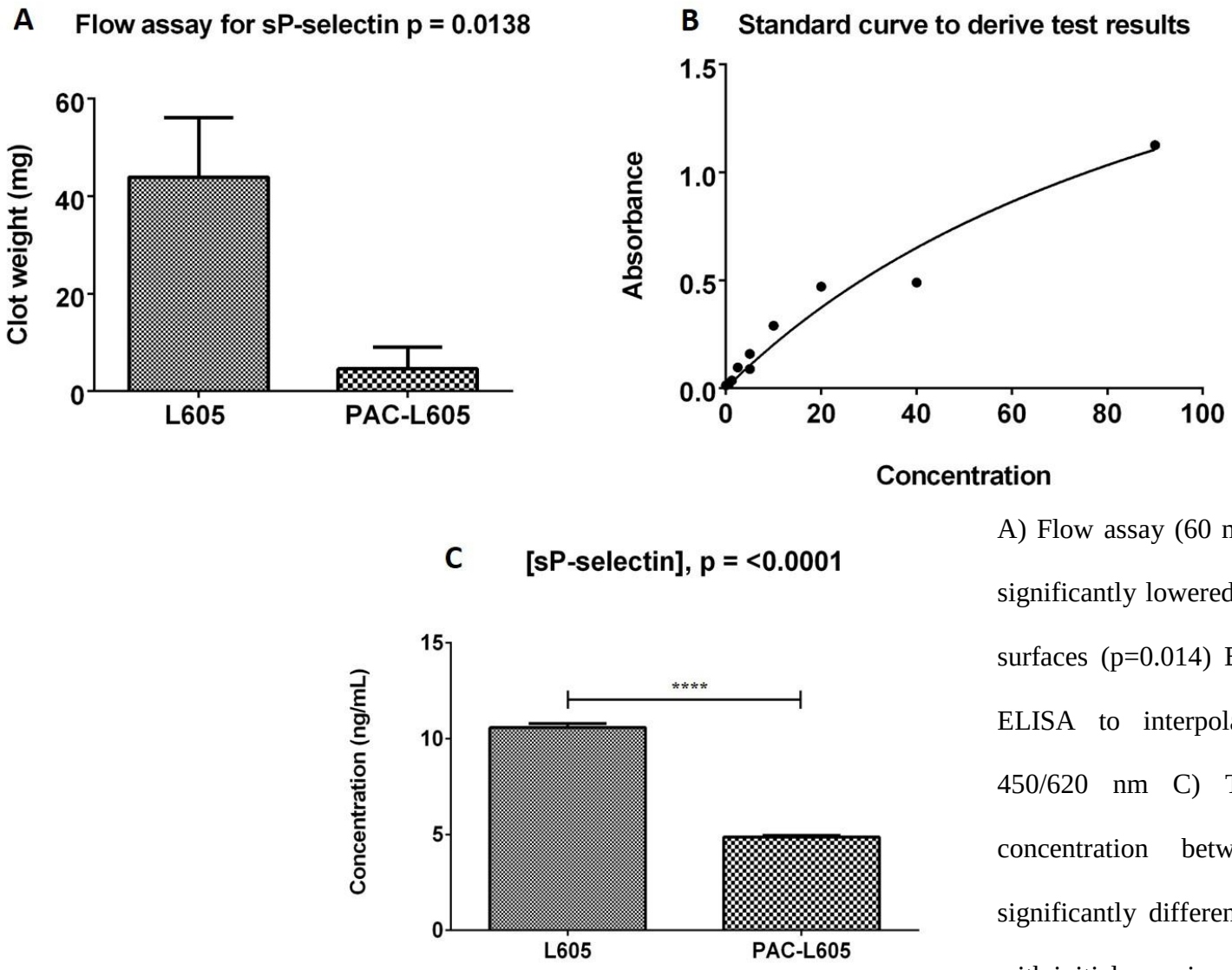

A) Flow assay (60 min) for L605 vs. PACL05 shows significantly lowered thrombus formation on modified surfaces (p=0.014) B) Standard curve for sP-selectin ELISA to interpolate unknown concentrations at 450/620 nm C) The average sP-selectin (1:30) concentration between the two surfaces was significantly different (p=<0.0001). Graphs presented with initial experimental dilution.

Figure 5.6

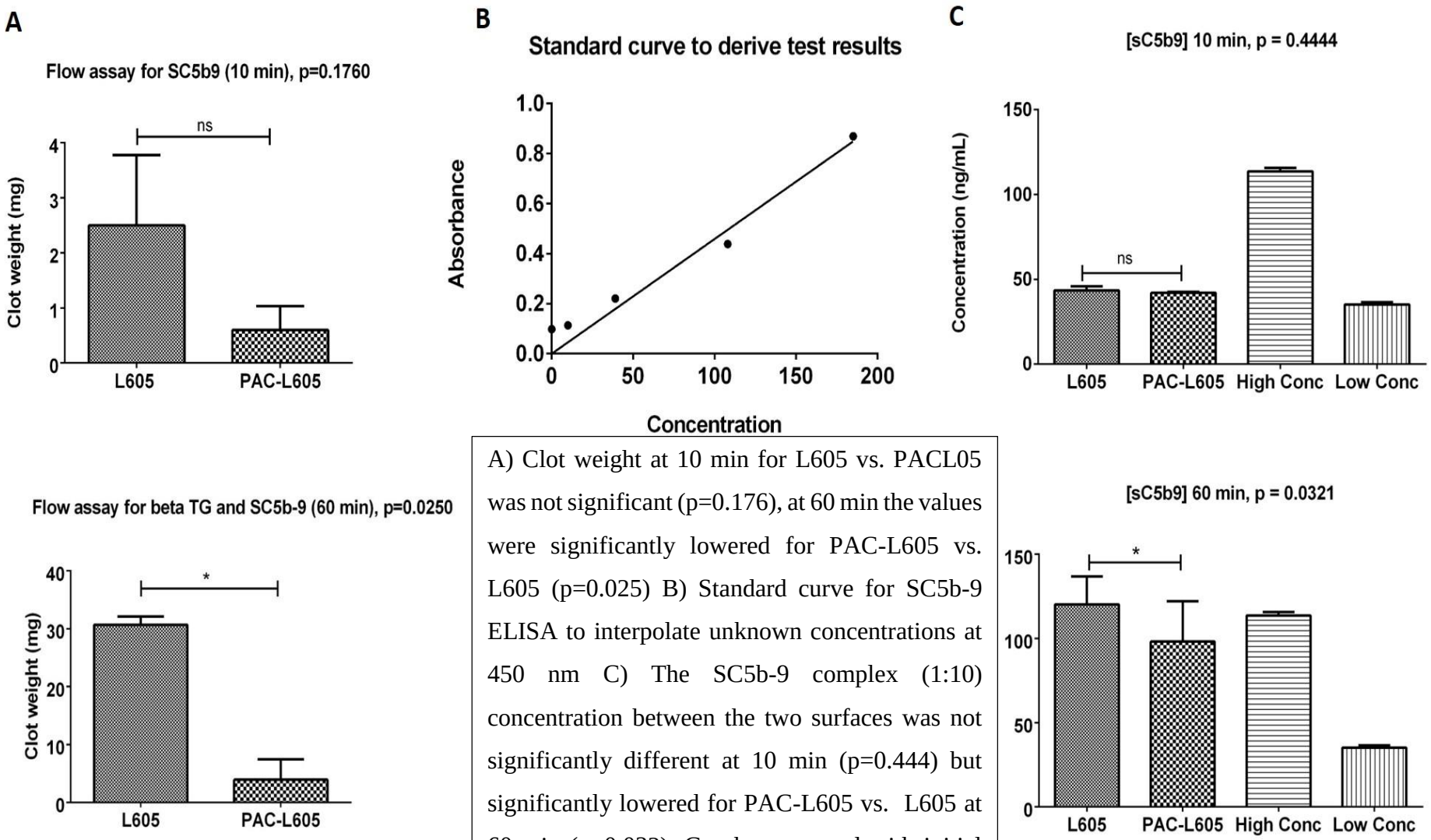

A) Clot weight at 10 min for L605 vs. PACL05 was not significant (p=0.176), at 60 min the values were significantly lowered for PAC-L605 vs. L605 (p=0.025) B) Standard curve for SC5b-9 ELISA to interpolate unknown concentrations at 450 nm C) The SC5b-9 complex (1:10) concentration between the two surfaces was not significantly different at 10 min (p=0.444) but significantly lowered for PAC-L605 vs. L605 at 60 min (p=0.032). Graphs presented with initial experimental dilution.

Figure 5.7

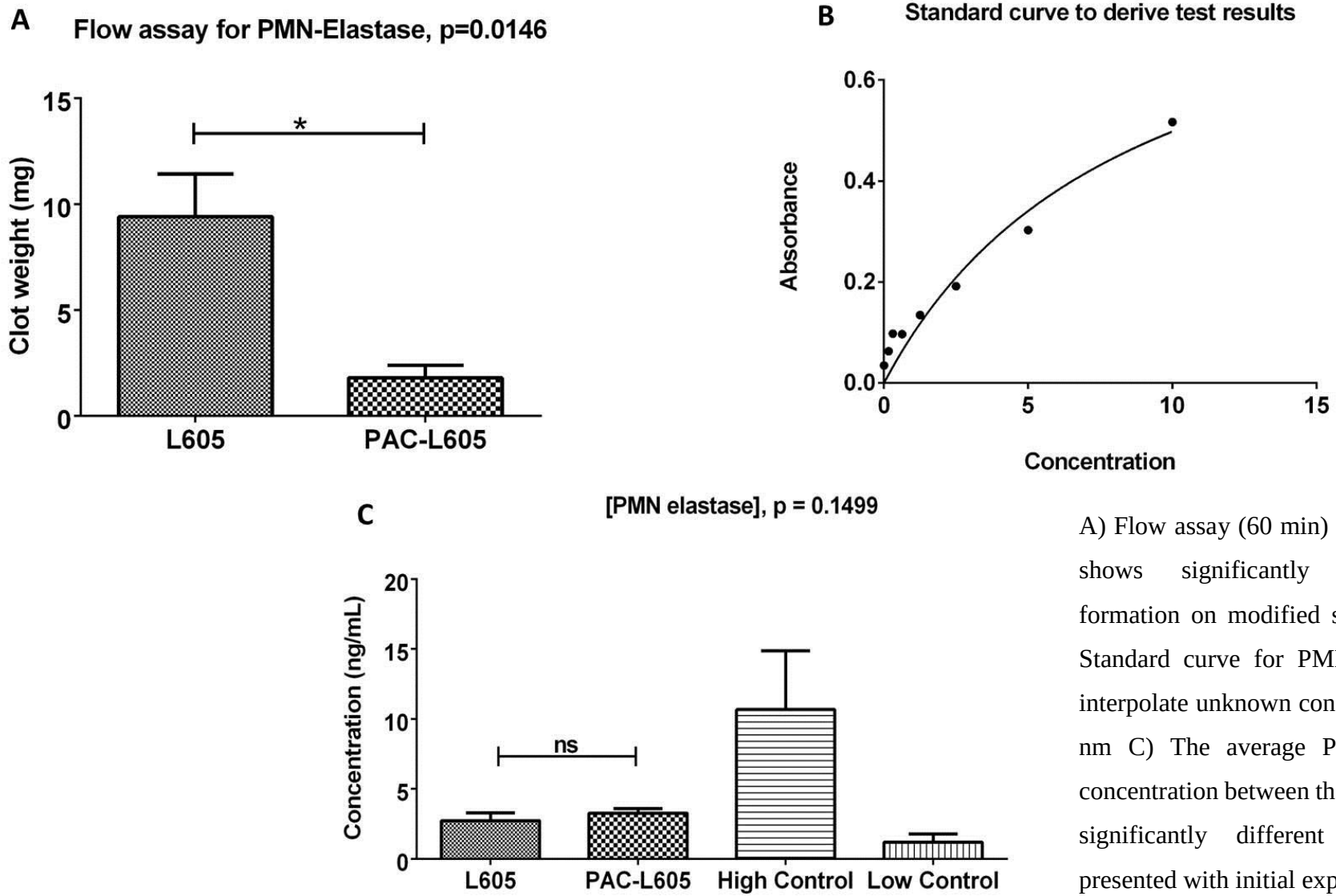

A) Flow assay (60 min) for L605 vs. PACL05 shows significantly lowered thrombus formation on modified surfaces (p=0.015) B) Standard curve for PMN elastase ELISA to interpolate unknown concentrations at 450/620 nm C) The average PMN elastase (1:100) concentration between the two surfaces was not significantly different (p=0.150). Graphs presented with initial experimental dilution.

5.4 Discussion

During first 2 weeks of stent implantation, sub-acute stent thrombosis and an early inflammatory response are two main clinical complications that occur after undesired blood-stent interactions [252, 331]. We investigated plasma biomarkers of coagulation and inflammation; TAT, β-TG, sP-selectin, SC5b-9, and PMN elastase, after modified chandler loop, with enzyme immunosorbent assays (EIA) *in vitro*. In contrast to animal models, an *in vitro* model allows early investigation of blood-material contact in relation to several biochemical cascades. Plasma isolated after blood-material contact was used for investigations, in accordance to ISO 10993-4 recommendations [299]. Key findings of this study include; significantly reduced TAT complex, β-TG and sP-selectin (markers of coagulation/platelet activation) for PAC-L605 compared to bare metal alloy L605. Further findings include significantly reduced SC5b-9 complex; marker of complement activation for PAC compared to L605. There was no significant difference between plasma levels of PMN elastase; leukocyte activation for the two biomaterials.

5.4.1 Dynamics of blood-biomaterial contact – A hypothesis

It is generally accepted that hydrophobic surfaces adsorb more proteins than hydrophilic surfaces (Bergs Law) [259]. Proteins thus adsorbed form a monolayer on the surface, with up to 1000-fold higher concentration than in solution [336]. Platelet adhesion is promoted in the presence of surface proteins fibrinogen, von Willebrand factor, fibrin, and reduced in the presence of surface proteins; albumin and/or high density lipoprotein (HDL) [337]. Adsorbed proteins are subject to change over time, in a phenomenon termed Vroman effect [338]; largely applicable to hydrophilic surfaces [339, 340]. According to the phenomenon, plasma proteins compete for occupation on a surface, resulting in competitive adsorption, more effective on

hydrophilic materials. With hydrophobic surfaces, proteins undergo conformational changes on surface, become immunologically undetectable, and adsorb irreversibly [341, 342].

To explain results of the present study, we hypothesize that modified hydrophilic PAC-L605 conform to Vroman effect, and may predominantly adsorb plasma proteins albumin and HDL. Keeping in mind both proteins reduced surface platelet aggregation and activation [337], as also observed with PAC-L605, in this chapter. In support of hypothesis, previous studies have shown significantly higher levels of plasma HDL adsorption to hydrophilic surfaces [342], and significantly higher adsorption of surface albumin, compared to hydrophobic surfaces [343]. Fibrinogen, the more abundant plasma protein promotes platelet adhesion, but as observed in chapter 4, has lower adsorption on hydrophilic PAC-L605 compared to bare alloy L605. Fibrinogen exists in two distinct experimentally observed conformations; irreversible and reversible adsorption, replaced by other proteins [344]; in further agreement with our results.

5.4.1.1 Thrombosis and TAT ELISA: Reduced coagulation marker on PAC

Active thrombin formed via conversion of prothrombin by tissue factor Xa (TF Xa), is a main effector protease of the coagulation cascade [305] (figure 5.1). TF is also expressed at low levels on circulating monocytes and leukocytes *in vivo*. When blood contacts a material, the surface triggers coagulation activation (and complement systems) via intrinsic, extrinsic and common pathways (figure 4.1) [345]. Materials widely incorporated for implants are generally biocompatible, although clinical complications [213] lead to adverse outcomes, and should be avoided. Under physiological conditions, we demonstrated ability of PAC to significantly reduce TAT complex formed after blood-material contact, using flow assays and EIA *in vitro*.

In vivo TAT complex is formed when prothrombin is converted to thrombin during blood clotting, and both antithrombin III and antithrombin IV, neutralize the thrombin formed [346]. Antithrombin III (AT) is a high-capacity inhibitor of both thrombin and autoprothrombin C

(precursor of thrombin) proteases in blood coagulation [347]. However, under special conditions/disease, thrombin may regenerate from the TAT complex [347], forming a positive feedback loop.

In the presence of anticoagulant heparin, capacity of antithrombin (AT) to inhibit thrombin is accelerated [346]. In the presence of heparin, TAT complex is hypothesized to form via 3 different pathways (both *in vivo* or *in vitro*) [348]; 1) heparin may first bind to AT - enhance the rate of inhibitor-protease reaction [349], 2) heparin may bind to thrombin first - form a complex and be rapidly inactivated by free AT [350], 3) finally, heparin may act as a template - bringing the protease and inhibitor closer [351]. The second hypothesis has been proven correct on evaluating the role of heparin in TAT complex formation [350]. Systematically therefore, increased levels of plasma TAT complex is a marker of coagulation; indicating high levels of the serine protease thrombin and its corresponding inhibitor AT in plasma.

Normal human plasma levels of TAT are estimated to be at a range of 0.5-10 ng/mL (abcam ELISA manual, Cambridge, MA, USA). In our study, after 60 min flow within physiological conditions, the plasma levels of TAT after PAC-L605 contact was 7.22±1.33 ng/mL (within the normal TAT complex range). Within same conditions, plasma levels of TAT after L605 contact was 15.93±2.55 ng/mL; ~50% above the normal plasma range of TAT. It appears PAC surfaces are hemocompatible, lowers clot formation within a modified chandler loop at 60 min and contributes to lowered plasma markers of coagulation *in vitro*. The present study shows that aside from hemocompatibility, modified surfaces are also cytocompatible, compared to the bare metal alloy.

5.4.2 Reduced levels of platelet activation marker β-TG on PAC surfaces

Plasma beta-thromboglobulin (β-TG) is a platelet-specific protein marker released via platelet degranulation [352]. In atherosclerotic vascular disease and arterial thrombosis, platelet materials released are measured, to provide a clinical index of platelet activation [353]. A number of effects on platelet function predispose to atherosclerosis, coronary thrombosis and ischemic heart disease [354]. The primary role of platelets (bone marrow megakaryocytes), is recognition of vascular injury. Platelets stimulated via different ligand-receptor signals activate in four stages 1) development of stickiness (from non-sticky resting state), 2) changes in cell shape i.e. extend pseudopods to adhere to surface, 3) contraction and release granule contents, and 4) irreversible aggregation (most common on hydrophobic surfaces) [355]. We investigated two plasma markers relating to platelet degranulation and activation in plasma isolated via blood-material contact; β-TG and sP-selectin. We demonstrated the ability of a plasma modified surface to significantly reduce β-TG released and sP-selectin expressed on platelets, after blood-material contact using flow assays and EIA *in vitro*.

Clinical studies have shown contribution of platelet degranulation towards intima-media thickness of common carotid artery, in patients with diabetes mellitus type 2 [354]. Measurement of β-TG *in vitro* is an indirect index of platelet activation. Granule contents released to the surrounding medium during platelet activation include ADP, ATP, calcium, serotonin, platelet factors, β-TG, fibrinogen, fibronectin etc. [355]. The release promotes platelet/fibrin aggregate formation, previously observed via SEM and fluorescent staining on L605 (chapter 4). Consequently, higher concentrations of β-TG were quantified for L605 herein. Comparatively we observed a 38.84% reduction of β-TG expression on PAC-L605 surfaces.

5.4.2.1 Mechanisms of platelet degranulation: theory for hydrophilic surfaces

Platelet adherence to a surface is dependent on surface roughness (width of spaces between surfaces), charge, wettability, and flow conditions (characterized in chapter 3 & 4). Plasma proteins and their initial concentration/dilution, also promote platelet activation. Plasma proteins; albumin, fibrinogen and globulin rapidly deposit on artificial surfaces, replaced over time with high-molecular weight kininogen (HMWK) and hagmeman factor [338]. Protein-surface interaction dictates degree of platelet activation. For instance; laminin induces platelet focal adhesion, fibronectin promotes spreading and activation, and collagen supports aggregation/secretion [338]. Fibrinogen has higher adsorbance affinity, higher concentration on surfaces than in the bulk plasma, and promotes platelet response to surface. Fibrinogen plays a key role in platelet-surface attachment, aggregation and secretion (degranulation), extensively detailed by Vroman during initial evaluation of blood-surface interactions [356].

However, on hydrophilic surfaces "an entire parade of protein may adhere and leave the substrate" (after fibrinogen adherence and displacement), due to high turnover rate [356]. On the basis of data, Vroman concludes the sequence of adsorption is based on plasma proteins available from higher to lower concentration; i.e. albumin, immunoglobins (IgG), fibrinogen and fibronectin, followed by factor XII and high molecular weight kininogen (HMWK, coagulation initiator). On hydrophilic surfaces, such interactions cause a rapid turnover of adsorbed albumin, so that sites it occupies will be often but only briefly available to other proteins [356]. This has been further verified with a mathematical model for Vroman's effect [340].

5.4.3 Marker of platelet activation sP-selectin ELISA on PAC vs. L605

The concentration of plasma P-selectin circulating in normal human blood is about 100 ng/mL, which can rise to as much as 1 µg/mL during pathological disorders and arterial thrombosis *in*

vivo, suggesting clinical relevance of the plasma isoform [315, 321]. In our study, we showed an increased level of soluble P-selectin in plasma (diluted 30x), isolated from whole blood after material contact, although values were significantly lower for PAC-L605 surfaces compared to L605 ($p=<0.0001$). However, both values were above normal concentration of plasma P-selectin (~31.5% higher with PAC-L605 and 68.45% with L605) indicating platelet activation for both surfaces. The sP-selectin ELISA assay was chosen to detect soluble isomer of P-selectin biomarker since: it's an ISO recommended marker for surface hemocompatibility, and has a longer half-life (1 hour). Length of its activity in circulation also correlates to length of *in vitro* flow assay; therefore a better estimate of platelet activation than β-TG with shorter half-life [315].

In vitro, the activation dependent increase in platelet surface P-selectin is not reversible over time [357]. *In vivo*, circulating platelets tracked via biotinylation showed they; 1) rapidly lose surface P-selectin, yet continue to circulate and function 2) were degranulated by thrombin very rapidly (~1 minute) to form circulating aggregates with monocytes (half-life 30 mins) and neutrophils (half-life 5 mins). While P-selectin expressed on activated platelets is known for its role in platelet aggregation and coagulation, studies have failed to identify the physiological role of circulating forms of soluble P-selectin *in vivo* [358].

Independent *in vivo* studies also confirmed circulating monocyte-platelet aggregates were more sensitive of platelet activity, than platelet surface P-selectin [324]. *In vivo* circulating degranulated platelets rapidly lose their surface P-selectin yet continue to circulate, indicating sP-selectin was not a robust biomarker of platelet activation. Clinical studies in human PCI and platelet activation, were also in agreement with the hypothesis, showing lower levels of P-selectin positive platelets, in comparison to circulating monocyte/neutrophil-platelet aggregates [324]. In lieu of previous investigations, plasma levels of sP-selectin quantified in

this study are therefore debatable. Biocompatibility of materials was assessed with more sensitive biomarkers of complement activation and inflammation, next, in accordance to ISO tests.

5.4.4 Reduced levels of complement activation marker SC5b-9 on PAC

The human complement system is part of the body's innate immunity, comprised of 3 distinct pathways to eliminate microorganisms and other foreign substances in circulation [327]. The three pathways lead to formation of terminal complement complex (TCC) also known as C5b-9, via membrane attack complex (MAC), illustrated in figure 5.2. All forms of stable TCC, investigated in this study are termed (soluble) SC5b-9. Not all MAC formed are inserted into pathogen cell membrane (as illustrated, figure 5.2), sublytic concentrations of the MAC stimulate various cells including platelets [359]. Complement activation after blood-material contact is broadly a marker of inflammatory host response to implantation [360].

Plasma samples were diluted x10 from the initial concentration for SC5b-9 ELISA. Although complement activation was observed for both surfaces, an 18% reduction of SC5b-9 concentration was observed after PAC-L605 contact, compared to alloy L605 ($p=0.0321$). Direct and continuous activation of the alternative pathway (AP) is the driving force behind complement-related effects for biomaterials/foreign surfaces [360], with classical and lectin pathway contributions. Pathway of complement activation varies depending on properties of biomaterial; physical/chemical properties and hydrophobicity/hydrophilicity [361]. Hydrophobic surfaces are more potent activators than hydrophilic, as seen in our study. However, chemical groups such as NH_3, OH, or COOH also influence activation, via the lectin pathway[361]. The lectin pathway is physiologically activated by certain carbohydrates on microbial surfaces [327] (figure 5.2, blue highlight). Regardless of surface composition, plasma

proteins cover all biomaterials *in vivo* [361], the adsorbed C3 in this initial protein layer, is formed via all three pathways, and will generate C3 convertase. Bioengineering surfaces to regulate innate immune recognition can prevent an adverse immune response after implanting biomaterials.

5.4.4.1 Mechanism of Alternative Pathway (AP) activation in the presence of a biomaterial

Studies investigated if complement activation after blood contact with a model biomaterial, occurred directly on material surface or on top of its adsorbed protein layer [362]. In the presence of a biomaterial, complement activation is first triggered by the classical pathway activation, via adsorption of protein film (figure 5.2, highlighted in purple). Adsorbed albumin, IgG, ***but not fibrinogen*** allowed covalent C3b binding, convertase assembly and amplification, mediated by AP next, on top of the adsorbed protein film (AP = alternative pathway, figure 5.2, green highlight).

Main event in the activation of complement is therefore, proteolytic cleavage of C3, detailed in [362] mediated by biomaterial surface protein aggregates, and not biomaterial itself. A model C3 activation and SC5b-9 complex formation (measured in this study), is schematically presented on a biomaterial surface in figure 5.8 [361] to explain AP activation mechanism. Initiation of biomaterial associated AP amplification process loop, is triggered by C3 convertase enzymes from all 3 pathways (discussed above). A hydrophilic biomaterial that conforms to the Vroman effect, and binds low levels of plasma proteins, will therefore be a poor activator of the complement system, as seen herein, and verified in previous investigations [363]. We conducted a 10 min and 60 min flow assay respectively, for plasma isolation for EIA, to understand variation of sC5b-9 complex concentration, with time. With time (10-60

min), the concentration of sC5b-9 complex increased by 57% on PAC-L605 surfaces and 63.82% on bare alloy L605. The generated complement activation in turn triggers platelets (as mentioned before) [324], polymorphonuclear leukocytes (PMNs), and monocytes/macrophages, to elicit a thrombotic and inflammatory response (figure 5.8).

Figure 5.8

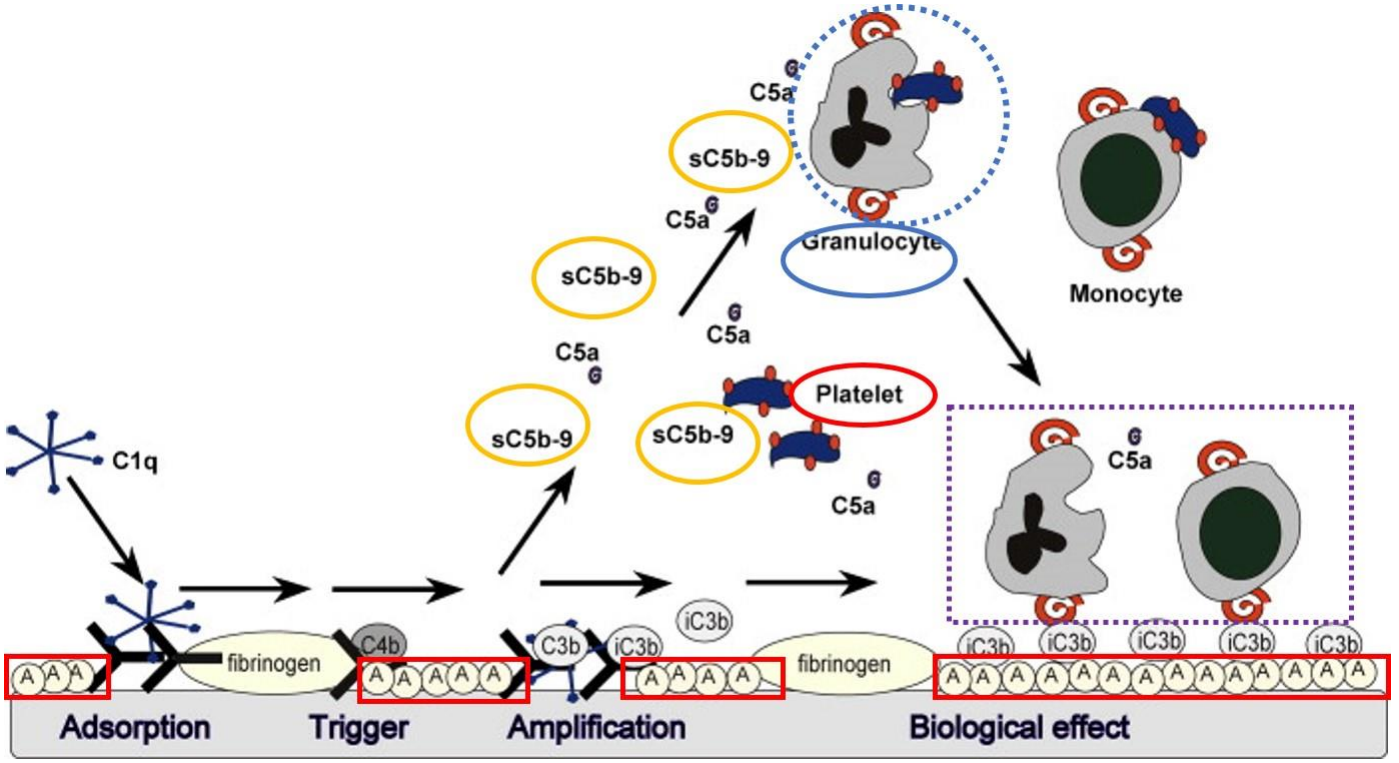

Model modified from [361], shows the initiation of complement activation on a biomaterial surface via alternative pathway-AP. Activation is triggered by protein film adsorbed initially to surface, including immunoglobins, fibrinogen, and human serum albumin (A) - highlighted in red, since it is predominantly involved in the catalysis of C3 to C3b. The generated C5a and SC5b-9 complex (yellow highlight, quantified in 5.2.7), activate platelets (red highlight, markers quantified in 5.2.5&6) as well as granulocytes (blue/dotted, quantified in 5.2.8), and monocytes. The complexes bind again to protein-bound iC3b (purple) to release proteolytic enzymes, more details in [361].

5.4.5 Factors contributing to PMN elastase - marker of leukocyte activation

Activation of each pathway discussed in this chapter, trigger amplification reactions and contribute to coagulation and inflammation [364]. PMN elastase, released via polymorphonuclear (PMN) granulocytes, is a marker of leukocyte activation. Concentration of PMN elastase was not significantly different between PAC-L605 and L605 surfaces ($p=0.1499$) (figure 5.7). The initial concentration of PMN elastase was relatively high requiring x100 dilution of original plasma content, for ELISA. The values were still comparatively lower than markers of complement SC5b-9 complex; which triggered the leukocyte activation (PMNs) and subsequent PMN elastase (proteolytic enzyme) release.

Mechanistically, the material-induced alternate pathway (AP) of complement cascade triggers leukocyte activation (figure 5.8). Note the complement-granulocyte-platelet aggregates formed (blue dotted line, figure 5.8), adhere to artificial surfaces via albumin-ic3b complexes (purple highlight, figure 5.8). The adherent neutrophils and monocytes then release their array of oxygen metabolites, growth factors, cytokines and proteolytic enzymes (PMN elastase) [365].

Hydrophobic surfaces are presumed to adhere, activate and release higher leukocyte proteases and cytokines [366], but we observed relatively higher PMN elastase concentration on hydrophilic PAC-L605 (values were not significant). This could be due to the higher turnover rate of albumin protein (Vroman effect) proposed on hydrophilic PAC-L605, compared to fibrinogen (abundant on L605). Given that leukocyte aggregates adhere to biomaterial surfaces specifically via ic3b bound to albumin protein (seen in figure 5.8), albumin may be predominant on PAC-L605, leading to observed higher PMN elastase concentrations on PAC-L605.

Overall, the highest concentration of biomarkers calculated in chapter 5, is in relation to complement activation (SC5B-9 complex). Complement activation occurs via 3 different

pathways, including AP, therefore higher concentration observed for L605 is as theoretically predicted. Furthermore, the complement cascade promotes leukocyte activation (figure 5.8, AP) [361], previous studies have shown inhibiting complement activation reduces material induced leukocyte activation *in vivo* [366]. Events occurring after blood-material contact quantified in this chapter, are schematically summarized in figure 5.9.

Figure 5.9

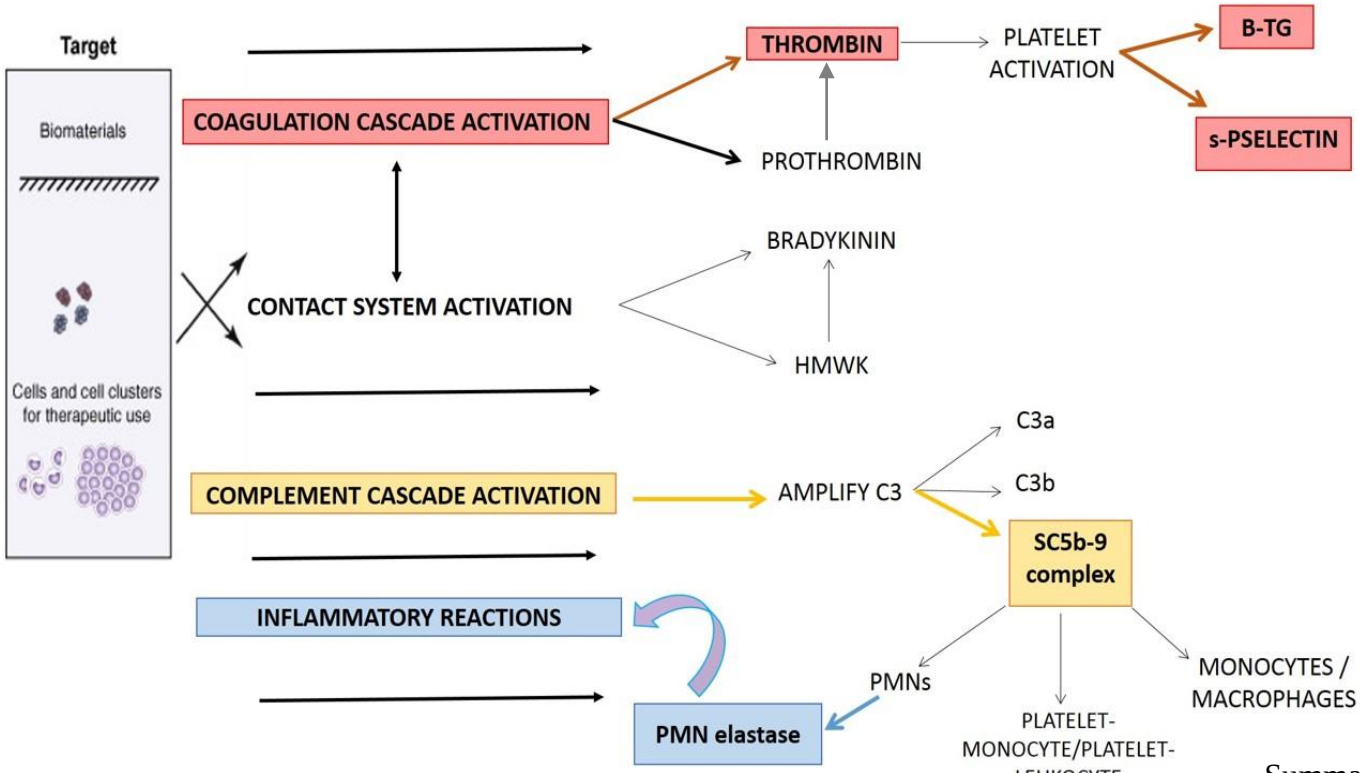

ELISA	L605	PAC-L605	Statistics	High Control	Low control
TAT (no dilution)	15.93±2.55 ng/mL	7.22±1.33 ng/mL	p=0.002	-	-
B-TG (no dilution)	27.16±3.75 ng/mL	16.61±3.33 ng/mL	p=0.025	-	-
sP-selectin (x30)	10.575±020 ng/mL **(317.25±6 ng/mL)**	4.87±0.07 ng/mL **(146.19±2.1 ng/mL)**	P=<0.0001	Beyond the standard values	2.078±0.090 (62.34±2.7 ng/mL)
sC5b-9 (x10)	120.27±15.05 ng/mL **(1202.77±150.53 ng/mL)**	98.18±21.88 ng/mL **(981.91±218.84 ng/mL)**	p=0.032	113.66±1.41 ng/mL (1136.6±14.16)	34.20±1.98 ng/mL, (342.0±19.80)
PMN elastase (x100)	2.72±0.45 ng/mL **(272.75±45.17 ng/mL)**	3.26±0.26 ng/mL **(326.84±26.03 ng/mL)**	p=0.149	10.67±2.9 ng/mL (1067.52±296.83 ng/mL)	1.19±0.41 (119.66±40.82 ng/mL)

Summary: Incompatibility reactions triggered via biomaterials upon exposure to blood and their *in vitro* quantification. The highlighted pathways and products were quantified in this study and presented respectively on adjacent table. Image modified from (68).

5.5 Conclusion and Future directions

The ISO10993-4 are a selection of recommended tests for hemocompatibility of biomedical devices after contact with human blood. The principle of *in vitro* flow assays is to quantify specific biological markers of coagulation, and inflammation, after blood-material contact under physiological conditions, via enzyme linked immunoabsorbent assays (ELISA).

PAC-L605 showed superior hemocompatibility compared to alloy L605, for clot formation at 60 mins via chandler loop assay, for all 5 assays. Plasma markers for TAT complex (thrombin-antithrombin formed), β-TG (platelet activation/degranulation), sP-selectin (1:30, platelet activation) and SC5b-9 (1:10, complement activation) were significantly low for PAC-L605 compared to alloy L605 bare metal. Markers of leukocyte activation, PMN elastase (1:100) were not significantly different between the two materials, although PAC-L605 surfaces showed an unexpected, and slightly higher concentration of the protease. As explained within context, high turnover rate of surface albumin (and HDL) proposed (Vroman effect), may contribute to overall results observed on hydrophilic PAC-L605 surfaces, including increased concentration of PMN elastase. This can be verified via comparative immunofluoroscent staining specifically for albumin protein, on PAC vs. L605 surfaces after 60 min flow assay, with anti-albumin antibody (ab106582, abcam, Cambridge MA, USA).

Since sP-selectin is not a reliable marker of platelet activation, due to soluble isoform shedding off in circulation, a platelet count (in accordance to ISO10993-4) can be conducted instead. Furthermore, ISO 10933-4 tests only apply to the evaluation of fabricated devices in their final form, not the modified material itself. Preliminary tests conducted here, should therefore be repeated after PAC technology is transferred to alloy L605, cobalt chromium commercial stents ML8 *in vitro*, to assess biocompatibility, prior to translation *in vivo*.

Chapter 6 – General Discussion

Two biomaterials of interest, alloy L605 and 316LSS, used to fabricate commercial stents were investigated in this study, with predominant focus on cobalt chromium metal alloy L605. The thesis initially describes a preliminary *in vivo* study of commercial 316L stainless steel (SS) stents modified with PAC, in a rabbit bilateral iliac artery model of endothelialization. Comparative physiological responses of PAC vs. BMS at the stent/artery interface, assessed degree of stent biointegration after implantation. The second biomaterial investigated was alloy L605, chosen for its composition as bare metal for new generation multi-link 8 (ML8) cobalt chromium stent system (Abbott Vascular). We conducted extensive *in vitro* investigations on PAC-L605 surfaces, coated with an optimized plasma recipe. The aim was improving surface biocompatibility, prior to transferring PAC technology to a commercial ML8 alloy L605 stent platform for *in vitro/in vivo* investigations, thereafter.

A biofunctionalized material for cardiovascular devices aim to promote desired physiological responses and achieve biointegration of the stent following implantation. Stents are used increasingly to treat coronary artery disease (CAD), a leading cause of death worldwide. Cardiovascular disease, its causes, intervention, stent incompatibility and novel stent modification techniques were detailed in chapter 1. Clinically, stents are limited by their potential to trigger biological responses in relation to coagulation, inflammation and restenosis *in vivo.* The work in this thesis examines a bioengineering approach to achieve a biomimetic stent coating. Initial PAC vs. BMS (316LSS stent) histopathology studies were followed by PAC-L605 vs. L605 mechanical characterization, at the molecular/atomic levels of cobalt chromium material. The study further investigated plasma kinetics, and *in vitro* biofunctionalization; via cytocompatibility, hemocompatibility and standardized tests, under physiological conditions.

6.1 Covalent immobilization of TE on PAC

Plasma modification of a material confers the unique ability to covalently bind a biomolecule of interest, in its bioactive state, on material surface [103]. Controlled covalent attachment of a protein candidate – tropoelastin (TE) (freely available in the subendothelial ECM), influenced material biocompatibility of both PAC-316LSS and PAC-L605, as predicted [187]. Prior to pilot *in vivo* study, *in vitro* covalent binding capacity of PAC-316LSS stents were investigated in chapter 2 with ELISA and radiolabelled TE. We showed increased levels of tropoelastin bound to PAC-316LSS stent surfaces after SDS wash, confirming covalent surface protein attachment (figure 2.2). The thesis next characterized covalent immobilization of TE, on PAC-L605 surfaces for the first time in chapter 4 with ELISA and SDS, showing similar results (figure 4.3).

However, recipe for PAC on L605 flat surfaces was markedly different from previous deposits on 316LSS stents/flat metal, due to present optimization and changed conditions of treatment. The previous plasma coating on alloy 316LSS was 200 nm in thickness; allowing a full monolayer of TE binding at ~50 nm [145]. In the present study, optimized PAC recipe for L605 was 20 nm in thickness. Absorbance values of covalent attachment after SDS were therefore markedly higher for PAC-316LSS compared to PAC-L605. The ability to control surface protein density allows customized applications of the material for specific uses. In the context of coronary stents, binding a monolayer of TE to encourage rapid *in vivo* endothelialization was beneficial. Even with a 20 nm PAC on L605, we observed improved covalent binding capacity and long-term biocompatibility, compared to bare alloy L605. In future, new PAC-L605 recipe could be tested over a range of deposition thicknesses, to assess density of TE molecules - forming a monolayer *in vitro*.

6.2 Biocompatibility of PAC-316LSS stent surfaces *in vivo*

In chapter 2, plasma technology was applied to a custom-built BMS (316LSS) with an altered deposition method, to that used on flat 316LSS surfaces. The surface deposition method produced a nodule-like nanomorphology combined with an ion stitched grading from 316LSS to PAC. The approach provided additional stability to the layer to prevent large scale delamination. The altered structure for PAC stents retained unique covalent protein binding capacity *in vitro* (chapter 2). In chapter 3, resistance to delamination was characterized, and verified on flat PAC-L605 (same plasma technology, different recipe and thickness), with focused ion beam (FIB) and transmission electron microscopy (TEM), for the first time on a cobalt chromium metal (figure 3.14).

Also for the first time, *in vivo* evaluation of PAC and PAC+TE was performed, in a well-established rabbit iliac artery model within chapter 2. In the pilot study, PAC, PAC+TE stents and BMS were implanted for 7-10 days. In this study, we focused only on 7 day, animal model comparing PAC+TE vs. BMS (chapter 2). Initial SEM, histology (H&E) and immunofluorescence analyses, revealed feasible implantation for both stent types, with no gross inflammatory reaction observed. Additionally PAC did not show evidence of significant delamination after implantation. Both stent types were analyzed for strut cell coverage with SEM and immunofluorescence with CD31 marker, specific to endothelial cells to confirm endothelialization at 7 days. Extent of endothelialization and cell coverage were equivalent for both stent types. This was the first *in vivo* investigation of a monomeric TE layer in a blood-contacting environment.

The stented artery segments were embedded in MMA resin for stent/artery interface histopathology. Methods of segmenting and deplasticizing resin-artery were trialled prior to staining. We used H&E to quantify early neointimal hyperplasia – NIH (neointimal thickness

and area), followed by Carstairs' staining to detect early markers of thrombosis (collagen, RBC, fibrin). Immunohistochemistry (IHC) with molecular markers for surface endothelialization (CD31) and macrophage/neutrophil infiltration (MAC387) was conducted on stent-artery cross sections thereafter.

The sectioning procedure was optimized using automated microtomes, for decreased section thickness, and increased staining uptake. Section adhesion was trialled to improve hydrophobic resin retention on a hydrophilic glass slide, throughout >3 hour protocols. At day 7, NIH was small for both stent types, but significantly low for PAC compared to BMS; in relation to thickness and area (figure 2.7). Carstairs staining showed significantly lowered fibrin on PAC vs. BMS, with no significant difference for collagen and RBC (figure 2.8). Immunostaining for MMA resin, followed by protein induced epitope retrieval (PIER) was trialled herein also for the first time, requiring multiple optimizations. The CD31 marker of endothelialization indicated presence of an incomplete monolayer of luminal endothelium at 7 days, as expected within the timeframe. However results were inconsistent on sections, potentially due to short timeline for healing and the resin type, as discussed in detail within chapter 2. Markers of macrophage/neutrophil (MAC 387) infiltration were similarly inconsistent and observed on both L605 and PAC+TE -artery cross sections. Markers of smooth muscle cell α actin were up taken non-specifically (figure 2.10) requiring further optimization of protocols.

Inflammatory neutrophil infiltration observed on PAC (day 7), resonates with high levels of plasma inflammatory marker PMN elastase (protease released from leukocytes), observed *in vitro* for PAC-L605 compared to bare L605 (chapter 5, figure 5.7). Even though markers of inflammation in the thesis appear to indicate an inflammatory response towards PAC or PAC+TE (potentially elicited via high surface albumin turnover rate), overall results of hemocompatibility and cytocompatibility quantified, significantly outweigh this observation (chapter 2/4/5 *in vivo* and *in vitro*).

Implanting PAC+TE stents was feasible at 7 days (0% mortality rate after PCI, until euthanasia). Future studies may increase timeline (28 days) for complete endothelialization, and animal number for a statistically robust outcome. Furthermore, biomarkers of inflammation (PMN elastase) could be measured from arterial blood collections at euthanasia (stored at -20^{o}C or -80^{o}C until ELISA), to assess *in vivo* inflammatory response. [Results here presented sequentially at the Scientific Sessions: American Heart Association; Dallas, Texas, USA 2013 [367], and World Congress of Cardiology, Melbourne, Australia, 2014 [368]].

6.3 Characterization of surface modification with PAC-L605

In chapter 3, for the first time herein, we addressed a key question on how plasma modified surfaces do not delaminate. At present, polymer delamination of DES has presented itself as a key issue, contributing to adverse clinical complications *in vivo* [192]. In contrast, PAC stent surfaces have shown to remain intact after compressive stress, both *in vitro* and after implantation *in vivo* [106]. Although the principle of delamination is outlined in plasma physics [103], the concept had not been experimentally confirmed, with the novel PAC recipe on a novel CoCr material. We therefore sought to analyze surface coating integrity on an alloy L605 surface via traditional technique of nanoindentation [202]. With increasing external load, the plasma coating stiffness increased, however at highest load, it did not surpass stiffness of the metal alloy, confirming coating integrity (figure 3.12). No delamination was seen at interface, and no plateau seen in load-displacement raw data (used to compute coating stiffness).

Furthermore, we investigated the interface of PAC-L605, via extensive techniques in material science characterization. The methods included tripod polishing, focussed ion beam (FIB) milling, and high resolution transmission electron microscopy (HRTEM) with inverse fast Fourier transform (IFFT), and selected area electron diffraction (SAED) method. The

techniques allowed visualization of surface modification at the PAC-L605 interface, to explain deposition methods in plasma physics that contributed to the unique, non-delaminating nature of this plasma coating - PAC (figure 3.14-3.16). [Initial results presented at the Arteriosclerosis, Thrombosis, Vascular Biology conference, 2015, San Francisco, California [369]].

Prior to extensive characterization of PAC modification, we quantified surface hydrophilicity of PAC on alloy L605, in accordance to previous investigations in applied plasma physics [209]. The results indicated decreased water contact angle and increased correlating surface energy, 15 mins post PAC deposition, confirming hydrophilicity of surface modification (figure 3.5-3.6). The surfaces were described as "functionalized" or activated via free radicals [103]. However, with time, on exposure to air, surface hydrophilicity decreased, as observed in preceding investigations [103, 209, 370] . Bilek et al, previously explained variation of surface free energy of PAC, with time, in relation to electron spin resonance (ESR) [103, 371]. With time, the PAC modification showed increased ESR for carbonyl (C=O) groups, and decreased ESR for free radicals (R*) [103, 371]. Investigations on surface energy variation of PAC-L605 herein, showed significantly decreased levels of polar surface free energy, in agreement with decreased levels of surface free radical (R*) ESR previously observed. The dispersive energy component correlating to surface oxidation, did not vary significantly from the calculated total surface energy (figure 3.7); also in agreement to increased levels of surface carbonyl groups (C=O) previously observed [103], as a result of oxidation with time. We did not quantify surface chemistry of ageing PAC-L605 via ESR in this study, since the substrate on which PAC was deposited is a metal alloy.

6.4 Enhanced endothelial cell interaction on PAC-L605-TE *in vitro*

Alloy L605, cobalt chromium metal was deposited with PAC for the first time in chapters 3-4. Two different PAC recipes were investigated on alloy L605, to assess plasma-based

biofunctionalization *in vitro*. PAC1: C-1, N-10, 500 V, t=20 min was compared with PAC2: C-2, N-10, 1000 V, t=10 min, via several methods including human coronary artery endothelial cell (HCAEC) culture. Biomaterial assisted-endothelialization aims to assist healing after the single layer of endothelial cells lining the vascular wall lumen [236], undergo injury during PCI, initiating coagulation and inflammation cascades [237]. Delays in healing vascular injury, mainly observed with DES, led to neointimal thickening and hyperplasia [114, 183, 237]. As a result, surface engineering materials aim to produce devices that promote endothelialization and assist natural healing process. Initially HCAEC proliferation on biomaterials at 3-5 days were visualized and quantified with crystal violet on PAC (with or without TE) vs. bare alloy L605. The quantified absorbance was highest for PAC+TE surfaces, followed by PAC and L605 (figure 4.6 A, B).

Bright field crystal violet staining showed HCAEC aggregates without specific organization on all material surfaces (Chapter 4, figure 4.6A). To identify intracellular organization, and visualize surface anchorage at 5 days, cellular cytoskeleton was stained with f-actin specific antibody phalloidin-TRITC. At high magnification, material surfaces best supporting cell attachment were PAC2-L605 and PAC2-L605-TE (Chapter 4, figure 4.7). In chapter 4, we conclude that surfaces with PAC2 surfaces, coupled with an ECM protein TE, supported homogenous cell proliferation compared to uncoated L605 and uncoated PAC1. Improved cell proliferation also proved that covalently bound TE remained bioactive on a material surface. Further, change in cell shape in response to substrate interaction is based on the cell's cytoskeleton. The HCAEC cytoskeleton seen on PAC2 with/without TE, mechanically stabilized the cell in a coordinated manner, compared to other biomaterial surfaces investigated (figure 4.7).

Further, we investigated endothelial cell specific marker vWF, present in Weibel-Palade bodies via vWF antibody, on PAC2 and alloy L605, at day 5. Morphology of vWF on the two surfaces

was not different. The protocol was optimized with 5% bovine serum albumin (BSA), to reduce background fluorescence, and optimize/heighten visualization of vWF. Although vWF is a prothrombogenic protein, similar antigen expression observed on both surfaces is a result of enhanced staining protocol. High magnification SEM showed improved surface integration of HCAECs on PAC+TE surfaces, followed by PAC alone, compared to bare metal (figure 4.8 C).

6.5 Thrombogenicity assessment of PAC-L605 and PAC+TE

In chapter 4, thrombogenicity of bioengineered surfaces investigated was in accordance to ISO 10993-12 standards [252]. Surface engineered biocompatibility was assessed via static and flow experiments with whole blood, and plasma, under physiological conditions *in vitro*. Platelet rich plasma (PRP) isolated from whole blood, was used to determine surface thrombogenicity, followed by static whole blood adhesion, within defined timelines. We confirmed improved surface hemocompatibility for PAC-L605 with or without TE, compared to L605. Superior hemocompatibility was observed in relation to platelet/fibrin aggregates, and whole blood adhesion (Figures 4.9 and 4.11). For the first time, we conducted an ageing study of TE incubated surfaces stored long term, by assessing hemocompatibility, in chapter 4. We saw no changes to surface hemocompatibility of PAC+TE stored overnight (4^{o}C), and PAC+TE stored for 2 weeks (-20^{o}C). Results were also similar to uncoated PAC aged for 1 month, and as before fibrin/platelet deposition was observed on alloy L605 (figure 4.10). Retention of activity over time, has implications for long-term storage, prior to preclinical studies in future.

For chandler loop assessments under flow we investigated hemocompatibility of PAC1 and PAC2 recipes, with or without tropoelastin and alloy L605. We chose PAC1 surfaces for future flow assays, due to improved hemocompatibility seen (lower clot formation than PAC2; results

not significant) (figure 4.13 A). All blood-material experiments were conducted with heparinized whole blood. Heparin was chosen as the suited anticoagulant, due to minimal inhibition of coagulation components and platelets.

Overall, PAC2 (C-2, N-10, t=10 min) surfaces showed higher cytocompatibility, while PAC1 (C-1, N-10, t=20 min) surfaces showed higher hemocompatibility (chapter 4). For an ideal PAC surface, the 2 recipes could be merged to form; C-1, N-10, t>20 min deposition (PAC3). The resulting surface would have a stoichiometry of C: N similar to PAC1 (1:10), but with higher deposition thickness, for equivalent cytocompatibility and hemocompatibility.

6.6 ISO tests for modified materials prior to L605 stent evaluation

In chapter 5, a series of enzyme linked immunoabsorbent assays (ELISAs), were conducted after *in vitro* whole blood flow. The aim was to investigate markers of coagulation and inflammation, after blood-material contact, in accordance to ISO10993-4 regulations. Modified chandler loop flow assays were conducted prior to each plasma isolation, for PAC1 vs. L605. PAC1 was chosen due to superior hemocompatibility, observed in chapter 4 (ISO 10993-12 tests). Individual plasma biomarkers for TAT complex, β-TG, sP-selectin, SC5b-9 and PMN elastase were quantified.

As observed in chapter 4, PAC surfaces had significantly lower clot formation at 60 min, compared to alloy L605. Plasma biomarkers for TAT, β-TG, sP-selectin and SC5b-9 were significantly lower on PAC, indicating lowered coagulation, platelet activation and complement activation respectively (figures 5.3-5.6). Results for sP-selectin were widely variable between the two surfaces, therefore average values were chosen for GraphPad prism (figure 5.7). However, overall quantification of sP-selectin as a biomarker of plasma activation

was debated, based on previous *in vivo* data. For instance former studies showed the physiological role of circulating soluble P-selectin wasn't determined *in vivo* [358], and circulating platelets rapidly lost their surface P-selectin *in vivo* [324]. Platelet count after blood-material contact and plasma isolation, was suggested as an alternative to quantify levels of plasma protein, also in accordance to ISO 10993-4 tests.

Plasma levels of PMN elastase, proteolytic enzyme released by leukocyte activation, were not significantly different between the two surfaces (figure 5.7). Trends were however indicative of increased levels of PMN elastase, for PAC vs. L605. This was an unexpected result. Previously, we explained results of hemocompatibility in relation to reduced markers of initial coagulation and complement activation on PAC, via the Vroman effect [338]. The same effect, may result in a high turnover rate of albumin on PAC, contributing to activation of leukocytes via the alternative pathway (AP) discussed in 5.4.5 (figure 5.8). Additionally, surfaces can be investigated for albumin in future, as conducted with fibrinogen after flow experiments in chapter 4. In future, PAC-L605 incubated with tropoelastin (PAC-L605-TE) can be included as a variable, to investigate impact of TE on plasma biomarkers and surface biocompatibility.

6.7 Implications and future development for stent platform

The series of investigations in this thesis intend to modify commercially available biomaterials for biocompatibility. The proprietary plasma technology, aimed at surface modification to create a strong, non-delaminating plasma-material interface that covalently bound a protein, in its bioactive conformation. The two biomaterials of interest; commercially available stainless steel (alloy 316L), and cobalt chromium (alloy L605), are presently used in stenting technology [372]. Alloy 316LSS stents were investigated initially in an *in vivo* stent platform, to indicate PAC+TE stent feasibility. A longer time point, larger study cohort, and optimized technical

methods would allow assessment of complete NIH, including extensive histopathological studies for markers of endothelialization, and inflammation - in future. Reduction of restenosis would be apparent at 28 days, and should be investigated *in vivo*, since no reliable *in vitro* model exists.

The technology was modified and optimized on alloy L605 surfaces for the first time. Alloy L605 with ASTM F90 specifications was chosen - for its composition is the same as bare metal for new generation multi-link 8 (ML8) cobalt chromium stent system (Abbott Vascular). This study was a first to investigate PAC-L605 interface via TEM, to show ionic stitching and confirm non-delaminating features of PAC, unique to plasma technology. Also for the first time for PAC-L605, we investigated surface biofunctionalization, and proposed optimum conditions for PAC recipe to equally meet *in vitro* cytocompatibility and hemocompatibility. The PAC recipe will be translated to a coronary stent platform, in future, to comparatively assess biocompatibility of PAC-ML8 vs. ML8 (Abbott Vascular). As mentioned, ISO 10993-4 biocompatibility tests should be repeated on PAC-ML8 stents, prior to translational studies *in vivo.*

Recent developments on stent design (since five years - leading to 2012), to prevent restenosis and LST are outlined in table 6.1, from [372]. Bioeresorbable stents, biodegradable polymers and biocompatible permanent polymer stents have received much medical attention due to their innovative technologies [372-374]. When a stent polymer coating disintegrates after its defined period of drug elution *in vivo*, or delaminates due to flow shear [192], the underlying bare metal will be exposed to coronary artery flow. The underlying metal should therefore biointegrate, for sustained biocompatibility. An optimized PAC stent surface aims to maintain long-term biocompatibility, and is therefore an ideal candidate as an underlying stent for a DES platform, such as with Polyzene-F Nanocoated cobalt-chromium stents [373], or in its bare PAC-cobalt chromium form.

For future directions *in vitro*, chandler loop model of a stent requires additional flow characterization, since level of shear stress can influence platelet, endothelial cell activation, and coagulation rates [252]. Key fluid mechanics parameters characterize curved blood flow, fluid friction, and sample volume in a chandler loop-stent model. All parameters should be investigated to determine model sensitivity and outcome.

Table 6.1. Developments in preventive measures for restenosis, from [372]

Target	Development	Status
Antiproliferative drug	Sirolimus derivatives (biolimus A9[375, 376] and novolimus[377]	Clinical
Polymer	Biolinx® (Medtronic Vascular, Inc, Santa Roasa, CA, USA)[378]	Clinical preliminary
Polymer	Polyzene-F [373], [379]	Clinical preliminary
Polymer	Biodegradable (polylactic acid, polylactic-co-glycolic acid, [380, 381] Synbiosys® [InnoCore Technologies, Groningen, Netherlands], Eureka® SOLO [Surmodics, Inc., MN, USA]	Clinical
Stent design	Polymer free stent (Biofreedom®, Biosensors International Group, Hamilton, Bermuda) [382]	Clinical preliminary
Coating	Endothelial progenitor cell capturing stent (Genous®[383, 384], Combo stent® [385] [OrbusNeich Medical, Inc., FL, USA])	Clinical
Coating	Titanium-nitride-oxide-coated stents (Titan2™ stent [Hexacath, France])[386-389]	Clinical
Stent platform	Bioabsorbable stent (magnesium stent [Biotronik, Berlin, Germany])[390-392]	Clinical
Drug delivery	Nanomedicine[393, 394]	Preclinical

Stent platform/metal alloys	Platinum-chromium alloy stents (Promus Element® and Taxus Element® (Boston Scientific, MN, USA) [176, 395]	Clinical
Drug delivery	Magnetic targeting stents [374]	Preclinical
Miscellaneous	Gene-based therapy[396-399]	Preclinical
Miscellaneous	Systemic treatment[400-402]	Clinical

6.8 Conclusions

The plasma technology - PAC is robust, hemocompatible and cytocompatible, capable of binding a monolayer of tropoelastin on biomaterial surfaces. *In vivo* stenting was feasible for PAC316LSS stents at 7 days, and has potential for future translational studies within an increased timeframe. *In vitro* PAC-L605 showed non-delaminating coating technology and superior biocompatibility, to the bare metal alloy L605. Prior to translating PAC technology to a new generation alloy L605 cobalt chromium coronary stent, it was essential to experimentally prove coating integrity, and biological superiority of PAC-L605 surfaces; so a cost-effective flat biomaterial was chosen. We now have promising implications to modify a commercially available cobalt chromium stenting technology - ML8, composed of the alloy L605, in future. This was the overall aim and outcome of the present study.

References

1. de Mel, A., B.G. Cousins, and A.M. Seifalian, *Surface modification of biomaterials: a quest for blood compatibility.* Int J Biomater, 2012. **2012**: p. 707863.
2. Allender, S., et al., *Patterns of coronary heart disease mortality over the 20th century in England and Wales: Possible plateaus in the rate of decline.* BMC Public Health, 2008. **8**: p. 148.
3. de Mel, A., et al., *Biofunctionalization of biomaterials for accelerated in situ endothelialization: a review.* Biomacromolecules, 2008. **9**(11): p. 2969-79.
4. Sigwart, U., et al., *Intravascular stents to prevent occlusion and restenosis after transluminal angioplasty.* N Engl J Med, 1987. **316**(12): p. 701-6.
5. Palmaz, J.C., et al., *Expandable intraluminal vascular graft: a feasibility study.* Surgery, 1986. **99**(2): p. 199-205.
6. Wright, K.C., et al., *Percutaneous endovascular stents: an experimental evaluation.* Radiology, 1985. **156**(1): p. 69-72.
7. Schatz, R.A., *Coronary Stenting, Report of the Initial Clinical-Experience with the Palmaz-Schatz Tm Balloon Expandable Stent.* Quantitative Coronary Arteriography, 1991. **117**: p. 313-325.
8. Schatz, R.A., et al., *Clinical-Experience with the Palmaz-Schatz Coronary Stent.* Journal of the American College of Cardiology, 1991. **17**(6): p. B155-B159.
9. Hofma, S.H., et al., *Increasing arterial wall injury after long-term implantation of two types of stent in a porcine coronary model.* European Heart Journal, 1998. **19**(4): p. 601-609.
10. Lau, A.K., et al., *Probucol promotes functional reendothelialization in balloon-injured rabbit aortas.* Circulation, 2003. **107**(15): p. 2031-2036.
11. Wu, K.K. and P. Thiagarajan, *Role of endothelium in thrombosis and hemostasis.* Annual Review of Medicine, 1996. **47**: p. 315-331.
12. Joner, M., et al., *Pathology of drug-eluting stents in humans - Delayed healing and late thrombotic risk.* Journal of the American College of Cardiology, 2006. **48**(1): p. 193-202.
13. Serruys, P.W., et al., *Periprocedural quantitative coronary angiography after Palmaz-Schatz stent implantation predicts the restenosis rate at six months - Results of a meta-analysis of the Belgian Netherlands Stent Study (BENESTENT) I, BENESTENT II pilot, BENESTENT II and MUSIC trials.* Journal of the American College of Cardiology, 1999. **34**(4): p. 1067-1074.
14. Cutlip, D.E., et al., *Clinical end points in coronary stent trials - A case for standardized definitions.* Circulation, 2007. **115**(17): p. 2344-2351.
15. Daemen, J., et al., *Early and late coronary stent thrombosis of sirolimus-eluting and paclitaxel-eluting stents in routine clinical practice: data from a large two-institutional cohort study.* Lancet, 2007. **369**(9562): p. 667-678.
16. Kedhi, E., et al., *Second-generation everolimus-eluting and paclitaxel-eluting stents in real-life practice (COMPARE): a randomised trial.* Lancet, 2010. **375**(9710): p. 201-209.
17. Lemesle, G., et al., *Stent thrombosis in 2008: Definition, predictors, prognosis and treatment.* Archives of Cardiovascular Diseases, 2008. **101**(11-12): p. 769-777.
18. Mani, G., et al., *Coronary stents: A materials perspective.* Biomaterials, 2007. **28**(9): p. 1689-1710.

19. Le Feuvre, C., et al., *Long-term follow-up of patients with sirolimus-eluting stents for treatment of bare-metal in-stent restenosis.* International Journal of Cardiology, 2010. **140**(2): p. 219-225.
20. Serruys, P.W., et al., *Peri-procedural PCA following Palmaz-Schatz stent implantation predicts restenosis rate at 6 months: Result of a meta-analysis of BENESTENT-I, BENESTENT-II pilot, BENESTENT-II and MUSIC.* Journal of the American College of Cardiology, 1998. **31**(2): p. 64a-64a.
21. Price, M., *Coronary Stenting: A Companion to Topol's Textbook of Interventional Cardiology E-Book*. 1 ed. 2013: Elsevier.
22. Kereiakes, D.J., et al., *Usefulness of a cobalt chromium coronary stent alloy.* American Journal of Cardiology, 2003. **92**(4): p. 463-466.
23. Kiemeneij, F., et al., *Continued benefit of coronary stenting versus balloon angioplasty: Five-year clinical follow-up of Benestent-I trial.* Journal of the American College of Cardiology, 2001. **37**(6): p. 1598-1603.
24. Park, S.W., et al., *Immediate and late clinical and angiographic outcomes after GFX coronary stenting: Is high-pressure balloon dilatation necessary?* Clinical Cardiology, 2000. **23**(8): p. 595-599.
25. Ooya, T., J. Lee, and K. Park, *Effects of ethylene glycol-based graft, star-shaped, and dendritic polymers on solubilization and controlled release of paclitaxel.* Journal of Controlled Release, 2003. **93**(2): p. 121-127.
26. Yan, B.P., A.E. Ajani, and R. Waksman, *Drug-eluting stents for the treatment of in-stent restenosis: a clinical review.* Cardiovasc Revasc Med, 2005. **6**(1): p. 38-43.
27. Moses, J.W., et al., *Sirolimus-eluting stents versus standard stents in patients with stenosis in a native coronary artery.* N Engl J Med, 2003. **349**(14): p. 1315-23.
28. Lowe, H.C. and L.M. Khachigian, *Coating stents with antirestenotic drugs: the blunderbuss or the magic bullet?* Circulation, 2002. **105**(4): p. E29.
29. Sehgal, S.N., *Rapamune (RAPA, rapamycin, sirolimus): mechanism of action immunosuppressive effect results from blockade of signal transduction and inhibition of cell cycle progression.* Clin Biochem, 1998. **31**(5): p. 335-40.
30. Steffel, J., T.F. Luscher, and F.C. Tanner, *Tissue factor in cardiovascular diseases - Molecular mechanisms and clinical implications.* Circulation, 2006. **113**(5): p. 722-731.
31. Steffel, J., et al., *Rapamycin, but not FK-506, increases endothelial tissue factor expression: implications for drug-eluting stent design.* Circulation, 2005. **112**(13): p. 2002-11.
32. O'Brien, B. and W. Carroll, *The evolution of cardiovascular stent materials and surfaces in response to clinical drivers: a review.* Acta Biomater, 2009. **5**(4): p. 945-58.
33. Joner, M., et al., *Endothelial cell recovery between comparator polymer-based drug-eluting stents.* J Am Coll Cardiol, 2008. **52**(5): p. 333-42.
34. Planer, D., et al., *Comparison of everolimus- and paclitaxel-eluting stents in patients with acute and stable coronary syndromes: pooled results from the SPIRIT (A Clinical Evaluation of the XIENCE V Everolimus Eluting Coronary Stent System) and COMPARE (A Trial of Everolimus-Eluting Stents and Paclitaxel-Eluting Stents for Coronary Revascularization in Daily Practice) Trials.* JACC Cardiovasc Interv, 2011. **4**(10): p. 1104-15.
35. Windecker, S., et al., *Biolimus-eluting stent with biodegradable polymer versus sirolimus-eluting stent with durable polymer for coronary revascularisation (LEADERS): a randomised non-inferiority trial.* Lancet, 2008. **372**(9644): p. 1163-73.

36. Costa, R.A., et al., *Angiographic results of the first human experience with the Biolimus A9 drug-eluting stent for de novo coronary lesions.* Am J Cardiol, 2006. **98**(4): p. 443-6.
37. Abizaid, A. and J.R. Costa, Jr., *New drug-eluting stents: an overview on biodegradable and polymer-free next-generation stent systems.* Circ Cardiovasc Interv, 2010. **3**(4): p. 384-93.
38. Haude, M., et al., *The REMEDEE trial: a randomized comparison of a combination sirolimus-eluting endothelial progenitor cell capture stent with a paclitaxel-eluting stent.* JACC Cardiovasc Interv, 2013. **6**(4): p. 334-43.
39. Pendyala, L., et al., *Passive and active polymer coatings for intracoronary stents: novel devices to promote arterial healing.* J Interv Cardiol, 2009. **22**(1): p. 37-48.
40. Luscher, T.F., et al., *Drug-eluting stent and coronary thrombosis: biological mechanisms and clinical implications.* Circulation, 2007. **115**(8): p. 1051-8.
41. Urban, P. and E. De Benedetti, *Thrombosis: the last frontier of coronary stenting?* Lancet, 2007. **369**(9562): p. 619-21.
42. Eshaghian, S., et al., *Role of clopidogrel in managing atherothrombotic cardiovascular disease.* Ann Intern Med, 2007. **146**(6): p. 434-41.
43. Yan, B.P., R. Gurvitch, and A.E. Ajani, *Double jeopardy: balance between bleeding and stent thrombosis with prolonged dual antiplatelet therapy after drug-eluting stent implantation.* Cardiovasc Revasc Med, 2006. **7**(3): p. 155-8.
44. Nebeker, J.R., et al., *Hypersensitivity cases associated with drug-eluting coronary stents: a review of available cases from the Research on Adverse Drug Events and Reports (RADAR) project.* J Am Coll Cardiol, 2006. **47**(1): p. 175-81.
45. Eisenstein, E.L., et al., *Clopidogrel use and long-term clinical outcomes after drug-eluting stent implantation.* Jama-Journal of the American Medical Association, 2007. **297**(2): p. 159-168.
46. Stone, G.W., et al., *Effect of Prolonged Thienopyridine Use After Drug-Eluting Stent Implantation (from the TAXUS Landmark Trials Data).* American Journal of Cardiology, 2008. **102**(8): p. 1017-1022.
47. Sarno, G., et al., *Lower risk of stent thrombosis and restenosis with unrestricted use of onew-generation' drug-eluting stents: a report from the nationwide Swedish Coronary Angiography and Angioplasty Registry (SCAAR).* European Heart Journal, 2012. **33**(5): p. 606-613.
48. Galasso, G., et al., *Unrestricted Use of Endeavor Resolute Zotarolimus-Eluting Stent in Daily Clinical Practice: A Prospective Registry.* Journal of Invasive Cardiology, 2012. **24**(6): p. 251-255.
49. Stone, G.W., et al., *Randomized Comparison of Everolimus-Eluting and Paclitaxel-Eluting Stents Two-Year Clinical Follow-Up From the Clinical Evaluation of the Xience V Everolimus Eluting Coronary Stent System in the Treatment of Patients With De Novo Native Coronary Artery Lesions (SPIRIT) III Trial.* Circulation, 2009. **119**(5): p. 680-686.
50. Sarno, G., et al., *Initial clinical experience with an everolimus eluting platinum chromium stent (Promus Element) in unselected patients from the Swedish Coronary Angiography and Angioplasty Registry (SCAAR).* International Journal of Cardiology, 2013. **167**(1): p. 146-150.
51. Shi, Q., et al., *Evidence for circulating bone marrow-derived endothelial cells.* Blood, 1998. **92**(2): p. 362-367.
52. Marx, S.O., et al., *Rapamycin-Fkbp Inhibits Cell-Cycle Regulators of Proliferation in Vascular Smooth-Muscle Cells.* Circulation Research, 1995. **76**(3): p. 412-417.

53. Guba, M., et al., *Rapamycin inhibits primary and metastatic tumor growth by antiangiogenesis: involvement of vascular endothelial growth factor.* Nature Medicine, 2002. **8**(2): p. 128-135.
54. Butzal, M., et al., *Rapamycin inhibits proliferation and differentiation of human endothelial progenitor cells in vitro.* Experimental Cell Research, 2004. **300**(1): p. 65-71.
55. Chen, T.G., J.Z. Chen, and X.X. Wang, *Effects of rapamycin on number activity and eNOS of endothelial progenitor cells from peripheral blood.* Cell Proliferation, 2006. **39**(2): p. 117-125.
56. Iakovou, I., et al., *Incidence, predictors, and outcome of thrombosis after successful implantation of drug-eluting stents.* Jama-Journal of the American Medical Association, 2005. **293**(17): p. 2126-2130.
57. Koster, R., et al., *Nickel and molybdenum contact allergies in patients with coronary in-stent restenosis.* Lancet, 2000. **356**(9245): p. 1895-1897.
58. Schofer, J., et al., *Sirolimus-eluting stents for treatment of patients with long atherosclerotic lesions in small coronary arteries: double-blind, randomised controlled trial (E-SIRIUS).* Lancet, 2003. **362**(9390): p. 1093-1099.
59. Virmani, R., et al., *Localized hypersensitivity and late coronary thrombosis secondary to a sirolimus-eluting stent: should we be cautious?* Circulation, 2004. **109**(6): p. 701-5.
60. Finn, A.V., et al., *Differential response of delayed healing and persistent inflammation at sites of overlapping sirolimus- or paclitaxel-eluting stents.* Circulation, 2005. **112**(2): p. 270-278.
61. Niemi, S.M., et al., *Evaluation of Ethylene-Vinyl Acetate Copolymer as a Noninflammatory Alternative to Freunds Complete Adjuvant in Rabbits.* Laboratory Animal Science, 1985. **35**(6): p. 609-612.
62. Farb, A., et al., *Morphological predictors of restenosis after coronary stenting in humans.* Circulation, 2002. **105**(25): p. 2974-2980.
63. Chen, M.C., et al., *A novel drug-eluting stent spray-coated with multi-layers of collagen and sirolimus.* Journal of Controlled Release, 2005. **108**(1): p. 178-189.
64. Huang, Y.Y., et al., *In vitro and in vivo performance of a dual drug-eluting stent (DDES).* Biomaterials, 2010. **31**(15): p. 4382-4391.
65. Levy, Y., et al., *Evaluation of Drug-Eluting Stents' Coating Durability-Clinical and Regulatory Implications.* Journal of Biomedical Materials Research Part B-Applied Biomaterials, 2009. **91b**(1): p. 441-451.
66. Basalus, M., et al., *Coating irregularities of durable polymer-based drug-eluting stents as assessed by scanning electron microscopy.* European Heart Journal, 2009. **30**: p. 241-241.
67. Otsuka, F., et al., *Pathology of Second-Generation Everolimus-Eluting Stents Versus First-Generation Sirolimus- and Paclitaxel-Eluting Stents in Humans.* Circulation, 2014. **129**(2): p. 211-223.
68. Wiemer, M., et al., *Scanning Electron Microscopic Analysis of Different Drug Eluting Stents After Failed Implantation: From Nearly Undamaged to Major Damaged Polymers.* Catheterization and Cardiovascular Interventions, 2010. **75**(6): p. 905-911.
69. Finn, A.V., et al., *Vascular responses to drug eluting stents - Importance of delayed healing.* Arteriosclerosis Thrombosis and Vascular Biology, 2007. **27**(7): p. 1500-1510.
70. Reifart, N., et al., *The NUGGET study: NIR ultra gold-gilded equivalency trial.* Catheterization and Cardiovascular Interventions, 2004. **62**(1): p. 18-25.

71. Gutensohn, K., et al., *In vitro analyses of diamond-like carbon coated stents: Reduction of metal ion release, platelet activation, and thrombogenicity.* Thrombosis Research, 2000. **99**(6): p. 577-585.
72. Antoniucci, D., et al., *Clinical and angiographic outcomes following elective implantation of the Carbostent in patients at high risk of restenosis and target vessel failure.* Catheterization and Cardiovascular Interventions, 2001. **54**(4): p. 420-426.
73. Lewis, A.L., *Phosphorylcholine-based polymers and their use in the prevention of biofouling.* Colloids and Surfaces B-Biointerfaces, 2000. **18**(3-4): p. 261-275.
74. Whelan, D.M., et al., *Biocompatibility of phosphorylcholine coated stents in normal porcine coronary arteries.* Heart, 2000. **83**(3): p. 338-345.
75. Wohrle, J., et al., *Comparison of the heparin coated vs the uncoated Jostent (R) - no influence on restenosis or clinical outcome.* European Heart Journal, 2001. **22**(19): p. 1808-1816.
76. Aoki, J., et al., *Endothelial progenitor cell capture by stents coated with antibody against CD34: the HEALING-FIM (Healthy Endothelial Accelerated Lining Inhibits Neointimal Growth-First In Man) Registry.* J Am Coll Cardiol, 2005. **45**(10): p. 1574-9.
77. Inoue, T., et al., *Mobilization of CD34-positive bone marrow-derived cells after coronary stent implantation - Impact on restenosis.* Circulation, 2007. **115**(5): p. 553-561.
78. Beijk, M.A.M., et al., *Genous (TM) endothelial progenitor cell capturing stent vs. the Taxus Liberte stent in patients with de novo coronary lesions with a high-risk of coronary restenosis: a randomized, single-centre, pilot study.* European Heart Journal, 2010. **31**(9): p. 1055-1064.
79. Larsen, K., et al., *Capture of circulatory endothelial progenitor cells and accelerated re-endothelialization of a bio-engineered stent in human ex vivo shunt and rabbit denudation model.* European Heart Journal, 2012. **33**(1): p. 120-128.
80. Blindt, R., et al., *A novel drug-eluting stent coated with an integrin-binding cyclic Arg-Gly-Asp peptide inhibits neointimal hyperplasia by recruiting endothelial progenitor cells.* Journal of the American College of Cardiology, 2006. **47**(9): p. 1786-1795.
81. Ormiston, J.A. and P.W.S. Serruys, *Bioabsorbable Coronary Stents.* Circulation-Cardiovascular Interventions, 2009. **2**(3): p. 255-260.
82. Garg, S., H.J. Duckers, and P.W. Serruys, *Endothelial progenitor cell capture stents: will this technology find its niche in contemporary practice?* European Heart Journal, 2010. **31**(9): p. 1032-1035.
83. Tamai, H., et al., *Initial and 6-month results of biodegradable poly-l-lactic acid coronary stents in humans.* Circulation, 2000. **102**(4): p. 399-404.
84. *A randomized comparison of a durable polymer everolimus eluting coronary stent with a bare metal coronary stent: The SPIRIT first trial 12-month results.* Circulation, 2005. **112**(17): p. U612-U612.
85. Erbel, R., et al., *Temporary scaffolding of coronary arteries with bioabsorbable magnesium stents: a prospective, non-randomised multicentre trial.* Lancet, 2007. **369**(9576): p. 1869-1875.
86. Ormiston, J.A., et al., *Six-month angiographic and 12-month clinical follow-up of multilink long (25 to 35 mm) stents for long coronary narrowings in patients with angina pectoris.* American Journal of Cardiology, 2002. **90**(3): p. 222-226.
87. Jabara, R., et al., *In-Vivo Intravascular Imaging of Novel Fully Bioabsorbable Salicylate-Based Sirolimus-Eluting Stent.* Journal of the American College of Cardiology, 2009. **53**(10): p. A17-A18.

88. Grube, E., et al., *A Novel Paclitaxel-Eluting Stent With an Ultrathin Abluminal Biodegradable Polymer 9-Month Outcomes With the JACTAX HD Stent.* Jacc-Cardiovascular Interventions, 2010. **3**(4): p. 431-438.
89. Onuma, Y., J. Ormiston, and P.W. Serruys, *Bioresorbable Scaffold Technologies.* Circulation Journal, 2011. **75**(3): p. 509-520.
90. Bittl, J.A., *Bioresorbable Stents The Next Revolution.* Circulation, 2010. **122**(22): p. 2236-2238.
91. Mu, L. and S.S. Feng, *PLGA/TPGS nanoparticles for controlled release of paclitaxel: Effects of the emulsifier and drug loading ratio.* Pharmaceutical Research, 2003. **20**(11): p. 1864-1872.
92. Locatelli, E. and M.C. Franchini, *Biodegradable PLGA-b-PEG polymeric nanoparticles: synthesis, properties, and nanomedical applications as drug delivery system.* Journal of Nanoparticle Research, 2012. **14**(12).
93. Soppimath, K.S., et al., *Biodegradable polymeric nanoparticles as drug delivery devices.* Journal of Controlled Release, 2001. **70**(1-2): p. 1-20.
94. Feng, S.S., L.Y. Zhao, and J.T. Tang, *Nanomedicine for oral chemotherapy.* Nanomedicine, 2011. **6**(3): p. 407-410.
95. Otake, H., et al., *Intravascular Ultrasound Results From the NEVO ResElution-I Trial A Randomized, Blinded Comparison of Sirolimus-Eluting NEVO Stents With Paclitaxel-Eluting Taxus Liberte Stents in De Novo Native Coronary Artery Lesions.* Circulation-Cardiovascular Interventions, 2011. **4**(2): p. 146-U69.
96. Ormiston, J.A., et al., *Six-Month Results of the NEVO RES-ELUTION I (NEVO RES-I) Trial A Randomized, Multicenter Comparison of the NEVO Sirolimus-Eluting Coronary Stent With the TAXUS Liberte Paclitaxel-Eluting Stent in De Novo Native Coronary Artery Lesions.* Circulation-Cardiovascular Interventions, 2010. **3**(6): p. 556-564.
97. Stone, G.W., et al., *Prospective, Randomized, Multicenter Evaluation of a Polyethylene Terephthalate Micronet Mesh-Covered Stent (MGuard) in ST-Segment Elevation Myocardial Infarction The MASTER Trial.* Journal of the American College of Cardiology, 2012. **60**(19): p. 1975-1984.
98. Cheruthazhekatt, S., et al., *Gas plasmas and plasma modified materials in medicine.* Journal of Applied Biomedicine, 2010. **8**(2): p. 55-66.
99. Svorcik, V., et al., *Plasma-Modified and Polyethylene Glycol-Grafted Polymers for Potential Tissue Engineering Applications.* Journal of Nanoscience and Nanotechnology, 2012. **12**(8): p. 6665-6671.
100. Montgomery, D., *Plasma physics. An introduction to the theory of astrophysical, geophysical, and laboratory plasmas - Sturrock,PA.* Science, 1996. **271**(5247): p. 309-309.
101. Wise, S.G., et al., *Plasma-based biofunctionalization of vascular implants.* Nanomedicine, 2012. **7**(12): p. 1907-1916.
102. Yin, Y.B., et al., *Acetylene plasma polymerized surfaces for covalent immobilization of dense bioactive protein monolayers.* Surface & Coatings Technology, 2009. **203**(10-11): p. 1310-1316.
103. Bilek, M.M.M., et al., *Free radical functionalization of surfaces to prevent adverse responses to biomedical devices.* Proceedings of the National Academy of Sciences of the United States of America, 2011. **108**(35): p. 14405-14410.
104. Siow, K.S., et al., *Plasma methods for the generation of chemically reactive surfaces for biomolecule immobilization and cell colonization - A review.* Plasma Processes and Polymers, 2006. **3**(6-7): p. 392-418.

105. Waterhouse, A., et al., *The immobilization of recombinant human tropoelastin on metals using a plasma-activated coating to improve the biocompatibility of coronary stents.* Biomaterials, 2010. **31**(32): p. 8332-8340.
106. Waterhouse, A., et al., *In vivo biocompatibility of a plasma-activated, coronary stent coating.* Biomaterials, 2012. **33**(32): p. 7984-7992.
107. Jeewandara, T.M., S.G. Wise, and M.K.C. Ng, *Biocompatibility of Coronary Stents.* Materials, 2014. **7**(2): p. 769-786.
108. Go, A.S., et al., *Heart disease and stroke statistics--2014 update: a report from the American Heart Association.* Circulation, 2014. **129**(3): p. e28-e292.
109. Zaragoza, C., et al., *Animal Models of Cardiovascular Diseases.* Journal of Biomedicine and Biotechnology, 2011. **2011**.
110. VanBelle, E., et al., *Stent endothelialization - Time course, impact of local catheter delivery, feasibility of recombinant protein administration, and response to cytokine expedition.* Circulation, 1997. **95**(2): p. 438-448.
111. Schwartz, R.S., et al., *Drug-Eluting Stents in Preclinical Studies Updated Consensus Recommendations for Preclinical Evaluation.* Circulation. Cardiovascular interventions, 2008. **1**(2): p. 143-153.
112. Nakazawa, G., et al., *The Significance of Preclinical Evaluation of Sirolimus-, Paclitaxel-, and Zotarolimus-Eluting Stents.* The American Journal of Cardiology, 2007. **100**(8, Supplement 2): p. S36-S44.
113. de Prado, A.P., et al., *Preclinical evaluation of coronary stents: focus on safety issues.* Curr Vasc Pharmacol, 2013. **11**(1): p. 74-99.
114. Virmani, R., et al., *Drug eluting stents: are human and animal studies comparable?* Heart, 2003. **89**(2): p. 133-8.
115. Carpenter, A.W. and M.H. Schoenfisch, *Nitric oxide release: Part II. Therapeutic applications.* Chemical Society Reviews, 2012. **41**(10): p. 3742-3752.
116. Garasic, J.M., et al., *Stent and artery geometry determine intimal thickening independent of arterial injury.* Circulation, 2000. **101**(7): p. 812-8.
117. Rogers, C. and E.R. Edelman, *Endovascular stent design dictates experimental restenosis and thrombosis.* Circulation, 1995. **91**(12): p. 2995-3001.
118. Pfisterer, M., et al., *Late clinical events after clopidogrel discontinuation may limit the benefit of drug-eluting stents: an observational study of drug-eluting versus bare-metal stents.* J Am Coll Cardiol, 2006. **48**(12): p. 2584-91.
119. Hofma, S.H., et al., *Indication of long-term endothelial dysfunction after sirolimus-eluting stent implantation.* Eur Heart J, 2006. **27**(2): p. 166-70.
120. Togni, M., et al., *Sirolimus-eluting stents associated with paradoxic coronary vasoconstriction.* J Am Coll Cardiol, 2005. **46**(2): p. 231-6.
121. Finn, A.V., et al., *Vascular responses to drug eluting stents: importance of delayed healing.* Arterioscler Thromb Vasc Biol, 2007. **27**(7): p. 1500-10.
122. Suzuki, T., et al., *Stent-based delivery of sirolimus reduces neointimal formation in a porcine coronary model.* Circulation, 2001. **104**(10): p. 1188-93.
123. Finn, A.V., et al., *Pathological correlates of late drug-eluting stent thrombosis: strut coverage as a marker of endothelialization.* Circulation, 2007. **115**(18): p. 2435-41.
124. Dangas, G. and F. Kuepper, *Cardiology patient page. Restenosis: repeat narrowing of a coronary artery: prevention and treatment.* Circulation, 2002. **105**(22): p. 2586-7.
125. Mehran, R., et al., *Angiographic Patterns of In-Stent Restenosis: Classification and Implications for Long-Term Outcome.* Circulation, 1999. **100**(18): p. 1872-1878.
126. Kolandaivelu, K., et al., *Stent thrombogenicity early in high-risk interventional settings is driven by stent design and deployment and protected by polymer-drug coatings.* Circulation, 2011. **123**(13): p. 1400-9.

127. Rumbaut, R.E. and P. Thiagarajan, in *Platelet-Vessel Wall Interactions in Hemostasis and Thrombosis*. 2010: San Rafael (CA).
128. Virmani, R. and A. Farb, *Pathology of in-stent restenosis.* Curr Opin Lipidol, 1999. **10**(6): p. 499-506.
129. Moses, J.W., et al., *Sirolimus-eluting stents versus standard stents in patients with stenosis in a native coronary artery.* New England Journal of Medicine, 2003. **349**(14): p. 1315-1323.
130. Oikawa, Y., et al., *Intravascular ultrasound, angioscopic and histopathological characterisation of heterogeneous patterns of restenosis after sirolimus-eluting stent implantation: insights into potential "thromborestenosis" phenomenon.* EuroIntervention, 2010. **6**(3): p. 380-7.
131. Lowe, H.C. and L.M. Khachigian, *Coating stents with antirestenotic drugs: The blunderbuss or the magic bullet?* Circulation, 2002. **105**(4): p. E29-E29.
132. McFadden, E.P., et al., *Late thrombosis in drug-eluting coronary stents after discontinuation of antiplatelet therapy.* Lancet, 2004. **364**(9444): p. 1519-21.
133. Serruys, P.W. and C. Di Mario, *Who was thrombogenic: the stent or the doctor?* Circulation, 1995. **91**(6): p. 1891-3.
134. Silva, J.A., et al., *Primary stenting in acute myocardial infarction: influence of diabetes mellitus in angiographic results and clinical outcome.* Am Heart J, 1999. **138**(3 Pt 1): p. 446-55.
135. Mauri, L., et al., *Twelve or 30 months of dual antiplatelet therapy after drug-eluting stents.* N Engl J Med, 2014. **371**(23): p. 2155-66.
136. Waterhouse, A., et al., *Stability of a therapeutic layer of immobilized recombinant human tropoelastin on a plasma-activated coated surface.* Pharm Res, 2011. **28**(6): p. 1415-21.
137. Waterhouse, A., et al., *The immobilization of recombinant human tropoelastin on metals using a plasma-activated coating to improve the biocompatibility of coronary stents.* Biomaterials, 2010. **31**(32): p. 8332-40.
138. Yin, Y.B., et al., *Covalent immobilisation of tropoelastin on a plasma deposited interface for enhancement of endothelialisation on metal surfaces.* Biomaterials, 2009. **30**(9): p. 1675-1681.
139. Wilson, B.D., et al., *Novel approach for endothelializing vascular devices: understanding and exploiting elastin-endothelial interactions.* Ann Biomed Eng, 2011. **39**(1): p. 337-46.
140. Malik, N., et al., *Intravascular stents: a new technique for tissue processing for histology, immunohistochemistry, and transmission electron microscopy.* Heart, 1998. **80**(5): p. 509-516.
141. Rippstein, P., et al., *Comparison of processing and sectioning methodologies for arteries containing metallic stents.* J Histochem Cytochem, 2006. **54**(6): p. 673-81.
142. Chen, Y.X., et al., *Novel antiinflammatory vascular benefits of systemic and stent-based delivery of ethylisopropylamiloride.* Circulation, 2004. **110**(24): p. 3721-6.
143. Martin, S.L., B. Vrhovski, and A.S. Weiss, *Total Synthesis and Expression in Escherichia-Coli of a Gene Encoding Human Tropoelastin.* Gene, 1995. **154**(2): p. 159-166.
144. Wu, W.J., B. Vrhovski, and A.S. Weiss, *Glycosaminoglycans mediate the coacervation of human tropoelastin through dominant charge interactions involving lysine side chains.* Journal of Biological Chemistry, 1999. **274**(31): p. 21719-21724.
145. Yin, Y.B., et al., *Covalently Bound Biomimetic Layers on Plasma Polymers with Graded Metallic Interfaces for in vivo Implants.* Plasma Processes and Polymers, 2009. **6**(10): p. 658-666.

146. Waterhouse, A., et al., *Stability of a Therapeutic Layer of Immobilized Recombinant Human Tropoelastin on a Plasma-Activated Coated Surface.* Pharmaceutical Research, 2011. **28**(6): p. 1415-1421.
147. Joner, M., et al., *Endothelial cell recovery between comparator polymer-based drug-eluting stents.* Journal of the American College of Cardiology, 2008. **52**(5): p. 333-342.
148. Balakrishnan, B., et al., *Strut position, blood flow, and drug deposition - Implications for single and overlapping drug-eluting stents.* Circulation, 2005. **111**(22): p. 2958-2965.
149. Farooq, V., B.D. Gogas, and P.W. Serruys, *Restenosis Delineating the Numerous Causes of Drug-Eluting Stent Restenosis.* Circulation-Cardiovascular Interventions, 2011. **4**(2): p. 195-205.
150. Waentig, L., et al., *Iodination of proteins, proteomes and antibodies with potassium triodide for LA-ICP-MS based proteomic analyses.* Journal of Analytical Atomic Spectrometry, 2011. **26**(8): p. 1610-1618.
151. Marcela M. Bilek, D.R.M., *Plasma modified surfaces for covalent immobilization of functional biomolecules in the absence of chemical linkers: towards better biosensors and a new generation of medical implants.* Biophysical Reviews, 2010. **2**(2).
152. Schwartz, R.S., N.A. Chronos, and R. Virmani, *Preclinical restenosis models and drug-eluting stents: Still important, still much to learn.* Journal of the American College of Cardiology, 2004. **44**(7): p. 1373-1385.
153. Rogers, C., M.J. Karnovsky, and E.R. Edelman, *Inhibition of Experimental Neointimal Hyperplasia and Thrombosis Depends on the Type of Vascular Injury and the Site of Drug Administration.* Circulation, 1993. **88**(3): p. 1215-1221.
154. Waterhouse, A., et al., *Elastin as a nonthrombogenic biomaterial.* Tissue Eng Part B Rev, 2011. **17**(2): p. 93-9.
155. Almine, J.F., et al., *Elastin-based materials.* Chem Soc Rev, 2010. **39**(9): p. 3371-9.
156. Carmeliet, P., *VEGF gene therapy: stimulating angiogenesis or angioma-genesis?* Nat Med, 2000. **6**(10): p. 1102-3.
157. Farb, A., et al., *Pathology of acute and chronic coronary stenting in humans.* Circulation, 1999. **99**(1): p. 44-52.
158. Farooq, V., B.D. Gogas, and P.W. Serruys, *Restenosis: delineating the numerous causes of drug-eluting stent restenosis.* Circ Cardiovasc Interv, 2011. **4**(2): p. 195-205.
159. Soucy, N.V., et al., *Strut tissue coverage and endothelial cell coverage: a comparison between bare metal stent platforms and platinum chromium stents with and without everolimus-eluting coating.* Eurointervention, 2010. **6**(5): p. 630-637.
160. Carter, A.J., et al., *Coronary stenting with a novel stainless steel balloon-expandable stent: determinants of neointimal formation and changes in arterial geometry after placement in an atherosclerotic model.* J Am Coll Cardiol, 1996. **27**(5): p. 1270-7.
161. Korshunov, V.A., S.M. Schwartz, and B.C. Berk, *Vascular remodeling: hemodynamic and biochemical mechanisms underlying Glagov's phenomenon.* Arterioscler Thromb Vasc Biol, 2007. **27**(8): p. 1722-8.
162. Welt, F.G., et al., *Neutrophil, not macrophage, infiltration precedes neointimal thickening in balloon-injured arteries.* Arterioscler Thromb Vasc Biol, 2000. **20**(12): p. 2553-8.
163. Donachie, M., *Biomedical alloys.* Advanced Materials & Processes, 1998. **154**(1): p. 63-65.
164. Williams, D.F., *Titanium: epitome of biocompatibility or cause for concern.* J Bone Joint Surg Br, 1994. **76**(3): p. 348-9.
165. Cohen, J., *Current concepts review. Corrosion of metal orthopaedic implants.* J Bone Joint Surg Am, 1998. **80**(10): p. 1554.

166. Poncin, P., et al., *Comparing and optimizing Co-Cr tubing for stent applications.* Medical Device Materials II: Proceedings from the Materials & Processes for Medical Devices Conference 2004, 2005: p. 279-283.
167. Poncin, P. and J.L. Proft, *Stent Tubing: Understanding the Desired Attributes.* Medical Device Materials II: Proceedings from the Materials & Processes for Medical Devices Conference 2003, 2003: p. 279-283.
168. International, A., *ASTM F90-14 Standard Specification for Wrought Cobalt-20Chromium-15Tungsten-10Nickel Alloy for Surgical Implant Applications (UNS R30605).*
169. Vascular, A. *MULTI-LINK 8™ SV, MULTI-LINK 8, and MULTI-LINK 8 LL Coronary Stent System*. 2012 [cited 2015 20th June]; Available from: http://www.abbottvascular.com/docs/ifu/coronary_intervention/eIFU_ML8.pdf.
170. Stoeckel D., B.C., Duda S., *A survey of stent designs.* Minim Invasive Ther Allied Technol, 2002. **11**(4): p. 137-47.
171. Duerig, W., *A comparison of balloon- and self-expanding stents.* Minim Invasive Ther Allied Technol, 2002. **11**(4): p. 173-8.
172. Kastrati, A., et al., *Restenosis after coronary placement of various stent types.* Am J Cardiol, 2001. **87**(1): p. 34-9.
173. Elbaz, M., et al., *Does stent design affect the long-term outcome after coronary stenting?* Catheter Cardiovasc Interv, 2002. **56**(3): p. 305-11.
174. Topol, E.J. and P.W. Serruys, *Frontiers in interventional cardiology.* Circulation, 1998. **98**(17): p. 1802-20.
175. Hoffmann, R., et al., *Patterns and mechanisms of in-stent restenosis. A serial intravascular ultrasound study.* Circulation, 1996. **94**(6): p. 1247-54.
176. Kastrati, A., et al., *Intracoronary stenting and angiographic results: strut thickness effect on restenosis outcome (ISAR-STEREO) trial.* Circulation, 2001. **103**(23): p. 2816-21.
177. Kereiakes, D.J., et al., *Usefulness of a cobalt chromium coronary stent alloy.* Am J Cardiol, 2003. **92**(4): p. 463-6.
178. Hoffmann, R., et al., *Stent design related neointimal tissue proliferation in human coronary arteries; an intravascular ultrasound study.* Eur Heart J, 2001. **22**(21): p. 2007-14.
179. Ormiston, J.A., et al., *Six-month results of the NEVO Res-Elution I (NEVO RES-I) trial: a randomized, multicenter comparison of the NEVO sirolimus-eluting coronary stent with the TAXUS Liberte paclitaxel-eluting stent in de novo native coronary artery lesions.* Circ Cardiovasc Interv, 2010. **3**(6): p. 556-64.
180. Honda, Y., *Drug-eluting stents. Insights from invasive imaging technologies.* Circ J, 2009. **73**(8): p. 1371-80.
181. Lagerqvist, B., et al., *Long-term outcomes with drug-eluting stents versus bare-metal stents in Sweden.* N Engl J Med, 2007. **356**(10): p. 1009-19.
182. Pinto Slottow, T.L. and R. Waksman, *Overview of the 2006 Food and Drug Administration Circulatory System Devices Panel meeting on drug-eluting stent thrombosis.* Catheter Cardiovasc Interv, 2007. **69**(7): p. 1064-74.
183. Curfman, G.D., et al., *Drug-eluting coronary stents--promise and uncertainty.* N Engl J Med, 2007. **356**(10): p. 1059-60.
184. Grines, C.L., et al., *Prevention of premature discontinuation of dual antiplatelet therapy in patients with coronary artery stents: a science advisory from the American Heart Association, American College of Cardiology, Society for Cardiovascular Angiography and Interventions, American College of Surgeons, and American Dental*

Association, with representation from the American College of Physicians. Circulation, 2007. **115**(6): p. 813-8.
185. Cutlip, D.E., et al., *Thrombotic complications associated with early and late nonadherence to dual antiplatelet therapy.* JACC Cardiovasc Interv, 2015. **8**(3): p. 404-10.
186. Youssef, A.A., et al., *Cobalt chromium coronary stents and drug-eluting stents in real practice.* Int Heart J, 2010. **51**(4): p. 231-7.
187. Bilek, M.M., McKenzie D.R.,, *Plasma modified surfaces for covalent immobilization of functional biomolecules in the absence of chemical linkers: towards better biosensors and a new generation of medical implants.* Biophys Rev, 2010. **2**(1): p. 55-65.
188. Lewis, A.L. and P.W. Stratford, *Phosphorylcholine-coated stents.* J Long Term Eff Med Implants, 2002. **12**(4): p. 231-50.
189. Otsuka, Y., et al., *Scanning electron microscopic analysis of defects in polymer coatings of three commercially available stents: comparison of BiodivYsio, Taxus and Cypher stents.* J Invasive Cardiol, 2007. **19**(2): p. 71-6.
190. Ormiston, J.A. *Polymer Integrity After CYPHER and TAXUS Stent Implantation: A Scanning Electron Microscopy Study*. TCTMD 2005 [cited 2015 13th June]; Available from: http://www.tctmd.com/show.aspx?id=58632.
191. Regar, E., G. Sianos, and P.W. Serruys, *Stent development and local drug delivery.* Br Med Bull, 2001. **59**: p. 227-48.
192. Fujimoto, Y., Y. Kobayashi, and M. Yamaguchi, *Delamination of abluminal polymer of biolimus-eluting stent.* JACC Cardiovasc Interv, 2012. **5**(3): p. e5-6.
193. Hopkins, C.G., P.E. McHugh, and J.P. McGarry, *Computational investigation of the delamination of polymer coatings during stent deployment.* Ann Biomed Eng, 2010. **38**(7): p. 2263-73.
194. McGarry, J.P., et al., *Computational examination of the effect of material inhomogeneity on the necking of Stent struts under tensile loading.* Journal of Applied Mechanics-Transactions of the Asme, 2007. **74**(5): p. 978-989.
195. Fujimoto, Y., Y. Kobayashi, and M. Yamaguchi, *Delamination of Abluminal Polymer of Biolimus-Eluting Stent.* JACC: Cardiovascular Interventions, 2012. **5**(3): p. e5-e6.
196. Kondyurin, A. and M. Bilek, *Ion Beam Treatment of Polymers: Application Aspects from Medicine to Space*. 2014: Elsevier Science & Technology Books.
197. Kuphaldt, T.R. *Lessons In Electric Circuits -- Volume II*. Lessons In Electric Circuits 2000 [cited 2015; Available from: http://www.ibiblio.org/kuphaldt/electricCircuits/AC/AC_6.html#xtocid98728.
198. Sader, J.E., J.W.M. Chon, and P. Mulvaney, *Calibration of rectangular atomic force microscope cantilevers.* Review of Scientific Instruments, 1999. **70**(10): p. 3967-3969.
199. Sader, J.E. *Normal spring constants of cantilevers of arbitrary shape using the Sader method Optical lever sensitivities using the thermal method* 2014 [cited 2014 31st Oct]; Spring constant calculation]. Available from: http://www.ampc.ms.unimelb.edu.au/afm/webapp.html.
200. Horcas, I., et al., *WSXM: a software for scanning probe microscopy and a tool for nanotechnology.* Rev Sci Instrum, 2007. **78**(1): p. 013705.
201. Miller, J.D., Veeramasuneni, S., Drelich J., Yalamanchili M.R *Effect of Roughness as Determined by Atomic Force Microscopy on the Wetting Properties of PTFE Thin Films.* Polymer Engineering and Science, 1996. **36**(14): p. 1849-1855.
202. Oliver, W.C. and G.M. Pharr, *Measurement of hardness and elastic modulus by instrumented indentation: Advances in understanding and refinements to methodology.* Journal of Materials Research, 2004. **19**(1): p. 3-20.

203. Iakoubovskii, K., et al., *Mean free path of inelastic electron scattering in elemental solids and oxides using transmission electron microscopy: Atomic number dependent oscillatory behavior.* Physical Review B, 2008. **77**(10).
204. Barr, T.L., *Advances in the Application of X-Ray Photoelectron-Spectroscopy (Esca) .2. New Methods.* Critical Reviews in Analytical Chemistry, 1991. **22**(3-4): p. 229-325.
205. Koishi, T., et al., *Coexistence and transition between Cassie and Wenzel state on pillared hydrophobic surface.* Proceedings of the National Academy of Sciences of the United States of America, 2009. **106**(21): p. 8435-8440.
206. Sollier, E., et al., *Rapid prototyping polymers for microfluidic devices and high pressure injections.* Lab on a Chip, 2011. **11**(22): p. 3752-3765.
207. Bilek, M.M.M., *Biofunctionalization of surfaces by energetic ion implantation: Review of progress on applications in implantable biomedical devices and antibody microarrays.* Applied Surface Science, 2014. **310**: p. 3-10.
208. R., J., *Micro/nano scale surface roughness tailoring and its effect on microfluidic flow*, in *Mechanical Engineering*. 2013, Iowa State University: Iowa, USA. p. 174.
209. Kondyurin, A.V., et al., *Mechanisms for covalent immobilization of horseradish peroxidase on ion-beam-treated polyethylene.* Scientifica (Cairo), 2012. **2012**: p. 126170.
210. Zhang, Y. and S. Sundararajan, *Method to generate surfaces with desired roughness parameters.* Langmuir, 2007. **23**(16): p. 8347-51.
211. Rupp, F., et al., *Enhancing surface free energy and hydrophilicity through chemical modification of microstructured titanium implant surfaces.* Journal of Biomedical Materials Research Part A, 2006. **76A**(2): p. 323-334.
212. Prentner, S., et al., *Effects of channel surface finish on blood flow in microfluidic devices.* Microsystem Technologies-Micro-and Nanosystems-Information Storage and Processing Systems, 2010. **16**(7): p. 1091-1096.
213. Werner, C., M.F. Maitz, and C. Sperling, *Current strategies towards hemocompatible coatings.* Journal of Materials Chemistry, 2007. **17**(32): p. 3376-3384.
214. Seeger, J.M., et al., *Hydrophilic Surface Modification of Metallic Endoluminal Stents.* Journal of Vascular Surgery, 1995. **22**(3): p. 327-336.
215. Wilcox, J., *Importance of Polymer biocompatibility for drug eluting stent (DES) outcomes*, in *Biointerface conference* 2010: Les Diablerets, Switzerland
216. Carter, A.J., et al., *Long-term effects of polymer-based, slow-release, sirolimus-eluting stents in a porcine coronary model.* Cardiovascular Research, 2004. **63**(4): p. 617-624.
217. Perkins, L.E.L., et al., *XIENCE V (TM) Everolimus-Eluting Coronary Stent System: A Preclinical Assessment.* Journal of Interventional Cardiology, 2009. **22**: p. S28-S40.
218. Beijk, M.A.M. and J.J. Piek, *XIENCE V everolimus-eluting coronary stent system: a novel second generation drug-eluting stent.* Expert Review of Medical Devices, 2007. **4**(1): p. 11-21.
219. Laskey, W.K., *Cardiovascular device development: drug-eluting stents and implantable devices for the treatment of heart failure--the view from the Circulatory System Advisory Panel.* Am J Ther, 2005. **12**(2): p. 179-82.
220. Kollum, M., et al., *Particle debris from a nanoporous stent coating obscures potential antiproliferative effects of tacrolimus-eluting stents in a porcine model of restenosis.* Catheter Cardiovasc Interv, 2005. **64**(1): p. 85-90.
221. Abdul-Baqi, A. and E. Van der Giessen, *Numerical analysis of indentation-induced cracking of brittle coatings on ductile substrates.* International Journal of Solids and Structures, 2002. **39**(6): p. 1427-1442.
222. Abdul-Baqi, A. and E. Van der Giessen, *Indentation-induced interface delamination of a strong film on a ductile substrate.* Thin Solid Films, 2001. **381**(1): p. 143-154.

223. van der Varst, P.G.T. and G. de With, *Energy based approach to the failure of brittle coatings on metallic substrates.* Thin Solid Films, 2001. **384**(1): p. 85-89.
224. Bilek, M.M., et al., *Free radical functionalization of surfaces to prevent adverse responses to biomedical devices.* Proc Natl Acad Sci U S A, 2011. **108**(35): p. 14405-10.
225. Coutinho D., C.P., Neves N., Gomes M.E., Rui L.R., *Micro and Nanotechnology in Tissue Engineering*, in *Tissue Engineering from Lab to Clinic*, S.C.v. Pallua N., Editor. 2011, Springer: Berlin, Germany.
226. LeDuc, P.P. and R.R. Bellin, *Nanoscale intracellular organization and functional architecture mediating cellular behavior.* Ann Biomed Eng, 2006. **34**(1): p. 102-13.
227. Kaibuchi, K., S. Kuroda, and M. Amano, *Regulation of the cytoskeleton and cell adhesion by the Rho family GTPases in mammalian cells.* Annual Review of Biochemistry, 1999. **68**: p. 459-486.
228. Wozniak, M.A., et al., *Focal adhesion regulation of cell behavior.* Biochimica Et Biophysica Acta-Molecular Cell Research, 2004. **1692**(2-3): p. 103-119.
229. Sarker, B., et al., *Evaluation of Fibroblasts Adhesion and Proliferation on Alginate-Gelatin Crosslinked Hydrogel.* Plos One, 2014. **9**(9).
230. Malmsten, M., *Formation of adsorbed protein layers.* Journal of Colloid and Interface Science, 1998. **207**(2): p. 186-199.
231. Latour, R.A., *Control of biological response by biomaterials surface design.* Abstracts of Papers of the American Chemical Society, 2002. **224**: p. U30-U30.
232. Waterhouse, A., et al., *Elastin as a Nonthrombogenic Biomaterial.* Tissue Engineering Part B-Reviews, 2011. **17**(2): p. 93-99.
233. Thevenot, P., W.J. Hu, and L.P. Tang, *Surface chemistry influences implant biocompatibility.* Current Topics in Medicinal Chemistry, 2008. **8**(4): p. 270-280.
234. Anderson, J.M., *Biological responses to materials.* Annual Review of Materials Research, 2001. **31**: p. 81-110.
235. Touma, H., et al., *Numerical investigation of fluid flow in a chandler loop.* J Biomech Eng, 2014. **136**(7).
236. Baiguera, S. and D. Ribatti, *Endothelialization approaches for viable engineered tissues.* Angiogenesis, 2013. **16**(1): p. 1-14.
237. Ong, A.T.L., et al., *How to accelerate the endothelialization of stents.* Archives Des Maladies Du Coeur Et Des Vaisseaux, 2005. **98**(2): p. 123-126.
238. Kirkpatrick, C.J., et al., *Tissue response and biomaterial integration: the efficacy of in vitro methods.* Biomol Eng, 2002. **19**(2-6): p. 211-7.
239. Treves, C., et al., *In vitro biocompatibility evaluation of surface-modified titanium alloys.* J Biomed Mater Res A, 2010. **92**(4): p. 1623-34.
240. Chen, J.Y., et al., *Behavior of cultured human umbilical vein endothelial cells on titanium oxide films fabricated by plasma immersion ion implantation and deposition.* Surface & Coatings Technology, 2004. **186**(1-2): p. 270-276.
241. Pu, F.R., et al., *Effects of plasma treated PET and PTFE on expression of adhesion molecules by human endothelial cells in vitro.* Biomaterials, 2002. **23**(11): p. 2411-2428.
242. Sanborn, S.L., et al., *Endothelial cell formation of focal adhesions on hydrophilic plasma polymers.* Biomaterials, 2002. **23**(1): p. 1-8.
243. Vranckx, P., et al., *Identifying stent thrombosis, a critical appraisal of the academic research consortium (ARC) consensus definitions: a lighthouse and as a toe in the water.* EuroIntervention, 2008. **4 Suppl C**: p. C39-44.

244. Zhang, K., et al., *Surface modification of implanted cardiovascular metal stents: From antithrombosis and antirestenosis to endothelialization.* Journal of Biomedical Materials Research Part A, 2014. **102**(2): p. 588-609.
245. Undas, A. and R.A. Ariens, *Fibrin clot structure and function: a role in the pathophysiology of arterial and venous thromboembolic diseases.* Arterioscler Thromb Vasc Biol, 2011. **31**(12): p. e88-99.
246. Grove, E.L., et al., *Increased platelet turnover in patients with previous definite stent thrombosis.* J Thromb Haemost, 2011. **9**(7): p. 1418-9.
247. Kristensen, S.L., et al., *Stent thrombosis is the primary cause of ST-segment elevation myocardial infarction following coronary stent implantation: a five year follow-up of the SORT OUT II study.* PLoS One, 2014. **9**(11): p. e113399.
248. Clemmensen, P., et al., *Acute stent thrombosis after primary percutaneous coronary intervention: insights from the EUROMAX trial (European Ambulance Acute Coronary Syndrome Angiography).* JACC Cardiovasc Interv, 2015. **8**(1 Pt B): p. 214-20.
249. Niccoli, G., et al., *The evolving role of inflammatory biomarkers in risk assessment after stent implantation.* J Am Coll Cardiol, 2010. **56**(22): p. 1783-93.
250. Kristensen, S.D., Grove E. C. L. *Stent thrombosis: definitions, mechanisms and prevention*. 2008 08 May 2007 [cited 2015; Available from: http://www.escardio.org/Guidelines-&-Education/Journals-and-publications/ESC-journals-family/E-journal-of-Cardiology-Practice/Volume-5/Stent-thrombosis-definitions-mechanisms-and-prevention-Title-Stent-thrombos.
251. Chandler, A.B., *In vitro thrombotic coagulation of the blood; a method for producing a thrombus.* Lab Invest, 1958. **7**(2): p. 110-4.
252. Gaamangwe, T., S. Peterson, and M. Gorbet, *Investigating the Effect of Blood Sample Volume in the Chandler Loop Model: Theoretical and Experimental Analysis.* Cardiovascular Engineering and Technology, 2014. **5**(2): p. 133-144.
253. Glagov, S., et al., *Hemodynamics and atherosclerosis. Insights and perspectives gained from studies of human arteries.* Arch Pathol Lab Med, 1988. **112**(10): p. 1018-31.
254. Sinn, S., et al., *A novel in vitro model for preclinical testing of the hemocompatibility of intravascular stents according to ISO 10993-4.* J Mater Sci Mater Med, 2011. **22**(6): p. 1521-8.
255. Tepe, G., et al., *Thrombogenicity of various endovascular stent types: an in vitro evaluation.* J Vasc Interv Radiol, 2002. **13**(10): p. 1029-35.
256. Hirsh, J., et al., *Guide to Anticoagulant Therapy: Heparin: A Statement for Healthcare Professionals From the American Heart Association.* Circulation, 2001. **103**(24): p. 2994-3018.
257. Wei, Q., et al., *Protein Interactions with Polymer Coatings and Biomaterials.* Angewandte Chemie International Edition, 2014. **53**(31): p. 8004-8031.
258. Stuart, M.A.C., et al., *Emerging applications of stimuli-responsive polymer materials.* Nat Mater, 2010. **9**(2): p. 101-113.
259. Vogler, E.A., *Structure and reactivity of water at biomaterial surfaces.* Advances in Colloid and Interface Science, 1998. **74**(1–3): p. 69-117.
260. Stuart, M.A., et al., *Emerging applications of stimuli-responsive polymer materials.* Nat Mater, 2010. **9**(2): p. 101-13.
261. Hoffman, A.S., *The origins and evolution of "controlled" drug delivery systems.* Journal of Controlled Release, 2008. **132**(3): p. 153-163.
262. Mendes, P.M., *Stimuli-responsive surfaces for bio-applications.* Chem Soc Rev, 2008. **37**(11): p. 2512-29.
263. Rant, U., et al., *Dynamic electrical switching of DNA layers on a metal surface.* Nano Letters, 2004. **4**(12): p. 2441-2445.

264. Zhang, K., et al., *Surface modification of implanted cardiovascular metal stents: from antithrombosis and antirestenosis to endothelialization.* J Biomed Mater Res A, 2014. **102**(2): p. 588-609.
265. Chen, J.Y., et al., *Effect of hydrogen on the behavior of cultured human umbilical vein endothelial cells (HUVEC) on titanium oxide films fabricated by plasma immersion ion implantation and deposition.* Surface & Coatings Technology, 2007. **201**(19-20): p. 8140-8145.
266. Huang, N., et al., *Surface modification of biomaterials by plasma immersion ion implantation.* Surface and Coatings Technology, 2004. **186**(1–2): p. 218-226.
267. Shao, H.H., et al., *Influence of Ti nanocrystallization on microstructure, interface bonding, surface energy and blood compatibility of surface TiO2 films.* Applied Surface Science, 2010. **257**(5): p. 1649-1654.
268. Shahryari, A., et al., *The positive influence of electrochemical cyclic potentiodynamic passivation (CPP) of a SS316LS surface on its response to fibronectin and pre-osteoblasts.* Phys Chem Chem Phys, 2009. **11**(29): p. 6218-24.
269. Yang, Z., et al., *The covalent immobilization of heparin to pulsed-plasma polymeric allylamine films on 316L stainless steel and the resulting effects on hemocompatibility.* Biomaterials, 2010. **31**(8): p. 2072-2083.
270. Leng, Y.X., et al., *The biocompatibility of the tantalum and tantalum oxide films synthesized by pulse metal vacuum arc source deposition.* Nuclear Instruments and Methods in Physics Research Section B: Beam Interactions with Materials and Atoms, 2006. **242**(1–2): p. 30-32.
271. Freitas, S.C., et al., *Bioengineered surfaces to improve the blood compatibility of biomaterials through direct thrombin inactivation.* Acta Biomaterialia, 2012. **8**(11): p. 4101-4110.
272. Chen, M., S. Osaki, and P.O. Zamora, *Biological response of stainless steel surface modified by N2O/O-2 glow discharge plasma.* Applied Surface Science, 2009. **255**(16): p. 7257-7262.
273. Shen, Y., et al., *Investigation of surface endothelialization on biomedical nitinol (NiTi) alloy: Effects of surface micropatterning combined with plasma nanocoatings.* Acta Biomater, 2009. **5**(9): p. 3593-604.
274. Thierry, B., et al., *Radionuclides-hyaluronan-conjugate thromboresistant coatings to prevent in-stent restenosis.* Biomaterials, 2004. **25**(17): p. 3895-3905.
275. Tellez, A., et al., *Very Long-Term (1 and 2-Year) Comparison of Bioresorbable Vs. Permanent Polymer Limus-Eluting Stents in a Porcine Coronary Artery Model.* Journal of the American College of Cardiology, 2012. **59**(13): p. E223-E223.
276. Wise, S.G., et al., *Tropoelastin: a versatile, bioactive assembly module.* Acta Biomater, 2014. **10**(4): p. 1532-41.
277. Bax, D.V., et al., *Cell Adhesion to Tropoelastin Is Mediated via the C-terminal GRKRK Motif and Integrin α(V)β(3).* The Journal of Biological Chemistry, 2009. **284**(42): p. 28616-28623.
278. Kielty, C.M., et al., *Applying elastic fibre biology in vascular tissue engineering.* Philos Trans R Soc Lond B Biol Sci, 2007. **362**(1484): p. 1293-312.
279. Tersteeg, C., et al., *A fibronectin-fibrinogen-tropoelastin coating reduces smooth muscle cell growth but improves endothelial cell function.* Journal of Cellular and Molecular Medicine, 2012. **16**(9): p. 2117-2126.
280. Williamson, M.R., et al., *The role of endothelial cell attachment to elastic fibre molecules in the enhancement of monolayer formation and retention, and the inhibition of smooth muscle cell recruitment.* Biomaterials, 2007. **28**(35): p. 5307-5318.

281. Martin, S.L., B. Vrhovski, and A.S. Weiss, *Total synthesis and expression in Escherichia coli of a gene encoding human tropoelastin.* Gene, 1995. **154**(2): p. 159-66.
282. Latour, R.A., *Biomaterials: Protein-Surface Interactions*, in *Encyclopedia of Biomaterials and Biomedical Engineering*. 2005, Taylor and Francis.
283. Collins, T.J., *ImageJ for microscopy.* Biotechniques, 2007. **43**(1): p. 25-+.
284. Gardner, R.A., *An examination of the fluid mechanics and thrombus formation time parameters in a Chandler rotating loop system.* J Lab Clin Med, 1974. **84**(4): p. 494-508.
285. Shlyakhtenko, L.S., et al., *Atomic force microscopy imaging of DNA covalently immobilized on a functionalized mica substrate.* Biophys J, 1999. **77**(1): p. 568-76.
286. Zhou, S., *Separation and detection methods for covalent drug-protein adducts.* J Chromatogr B Analyt Technol Biomed Life Sci, 2003. **797**(1-2): p. 63-90.
287. Wrenn, D.S., et al., *Characterization of biologically active domains on elastin: identification of a monoclonal antibody to a cell recognition site.* Biochemistry, 1986. **25**(18): p. 5172-6.
288. Humphries, M.J., *Cell adhesion assays.* Methods Mol Biol, 2009. **522**: p. 203-10.
289. *SECTION II.6 - Applications of Biomaterials in Functional Tissue Engineering*, in *Biomaterials Science (Third Edition)*, B.D.R.S.H.J.S.E. Lemons, Editor. 2013, Academic Press. p. 1119-1122.
290. Huh, D., et al., *Microfabrication of human organs-on-chips.* Nat. Protocols, 2013. **8**(11): p. 2135-2157.
291. Ingber, D.E., *Cellular tensegrity: defining new rules of biological design that govern the cytoskeleton.* J Cell Sci, 1993. **104 (Pt 3)**: p. 613-27.
292. Gorbet, M.B. and M.V. Sefton, *Biomaterial-associated thrombosis: roles of coagulation factors, complement, platelets and leukocytes.* Biomaterials, 2004. **25**(26): p. 5681-5703.
293. Turitto, V.T., H.J. Weiss, and H.R. Baumgartner, *The effect of shear rate on platelet interaction with subendothelium exposed to citrated human blood.* Microvascular Research, 1980. **19**(3): p. 352-365.
294. Foin, N., et al., *Incomplete Stent Apposition Causes High Shear Flow Disturbances and Delay in Neointimal Coverage as a Function of Strut to Wall Detachment Distance: Implications for the Management of Incomplete Stent Apposition.* Circulation: Cardiovascular Interventions, 2014. **7**(2): p. 180-189.
295. Kono, K. and T. Terada, *Hemodynamics of 8 Different Configurations of Stenting for Bifurcation Aneurysms.* American Journal of Neuroradiology, 2013. **34**(10): p. 1980-1986.
296. Desroches, M.J. and S. Omanovic, *Adsorption of fibrinogen on a biomedical-grade stainless steel 316LVM surface: a PM-IRRAS study of the adsorption thermodynamics, kinetics and secondary structure changes.* Phys Chem Chem Phys, 2008. **10**(18): p. 2502-12.
297. Siegismund, D., et al., *Quantitative Modeling of Fibrinogen Adsorption on Different Biomaterials.* Cellular and Molecular Bioengineering, 2013. **6**(2): p. 210-219.
298. Collet, J.P., et al., *The elasticity of an individual fibrin fiber in a clot.* Proc Natl Acad Sci U S A, 2005. **102**(26): p. 9133-7.
299. AAMI, A.f.t.A.o.M.I. *Biological evaluation of medical devices - part 4: Selection of tests for interactions with blood* American National Standards, 2013. **02**, 13.
300. Health, C.f.D.a.R. *Use of International Standard ISO-10993, Biological Evaluation of Medical Devices Part 1: Evaluation and Testing*. Draft Guidance for Industry and Food and Drug Administration, 2013. **02**.

301. National Heart, L., I. Blood, and H. National Institutes of, *Guidelines for blood-material interactions: report of the National Heart, Lung, and Blood Insitute Working Group*. NIH publication ;no. 85-2185. 1985, [Bethesda, Md.]: U.S. Dept. of Health and Human Services, Public Health Service, National Institutes of Health. vi, 362, A-53 p.
302. Chen, E.A., et al., *FDA's perspectives on cardiovascular devices.* J Cardiovasc Transl Res, 2009. **2**(2): p. 143-6.
303. Maitz, M.F., et al., *Surface endotoxin contamination and hemocompatibility evaluation of materials.* Journal of Biomedical Materials Research - Part B Applied Biomaterials, 2009. **90 B**(1): p. 18-25.
304. Sinn, S., et al., *A novel in vitro model for preclinical testing of the hemocompatibility of intravascular stents according to ISO 10993-4.* Journal of Materials Science: Materials in Medicine, 2011. **22**(6): p. 1521-1528.
305. Coughlin, S.R., *Thrombin signalling and protease-activated receptors.* Nature, 2000. **407**(6801): p. 258-64.
306. Monroe, D.M., M. Hoffman, and H.R. Roberts, *Platelets and thrombin generation.* Arterioscler Thromb Vasc Biol, 2002. **22**(9): p. 1381-9.
307. Hoffman, M. and D.M. Monroe, 3rd, *A cell-based model of hemostasis.* Thromb Haemost, 2001. **85**(6): p. 958-65.
308. Inc, U.L.S. *Beta-Thromboglobulin (bTG)*. 2009-2015.
309. Kaplan, K.L. and J. Owen, *Plasma-Levels of Beta-Thromboglobulin and Platelet Factor-4 as Indexes of Platelet Activation Invivo.* Blood, 1981. **57**(2): p. 199-202.
310. Nichols, A.B., et al., *Fibrinopeptide-a, Platelet Factor-4, and Beta-Thromboglobulin Levels in Coronary Heart-Disease.* Blood, 1982. **60**(3): p. 650-654.
311. Pumphrey, C.W. and J. Dawes, *Plasma beta-thromboglobulin as a measure of platelet activity: Effect of risk factors and findings in ischemic heart disease and after acute myocardial infarction.* The American Journal of Cardiology, 1982. **50**(6): p. 1258-1261.
312. Courtney, J.M., Travers, J.T., Douglas, G.D.O., Lowe, C.D., Forbes, C.J., Ryan S.K., Prentice C.R.M, *Assessment of blood biocompatibility*, in *Blood compatible materials and their testing* S. Dawids, Editor. 1986, Springer: Netherlands.
313. Mayer, A., et al., *The role of nanoparticle size in hemocompatibility.* Toxicology, 2009. **258**(2–3): p. 139-147.
314. Gebert, A., et al., *[Comparative analysis of in vitro test procedures for evaluating hemocompatibility of cardiovascular stents]*. Biomed Tech (Berl), 2002. **47 Suppl 1 Pt 2**: p. 827-30.
315. Merten, M. and P. Thiagarajan, *P-selectin in arterial thrombosis.* Z Kardiol, 2004. **93**(11): p. 855-63.
316. Ikeda, H., et al., *Increased soluble form of P-selectin in patients with unstable angina.* Circulation, 1995. **92**(7): p. 1693-6.
317. Hollander, J.E., et al., *Risk stratification of emergency department patients with acute coronary syndromes using P-Selectin.* Journal of the American College of Cardiology, 1999. **34**(1): p. 95-105.
318. Gawaz, M., et al., *Changes in membrane glycoproteins of circulating platelets after coronary stent implantation.* Heart, 1996. **76**(2): p. 166-72.
319. Blann, A.D., E.B. Faragher, and C.N. McCollum, *Increased soluble P-selectin following myocardial infarction: a new marker for the progression of atherosclerosis.* Blood Coagul Fibrinolysis, 1997. **8**(7): p. 383-90.
320. Ridker, P.M., J.E. Buring, and N. Rifai, *Soluble P-selectin and the risk of future cardiovascular events.* Circulation, 2001. **103**(4): p. 491-5.

321. Ishiwata, N., et al., *Alternatively spliced isoform of P-selectin is present in vivo as a soluble molecule.* J Biol Chem, 1994. **269**(38): p. 23708-15.
322. Andre, P., et al., *Pro-coagulant state resulting from high levels of soluble P-selectin in blood.* Proc Natl Acad Sci U S A, 2000. **97**(25): p. 13835-40.
323. Subramaniam, M., et al., *Defects in hemostasis in P-selectin-deficient mice.* Blood, 1996. **87**(4): p. 1238-42.
324. Michelson, A.D., et al., *Circulating monocyte-platelet aggregates are a more sensitive marker of in vivo platelet activation than platelet surface P-selectin: studies in baboons, human coronary intervention, and human acute myocardial infarction.* Circulation, 2001. **104**(13): p. 1533-7.
325. Carter, A.M., *Complement activation: an emerging player in the pathogenesis of cardiovascular disease.* Scientifica (Cairo), 2012. **2012**: p. 402783.
326. Hogasen, K., et al., *Characterization of soluble terminal complement complex assembled in C8beta-deficient plasma and serum.* Scand J Immunol, 1998. **48**(3): p. 261-8.
327. Lambris, J.D., D. Ricklin, and B.V. Geisbrecht, *Complement evasion by human pathogens.* Nat Rev Micro, 2008. **6**(2): p. 132-142.
328. Videm, V., et al., *Reduced complement activation with heparin-coated oxygenator and tubings in coronary bypass operations.* J Thorac Cardiovasc Surg, 1992. **103**(4): p. 806-13.
329. Théroux, P. and C. Martel, *Complement activity and pharmacological inhibition in cardiovascular disease.* The Canadian Journal of Cardiology, 2006. **22**(Suppl B): p. 18B-24B.
330. Deservi, S., et al., *Granulocyte Activation after Coronary Angioplasty in Humans.* Circulation, 1990. **82**(1): p. 140-146.
331. Inoue, T., et al., *Stent-induced expression and activation of the leukocyte integrin Mac-1 is associated with neointimal thickening and restenosis.* Circulation, 2003. **107**(13): p. 1757-1763.
332. Gach, O., et al., *Early release of neutrophil markers of activation after direct stenting in patients with unstable angina.* Coronary Artery Disease, 2005. **16**(1): p. 59-65.
333. Brennan, M.-L., et al., *Prognostic Value of Myeloperoxidase in Patients with Chest Pain.* New England Journal of Medicine, 2003. **349**(17): p. 1595-1604.
334. Andersen, J.C., *Hemostasis and Thrombosis—Basic Principles and Clinical Practice.* Annals of Surgery, 1983. **197**(1): p. 116-117.
335. Neumann, F.-J., et al., *Neutrophil and platelet activation at balloon-injured coronary artery plaque in patients undergoing angioplasty.* Journal of the American College of Cardiology, 1996. **27**(4): p. 819-824.
336. Wilson, C.J., et al., *Mediation of biomaterial-cell interactions by adsorbed proteins: a review.* Tissue Eng, 2005. **11**(1-2): p. 1-18.
337. Turbill, P., T. Beugeling, and A.A. Poot, *Proteins involved in the Vroman effect during exposure of human blood plasma to glass and polyethylene.* Biomaterials, 1996. **17**(13): p. 1279-87.
338. Vroman, L. and A.L. Adams, *Identification of rapid changes at plasma–solid interfaces.* Journal of Biomedical Materials Research, 1969. **3**(1): p. 43-67.
339. Vilaseca, P., K.A. Dawson, and G. Franzese, *Understanding and modulating the competitive surface-adsorption of proteins through coarse-grained molecular dynamics simulations.* Soft Matter, 2013. **9**(29): p. 6978-6985.
340. LeDuc, C.A., L. Vroman, and E.F. Leonard, *A Mathematical Model for the Vroman Effect.* Industrial & Engineering Chemistry Research, 1995. **34**(10): p. 3488-3495.

341. Green, R.J., et al., *Competitive protein adsorption as observed by surface plasmon resonance.* Biomaterials, 1999. **20**(4): p. 385-391.
342. Knetsch, M.L.W., Y.B.J. Aldenhoff, and L.H. Koole, *The effect of high-density-lipoprotein on thrombus formation on and endothelial cell attachement to biomaterial surfaces.* Biomaterials, 2006. **27**(14): p. 2813-2819.
343. Jeyachandran, Y.L., et al., *Quantitative and Qualitative Evaluation of Adsorption/Desorption of Bovine Serum Albumin on Hydrophilic and Hydrophobic Surfaces.* Langmuir, 2009. **25**(19): p. 11614-11620.
344. Wertz, C.F. and M.M. Santore, *Fibrinogen Adsorption on Hydrophilic and Hydrophobic Surfaces: Geometrical and Energetic Aspects of Interfacial Relaxations.* Langmuir, 2002. **18**(3): p. 706-715.
345. Hong, J., et al., *Material-specific thrombin generation following contact between metal surfaces and whole blood.* Biomaterials, 2005. **26**(12): p. 1397-1403.
346. Seegers, W.H., J.F. Johnson, and C. Fell, *An antithrombin reaction to prothrombin activation.* Am J Physiol, 1954. **176**(1): p. 97-103.
347. Seegers, W.H., *Antithrombin III: a backward glance o'er travel'd roads.* Adv Exp Med Biol, 1975. **52**: p. 195-215.
348. Maaroufi, R.M., et al., *Mechanism of thrombin inhibition by antithrombin and heparin cofactor II in the presence of heparin.* Biomaterials, 1997. **18**(3): p. 203-211.
349. Jordan, R., D. Beeler, and R. Rosenberg, *Fractionation of Low-Molecular Weight Heparin Species and Their Interaction with Anti-Thrombin.* Journal of Biological Chemistry, 1979. **254**(8): p. 2902-2913.
350. Machovich, R., *Mechanism of action of heparin through thrombin on blood coagulation.* Biochim Biophys Acta, 1975. **412**(1): p. 13-7.
351. Griffith, M.J., *The heparin-enhanced antithrombin III/thrombin reaction is saturable with respect to both thrombin and antithrombin III.* J Biol Chem, 1982. **257**(23): p. 13899-302.
352. Rubenstein, M.D. and R.T. Wall, *Clinical use of beta-thromboglobulin levels in diagnosing and treating consumptive and immune thrombocytopenia.* Am J Hematol, 1981. **10**(4): p. 369-73.
353. Kaplan, K. and J. Owen, *Plasma levels of beta-thromboglobulin and platelet factor 4 as indices of platelet activation in vivo*. Vol. 57. 1981. 199-202.
354. Fateh-Moghadam, S., et al., *Platelet degranulation is associated with progression of intima-media thickness of the common carotid artery in patients with diabetes mellitus type 2.* Arteriosclerosis Thrombosis and Vascular Biology, 2005. **25**(6): p. 1299-1303.
355. Rao, G.H.R. and T. Chandy, *Role of platelets in blood-biomaterial interactions.* Bulletin of Materials Science, 1999. **22**(3): p. 633-639.
356. Vroman, L., *The Life of an Artificial Device in Contact with Blood - Initial Events and Their Effect on Its Final-State.* Bulletin of the New York Academy of Medicine, 1988. **64**(4): p. 352-357.
357. Michelson, A.D., et al., *The Activation-Induced Decrease in the Platelet Surface Expression of the Glycoprotein Ib-Ix Complex Is Reversible.* Blood, 1994. **83**(12): p. 3562-3573.
358. Ushiyama, S., et al., *Structural and functional characterization of monomeric soluble P-selectin and comparison with membrane P-selectin.* J Biol Chem, 1993. **268**(20): p. 15229-37.
359. Spycher, M.O. and U.E. Nydegger, *Participation of the Blood Platelet in Immune Reactions Due to Platelet-Complement Interaction.* Transfusion Medicine and Hemotherapy, 1995. **22**(1): p. 36-43.

360. Kourtzelis, I., et al., *Inhibition of biomaterial-induced complement activation attenuates the inflammatory host response to implantation.* The FASEB Journal, 2013. **27**(7): p. 2768-2776.
361. Nilsson, B., et al., *The role of complement in biomaterial-induced inflammation.* Molecular Immunology, 2007. **44**(1–3): p. 82-94.
362. Andersson, J., et al., *Binding of C3 fragments on top of adsorbed plasma proteins during complement activation on a model biomaterial surface.* Biomaterials, 2005. **26**(13): p. 1477-1485.
363. Ekdahl, K.N., et al., *Complement Activation on Radio-Frequency Plasma Modified Polystyrene Surfaces.* Journal of Colloid and Interface Science, 1993. **158**(1): p. 121-128.
364. Nilsson, B., et al., *Can cells and biomaterials in therapeutic medicine be shielded from innate immune recognition?* Trends in Immunology, 2010. **31**(1): p. 32-38.
365. Anderson, J.M., *Chapter 4 Mechanisms of inflammation and infection with implanted devices.* Cardiovascular Pathology, 1993. **2**(3, Supplement): p. 33-41.
366. Brodbeck, W.G., et al., *In vivo leukocyte cytokine mRNA responses to biomaterials are dependent on surface chemistry.* Journal of Biomedical Materials Research Part A, 2003. **64A**(2): p. 320-329.
367. American Heart, A. *Presentation Abstract*. Scientific Sessions 2013 2013 [cited 2015 210915]; Presentation Abstract]. Available from: http://www.abstractsonline.com/plan/ViewAbstract.aspx?mID=3281&sKey=d544c41a-6178-4b68-b82a-98c6d99b425a&cKey=0e10b366-bcc7-40d1-a10c-589444146d17&mKey=951e351e-429c-4b2e-84d0-8da73b00de45.
368. Jeewandara, T., et al., *PM049 Bioengineering Stents With Proactive Biocompatibility.* Global Heart. **9**(1): p. e70-e71.
369. Jeewandara, T., et al., *Abstract 387: Bioengineering L-605 Cobalt Chromium Cardiovascular Stent Biomaterial With Plasma Activated Coating, for Proactive Biocompatibility.* Arteriosclerosis, Thrombosis, and Vascular Biology, 2015. **35**(Suppl 1): p. A387.
370. Yin, Y., et al., *Plasma Polymer Surfaces Compatible with a CMOS Process for Direct Covalent Enzyme Immobilization.* Plasma Processes and Polymers, 2009. **6**(1): p. 68-75.
371. *Front Matter*, in *Biomaterials Science (Third Edition)*, B.D.R.S.H.J.S.E. Lemons, Editor. 2013, Academic Press. p. iii.
372. Jukema, J.W., et al., *Restenosis after PCI. Part 2: prevention and therapy.* Nature Reviews Cardiology, 2012. **9**(2): p. 79-90.
373. Radeleff, B., et al., *Restenosis of the CYPHER-Select, TAXUS-Express, and Polyzene-F Nanocoated Cobalt-Chromium Stents in the Minipig Coronary Artery Model.* CardioVascular and Interventional Radiology, 2008. **31**(5): p. 971-980.
374. Chorny, M., et al., *Targeting stents with local delivery of paclitaxel-loaded magnetic nanoparticles using uniform fields.* Proc Natl Acad Sci U S A, 2010. **107**(18): p. 8346-51.
375. Ostojic, M., et al., *The pharmacokinetics of Biolimus A9 after elution from the Nobori stent in patients with coronary artery disease: The NOBORI PK study.* Catheterization and Cardiovascular Interventions, 2008. **72**(7): p. 901-908.
376. Ostojic, M.C., et al., *The pharmacokinetics of Biolimus A9 after elution from the BioMatrix II stent in patients with coronary artery disease: The Stealth PK Study.* European Journal of Clinical Pharmacology, 2011. **67**(4): p. 389-398.

377. Serruys, P.W., et al., *A randomised comparison of novolimus-eluting and zotarolimus-eluting coronary stents: 9-month follow-up results of the EXCELLA II study.* EuroIntervention, 2010. **6**(2): p. 195-205.
378. Udipi, K., et al., *The next generation Endeavor Resolute Stent: role of the BioLinx Polymer System.* EuroIntervention, 2007. **3**(1): p. 137-9.
379. Tamburino, C., et al., *First-in-Man 1-Year Clinical Outcomes of the Catania Coronary Stent System With Nanothin Polyzene-F in De Novo Native Coronary Artery Lesions: The ATLANTA (Assessment of The LAtest Non-Thrombogenic Angioplasty stent) Trial.* JACC: Cardiovascular Interventions, 2009. **2**(3): p. 197-204.
380. Windecker, S., et al., *Biolimus-eluting stent with biodegradable polymer versus sirolimus-eluting stent with durable polymer for coronary revascularisation (LEADERS): a randomised non-inferiority trial.* The Lancet. **372**(9644): p. 1163-1173.
381. Byrne, R.A., et al., *Randomized, non-inferiority trial of three limus agent-eluting stents with different polymer coatings: the Intracoronary Stenting and Angiographic Results: Test Efficacy of 3 Limus-Eluting Stents (ISAR-TEST-4) Trial.* European Heart Journal, 2009. **30**(20): p. 2441-2449.
382. Tada, N., et al., *Polymer-Free Biolimus A9-Coated Stent Demonstrates More Sustained Intimal Inhibition, Improved Healing, and Reduced Inflammation Compared With a Polymer-Coated Sirolimus-Eluting Cypher Stent in a Porcine Model.* Circulation: Cardiovascular Interventions, 2010. **3**(2): p. 174-183.
383. Co, M., et al., *Use of endothelial progenitor cell capture stent (Genous Bio-Engineered R Stent) during primary percutaneous coronary intervention in acute myocardial infarction: Intermediate- to long-term clinical follow-up.* American Heart Journal, 2008. **155**(1): p. 128-132.
384. Lee, Y.P., et al., *Endothelial progenitor cell capture stent implantation in patients with ST-segment elevation acute myocardial infarction: one year follow-up.* Eurointervention, 2010. **5**(6): p. 698-702.
385. Granada, J.F., et al., *Development of a Novel Prohealing Stent Designed to Deliver Sirolimus From a Biodegradable Abluminal Matrix.* Circulation: Cardiovascular Interventions, 2010. **3**(3): p. 257-266.
386. Garg, S. and P.W. Serruys, *Coronary Stents: Looking Forward.* Journal of the American College of Cardiology, 2010. **56**(10, Supplement): p. S43-S78.
387. Windecker, S., et al., *Randomized Comparison of a Titanium-Nitride-Oxide–Coated Stent With a Stainless Steel Stent for Coronary Revascularization: The TiNOX Trial.* Circulation, 2005. **111**(20): p. 2617-2622.
388. Moschovitis, A., et al., *Randomised comparison of titanium-nitride-oxide coated stents with bare metal stents: five year follow-up of the TiNOX trial.* Eurointervention, 2010. **6**(1): p. 63-68.
389. Pilgrim, T., et al., *Comparison of Titanium-Nitride-Oxide–Coated Stents With Zotarolimus-Eluting Stents for Coronary Revascularization: A Randomized Controlled Trial.* JACC: Cardiovascular Interventions, 2011. **4**(6): p. 672-682.
390. Serruys, P.W., et al., *A bioabsorbable everolimus-eluting coronary stent system (ABSORB): 2-year outcomes and results from multiple imaging methods.* Lancet, 2009. **373**(9667): p. 897-910.
391. Erbel, R., et al., *Temporary scaffolding of coronary arteries with bioabsorbable magnesium stents: a prospective, non-randomised multicentre trial.* Lancet, 2007. **369**(9576): p. 1869-75.
392. Tanimoto, S., et al., *Comparison of in vivo acute stent recoil between the bioabsorbable everolimus-eluting coronary stent and the everolimus-eluting cobalt chromium*

coronary stent: Insights from the ABSORB and SPIRIT trials. Catheterization and Cardiovascular Interventions, 2007. **70**(4): p. 515-523.
393. Bhargava, B., et al., *A novel paclitaxel-eluting porous carbon-carbon nanoparticle coated, nonpolymeric cobalt-chromium stent: Evaluation in a porcine model.* Catheterization and Cardiovascular Interventions, 2006. **67**(5): p. 698-702.
394. Luderer, F., et al., *Biodegradable Sirolimus-loaded Poly(lactide) Nanoparticles as Drug Delivery System for the Prevention of In-Stent Restenosis in Coronary Stent Application.* Journal of Biomaterials Applications, 2011. **25**(8): p. 851-875.
395. Pache, J., et al., *Intracoronary stenting and angiographic results: Strut thickness effect on restenosis outcome (ISAR-STEREO-2) trial.* Journal of the American College of Cardiology, 2003. **41**(8): p. 1283-1288.
396. Brito, L.A., et al., *Non-viral eNOS gene delivery and transfection with stents for the treatment of restenosis.* Biomedical Engineering Online, 2010. **9**.
397. Takemoto, Y., et al., *Human Placental Ectonucleoside Triphosphate Diphosphohydrolase Gene Transfer via Gelatin-Coated Stents Prevents In-Stent Thrombosis.* Arteriosclerosis Thrombosis and Vascular Biology, 2009. **29**(6): p. 857-U207.
398. Yao, E.H., et al., *A pyrrole-imidazole polyamide targeting transforming growth factor-beta1 inhibits restenosis and preserves endothelialization in the injured artery.* Cardiovasc Res, 2009. **81**(4): p. 797-804.
399. Pires, N.M., et al., *Activation of nuclear receptor Nur77 by 6-mercaptopurine protects against neointima formation.* Circulation, 2007. **115**(4): p. 493-500.
400. Pesarini, G., et al., *Cytokines release inhibition from activated monocytes, and reduction of in-stent neointimal growth in humans.* Atherosclerosis, 2010. **211**(1): p. 242-8.
401. Lee, S.W., et al., *Drug-eluting stenting followed by cilostazol treatment reduces late restenosis in patients with diabetes mellitus the DECLARE-DIABETES Trial (A Randomized Comparison of Triple Antiplatelet Therapy with Dual Antiplatelet Therapy After Drug-Eluting Stent Implantation in Diabetic Patients).* J Am Coll Cardiol, 2008. **51**(12): p. 1181-7.
402. Jennings, D.L. and J.S. Kalus, *Addition of cilostazol to aspirin and a thienopyridine for prevention of restenosis after coronary artery stenting: a meta-analysis.* J Clin Pharmacol, 2010. **50**(4): p. 415-21.

Appendix A

Matlab Code 1 used to calculate the surface stiffness based on unloading displacement vs load for 21 indents from nanoindentation data.

Indentation_code.m

```
n=1;
x=1;
for n=1:1:10
    C=zeros(11,2);
    for x=1:1:11
        C(x,1)=B((P(n,1)+x-1),1);
        C(x,2)=A ((P(n,1)+x-1),1);
    end
    fit=polyfit(C(:,1),C(:,2),1);
    S(n,2)=fit(1,1);
end


figure(1)
loglog(S(:,1),S(:,2),'K.')
```